CENTRO DE INVESTIGACIÓN Y DE ESTUDIOS AVANZADOS DEL INSTITUTO POLITÉCNICO NACIONAL

Unidad Zacatenco

Tratamiento fotocatalítico en agua de organismos biológicos usando óxido de grafeno dopado con nanocompositos TiO_2 y $BiVO_4$

TESIS

Presenta:
M. C. Christeena Theresa Thomas

Para obtener el grado de:
Doctor en ciencias

En:
Nanociencias y Nanotecnologia

Director de Tesis:
Dr. Velumani Subramaniam
Dr. Benoît Schoefs

Ciudad de México   Noviembre, 2021

CENTER FOR RESEARCH AND ADVANCED STUDIES OF THE NATIONAL POLYTECHNIC INSTITUTE

Zacatenco

Photocatalytic treatment of biological organisms in water using graphene oxide doped TiO_2 and $BiVO_4$ nanocomposites.

THESIS

Presented by:
M. C. Christeena Theresa Thomas

To obtain the grade of:
Doctor in sciences

In:
Nanoscience and Nanotechnology

Thesis Directors:
Dr. Velumani Subramaniam
Dr. Benoît Schoefs

Mexico City   November, 2021

Examination jury

Supervisor

Dr Velumani Subramaniam (Department of Electrical Engineering – SEES, CINVESTAV-IPN, Mexico)

Co-supervisor

Dr Benoit Schoefs (Metabolism, Engineering of Microalgal Molecules and Applications (MIMMA), Mer Molécules Santé, Le Mans University, Le Mans, France)

Committee members:

Dra Ma. de la Luz Olvera Amador (Department of Electrical Engineering – SEES, CINVESTAV-IPN, Mexico)
Dr Arturo Maldonado Alvarez (Department of Electrical Engineering – SEES, CINVESTAV-IPN, Mexico)
Dr Miguel Garcia Rocha (Department of Physics, CINVESTAV-IPN, Mexico)

External examiner:

Dr Juan Carlos Durán Álvarez (Department of micro- and nanotechnologies, UNAM, Mexico)
Dra Martine Bertrand (Department of Biochemistry – Phycology, Institut National des Sciences et Techniques de la Mer, Conservatoire National des Arts et Métiers, Cherbourg, France)

French committee members

Dra Justine Marchand (Metabolism, Engineering of Microalgal Molecules and Applications (MIMMA), Mer Molécules Santé, Le Mans University, Le Mans, France)

Table of contents

Declaration

I hereby declare that the work presented in this thesis entitled "Photocatalytic treatment of biological organisms in water using graphene oxide doped TiO_2 and $BiVO_4$ nanocomposites" is submitted for the degree of Doctor of Philosophy in Science (Specialized in Nanoscience and Nanotechnology & Cell Biology) has been carried out by me at Center for Research and Advanced Studies of the National Polytechnic Institute (CINVESTAV-IPN), Zacatenco, Mexico city and Le Mans University, France under the joint supervision of Dr. Velumani Subramaniam and Dr. Benoit Schoefs. The work is original and has not been submitted in part or full by me for award of any other degree or diploma in any other University (other than CINVESTAV-IPN, Mexico and Le Mans University, France)

CHRISTEENA THERESA THOMAS

Resumen

La desinfección fotocatalítica del agua potable se realiza habitualmente mediante luz ultravioleta, la cual representa solo el 4% de la energía solar total, aumentando así el costo y duración del proceso. De ahí que, actualmente, se están desarrollando nano materiales funcionalizados que pueden allanar el camino para el uso de la luz visible y, por lo tanto, acelerar la velocidad del proceso de desinfección de una manera rentable. La investigación comenzó con la selección de varios materiales (MWCNTs, ZnO) y la optimización de las rutas de síntesis. En el presente estudio se sintetizaron nanopartículas de dióxido de titanio (anatasa) y vanadato de bismuto (monoclínico) mediante la técnica de sol-gel. Posteriormente, estas nanopartículas se mezclaron con óxido de grafeno (GO) para producir nanocompuestos, como GO/dióxido de titanio (GOT) y GO/vanadato de bismuto (GOB) variando las proporciones de nanoestructuras en consecuencia, y confirmado por diferentes técnicas de caracterización. 1.5 GOT y 1.5 GOB mostraron una mayor eficiencia de inactivación de *Escherichia coli* (*E. coli*) *K12* (microorganismo modelo). Se determinó que los radicales hidroxilo (•OH) y superóxido ($O_2•^-$) son los responsables de producir especies reactivas de oxígeno (ROS) que desempeñan un papel crucial en la desinfección fotocatalítica. Se logró la inactivación de *E. coli K12,* con una concentración inicial de 10^7 UFC/mL, usando una cantidad menor de 1.5 GOT (1.05 g/L), y obteniendo 99.9% de inactivación en 30 min de irradiación, mientras que para 1.5 GOB (0.1 g/L) se obtuvo un 89% de desinfección en 60 min. En este trabajo se propone una tecnología verde, amigable con el ambiente y sencilla para la síntesis de nanocatalizadores para la inactivación de bacterias en agua. La investigación se extendió también hacia estudios preliminares sobre la inactivación fotocatalítica de microalgas *Anabaena sp*. y *Phaeodactylum tricornutum*. Los resultados obtenidos fueron prometedores siendo, hasta nuestro conocimiento, el primer estudio que utiliza el nanocompuesto GOT para la destrucción de las algas mencionadas, realizándose también una breve investigación sobre los parámetros responsables de la inactivación fotocatalítica de microalgas.

Palabras clave : *Óxido de grafeno, dióxido de titanio, vanadato de bismuto, nanocompuesto, Escherichia coli K12, Anabaena sp., Phaeodactylum tricornutum, desinfección fotocatalítica*

Abstract

Photocatalytic disinfection of drinking water was habitually performed by the ultraviolet light that epitomizes only 4% of the total solar energy, increasing the cost and prolonging the whole process. Therefore, functionalized nanomaterials are currently developed that can pave the way for the utilization of visible light, thereby speeding up the rate of the disinfection process in a cost-effective manner. This research started with selecting various materials (MWCNTs, ZnO) and the optimization of synthesis routes. Titanium dioxide (anatase) and bismuth vanadate (monoclinic) nanoparticles were synthesized through the sol-gel technique. This was followed by a simple-blending process with graphene oxide (GO) to produce nanocomposites, such as GO/titanium dioxide (GOT) and GO/bismuth vanadate (GOB), by varying the ratios of nanostructures accordingly and confirmed by different characterization techniques. 1.5 GOT, and 1.5 GOB showed enhanced inactivation efficiency of *Escherichia coli (E. coli) K12* as a model microorganism. Hydroxyl ($\cdot$OH) and superoxide ($O_2\cdot^-$) radicals were found to be responsible for producing reactive oxygen species playing a crucial role in photocatalytic disinfection, which was evaluated through scavenger study. We attained disinfection of *E. coli K12* having a concentration of 10^7 CFU/mL with a small quantity of 1.5 GOT (1.05 g/L), obtaining 99.9 % of inactivity in 30 min. Conversily, for 1.5 GOB (0.1 g/L) it resulted in only 89 % of disinfection rate upon 60 min under simulated visible light. Here, we propose a environmentally friendly technology for the facile synthesis of nano-catalysts with enhanced disinfection power for bacteria, which corroborates well with the possible mechanism. The research extended towards the study on the photocatalytic disinfection of microalgae, namely, *Anabaena sp.* and *Phaeodactylum tricornutum.* The results were promising, and to the best of our knowledge, this is the first study using the GOT nanocomposite to destroy these algal cells. A brief investigation on the parameters responsible for the photocatalytic microalgal disinfection was performed.

Keywords: *Titanium dioxide, bismuth vanadate, Graphene oxide, nanocomposite, Escherichia coli K12, Anabaena sp., Phaeodactylum tricornutum, photocatalytic disinfection*

Résumé

La désinfection photocatalytique de l'eau potable est habituellement effectuée par une source ultraviolette qui incarne seulement 4% de l'énergie solaire totale, augmentant ainsi le coût et prolongeant l'ensemble du processus. Par conséquent, des nanomatériaux actuellement fonctionnalisés sont développés, ce qui peut ouvrir la voie à l'utilisation de la lumière visible et ainsi accélérer le rythme du processus de désinfection de manière rentable. La recherche a débuté par la sélection de divers matériaux (MWCNT, ZnO) et l'optimisation des voies de synthèse. Dans cette étude rapportée, nous avons synthétisé des nanoparticules de dioxyde de titane (anatase) et de vanadate de bismuth (monoclinique) par la technique sol-gel. Ceci est suivi d'un processus de mélange simple avec de l'oxyde de graphène (GO) pour produire des nanocomposites, tels que le GO / dioxyde de titane (GOT) et le vanadate de bismuth (GOB) en faisant varier les ratios de nanostructures en conséquence et confirmés par différentes techniques de caractérisation. 1,5 GOT et 1,5 GOB ont montré une efficacité d'inactivation améliorée *d'Escherichia coli (E. coli) K12* (micro-organisme modèle). Les radicaux hydroxyle ($^{•}OH$) et superoxyde ($O_2^{•-}$) se sont avérés responsables de la production d'espèces réactives de l'oxygène (ROS) jouant un rôle crucial dans la désinfection photocatalytique qui a été évaluée par une étude de piégeurs. Nous avons atteint la désinfection de *E. coli K12* ayant une concentration de 10^7 CFU / mL avec une plus petite quantité de 1,5 GOT (1,05 g / L) obtenant 99,9% d'inactivité en 30 minutes tandis que, pour 1,5 GOB (0,1 g / L) résultant en 89% de désinfection en 60 minutes sous lumière visible simulée Ici, nous proposons une technologie verte environnementale pour la synthèse facile de nano-catalyseurs avec une désinfection améliorée des bactéries qui corrobore bien avec le mécanisme possible. La recherche est également étendue à des études préliminaires sur la désinfection photocatalytique des microalgues à savoir, *Anabaena sp.* et *Phaeodactylum tricornutum*. Les résultats étaient prometteurs et à notre connaissance, il s'agit de la première étude utilisant le nanocomposite GOT pour la destruction des algues susmentionnées. Une brève enquête sur les paramètres responsables de la désinfection photocatalytique aux microalgues a été réalisée

Mots clés: Oxyde de graphène, dioxyde de titane, vanadate de bismuth, nanocomposite, Escherichia coli K12, Anabaena sp., Phaeodactylum tricornutum, désinfection photocatalytiq

Acknowledgement

I believe I have learned a lot from writing this thesis, searching for the truth of science and life. This thesis writing was the greatest treasure I will cherish in my future academic career and my whole life.

I want to take up this opportunity to express my heartfelt recognition to all those who have given their invaluable support and assistance. Throughout my writing of this dissertation, I have received a great deal of backing and support.

I want to express my utmost gratitude to my supervisor, Dr. Velumani Subramaniam, for his sincere and selfless support, prompt and helpful advice during my research. He gives me a lifetime unforgettable memory of his benevolence, patience, intelligence, diligence, and erudition.

I am very much acknowledged to my co-assessor, Dr. Benoit Schoefs, whose proficiency was valuable for formulating the research questions and methodology. Your insightful feedback accelerated me to sharpen my thinking and brought my work to a higher level.

I am obliged to the examination committee members: Dra. Ma. de la Luz Olvera Amador (Department of Electrical Engineering – SEES, CINVESTAV-IPN, Mexico), Dr. Arturo Maldonado Alvarez (Department of Electrical Engineering – SEES, CINVESTAV-IPN, Mexico), Dr. Miguel Garcia Rocha (Department of Physics, CINVESTAV-IPN, Mexico), External examiner Dr. Juan Carlos Durán Álvarez (Department of micro-and nanotechnologies, UNAM, Mexico), French committee members: Dra. Martine Bertrand (Department of Biochemistry – Phycology, Le CNAM, France) and Dra. Justine Marchand (Metabolism, Engineering of Microalgal Molecules

and Applications (MIMMA), Le Mans University, France) for their critical revision of my thesis and providing me with valuable comments and suggestions which helped in the improvement and enhanced quality of my thesis. I also wish to thank Nanoscience and Nanotechnology coordinator Dr. Jose Gerardo Cabanas Moreno for his complete and valuable support throughout my Ph.D. program.

My sincere thanks to department secretaries Alma Mercedes Zamudio Martinez, Roxana Yasmin De Lorenz Santos for their help in department and administrative processes. Thanks to Oscar Ivan Buendia Montano of the department of becas y estimulos for his helping hands during various scholarship documentations.

I want to acknowledge all the people whose assistance was a milestone in completing this project. I want to thank M. en C. Miguel Galvan Arellano (SEES, Raman spectroscopy), M.en C. Francisco Alvarado Cesar (MREB, XRD, and SEM), and Dr. Jaime Santoyo Salazar (Physics department, TEM), Dr. Abdelhadi Kassiba (Physics department, Le Mans University, UV light source), Dr. Maud Barre (Chemistry department, Le Mans University, isostatic pressure) Ing. Brigitte Veidl Moreau (Le Mans University, algal lab support) for their helping hands.

This thesis dissertation could not have been completed without the support of my friends, Dr. Ganesh Regmi and Dra. Drisya Karathuparathottathil Damodharan, who provided stimulating discussions and happy distractions to rest my mind outside of my research.

I want to acknowledge my colleagues from my group MREB at CINVESTAV, Mexico, Dra. Aracelli and Dra. Atzin Ferrel (post-doctoral fellows), Dr. Ashok Adhikari, Dr. Onyekachi Michael Nwakanma, Dr. Karthik Sekar, Dra. Mercyrani Babudhurai and Ayde Fernanda Rivera Lima, Josué Raúl Ramírez Paulino and Dr. Jaime Vega Pérez of our group for their excellent collaboration. Special thanks to Matteo Sarcasini of Le Mans University for the support given. Also, thank my friends from Le Mans University, France, Hiba Rez, and Dra. Wafae Halim for their valuable support. I want to single out my post-doctoral fellow at MREB, Dra. Myriam Solis Lopez, for her patient support and all the opportunities given throughout my academic life. I would also like to thank

Dr. Ravichandran Manisekaran for his valuable guidance throughout my studies. You provided me with the tools to choose the right direction and complete my dissertation.

I also wish to thank from the bottom of my heart Mrs. Malathy Velumani for her motherly affection and support during my stay in Mexico, making me more comfortable during my hard times.

Most thanks to my parents (Mr. Sunny P.J & Mrs. Metty Sunny) and siblings (Carolin Therasa Thomas & Mateson Theressa Thomas) for their wise counsel and sympathetic ear. Their unconditional love, care, prayers, and tolerance made the hardship of writing the thesis worthwhile. My family, you are always there for me. I am also thanking my husband, Alan Geo Mathew, for his kind patience and support to accomplish my aim. I thank my mother-in-law (Mrs. Mary Mathew) and family members: Amal Jo Mathew, Dr. Dinu Alexander, Dr. (Major) Georgekutty Thomas, Alize Maria Mathew, Arwin Mathew, Harin, and Danyl for their encouragement to complete my thesis.

Finally, I thank Lord Almighty for all His blessings.

Thank you all.

CHRISTEENA THERESA THOMAS

List of contents

List of figures

Chapter 4

Chapter 5

List of tables

List of abbreviations

AOP	Advanced oxidation processes
$(BiNO_3)_3 \cdot H_2O$	Bismuth nitrate pentahydrate
$BiVO4$	Bismuth vanadate
BOD	Biological oxygen demand
$C_{16}H_{10}N_2Na_2O_7S_2$	Orange G
$C_2H_6O_2$	Ethylene glycol
$C_{34}H_{24}N_6Na_4O_{14}S_4$	Evans Blue dye
C_6H_6O	Ethanol
CDBB	Colección Nacional de cepas microbianas celulares
CdS	Cadmium sulfide
CH_3OH	Methanol
DBPs	Disinfection by-products
E.coli	*Escherichia coli*
EDCs	Endocrine disrupting chemicals
EMB	Eosin methylene blue
EPR	Electron paramagnetic resonance
EU	European union
Fe_2O_3	Iron (III) oxide
GO	Graphene oxide
GOB	Graphene oxide/bismuth vanadate
GOT	Graphene oxide/titanium dioxide
HAAs	Halo acetic acid
HAB	Harmful algal bloom
HNO_3	Nitric acid
$HOC(COOH)(CH_2COOH)_2$	Citric acid
LB	Luria Bertani
MWCNT	Multi-walled carbon nanotubes
$NaHCO_3$	Sodium bicarbonate
NaOH	Sodium hydroxide

NGO	Non-governmental organizations
NH_4OH	Ammonium hydroxide
NH_4VO_3	Ammonium metavanadate
OECD	Organization for Economic Co-Operation and Development
PBS	Phosphate buffer saline
POPs	Persistent organic pollutants
RNS	Reactive nitrogen species
ROS	Reactive oxygen species
S_{BET}	Specific surface area
SEM	Scanning electron microscope
SO_4^-	Sulfate radicals
TEM	Transmission electron microscope
THM	Trihalomethanes
THMs	Trihalomethanes
$TiCl_4$	Titanium chloride
TiO_2	Titanium dioxide
TOC	Total organic carbon
UV	Ultra-violet
WHO	World health organization
WO_3	Tungsten trioxide
XRD	X-Ray diffraction
$ZnC_4H_6O_4$	Zinc acetate
$ZnCl_2$	Zinc chloride
ZnO	Zinc oxide
ZnS	Zinc sulfide

List of symbols

C	Celsius
Cm	Centimeter
eV	Electron-Volt
Gm	Gram
h	Hour
mg	Milligram
min	Minutes
ml	Milliliter
nm	Nanometer
%	Percentage
sec	Seconds
µg	Microgram
W	Watt

To my family, relatives, friends, and teachers….

Chapter 1

Introduction to water crisis and nanotechnology

Chapter 1: Introduction to water crisis and nanotechnology

1.1 Introduction

Water or availability of potable water is a most discussed topic worldwide, and the management of this water has become a decisive challenge for all the countries across the world due to the reasons that has depicted in Fig 1.1. Safe water can be defined as any water that does not cause any health risk to humankind after a lifetime consumption [1]. Water requirement for an individual is always a fundamental and human right. But the present plight does not allow this free access to water, as the government has a well-defined protocol to have an equal division of this limited resource among all humankind to ensure equity and well-being. Despite various conflicts regarding water shortage, allotting freshwater supply, preserving the available capital, and improving the ways to develop it more, it remains a question mark in front of man [2].
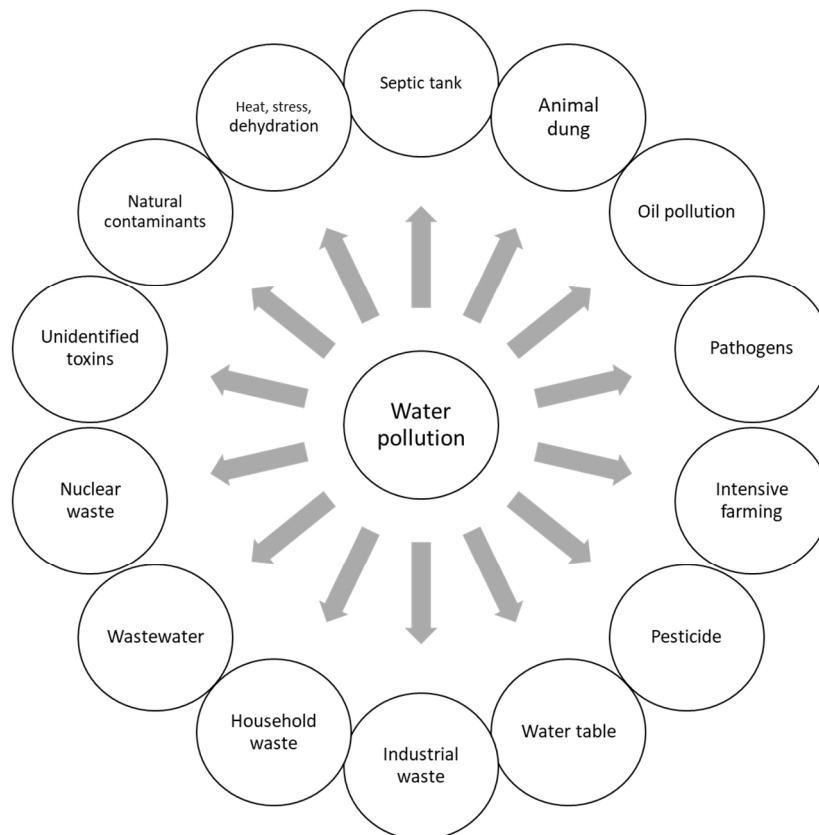
Fig 1.1: The causes of water pollution in the world [3,4]

1.2 Water crisis

1.2.1 A global outlook

While developed countries consider the availability of safe drinking water for granted, the other face of the world, i.e., developing, and underdeveloped nations, is struggling to access potable water (Fig 1.2). As per the World Health Organization (WHO), more than 1.2 billion people live in the water crisis [5]. Due to this reason, more than 5 billion people lost their lives by the intake of polluted or contaminated water and diseases associated with it. The shortage of potable water will not only make humankind and other organisms sick, but it will also lead to various issues. They include an economic crash in the developing countries, thus being a barrier in their growth and creating conflicts between the nations for resource use, diminishing the global security of the states that might collapse [6]. Over the past hundred years, the use of worldwide water has increased by a factor of six. The graph of water intake will continue rising at a rate of 1% per year because of the growing population, economic development, and shifting consumption patterns. The Organization for Economic Co-Operation and Development (OECD) reported that the demand for global water would increase by 55% between 2000 and 2050. This demand is shared between manufacturing (-400%), thermal power generation (+140%) and domestic use (+130%) (OECD,2012) [7].
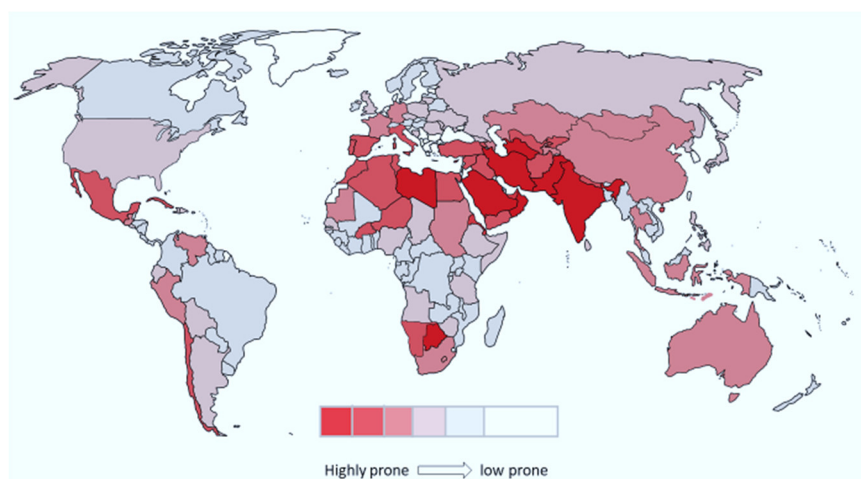
Fig 1.2: An index for level of water crisis from significantly affected to less stressed countries (The image is modified information from reference [8]*)*

Over the past few years, academic institutions, non-governmental organizations (NGOs), and government authorities have performed various activities to stop the

global water crisis. Still, the problem is not yet vanished, mainly because of illiteracy in the management of the water resource and high risk in the quality of water, i.e., limited availability of clean drinking water. When there is water contamination by pathogens or dangerous pollutants, one significant share of this cause is anthropogenic activities [7]. The reasons behind the increasing taint of fresh and marine water globally include the discharge of organic wastes, pathogens, fertilizer, pesticides, heavy metals, and/or other toxic pollutants. Water pollution due to organic matter is increasing worldwide due to municipal and industrial wastewater discharges into the natural water bodies, increasing agricultural and livestock farming, and high cutback in the river dilution capacity employing reduced runoff and water extractions [9].

In the same way, eutrophication is the aftermath of dispensing human-made nutrient-enriched materials from agriculture and industries to water systems. From the records of WHO and UNICEF, pathogen contamination remains the top reason for the low quality of water worldwide. Therefore, pollutants that already prevail and emerging contaminants such as oxadiazon, methiocarb, imidacloprid, etc., remain a significant challenge in developing countries to avoid a serious threat to human health ecosystems [10].

1.2.2 A peep to water availability and quality in Mexico

The United Mexican States extending over 1.964 million km^2 have their 67 % of its territory with arid or semi-arid conditions. The top three environmental issues prevailing in Mexico are air pollution, deforestation, and lack of clean water [11,12]. These facts are dire and an upcoming crisis that directly and indirectly affects millions of Mexicans and their environment (Fig 1.3). When lack of clean water and the increase of the human population is considered, an immediate urge for safe and clean drinking water for 127 million Mexicans is elevated. Usually, water is obtained from the aquifers of the Basin of Mexico River, which is in the southern part of the Central Volcanic Axis, an upland formation of Late Tertiary origin. The water extracted from these sources is near to three times the average recharge capacity, which leads to a reduction of moisture over time. The water is contaminated with bacteria due to the leaching of wastewater and heavy metals like lead, nickel, mercury, arsenic, chromium, etc. Due to the intake of polluted water, nearly one-fourth of the population is exposed to waterborne diseases. The water that is obtained from the water supplies

of Mexico is tinted and odor. For this reason, Mexicans spend 10% of their income to get clean water. The use of clean, polluted, and drinking canned water has become a part of their daily life [13,14].
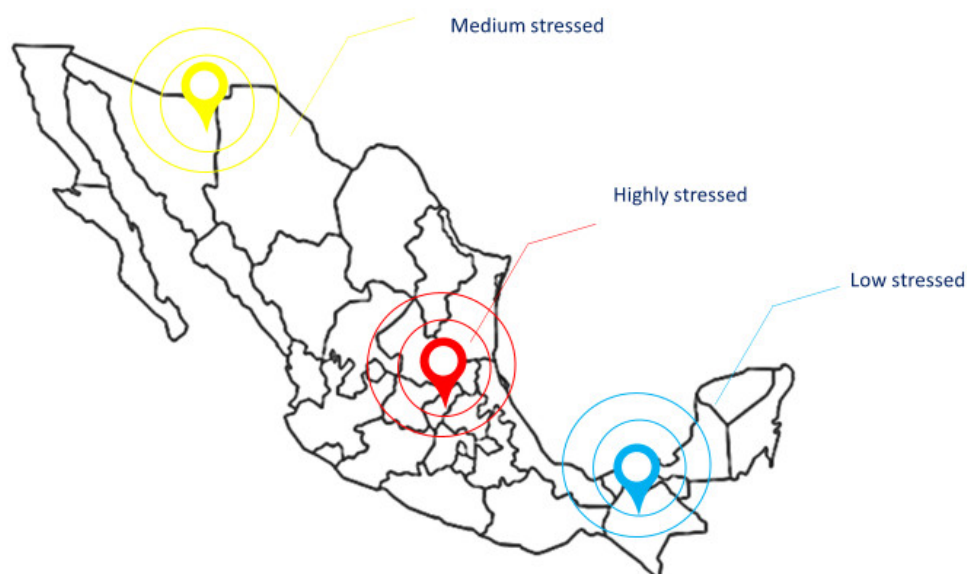
Fig 1.3: Water stress index of various parts in Mexico (reproduced from [15])

As per the World Health Organization (WHO) report, more than 80% of cases related to gastrointestinal infections and parasitic diseases result from using and consuming unsafe water. Due to this reason alone, one-third of the deaths have been reported. The Mexicans have witnessed various outbreaks associated with waterborne diseases, overcrowding, and harmful environmental conditions. These pathogens spread through the fecal-oral route and transmit through water used for different activities and through primary contact from contaminated recreational waters. Therefore, Mexico faces two significant challenges: to provide safe drinking water and essential sanitation services. The primary environmental argument for the cause of waterborne diseases and mortality rate is mentioned in Fig 1.2. In Mexico, chlorination above 0.2 mg/L is maintained to kill pathogenic bacteria and viruses that pass through the water supply system. Polluting water by the release of pesticides and other chemicals like lead has been reported in Mexico. Literature gave a piece of adequate information on the chronic effects of organochlorine insecticide deposition in the adipose tissue and human milk, and neurotoxic effects of organophosphorus insecticides, and pulmonary effects of certain dipyridyl-like herbicides [16] (Fig 1.4).
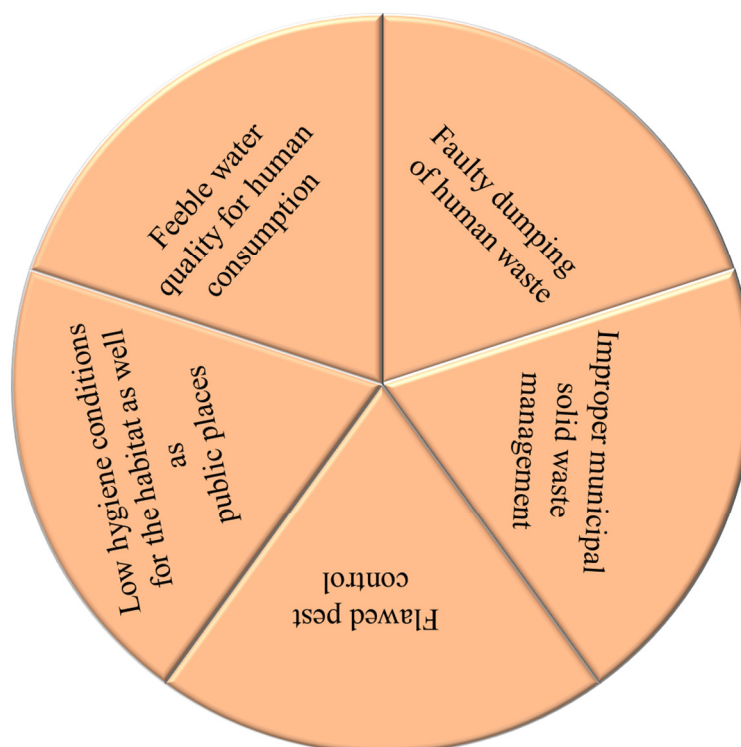
Fig 1.4: Reasons behind the cause of diseases and increase in the death rate of Mexico [16].

1.2.3 A peep to water availability and quality in European Union (EU)

France, Sweden, and Germany possess the most considerable number of freshwater resources considering freshwater availability in a country, climate conditions, transboundary water flows, and country size. But the quantity of freshwater divided among each EU member differs from abstraction practices, climate, and sectors (industrial and agricultural). Even though sustainable management of the water in the EU is under control, water scarcity has been faced by specific regions of Europe. This water scarcity is reported for the near future due to less rainfall, population expansion, and industrial and agricultural activities. The water supply is through public or private systems or private drills, but when it comes to the public pool, it relies on the economic status of the country, which is a negligible amount [17].

1.2.4 Current situation

The physical, chemical, and microbiological characteristics of water determine its quality. These properties are either intrinsic to the water or associated with the

substances dissolved or dispersed in water. The water which is used for drinking should satisfy various requirements (Table 1.1), which should be decisive and persistent for the customers [18].

Table 1.1: Requirements for drinking water [18]

	Property	Condition
1	Safe to drink	Harmful microorganisms or other toxic substances should be removed from water by a definite treatment process before used for drinking
2	Aesthetically pleasing	Drinking water must have clean and clear appearance, taste, and odor.
3	Chemically stable	Potable water should not act as a corrosion element or cause any deposits in pipes or fixtures during supply.

The available water treatment methods are collectively termed conventional water treatment techniques. Water is treated from its source through a series of processes to remove suspended particles, followed by disinfection and finally stabilizing the water chemically for future safe use. For the removal of suspended materials, coagulation (coagulating small colloidal particles), flocculation (small particles will form large flocs or aggregates), sedimentation, and sand filtration are the used techniques. Other methods are flotation, micro-filtration, and ultra-filtration. For coagulation and flocculation, chemicals are used to attain this. A specific amount of disinfectant is added to water for a pre-determined period under particular pH and temperature for the disinfection process. Commonly used chemicals for disinfection are chlorine, chlorine gas, ozone, chlorine dioxide, chlorine compounds like calcium hypochlorite (HTH) and, sodium hypochlorite (bleach). Due to the generation of chlorinated by-products like trihalomethanes (THMs) that can cause adverse health effects, the concentration of this disinfectant is kept at control in drinking water. Ultra-violet (UV) irradiation is becoming popular due to the formation of no by-products. Like conventional processes, advanced treatment processes for water treatment include reverse osmosis, nanofiltration, ultrafiltration, electrodialysis, activated carbon

adsorption, ozonation, and oxidation processes for iron and manganese removal [18]. The significant disadvantages of the current water purification techniques are tabulated in Table 1.2.

Table 1.2: Drawbacks of current water treatment techniques [19].

Process	Disadvantages
Chemical precipitation	Usage of chemicals like lime, oxidants, H_2S
Coagulation/Flocculation	Utilization of non-reusable chemicals as a coagulant and flocculant. pH is regulated physiochemically. The possibility for the management of sludge is low. Arsenic removal is low.
Flotation	High investment, energy, and maintenance costs. Chemicals are used. Selective in the process.
Biological methods	An optimal favorable environment is required. Management and maintenance of microbes. Pre-treatment is needed. The process is slow, and the biodegradability of some pollutants is low. The generation of biological sludge and management is complex.
Filtration	High cost for the materials and the maintenance of the system. Depends on the type of materials.
Chemical oxidation	Usage of chemicals. Production, transport, and management of the oxidants are harrowing. Activity depends on the type of the oxidant. Pre-treatment before the process is crucial. Short life of some of the chemicals. Some pollutants are resistant to the treatment.

	Formation of intermediates. Salinity matters. Formation of sludge. Generation of compounds that are volatile and aromatic amines.
Ion-exchange	Performance is sensitive. Costly. Selective in activity.
Incineration	Discharge of pollutants. Costly. Difficulty in storage and transportation.
Electrochemistry	The cost of capital and maintenance is high. Requires chemicals. Generation of sludge and difficulty for the management of sludge.
Membrane filtration	Costly in the capital, maintenance, and energy. Slow output. High specificity. Management of sludge is a risk.
Evaporation	Costly in every aspect. Pollution load in the concentrate.

1.3 Nanotechnology

Nanotechnology can be defined as the complete package of observing and studying the phenomenon at the nanometer scale and various approaches for manipulating matter on nanometer-scale as they have different properties when they are in larger scale [20]. This is a promising field studied and cited for water treatment. The application of this technology is better due to the structure and large surface area of nanomaterials. When treatment and remediation are considered, long-term water quality, access, and viability of water are promised using nanotechnology.

Sensors that can detect biological and chemical pollutants in water, even at shallow concentrations, are developed with nanotechnology. Nanotechnology is very efficient for monitoring and removing contaminants during water purification with low cost and high specificity [21]. Water treatment can be classified into three different groups (Table 1.3) [22–26].

Table 1.3: Three different groups of water treatment via nanotechnology

No	Group	Features
1	Nano-adsorbents	Organic or inorganic materials are used to synthesize these nanoparticles to have high affinity to any pollutants. These nanoparticles can remove various types of contaminants and have the properties like catalytic potential, high reactivity, small size, and considerable surface energy. This group includes metallic nanoparticles, magnetic nanoparticles, nanostructured mixed oxides, and metallic oxide nanoparticles.
2	Nano-catalysts	These materials, i.e., metallic nanoparticles, can interact with light energy-giving photocatalytic activities that generate radicals to destruct pollutants. Nano-catalysis uses semiconductors and metal oxides.
3	Nano-membranes	These materials separate particles from wastewater and efficiently remove dyes, heavy metals, and other contaminants from water. Nanotubes, nanoribbons, and graphene-based membranes, and nanofibers are examples of nano-membranes.

1.3.1 Role of nanotechnology in water treatment

When conventional water purification methods display limited efficiency, nanotechnology put forward ingenious remedies to overcome the failures in water purification. The nanomaterials possessing reactivity, tunable pore volume, hydrophilic, hydrophobic, and electrostatic features are considered for better

performance in adsorption, catalysis, and optoelectronics. The processes associated to nanotechnology are efficient, modular, and multifunctional. Nanomaterials possess a high specific surface area (S_{BET}), and therefore, a high surface-to-volume ratio, leading to high interaction with the pollutants or pathogens. This nanotechnology is a promising field for the purification of water in an economic way [27,28].

1.4 Organic matter as pollutants

With a tremendous increase in the agricultural field and other waste-generating sectors, the contribution to water pollution by the discharge of nutrients, salts, and sediments, livestock became a significant factor for the water pollution by organic matter, pathogens, and other emerging pollutants such as hormones and antibiotics. Wastes such as animal excreta, animal feed balance, animal-processing industries, and crop residues become the significant sources for organic matter pollution. The presence of organic matter is calculated by the biological oxygen demand (BOD). BOD is defined as the amount of oxygen taken up by microbes to decompose the biodegradable organic matter in the water (Table 1.4) [29]. The rising global population can also contribute to organic pollution [30–34].

Table 1.4: BOD of various wastes [9]*.*

Source	BOD (mg O_2/liter)
Milk	140000
Silage effluents	30000-80000
Pig slurry	20000-30000
Cattle slurry	10000-20000
Liquid effluent draining from slurry stores	1000-12000
Untreated domestic sewage	200-500
Treated domestic sewage	20-60
Clean river water	5

1.5 Advanced Oxidation Processes (AOPs)

Due to the disadvantages mentioned above (see Table 1.2) of the traditional water treatment techniques, advanced oxidation processes (AOPs) are well accepted [35,36] for water purification to make it potable. AOPs are promising due to the generation of reactive oxygen species (ROS) that can react with various pollutants to make the water free from organics, inorganics, and microorganisms [37,38]. AOPs are defined as the oxidation processes that are associated with the generation of hydroxyl radicals $(OH^{.})$ and some oxide and superoxide radicals, which aids in water purification, and it was proposed in the 1980s decade for the same. AOPs were later established in their field to oxidative processes using sulfate radicals (SO_4^{-}). ROS-mediated disinfection was extended for various types of wastewater treatment due to the formation of strong oxidants, which can cause destruction of organic as well as inorganic pollutants. AO processes include the generation of sufficient quantity of hydroxyl or sulfate radicals to degrade unmanageable organic pollutants, any small amount of organic matter or inorganic contaminants and fasten the wastewater biodegradability helping biological treatment [39]. These types of pollutants can be generally grouped into endocrine disrupting chemicals (EDCs), persistent organic pollutants (POPs), total organic carbon (TOC) and micropollutants [40,41]. Due to the facts mentioned above, during this process there is no conversion of pollutants to another phase (i.e., more hazardous, or toxic) which is the main drawback of traditional methods such as chemical precipitation and adsorption. Another point to be noted is that there is no discharge of any harmful sludge [42,43].

1.5.1 Classification of AOPs

The classified techniques as AOPs (Fig 1.5) generate ROS that degrades different kinds of pollutants. Sonolysis uses ultrasonic waves having a frequency of 20 kHz to 10 MHz. Due to the ultrasonic, cavitation bubbles are formed and then break down when they reach their resonance size, leading to the liberation of stored energy as explosions degrading the organic molecules in the surroundings. This technique does not use any toxic chemicals as an intermediate and uses only the ultrasound frequency, which is an ecofriendly process [44,45]. Ozonation uses ozone for the oxidation of inorganic and organic pollutants. This technique, widely used in European countries, has a very selective disadvantage due to the electrophilic nature of ozone molecules (ozonation). Ozonation is famous for its activity towards microbes,

decolorization, non-protonated amines, micropollutant removal, taste, and odor removal [46]. By absorbing UV light, the killing of microorganisms at the tertiary level of wastewater treatment and destruction of other aquatic organic compound occurs. Mercury arc lamps transmitting UV light at various intensities are used.
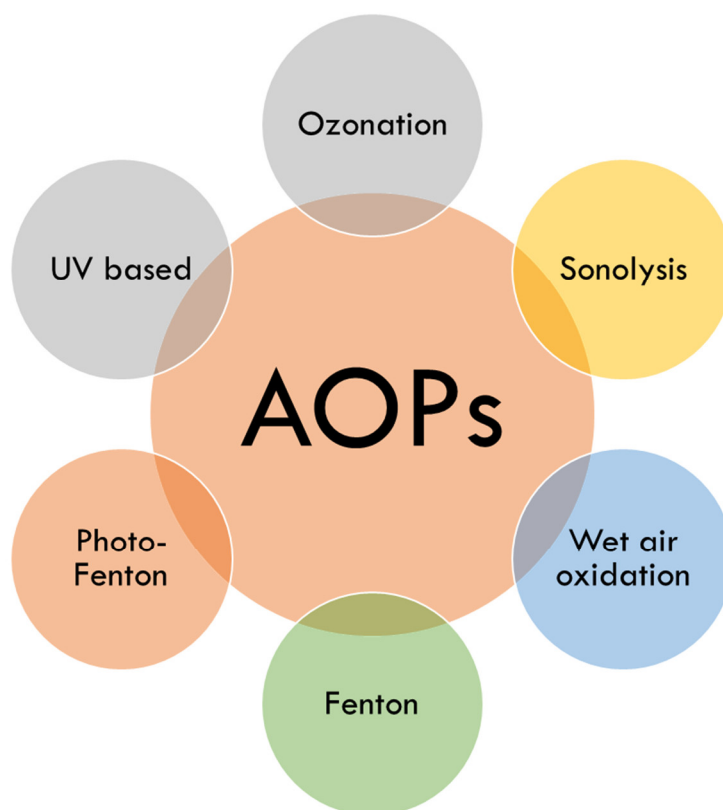
Fig 1.5: The general classification of advanced oxidation processes [47].

1.5.2 Homogenous and heterogeneous AOPs

AO processes ranges in two categories: (1) homogenous- and (2) heterogeneous-AOPs [48]. The former means that the degradation of compound is performed using the adsorption of UV radiation in the range of 100-400 nm. Whereas heterogeneous AOPs use catalysts for the degradation of compounds on the surface of the catalyst. In this process, the catalyst generates electron-hole pairs and activates the electrochemical process. The holes and electrons developed through photogeneration can undergo oxidation and reduction processes, respectively. At the presence of an aqueous and aerobic condition, water molecules are adsorbed to the catalyst, which under oxidation generates hydroxyl radicals and superoxide radicals, respectively. These radicals help in the oxidation of pollutants that have been adsorbed over the catalyst surface.

1.5.3 Photocatalyst as a weapon for water disinfection

Photocatalyst is defined as the catalyst, which is photoactive, photostable, visible or near UV light range, biologically and chemically inert, inexpensive (low cost), and toxic-free. For a semiconductor to be photocatalyst, it should be photochemically active and the redox potential of photogenerated valence band holes must be positive. The photogenerated conductance band electron must be high enough to generate superoxide radicals. The photocatalysis mechanism (Fig 1.6) can be explained as light irradiation of sufficient energy is incident on a semiconductor, electrons present in the valence band excites towards conduction band leaving behind the photo holes. The valence band holes, and conduction band electrons react with water to give mainly hydroxyl, superoxide, and other radicals. These species can react with the pollutants to give not harmful carbon dioxide and water [49–53].
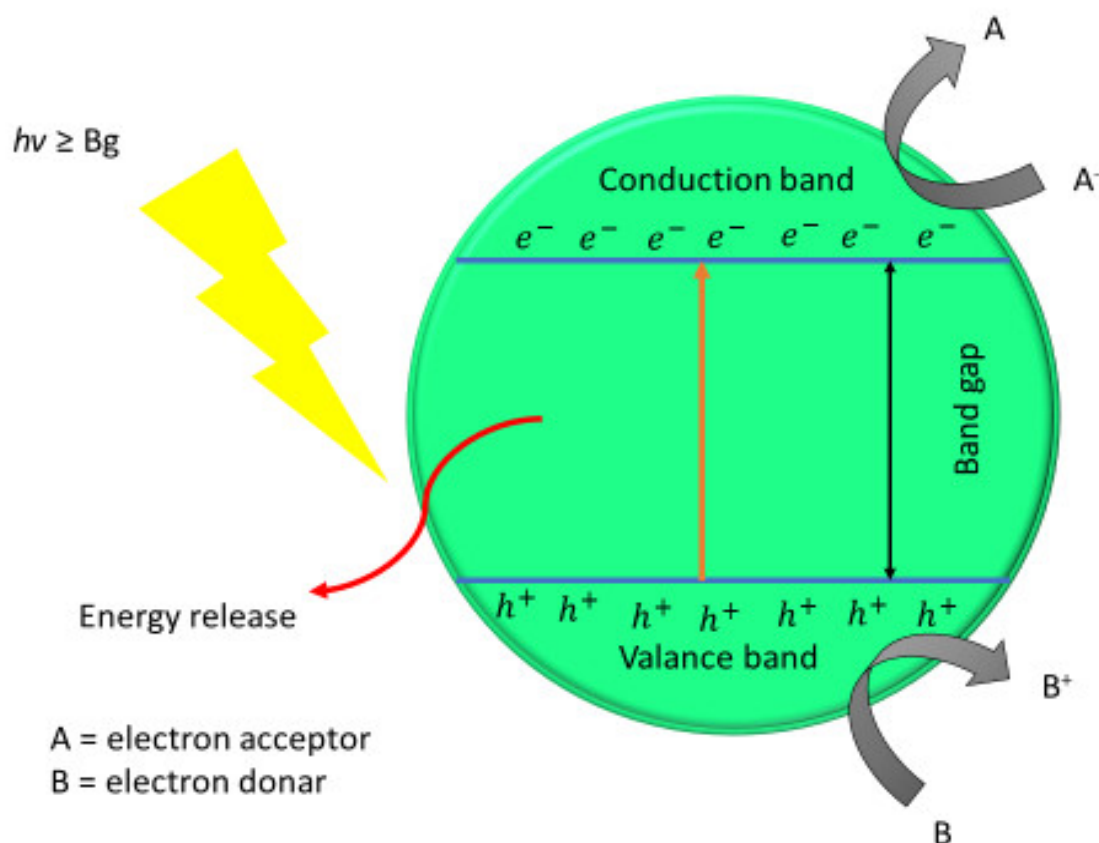
Fig 1.6: the general mechanism of photocatalysis by a semiconductor [54].

1.5.4 Nanoparticles for photocatalysis

1.5.4 (a) Graphene oxide (GO)

A two-dimensional honeycomb lattice structure made of carbon material is graphene, with a single layer atomic thickness. Graphene possesses high mechanical properties, excellent electrical properties, high thermodynamic properties, and a large surface area [55]. The existence of strong van der Waals interactions between graphene sheets limits its direct application. Graphene oxide, which is obtained through the chemical oxidation-stripping method, is a prominent derivative of graphene. It has the different oxygen functional groups that cover the basal plane of sp^2 carbon [56].
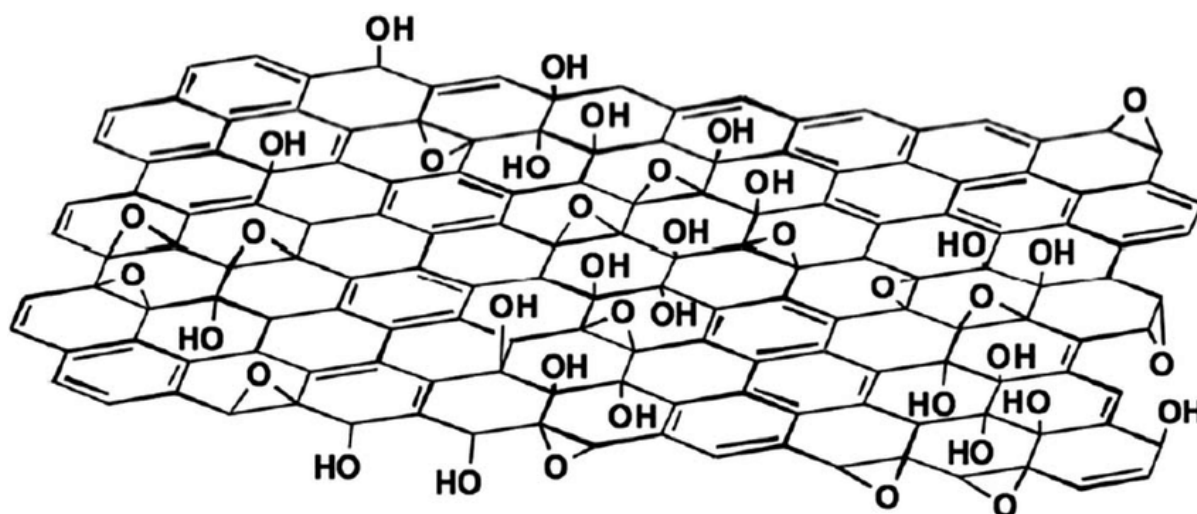
Fig 1.7: Lerf-Klinowsky model of GO showing the epoxy and hydroxyl bonds [56]

Due to reactive oxygen functional groups like hydroxyl groups and epoxy groups, GO is used for various applications through chemical functionalization. The oxygen groups make GO hydrophilic [57–59]. Lerf and Klinowsky proposed the GO chemical structure model (Fig 1.7), where it is described as a structure with non-oxidized aromatic areas which are separated by aliphatic 6-membered rings having hydroxyl groups, epoxide groups, and double bonds. These groups lie below and above the basal plane providing the polar nature and hydrophilic nature of GO [56].

The GO-based nanocomposites like GO/TiO$_2$ are synthesized through different methods and approaches like electrochemical co-deposition [60], hydrothermal method [61], microwave-assisted method [62], in situ polymerization [63], vacuum impregnation, and sol-gel technique [64]. By adjusting the abundance of functional groups over the GO, the electronic properties and the affinity towards bacteria cells

can be tuned [65]. Due to the excellent conductivity of GO, the photo-electrons that were generated from the light irradiated TiO_2 can migrate towards GO, thereby enhancing the charge separation, thus leaving behind the photo-holes and leading to an improved photocatalytic activity of TiO_2. Charge separation occurs due to the formation of superoxide radicals by the electrons in the GO sheets by the reaction of dissolved oxygen. The extraction and transfer of the electrons from TiO_2 towards GO lead to efficient charge carrier separation, thus enhancing the photocatalytic disinfection [66–68] (Fig 1.8).
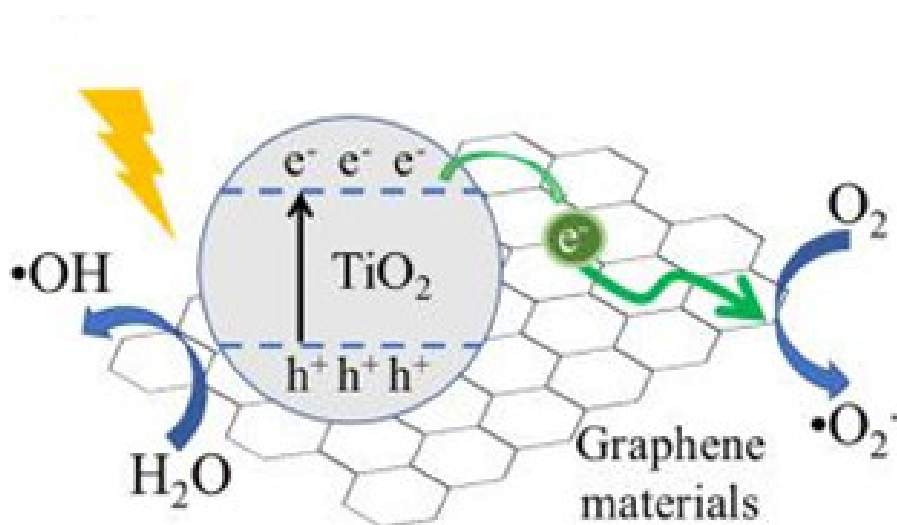
Fig 1.8: The mechanism of the photocatalytic disinfection by GO/TiO₂ composite [69]

1.5.4 (b) Titanium dioxide nanoparticles (TiO₂ nps)

Even though photocatalysis was discovered over the 1990s, its applications came into major existence after discovering photocatalytic splitting of water and hydrogen generation on TiO_2 photoelectrodes by Fujishima and Honda in 1972 [70]. This opened a separate research field to improve the technique, photocatalysis [71–76]. Due to the ability for decomposing organic pollutants, corrosion resistance, non-toxicity, durability, and low cost, TiO_2 has been explored in various fields [77,78]. Due to the strong redox power by the photogenerated electrons and holes, TiO_2 can inactivate the pathogenic organisms [79].

1.5.4 (c) Bismuth vanadate nanoparticles (BiVO₄ nps)

Bismuth-related nanoparticles like $BiOCOOH$, Bi_2WO_6, $(BiO)_2CO_3$, $BiVO_4$, $BiPO_4$, Bi_2O_3, and $BiOCl$ are used effectively for various applications due to their high photocatalytic performance, low toxicity, low cost, and high stability. These bismuth-

related nanoparticles are good in photocatalysis, anti-flogging, self-cleaning, disinfection, organic pollutant degradation, carbon dioxide reduction, air purification, hydrogen generation, etc [80]. Bismuth vanadate ($BiVO_4$) has three main phases: tetragonal scheelite, monoclinic scheelite, and tetragonal zircon. The monoclinic scheelite phase proved to be active in visible light because of its narrow bandgap, *i.e.*, 2.4 eV, and due to the presence of pair distortion of the Bi 6s orbital. Moreover, the valence band of $BiVO_4$ has an overlap of O 2p and Bi 6s orbitals, thereby enhancing the mobility of photogenerated charge carriers, which improves the photocatalytic ability of this semiconductor [81]. Due to this feature, $BiVO_4$ is widely used in photocatalysis, as it is non-toxic, low cost, environmentally friendly and highly resistant to photo corrosion [82]. The first photocatalytic report on $BiVO_4$ was put forward in 1999 by Kudo et al. The publication rate has increased till date [83]. $BiVO_4$ is an n-type semiconductor displaying high stability, with its flexible optical and electronic properties [84]. Due to the fast recombination of photoinduced charge carriers caused by the narrow bandgap, enormous efforts have been made to improve the separation of photogenerated charge carriers like controlling morphology, semiconductor coupling, doping with metal and non-metal elements, and exposed reactive facets of $BiVO_4$.

In the field of water disinfection, $BiVO_4$ based materials are gaining recognition due to their effectiveness. Using Z-scheme structures, like $AgI/BiVO_4$, which was synthesized through a chemical deposition precipitation route, the semiconductor applied for the inactivation of *Escherichia coli,* and has inactivated 7 x 10^7 CFU/mL in 50 min under visible light irradiation, with superoxide radical and holes as the ROS responsible for the disinfection [85]. The Z-scheme is inspired from the natural photosynthetic process. In photocatalysis, Z scheme is based on an oxidation semiconductor and a reduction semiconductor. A low valence band position and strong oxidation ability is associated with oxidation semiconductor while a reduction semiconductor possess high conduction band and strong reduction ability. Due to this charge transfer property, a particular photocatalyst with above mentioned characteristics can have various benefits like separation of photogenerated charge carriers, enhanced light harvesting, extended range of photocatalysts, etc [86]. *Pseudomonas aeruginosa, E. coli, and Staphylococcus aureus* bacterial growth was inhibited 100% within 30 mins of irradiation of the $Bi_2WO_6/BiVO_4$ heterostructure [87].

1.6 Photocatalytic disinfection

Photocatalysis and its applications have gained widespread attention as an alternative for several environmental issues. Among these issues, bacterial disinfection has its priority in the application due to the disadvantages of existing conventional methods (see Table 1.2). To be more specific, chlorination, a well-known technique, can generate by-products like choro-organic compounds, some of them are carcinogenic in nature [88]. At the same time, such as viruses, *Legionella pneumophilla* (bacteria), and cysts of *Cryptosporidium parvum* and *Giardia lamblia* (protozoa) are highly resistant to chlorination. Ozonation and the use of germicidal lamps can cause a reduction in residual effect or can induce the formation of colony mutants [89–91]. One of the hot topics under discussion is photocatalytic applications linked to solar photocatalysis for water and wastewater treatment [92–96]. Photocatalytic disinfection applies to resistant organisms to traditional methods [97,98].

ROS generation take place at the semiconductor particle–solution interface. The hydroxyl radical, followed by superoxide radical anion, hydroperoxyl radical, and hydrogen peroxide, are the essential ROS that causes disinfection. Upon forming ROS inside a biological system, various systematic defense mechanisms using an enzymatic pathway takes place to convert the generated ROS to non-toxic substances, as ROS in high concentration is lethal to living cells. Due to the absence of site-specific activity of ROS, the uses of photocatalyst have a significant impact on pathogens for their destruction. The point to be noted is that the concentration of ROS produced by a photocatalyst must be large enough to counteract the defense mechanism for the photocatalytic disinfection [99]. *Escherichia coli (E. coli)* is the most used organism for antibacterial study due to its ease of culture and detection. A typical bacterium possesses a cytoplasmic matrix which is covered by the cell membrane and outer layers. The cell contains genetic material and the biochemical system responsible for energy production, cell regulation, and reproduction. The bacterial viability lies on the cell membrane (depends on the cell wall) that maintains the integrity of the cell structure. Even though, the mechanisms taking place during the photocatalytic disinfection is still unknown. Various kinds of literature reports disintegration of peptidoglycan, formation of pores in the cell wall and cell membrane, lipid peroxidation, DNA damage, etc., as the outcome of photocatalytic inactivation [100–105]. Fig 1.9 shows a proposed mechanism of photocatalytic disinfection

[106,107]. In short, (a) photocatalysts and bacterium in an aqueous polluted media, (b) by adsorption, the photocatalyst particles got attached over the surface of the bacterium. The photocatalyst gains energy greater than its bandgap to generate ROS, (c) the generated ROS causes seizures on the microbe's cell membrane. Thus, the passage of particles becomes possible to react with the cellular components, (d) once the cellular integrity and the protein synthesis system are damaged, the cells are lysed, giving behind the cellular debris.
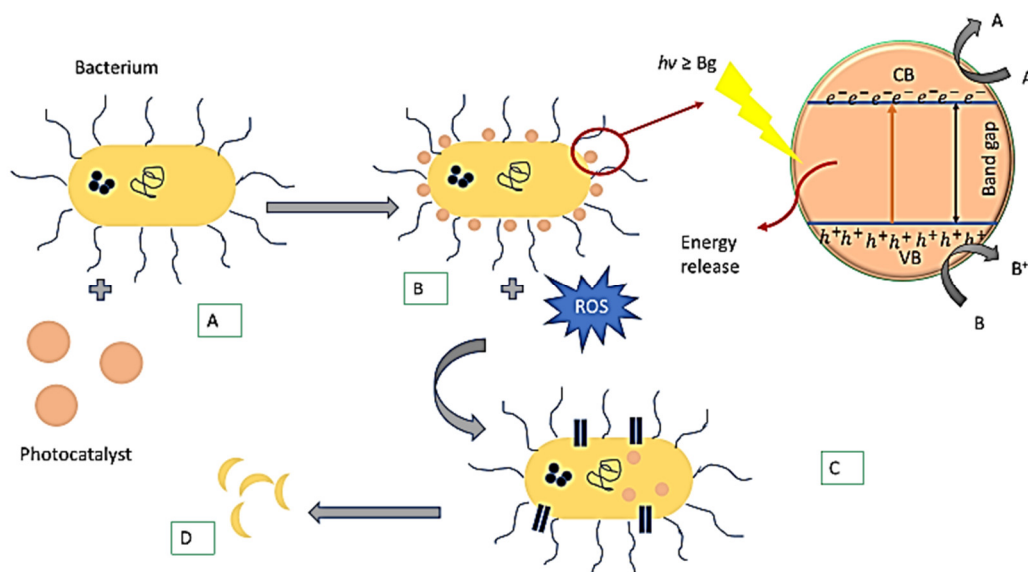
Fig 1.9: Mechanism of photocatalytic inactivation of microbes by a semiconductor through the generation of reactive oxygen species (Modified from [106]*)*

1.7 Microorganisms and Microalgae

Enteric pathogens, which are disease-causing organisms that transmit through drinking water, are of fecal origin. With the discovery of cholera by John Snow in the 1850s, a detailed study of other organisms that causes waterborne diseases like diarrhea was conducted. Even though the microorganisms responsible for diseases like cholera and typhoid fevers are *Vibrio cholera* and *Salmonella typhi* and *Salmonella paratyphi, E. coli* is considered as the major indicator organism for water-related diseases, and they are excreted out in the feces of mammals [108–112]. Some pathogens, especially chlorine-resistant parasitic protozoa, such as oocysts of *Cryptosporidium parvum* and some enteric viruses, are disinfection resistant and environmentally persistent. But the universal indicator for drinking water pollution is considered to be thermo-tolerant fecal *E. coli* [113,114].

When there is an imbalance in environmental conditions, such as temperature fluctuations and increased nutrient concentrations like nitrogen and phosphorous, an outbreak of algae occurs to form algal bloom or harmful algal bloom (HAB). This HAB in lakes, rivers, and estuaries severely threatens human and aquatic ecosystem health due to toxins (certain species) by these blooms and cause economic damage. HABs are characterized by color change (light to dark green, yellow, red, and brown) and odor and appear in water as scums, paint-like slicks, clotted mats, or foams. Even if there is no discoloration of water, the presence of algal toxins leads to health effects [115].

The most frequently occurring HABs in freshwater bodies is cyanobacteria. Cyanotoxins cause hepatic, neurologic, respiratory, and dermatologic ill-effects to exposed organisms. The diseases can be acute or chronic and sometimes fatal. Consumption of drinking water, fish, or shellfish contaminated with these toxins, close contact in the recreational water bodies polluted with toxins, or inhalation of aerosolized toxins can become reasons for the adverse health issues for human [116–118] .

Based on the light quality and quantity, cyanobacteria and algae were subjected to a change in their system. To adapt to these conditions, they have developed efficient photosynthetic apparatus to safeguard photosynthetic efficiency and photoprotection. During reduced light intensity, light capturing, and photosynthetic yield are performed by reorganizing its light-harvesting system. On the other hand, when there is increased light intensity, the excess light energy absorbed is dissipated as heat through nonphotochemical quenching (NPQ) to avoid photodamage or oxidative damage. Photodamage is more prone to evident in photosystem II (photosynthetic complex) [119].

1.8 Objectives, motivation, novelty, and outline of thesis

The primary aim of this research work is to develop graphene oxide, which will be incorporated with TiO_2 and $BiVO_4$ nanoparticles to obtain nanocomposite for the applications in the removal of micro-organisms and microalgae from drinking water. The research study started with the selection of materials i.e., multiwalled carbon nanotube (MWCNTs), zinc oxide (ZnO), titanium dioxide (TiO_2) and bismuth vanadate

(BiVO$_4$), from which the basement of the work was laid. The short summary of the objectives followed after the fixation of materials is described below:

(i) Synthesis of GO / MOx nanocomposite

- Metal oxides used are TiO$_2$ and BiVO$_4$ nanoparticles
- Five different ratios, namely 0.5, 1.0, 1.5, 2, 2.5 % (wt. % of GO) of nanocomposites are used
- The synthesized nanocomposites are characterized and optimized to perform the activity for visible light-driven photocatalysis

(ii) Culturing of microorganisms & microalgae

- For the investigation of photocatalytic disinfection by the synthesized nanocomposites, *E. coli* (bacteria), *Anabaena* (cyanobacteria), and *Phaeodactylum tricornutum* (diatom) was cultured and studied.

(iii) Photocatalytic disinfection study

- Various experiments were performed to obtain the conditions necessary for the microbial and microalgal disinfection that can occur under visible light irradiation.

The reported work focused on a green and facile methodology to synthesize GO/TiO$_2$ and GO/BiVO$_4$ nanocomposites. These nanocomposites could disinfect drinking water in a concise time with minimal dosage. Furthermore, the nanocomposites showed their effectiveness for microalgal disinfection with excellent stability. The reported results are first to the best of our knowledge.

This work mainly focuses on developing graphene oxide (GO) sheets incorporated with synthesized titanium dioxide (TiO$_2$) anatase and monoclinic bismuth vanadate (BiVO$_4$) nanoparticles to obtain nanocomposites namely, GO/TiO$_2$ and GO/BiVO$_4$ for the removal of bacteria, cyanobacteria, and microalgae from drinking water under visible light irradiation.

The thesis's objective lies in the synthesis of GO/TiO$_2$ and GO/BiVO$_4$ nanocomposites with five different loading ratios. The synthesized nanocomposites are characterized and are used for the visible-light-driven photocatalytic activity against the non-photosynthetic bacteria *E. coli*, the cyanobacteria *Anabaena, sp.,* and the microalga *Phaeodactylum tricornutum*. The obtained results are confirmed with the advanced

characterization techniques. Based on these objectives, the thesis is divided into four chapters with the following brief descriptions (Table 1.5).

Table 1.5: Structure of the thesis

Chapter	Brief description
Chapter 2	The second chapter comprises the synthesis, characterization techniques, experimental setup, and the establishment of cultures conducted to fulfill this work.
Chapter 3	This chapter gives detailed information regarding the selection of the nanoparticles during the beginning of visible-light-driven photocatalytic disinfection study and the various stages of optimizations considering the application.
Chapter 4	The fourth chapter discusses the characterization and application-level study of photocatalytic disinfection of microbes using GO/TiO_2 and $GO/BiVO_4$ nanocomposite. The results confirmed with advanced characterizations are also discussed here.
Chapter 5	This chapter reports the preliminary studies on the photosynthetic microorganism's disinfection study by the nanocomposite. It goes through various optimizations, and stages followed to accomplish the destruction of cyanobacteria and microalgae.

References

[1]   M.O. Dinka, Safe Drinking Water: Concepts, Benefits, Principles and Standards, in: Water   Challenges   an   Urban.   World,   2018. https://doi.org/10.5772/intechopen.71352.

[2]   CITIGROUP,   Solutions   for   a   Global   Water   Crisis,   2017. https://globalbanking.icg.citi.com/55FZFLn2YyizavUYwifLtd4NvPyHYBWbXcW hoKUZdSZfscsXTwhWcA%3D%3D.

[3]   R. Afroz, M.M. Masud, R. Akhtar, J.B. Duasa, Water pollution: Challenges and future direction for water resource management policies in malaysia, Environ. Urban. ASIA. 5 (2014) 63–81. https://doi.org/10.1177/0975425314521544.

[4]   S.A. Wimalawansa, S.J. Wimalawansa, Environmentally induced, occupational diseases with emphasis on chronic kidney disease of multifactorial origin affecting tropical countries, Ann. Occup. Environ. Med. 28 (2016). https://doi.org/10.1186/s40557-016-0119-y.

[5]   Unesco, World Water Assessment Programme, The United Nations World Water Development Report 3, United Nations World Water Dev. Rep. 3. (2012) 201. https://doi.org/10.4324/9781849773355.

[6]   N.L. Cain, P.H. Gleick, The global water crisis, Issues Sci. Technol. 21 (2005) 79–81.

[7]   United Nations / UNESCO, United Nations World Water Development Report: Water   And   Energy,   2014.   http://www.unesco.org/open-access/terms-use-ccbysa-en.

[8]   https://www.bloomberg.com/graphics/2019-countries-facing-water-crisis/)., (2019).   https://www.bloomberg.com/graphics/2019-countries-facing-water-crisis/). (accessed January 14, 2021).

[9]   S. Zandaryaa, U.N. Educational, Chapter 8 . Organic matter , in: 2019.

[10]   WHO, Climate-resilient water safety plans: Managing health risks associated with   climate   variability   and   change,   2017. http://apps.who.int/iris/bitstream/handle/10665/258722/9789241512794-eng.pdf?sequence=1.

[11]   N. Soto-Coloballes, The Development of Air Pollution in Mexico City, SAGE Open. 10 (2020) 1–10. https://doi.org/10.1177/2158244020931072.

[12]   T. Turrén-Cruz, J.A. García-Rodríguez, M.Á. López Zavala, Evaluation of sanitation strategies and initiatives implemented in Mexico from community capitals   point   of   view,   Water   (Switzerland).   11   (2019)   1–19. https://doi.org/10.3390/w11020295.

[13]   F. S., Assessing Water Quality in the Developing World: An Index for Mexico City, 2012. https://doi.org/10.5772/32055.

[14]   J. Greene, Bottled water in Mexico: The rise of a new access to water paradigm, WIREs Water. 5 (2018) e1286. https://doi.org/10.1002/wat2.1286.

[15]   Informe   2012,   (2012). https://apps1.semarnat.gob.mx:8443/dgeia/informe_12eng/06_agua/cap6_2.ht ml (accessed January 9, 2021).

[16]   K. Chanon, Indicators for Children's Health and the Environment in North America: A First Report on Available Indicators and Measures, 2005.

[17]   C.L. Ho, P.Y. Hwang, Endoscope-assisted Transorbital Keyhole Surgical Approach to Ruptured Supratentorial Aneurysms, J. Neurol. Surgery, Part A Cent. Eur. Neurosurg. 76 (2015) 376–383. https://doi.org/10.1055/s-0035-1547358.

[18]   F. Schutte, Handbook for The Operation of Water Treatment Works, 2011. http://content.ebscohost.com/ContentServer.asp?T=P&P=AN&K=57995235&S =R&D=bth&EbscoContent=dGJyMNXb4kSeprY4yOvsOLCmr06eqK9SsKi4SK +WxWXS&ContentCustomer=dGJyMPGut1C0rLNRuePfgeyx44Dt6flA.

[19]   G. Crini, E. Lichtfouse, Advantages and disadvantages of techniques used for wastewater treatment, Environ. Chem. Lett. 17 (2019) 145–155. https://doi.org/10.1007/s10311-018-0785-9.

[20]   J.J. Ramsden, What is nanotechnology?, in: Nanotechnol. Perceptions, 2005: pp. 3–17. https://doi.org/10.4024/n03ra05/01.01.

[21]   J. Theron, J.A. Walker, T.E. Cloete, Nanotechnology and water treatment: Applications and emerging opportunities, Crit. Rev. Microbiol. 34 (2008) 43–69. https://doi.org/10.1080/10408410701710442.

[22]   C. Santhosh, V. Velmurugan, G. Jacob, S.K. Jeong, A.N. Grace, A. Bhatnagar, Role of nanomaterials in water treatment applications: A review, Chem. Eng. J. 306 (2016) 1116–1137. https://doi.org/10.1016/j.cej.2016.08.053.

[23]   A.A. Basheer, New generation nano-adsorbents for the removal of emerging contaminants in water, J. Mol. Liq. 261 (2018) 583–593. https://doi.org/10.1016/j.molliq.2018.04.021.

[24]   M. Anjum, R. Miandad, M. Waqas, F. Gehany, M.A. Barakat, Remediation of wastewater using various nano-materials, Arab. J. Chem. 12 (2019) 4897–4919. https://doi.org/10.1016/j.arabjc.2016.10.004.

[25]   O. Akhavan, Lasting antibacterial activities of Ag-TiO2/Ag/a-TiO2 nanocomposite thin film photocatalysts under solar light irradiation, J. Colloid Interface Sci. 336 (2009) 117–124. https://doi.org/10.1016/j.jcis.2009.03.018.

[26]   R.A. Khaydarov, R.R. Khaydarov, O. Gapurova, Nano-photocatalysts for the destruction of chloro-organic compounds and bacteria in water, J. Colloid Interface Sci. 406 (2013) 105–110. https://doi.org/10.1016/j.jcis.2013.05.067.

[27]   R. Das, M.E. Ali, S.B.A. Hamid, S. Ramakrishna, Z.Z. Chowdhury, Carbon nanotube membranes for water purification: A bright future in water desalination, Desalination. 336 (2014) 97–109. https://doi.org/10.1016/j.desal.2013.12.026.

[28]   X. Qu, J. Brame, Q. Li, P.J.J. Alvarez, Nanotechnology for a safe and sustainable water supply: Enabling integrated water treatment and reuse, Acc. Chem. Res. 46 (2013) 834–843. https://doi.org/10.1021/ar300029v.

[29]   C.J. Vörösmarty, P.B. McIntyre, M.O. Gessner, D. Dudgeon, A. Prusevich, P. Green, S. Glidden, S.E. Bunn, C.A. Sullivan, C.R. Liermann, P.M. Davies, Global threats to human water security and river biodiversity, Nature. 467 (2010) 555–561. https://doi.org/10.1038/nature09440.

[30]   E. Malaj, P.C. Von Der Ohe, M. Grote, R. Kühne, C.P. Mondy, P. Usseglio-Polatera, W. Brack, R.B. Schäfer, Organic chemicals jeopardize the health of freshwater ecosystems on the continental scale, Proc. Natl. Acad. Sci. U. S. A. 111 (2014) 9549–9554. https://doi.org/10.1073/pnas.1321082111.

[31]   M. Meybeck, Global analysis of river systems: From Earth system controls to Anthropocene syndromes, Philos. Trans. R. Soc. B Biol. Sci. 358 (2003) 1935–1955. https://doi.org/10.1098/rstb.2003.1379.

[32]   K.L. Nelson, A. Murray, Sanitation for unserved populations: Technologies, implementation challenges, and opportunities, Annu. Rev. Environ. Resour. 33 (2008) 119–151. https://doi.org/10.1146/annurev.environ.33.022007.145142.

[33]   R.I. McDonald, P. Green, D. Balk, B.M. Fekete, C. Revenga, M. Todd, M. Montgomery, Urban growth, climate change, and freshwater availability, Proc. Natl. Acad. Sci. U. S. A. 108 (2011) 6312–6317.

https://doi.org/10.1073/pnas.1011615108.

[34] P.C.D. Milly, K.A. Dunne, A. V. Vecchia, Global pattern of trends in streamflow and water availability in a changing climate, Nature. 438 (2005) 347–350. https://doi.org/10.1038/nature04312.

[35] V. Kumar, M.P. Shah, Advanced oxidation processes for complex wastewater treatment, in: Adv. Oxid. Process. Effl. Treat. Plants, 2021: pp. 1–31. https://doi.org/10.1016/b978-0-12-821011-6.00001-3.

[36] S. Singh, A. Garg, Advanced oxidation processes for industrial effluent treatment, in: Adv. Oxid. Process. Effl. Treat. Plants, 2021: pp. 255–272. https://doi.org/10.1016/b978-0-12-821011-6.00012-8.

[37] N. Abdel-Raouf, A.A. Al-Homaidan, I.B.M. Ibraheem, Microalgae and wastewater treatment, Saudi J. Biol. Sci. 19 (2012) 257–275. https://doi.org/10.1016/j.sjbs.2012.04.005.

[38] A.K. Biń, S. Sobera-Madej, Comparison of the Advanced Oxidation Processes (UV, UV/H 2O 2 and O 3) for the Removal of Antibiotic Substances during Wastewater Treatment, Ozone Sci. Eng. 34 (2012) 136–139. https://doi.org/10.1080/01919512.2012.650130.

[39] W.H. Glaze, J.W. Kang, D.H. Chapin, The chemistry of water treatment processes involving ozone, hydrogen peroxide and ultraviolet radiation, Ozone Sci. Eng. 9 (1987) 335–352. https://doi.org/10.1080/01919518708552148.

[40] H.J. Geyer, G.G. Rimkus, I. Scheunert, A. Kaune, K.-W. Schramm, A. Kettrup, M. Zeeman, D.C.G. Muir, L.G. Hansen, D. Mackay, Bioaccumulation and Occurrence of Endocrine-Disrupting Chemicals (EDCs), Persistent Organic Pollutants (POPs), and Other Organic Compounds in Fish and Other Organisms Including Humans, Bioaccumulation – New Asp. Dev. 2 (2005) 1–166. https://doi.org/10.1007/10503050_1.

[41] O. Tsydenova, V. Batoev, A. Batoeva, Solar-enhanced advanced oxidation processes for water treatment: Simultaneous removal of pathogens and chemical pollutants, Int. J. Environ. Res. Public Health. 12 (2015) 9542–9561. https://doi.org/10.3390/ijerph120809542.

[42] P. Fernández-Castro, M. Vallejo, M.F. San Román, I. Ortiz, Insight on the fundamentals of advanced oxidation processes: Role and review of the determination methods of reactive oxygen species, J. Chem. Technol. Biotechnol. 90 (2015) 796–820. https://doi.org/10.1002/jctb.4634.

[43] K. Ayoub, E.D. van Hullebusch, M. Cassir, A. Bermond, Application of advanced oxidation processes for TNT removal: A review, J. Hazard. Mater. 178 (2010) 10–28. https://doi.org/10.1016/j.jhazmat.2010.02.042.

[44] P. Sathishkumar, R.V. Mangalaraja, S. Anandan, Review on the recent improvements in sonochemical and combined sonochemical oxidation processes - A powerful tool for destruction of environmental contaminants, Renew. Sustain. Energy Rev. 55 (2016) 426–454. https://doi.org/10.1016/j.rser.2015.10.139.

[45] P. Chowdhury, T. Viraraghavan, Sonochemical degradation of chlorinated organic compounds, phenolic compounds and organic dyes - A review, Sci. Total Environ. 407 (2009) 2474–2492. https://doi.org/10.1016/j.scitotenv.2008.12.031.

[46] M. Bourgin, E. Borowska, J. Helbing, J. Hollender, H.P. Kaiser, C. Kienle, C.S. McArdell, E. Simon, U. von Gunten, Effect of operational and water quality parameters on conventional ozonation and the advanced oxidation process O3/H2O2: Kinetics of micropollutant abatement, transformation product and

bromate formation in a surface water, Water Res. 122 (2017) 234–245. https://doi.org/10.1016/j.watres.2017.05.018.

[47] N. Mishra, R. Reddy, A. Kuila, A. Rani, A. Nawaz, S. Pichiah, A Review on Advanced Oxidation Processes for Effective Water Treatment, Curr. World Environ. 12 (2017) 469–489. https://doi.org/10.12944/cwe.12.3.02.

[48] M.A. Oturan, J.J. Aaron, Advanced oxidation processes in water/wastewater treatment: Principles and applications. A review, Crit. Rev. Environ. Sci. Technol. 44 (2014) 2577–2641. https://doi.org/10.1080/10643389.2013.829765.

[49] F.H. and J. Weiss, The catalytic decomposition of hydrogen peroxide by iron salts, Proc. R. Soc. London. Ser. A - Math. Phys. Sci. 147 (1934) 332–351. https://doi.org/10.1098/rspa.1934.0221.

[50] R. Bond, Advanced Oxidation Processes, in: White's Handb. Chlorination Altern. Disinfect. Fifth Ed., 2010: pp. 976–1002. https://doi.org/10.1002/9780470561331.ch18.

[51] W.G. Barb, J.H. Baxendale, P. George, K.R. Hargrave, Reactions of ferrous and ferric ions with hydrogen peroxide, Nature. 163 (1949) 692–694. https://doi.org/10.1038/163692a0.

[52] W.G. Barb, J.H. Baxendale, P. George, K.R. Hargrave, Reactions of ferrous and ferric ions with hydrogen peroxide. Part I. - The ferrous ion reaction, Trans. Faraday Soc. 47 (1951) 462–500. https://doi.org/10.1039/TF9514700462.

[53] W.G. Barb, J.H. Baxendale, P. George, K.R. Hargrave, Reactions of ferrous and ferric ions with hydrogen peroxide. Part II. - The ferric ion reaction, Trans. Faraday Soc. 47 (1951) 591–616. https://doi.org/10.1039/TF9514700591.

[54] J.A. Byrne, P.S.M. Dunlop, J.W.J. Hamilton, P. Fernández-Ibáñez, I. Polo-López, P.K. Sharma, A.S.M. Vennard, A review of heterogeneous photocatalysis for water and surface disinfection, Molecules. 20 (2015) 5574–5615. https://doi.org/10.3390/molecules20045574.

[55] Y. Liu, Application of graphene oxide in water treatment, IOP Conf. Ser. Earth Environ. Sci. 94 (2017) 1–6. https://doi.org/10.1088/1755-1315/94/1/012060.

[56] F. Perrozzi, S. Prezioso, L. Ottaviano, Graphene oxide: From fundamentals to applications, J. Phys. Condens. Matter. 27 (2015). https://doi.org/10.1088/0953-8984/27/1/013002.

[57] D.R. Dreyer, S. Park, C.W. Bielawski, R.S. Ruoff, The chemistry of graphene oxide, Chem. Soc. Rev. 39 (2010) 228–240. https://doi.org/10.1039/b917103g.

[58] A. Safavi, M. Tohidi, F.A. Mahyari, H. Shahbaazi, One-pot synthesis of large scale graphene nanosheets from graphite-liquid crystal composite via thermal treatment, J. Mater. Chem. 22 (2012) 3825–3831. https://doi.org/10.1039/c2jm13929d.

[59] G. Wang, B. Wang, J. Park, Y. Wang, B. Sun, J. Yao, Highly efficient and large-scale synthesis of graphene by electrolytic exfoliation, Carbon N. Y. 47 (2009) 3242–3246. https://doi.org/10.1016/j.carbon.2009.07.040.

[60] Y. Li, D. Wang, W. Li, Y. He, Photoelectric conversion properties of electrochemically codeposited graphene oxide-ZnO nanocomposite films, J. Alloys Compd. 648 (2015) 942–950. https://doi.org/10.1016/j.jallcom.2015.07.037.

[61] X. Xu, J. Shen, N. Li, M. Ye, Facile synthesis of reduced graphene oxide/CoWO4 nanocomposites with enhanced electrochemical performances for supercapacitors, Electrochim. Acta. 150 (2014) 23–34. https://doi.org/10.1016/j.electacta.2014.10.139.

[62] G. Xu, F. Jiang, Z. ang Ren, L. wen Yang, Polyhedral MnO nanocrystals anchored on reduced graphene oxide as an anode material with superior lithium storage capability, Ceram. Int. 41 (2015) 10680–10688. https://doi.org/10.1016/j.ceramint.2015.04.169.

[63] H. Wang, Q. Hao, X. Yang, L. Lu, X. Wang, A nanostructured graphene/polyaniline hybrid material for supercapacitors, Nanoscale. 2 (2010) 2164–2170. https://doi.org/10.1039/c0nr00224k.

[64] H.Y. He, Photoinduced superhydrophilicity and high photocatalytic activity of ZnO-reduced graphene oxide nanocomposite films for self-cleaning applications, Mater. Sci. Semicond. Process. 31 (2015) 200–208. https://doi.org/10.1016/j.mssp.2014.11.029.

[65] F. Perreault, A. Fonseca De Faria, M. Elimelech, Environmental applications of graphene-based nanomaterials, Chem. Soc. Rev. 44 (2015) 5861–5896. https://doi.org/10.1039/c5cs00021a.

[66] Y. Gu, M. Xing, J. Zhang, Synthesis and photocatalytic activity of graphene based doped TiO 2 nanocomposites, Appl. Surf. Sci. 319 (2014) 8–15. https://doi.org/10.1016/j.apsusc.2014.04.182.

[67] H. Park, P.R. Brown, V. Bulović, J. Kong, Graphene as transparent conducting electrodes in organic photovoltaics: Studies in graphene morphology, hole transporting layers, and counter electrodes, Nano Lett. 12 (2012) 133–140. https://doi.org/10.1021/nl2029859.

[68] X. Liu, W. Yang, C. Yu, H. Zhang, Influence of TiO2 morphology on adsorption-photocatalytic efficiency of TiO2-graphene composites for methylene blue degradation, J. Environ. Chem. Eng. 6 (2018) 4899–4907. https://doi.org/10.1016/j.jece.2018.07.009.

[69] J. He, A. Kumar, M. Khan, I.M.C. Lo, Critical review of photocatalytic disinfection of bacteria: from noble metals- and carbon nanomaterials-TiO2 composites to challenges of water characteristics and strategic solutions, Sci. Total Environ. 758 (2021). https://doi.org/10.1016/j.scitotenv.2020.143953.

[70] A. Fujishima, K. Honda, Electrochemical photolysis of water at a semiconductor electrode, Nature. 238 (1972) 37–38. https://doi.org/10.1038/238037a0.

[71] H. Dumortier, S. Lacotte, G. Pastorin, R. Marega, W. Wu, D. Bonifazi, J.P. Briand, M. Prato, S. Muller, A. Bianco, Functionalized carbon nanotubes are non-cytotoxic and preserve the functionality of primary immune cells, Nano Lett. 6 (2006) 1522–1528. https://doi.org/10.1021/nl061160x.

[72] T. Lammel, P. Boisseaux, M.L. Fernández-Cruz, J.M. Navas, Internalization and cytotoxicity of graphene oxide and carboxyl graphene nanoplatelets in the human hepatocellular carcinoma cell line Hep G2, Part. Fibre Toxicol. 10 (2013). https://doi.org/10.1186/1743-8977-10-27.

[73] A.F. De Faria, A.C.M. De Moraes, P.D. Marcato, D.S.T. Martinez, N. Durán, A.G.S. Filho, A. Brandelli, O.L. Alves, Eco-friendly decoration of graphene oxide with biogenic silver nanoparticles: Antibacterial and antibiofilm activity, J. Nanoparticle Res. 16 (2014). https://doi.org/10.1007/s11051-013-2110-7.

[74] M. Teta, M.M. Rankin, S.Y. Long, G.M. Stein, J.A. Kushner, Growth and Regeneration of Adult β Cells Does Not Involve Specialized Progenitors, Dev. Cell. 12 (2007) 817–826. https://doi.org/10.1016/j.devcel.2007.04.011.

[75] J. Li, Y. Zhu, W. Li, X. Zhang, Y. Peng, Q. Huang, Nanodiamonds as intracellular transporters of chemotherapeutic drug, Biomaterials. 31 (2010) 8410–8418. https://doi.org/10.1016/j.biomaterials.2010.07.058.

[76] J. Wen, X. Li, W. Liu, Y. Fang, J. Xie, Y. Xu, Photocatalysis fundamentals and

surface modification of TiO2 nanomaterials, Cuihua Xuebao/Chinese J. Catal. 36 (2015) 2049–2070. https://doi.org/10.1016/S1872-2067(15)60999-8.

[77] O.M. Alfano, D. Bahnemann, A.E. Cassano, R. Dillert, R. Goslich, Photocatalysis in water environments using artificial and solar light, Catal. Today. 58 (2000) 199–230. https://doi.org/10.1016/S0920-5861(00)00252-2.

[78] M.J. Benotti, B.D. Stanford, E.C. Wert, S.A. Snyder, Evaluation of a photocatalytic reactor membrane pilot system for the removal of pharmaceuticals and endocrine disrupting compounds from water, Water Res. 43 (2009) 1513–1522. https://doi.org/10.1016/j.watres.2008.12.049.

[79] M. Cho, H. Chung, W. Choi, J. Yoon, Linear correlation between inactivation of E. coli and OH radical concentration in TiO2 photocatalytic disinfection, Water Res. 38 (2004) 1069–1077. https://doi.org/10.1016/j.watres.2003.10.029.

[80] Y.C. Wu, Y.C. Chaing, C.Y. Huang, S.F. Wang, H.Y. Yang, Morphology-controllable Bi2O3 crystals through an aqueous precipitation method and their photocatalytic performance, Dye. Pigment. 98 (2013) 25–30. https://doi.org/10.1016/j.dyepig.2013.02.006.

[81] S. Sun, W. Wang, Advanced chemical compositions and nanoarchitectures of bismuth based complex oxides for solar photocatalytic application, RSC Adv. 4 (2014) 47136–47152. https://doi.org/10.1039/c4ra06419d.

[82] Z. Liu, F. Yan, The application of bismuth-based oxides in organic-inorganic hybrid photovoltaic devices, J. Am. Ceram. Soc. 95 (2012) 1944–1948. https://doi.org/10.1111/j.1551-2916.2012.05088.x.

[83] A. Kudo, K. Omori, H. Kato, A novel aqueous process for preparation of crystal form-controlled and highly crystalline BiVO4 powder from layered vanadates at room temperature and its photocatalytic and photophysical properties, J. Am. Chem. Soc. 121 (1999) 11459–11467. https://doi.org/10.1021/ja992541y.

[84] D. Lv, D. Zhang, X. Pu, D. Kong, Z. Lu, X. Shao, H. Ma, J. Dou, One-pot combustion synthesis of BiVO4/BiOCl composites with enhanced visible-light photocatalytic properties, Sep. Purif. Technol. 174 (2017) 97–103. https://doi.org/10.1016/j.seppur.2016.10.010.

[85] D.L. Guan, C.G. Niu, X.J. Wen, H. Guo, C.H. Deng, G.M. Zeng, Enhanced Escherichia coli inactivation and oxytetracycline hydrochloride degradation by a Z-scheme silver iodide decorated bismuth vanadate nanocomposite under visible light irradiation, J. Colloid Interface Sci. 512 (2018) 272–281. https://doi.org/10.1016/j.jcis.2017.10.068.

[86] Q. Xu, L. Zhang, J. Yu, S. Wageh, A.A. Al-ghamdi, M. Jaroniec, Direct Z-scheme photocatalysts : Principles , synthesis , and applications, Mater. Today. 21 (2018) 1042–1063.

[87] P. Ju, Y. Wang, Y. Sun, D. Zhang, Controllable one-pot synthesis of a nest-like Bi2WO6/BiVO4 composite with enhanced photocatalytic antifouling performance under visible light irradiation, Dalt. Trans. 45 (2016) 4588–4602. https://doi.org/10.1039/c6dt00118a.

[88] J.E. Naschitz, R. Mussafia-Priselac, Y. Kovalev, N. Zaigraykin, G. Slobodin, N. Elias, I. Rosner, Patterns of hypocapnia on tilt in patients with fibromyalgia, chronic fatigue syndrome, nonspecific dizziness, and neurally mediated syncope, 2006. https://doi.org/10.1097/00000441-200606000-00001.

[89] D.M. Blake, P.C. Maness, Z. Huang, E.J. Wolfrum, J. Huang, W.A. Jacoby, Application of the photocatalytic chemistry of titanium dioxide to disinfection and the killing of cancer cells, Sep. Purif. Methods. 28 (1999) 1–50. https://doi.org/10.1080/03602549909351643.

[90] K. Yogo, M. Ishikawa, Recent progress in environmental catalytic technology, Catal. Surv. from Japan. 4 (2000) 83–90. https://doi.org/10.1023/A:1019088121877.

[91] S. Korsgaard, A.R. Anderson, Enacting entrepreneurship as social value creation, Int. Small Bus. J. 29 (2011) 135–151. https://doi.org/10.1177/0266242610391936.

[92] D.Y. Goswami, D.M. Blake, Cleaning up with sunshine, Mech. Eng. 118 (1996) 56–59.

[93] D.Y. Goswami, A review of engineering developments of aqueous phiase solar photocatalytic detoxification and disinfection processes, J. Sol. Energy Eng. Trans. ASME. 119 (1997) 101–107. https://doi.org/10.1115/1.2887886.

[94] D.Y. Goswami, S. Vijayaraghavan, S. Lu, G. Tamm, New and emerging developments in solar energy, Sol. Energy. 76 (2004) 33–43. https://doi.org/10.1016/S0038-092X(03)00103-8.

[95] S. Malato, J. Blanco, D.C. Alarcón, M.I. Maldonado, P. Fernández-Ibáñez, W. Gernjak, Photocatalytic decontamination and disinfection of water with solar collectors, Catal. Today. 122 (2007) 137–149. https://doi.org/10.1016/j.cattod.2007.01.034.

[96] D. Bahnemann, Photocatalytic water treatment: Solar energy applications, Sol. Energy. 77 (2004) 445–459. https://doi.org/10.1016/j.solener.2004.03.031.

[97] M. Otaki, T. Hirata, S. Ohgaki, Aqueous microorganisms inactivation by photocatalytic reaction, in: Water Sci. Technol., 2000: pp. 103–108. https://doi.org/10.2166/wst.2000.0365.

[98] T. Kato, H. Tohma, O. Miki, T. Shibata, M. Tamura, Degradation of norovirus in sewage treatment water by photocatalytic ultraviolet disinfection, Nippon Steel Tech. Rep. (2005) 41–44.

[99] F. Goulhen-Chollet, S. Josset, N. Keller, V. Keller, M.C. Lett, Monitoring the bactericidal effect of UV-A photocatalysis: A first approach through 1D and 2D protein electrophoresis, Catal. Today. 147 (2009) 169–172. https://doi.org/10.1016/j.cattod.2009.06.001.

[100] J. Kiwi, V. Nadtochenko, Evidence for the mechanism of photocatalytic degradation of the bacterial wall membrane at the TiO2 interface by ATR-FTIR and laser kinetic spectroscopy, Langmuir. 21 (2005) 4631–4641. https://doi.org/10.1021/la0469831.

[101] P. Wu, R. Xie, J.A. Imlay, J.K. Shang, Visible-light-induced photocatalytic inactivation of bacteria by composite photocatalysts of palladium oxide and nitrogen-doped titanium oxide, Appl. Catal. B Environ. 88 (2009) 576–581. https://doi.org/10.1016/j.apcatb.2008.12.019.

[102] Z. Huang, P.C. Maness, D.M. Blake, E.J. Wolfrum, S.L. Smolinski, W.A. Jacoby, Bactericidal mode of titanium dioxide photocatalysis, J. Photochem. Photobiol. A Chem. 130 (2000) 163–170. https://doi.org/10.1016/S1010-6030(99)00205-1.

[103] M. Wainwright, Methylene blue derivatives - Suitable photoantimicrobials for blood product disinfection?, Int. J. Antimicrob. Agents. 16 (2000) 381–394. https://doi.org/10.1016/S0924-8579(00)00207-7.

[104] K. Sunada, T. Watanabe, K. Hashimoto, Studies on photokilling of bacteria on TiO 2 thin film, J. Photochem. Photobiol. A Chem. 156 (2003) 227–233. https://doi.org/10.1016/S1010-6030(02)00434-3.

[105] G. Carré, E. Hamon, S. Ennahar, M. Estner, M.C. Lett, P. Horvatovich, J.P. Gies, V. Keller, N. Keller, P. Andre, TiO2 photocatalysis damages lipids and proteins in Escherichia coli, Appl. Environ. Microbiol. 80 (2014) 2573–2581.

https://doi.org/10.1128/AEM.03995-13.

[106] P.V. Laxma Reddy, B. Kavitha, P.A. Kumar Reddy, K.H. Kim, TiO2-based photocatalytic disinfection of microbes in aqueous media: A review, Environ. Res. 154 (2017) 296–303. https://doi.org/10.1016/j.envres.2017.01.018.

[107] W. Wang, G. Huang, J.C. Yu, P.K. Wong, Advances in photocatalytic disinfection of bacteria: Development of photocatalysts and mechanisms, J. Environ. Sci. (China). 34 (2015) 232–247. https://doi.org/10.1016/j.jes.2015.05.003.

[108] L. Fewtrell, Water Quality: Guidelines, Standards and Health: Assessment of Risk and Risk Management for Water-Related Infectious Disease, Water Intell. Online. 12 (2013). https://doi.org/10.2166/9781780405889.

[109] P.R. Hunter, M. Waite, E. Ronchi, Drinking water and infectious disease: Establishing the links, 2002. https://doi.org/10.1258/jrsm.96.6.311.

[110] N. Paneth, P. Vinten-Johansen, H. Brody, M. Rip, A rivalry of foulness: Official and unofficial investigations of the London cholera epidemic of 1854, Am. J. Public Health. 88 (1998) 1545–1553. https://doi.org/10.2105/AJPH.88.10.1545.

[111] S.C. Edberg, E.W. Rice, R.J. Karlin, M.J. Allen, Escherichia coli: The best biological drinking water indicator for public health protection, J. Appl. Microbiol. Symp. Suppl. 88 (2000). https://doi.org/10.1111/j.1365-2672.2000.tb05338.x.

[112] C. Enriquez, N. Nwachuku, C.P. Gerba, Direct exposure to animal enteric pathogens, Rev. Environ. Health. 16 (2001) 117–131. https://doi.org/10.1515/REVEH.2001.16.2.117.

[113] A. Hambidge, Reviewing efficacy of alternative water treatment techniques., Health Estate. 55 (2001) 23–25.

[114] J.W. Li, Z.T. Xin, X.W. Wang, J.L. Zheng, F.H. Chao, Mechanisms of inactivation of hepatitis A virus by chlorine, Appl. Environ. Microbiol. 68 (2002) 4951–4955. https://doi.org/10.1128/AEM.68.10.4951-4955.2002.

[115] C.B. Lopez, E.B. Jewett, Q. Dortch, B.T. Walton, H.K. Hudnell, Scientific Assessment of Freshwater Harmful Algal Blooms, Sci. Assess. Freshw. Harmful Algal Bloom. (2008) 65.

[116] J.L. Graham, N.M. Dubrovsky, S.M. Eberts, Cyanobacterial Harmful Algal Blooms and U.S. Geological Survey Science Capabilities, Usgs. (2017) 12 pp. https://doi.org/10.3133/ofr20161174.

[117] L.M. Grattan, S. Holobaugh, J.G. Morris, Harmful algal blooms and public health, Harmful Algae. 57 (2016) 2–8. https://doi.org/10.1016/j.hal.2016.05.003.

[118] A. Chakraborty, S. Ghosh, P. Mukhopadhyay, S.M. Dinara, A. Bag, M.K. Mahata, R. Kumar, S. Das, J. Sanjay, S. Majumdar, D. Biswas, Trapping effect analysis of AlGaN/InGaN/GaN Heterostructure by conductance frequency measurement, 2014. https://doi.org/10.1007/s13398-014-0173-7.2.

[119] J.-D. Rochaix, The Dynamics of the Photosynthetic Apparatus in Algae, in: Appl. Photosynth. - New Prog., 2016. https://doi.org/10.5772/62261.

Chapter 2

Synthesis, characterization techniques, experimental set-up, and growth of cultures

Chapter 2: Synthesis, characterization techniques, experimental set-up, and growth of cultures

2.1 Materials

Multi-walled carbon nanotubes (MWCNTs), titanium dioxide anatase (TiO$_2$ anatase), orange G dye (C$_{16}$H$_{10}$N$_2$Na$_2$O$_7$S$_2$), zinc chloride (ZnCl$_2$), ammonium hydroxide (NH$_4$OH), sodium hydroxide (NaOH), zinc acetate (ZnC$_4$H$_6$O$_4$), methanol (CH$_3$OH), ethylene glycol (C$_2$H$_6$O$_2$), titanium chloride (TiCl$_4$), ethanol (C$_6$H$_6$O), bismuth nitrate pentahydrate ((BiNO$_3$)$_3$.H$_2$O), ammonium metavanadate (NH$_4$VO$_3$), nitric acid (HNO$_3$), citric acid (HOC(COOH)(CH$_2$COOH)$_2$), nutrient agar, eosin methylene blue (EMB) agar, agar-agar, Luria Bertani (LB) broth media, phosphate-buffered saline (PBS), Evans Blue dye (C$_{34}$H$_{24}$N$_6$Na$_4$O$_{14}$S$_4$) and sodium bicarbonate (NaHCO$_3$), Whatman filter paper, and nylon membrane were purchased from Sigma Aldrich, Mexico. Graphene oxide (GO) was purchased from Graphenemex, Mexico, and was maintained under appropriate conditions. All the chemical reagents were of analytical grade and used without any purification. The media necessary for the growth of cyanobacteria and microalgae, i.e., BG11 and F2, respectively, was prepared. The deionized (DI) water was produced in a Millipore Milli-Q water purification system.

This chapter consists of the methodology, and protocols followed through the research work and demonstrate the trial-and-error methods to satisfy the objectives of this work. The work was divided into two stages, *i.e.*, the first stage, where the selection and optimization of the materials and methodology were performed while the second stage consisted of the detailed study and applicative performance of the confirmed materials. Therefore, the methodology and techniques followed for the above-mentioned stages are discussed in this chapter. The steps that were undertaken during the process of selection and optimization are depicted in the flowchart given below (Fig: 2.1)
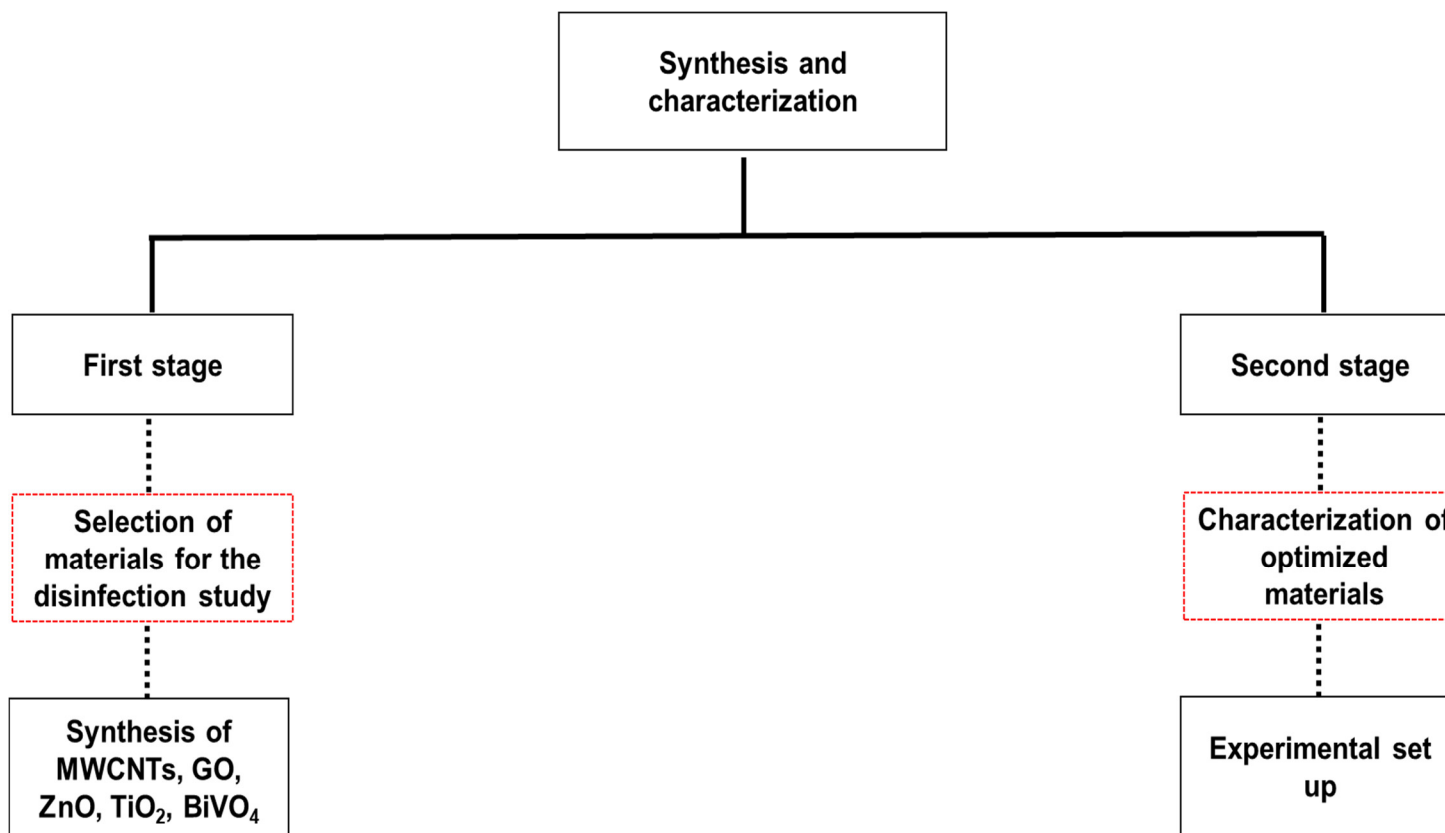
Fig 2.1: Flowchart showing the selection of functional materials. As a preliminary step, the materials were examined for their efficiency in the disinfection research. The optimized materials and conditions proceeded for the photocatalytic disinfection study as the second stage.

2.2. Cell cultivation

2.2.1 Bacterial culture (*Escherichia coli K12*)

The bacterial strains of *Escherichia coli K12 (E. coli K12)* (ATCC®10798™) (CBDB-11-1538) were obtained from the Colección Nacional de Cepas Microbianas Celulares (CDBB) of CINVESTAV, Mexico (Fig 2.2 (a)). *E. coli K12* was grown at 37°C overnight in LB broth under aerobic conditions with constant shaking. For the preparation of the bacterial stock suspension, 3 µl of *E. coli K12* was added into 3 mL of Luria Bertani (LB) medium and incubated for 16 h at 37 ˚C. The initial concentration of the bacterial suspension was around 10^9 CFU/mL. Then, bacterial cells were collected by centrifugation at 4000 rpm (RCF = 1792) for 20 min. The pellets were resuspended and washed with sterile phosphate buffer saline (PBS) solution three times. The bacterial stock suspension was enumerated by surface plating in triplicate samples on nutrient agar after serial dilution in PBS. The plates were incubated for 24 h at 37°C (Fig 2.2 (b) and (c)).
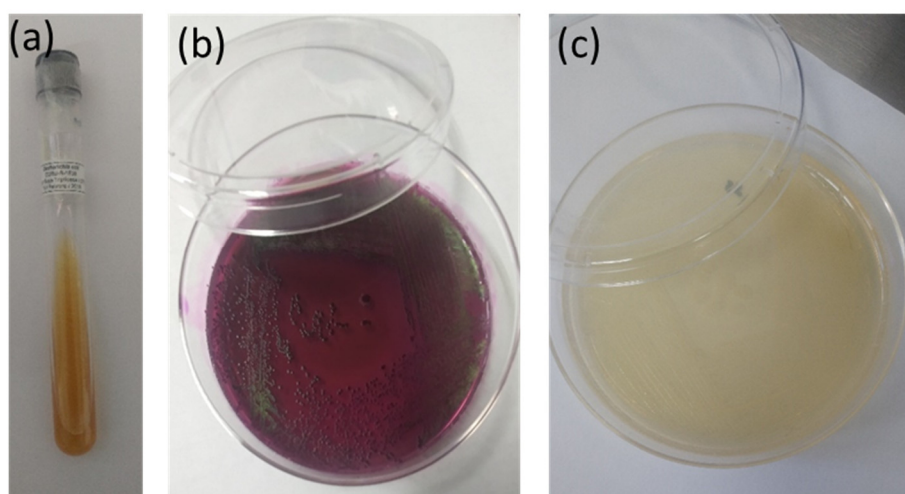
Fig 2.2: (a) Escherichia coli K12 (E. coli K12) (CBDB-11-1538), (b) E. coli K12 as green metallic sheen in Eosin Methylene Blue agar (EMB agar), (c) E. coli K12 as white translucent colonies in Nutrient agar

2.2.2 Algal culture

The cyanobacterium *Anabaena flos-aquae* PCC 7120 was cultured in a Blue Green (BG11) medium, whereas the diatom *Phaeodactylum tricornutum* UTEX 644 (Pt4) [1] were maintained in F2, in a 50 mL flask (Sarstedt). The gas exchange was performed through a membrane in the cap (Fig 2.3).
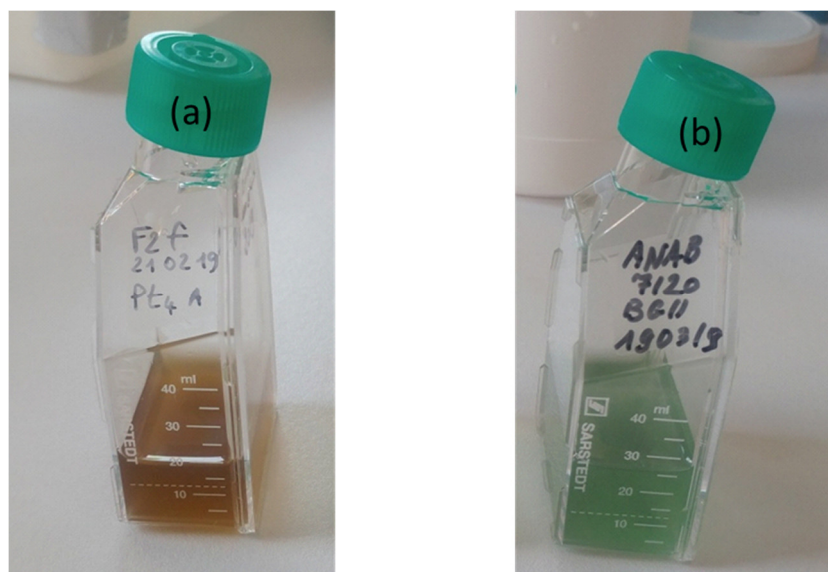
Fig 2.3: Culture of microalgae (a) Phaeodactylum tricornutum b) Anabaena flos aquae with air circulation through the cap.

2.3 Synthesis methods - First stage

2.3.1 Functionalization of MWCNTs and synthesis of MWCNTs/TiO$_2$ composite

MWCNTs underwent a functionalization process to convert them into more active-sited material. Oxidation of MWCNT was carried out by adding mixtures of concentrated nitric/sulphuric acid (HNO_3/H_2SO_4) followed by ultrasonication for 6 h at 60 °C. The functionalization process can be explained in short as follows: the measured quantity of MWCNT was added to a 100 mL mixture of HNO_3 (69 %) and H_2SO_4 (95-98%). The reaction mixture was kept in a reaction flask, coupled to a condenser. The whole mixture was refluxed and sonicated in an ultrasonic water bath at 60°C. After the process, the suspension was diluted using deionized water followed by centrifugation and filtration through a Millipore membrane (0.1 µm). The filtrate was washed using deionized water to attain a neutral pH and finally dried in the oven at 80°C for 6 h. The functionalized MWCNT material was put in contact with a definite amount of refluxed by a definite amount of TiO$_2$ anatase, synthesized through the sol-gel method, and refluxed [2,3]. The synthesized composite was characterized.

2.3.2 Photocatalytic dye degradation study using MWCNT/TiO$_2$ composite

The photocatalytic efficiency was studied by the reaction suspensions containing the MWCNT/TiO$_2$ nanoparticles with the Orange G dye, which is an azo dye that is grouped under the synthetic dyes that have -N=N- groups (azo group) (Fig 2.4). This

dye is particularly used in the textile industry. The composite dosage was fixed at 1 g/L and the suspension of the composite and orange G dye was kept in the dark for 30 mins under stirring to obtain the adsorption-desorption isotherm equilibrium. After the dark incubation, the suspension was exposed to visible light irradiation using a homemade reactor for a period of 2 h. The samples of 1 mL were taken every 10 min and measured using a UV-Vis spectrophotometer to determine the reduction in the concentration of Orange G through the photocatalysis test. The measurements were performed at 476 nm using a calibration curve [4].
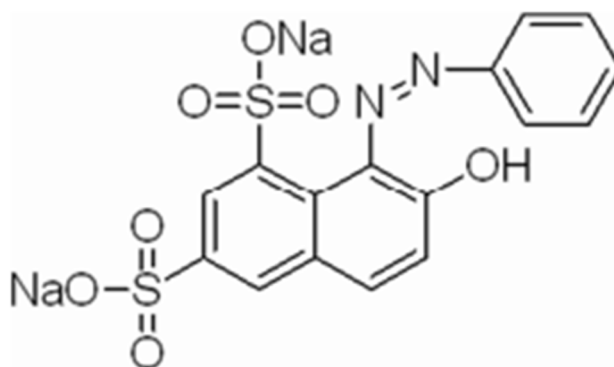
Fig 2.4: Orange G dye molecular structure [5]

2.3.3 Zinc oxide nanoparticle synthesis

Zinc oxide nanoparticles were synthesized through different methodologies adapted from the literature focusing on obtaining spherical nanoparticles. The various methodologies followed are discussed below.

2.3.3 (a) Precipitation method

This zinc oxide synthesis used zinc chloride as the precursor. In this methodology, a solution of zinc chloride was prepared by dissolving zinc chloride in deionized water. Followed by the preparation of zinc chloride solution, ammonium hydroxide was dropwise added to this suspension using a burette (Fig 2.5 (a)). The reaction mixture was continuously stirred in a magnetic stirrer at room temperature till the complete precipitation occurred (Fig 2.5 (b)). The precipitate was washed with deionized water and then dried in a hot air oven at 100° C for complete drying. The dried precipitate was crushed, milled, and then sieved to get uniform-sized particles. After sieving, the

precipitate was calcined in a muffle furnace at 450° C for 2 h by the heating rate at 5°C [6].
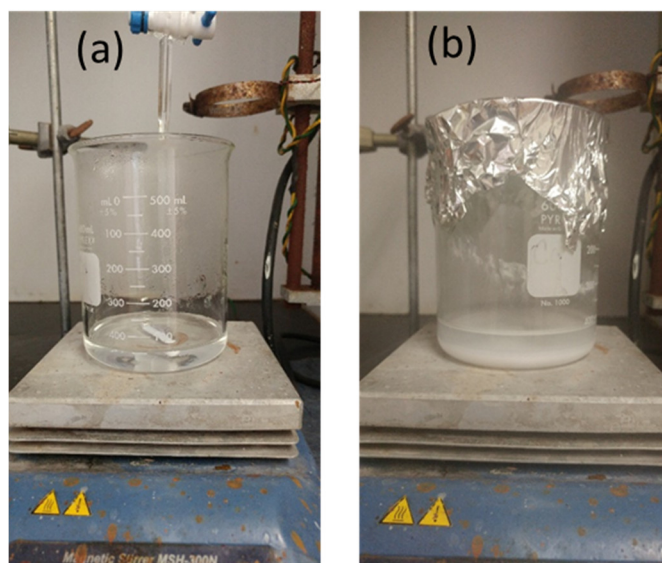
Fig 2.5: (a) Dropwise addition of ammonium hydroxide to zinc chloride solution to obtain the precipitate (b) the image displays the occurrence of precipitation after the reaction of ammonium hydroxide and zinc chloride

2.3.3 (b) Coprecipitation method

Zinc chloride ($ZnCl_2$) was dissolved in 100 ml of deionized water in a beaker and stirred using a magnetic stirrer at room temperature. Sodium hydroxide (NaOH) was dissolved in 100 ml of deionized water in a separate beaker and allowed to dissolve. 16 ml of sodium hydroxide was added to the beaker containing the $ZnCl_2$ solution with constant stirring (Fig 2.6 (a)). The aqueous solution turned into a milky white colloid without any precipitation (Fig 2.6 (b)). The reaction could proceed for 2 h after the complete addition of the sodium hydroxide. The solution could settle, and the supernatant was removed. The final supernatant must be maintained at neutral pH (pH = 7). The supernatant was dried at 100°C for overnight, and then it was calcinated [7]. In this methodology, different parameters were changed as per the need, and they were separated into three batches:

i.   20 g of zinc chloride is dissolved in deionized water at 90°C, 7.27 g of NaOH were dissolved, and 58 ml of sodium hydroxide were used for the reaction to take place, filtered using Whatman filter paper, dried in at 160°C for 7 h, and calcinated at 200°C for 2 h in an oven.

ii. 5.5 g of zinc chloride were dissolved in deionized water at 90°C, 20 g of NaOH were dissolved in deionized water, and 16 ml solution of sodium hydroxide was used during the process, washing with distilled water 5 times, and dried at 100°C for 30 min.

iii. 5.5 g of zinc chloride were dissolved in deionized water at room temperature, 20 g of NaOH were dissolved, and 16 ml of sodium hydroxide were added. The material was washed with distilled water and methanol 5 times, and dried at 100°C overnight, and then it was calcinated either at 300˚C, 400˚C, or 500˚C.
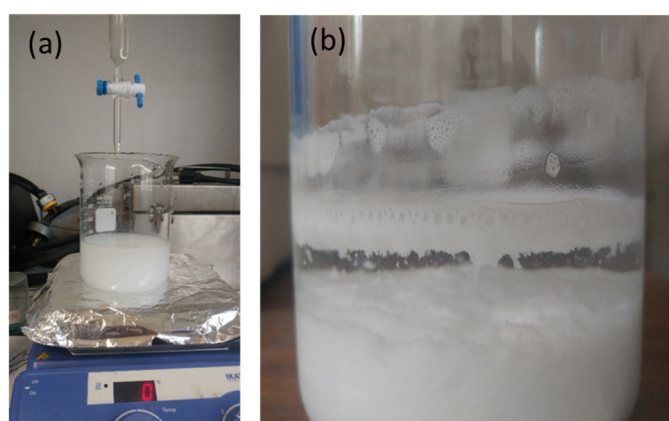
Fig 2.6: (a) To the zinc chloride solution, controlled addition of ammonium hydroxide was performed through a burette to mark the formation of precipitate (b) milky white or cloudy precipitate formation by the reaction of zinc chloride and ammonium hydroxide

2.3.3 (c) Microwave-assisted hydrothermal method

For the synthesis of zinc oxide nanoparticles, microwave-assisted hydrothermal method. Zinc acetate was the precursor. A mixture of 49ml of methanol, 10ml of ethylene glycol, and 1ml of NaOH (0.5 M) was prepared and 0.685g of zinc acetate were added. This suspension was transferred to a holder thermally protected (Fig 2.7 (a)) and kept in a microwave (flexiWAVE microwave with two 950-Watt magnetrons) (Fig 2.7 (b)) for 15 min at 180 °C. Followed by the centrifugation, the supernatant was dried at 100°C for 30 mins.
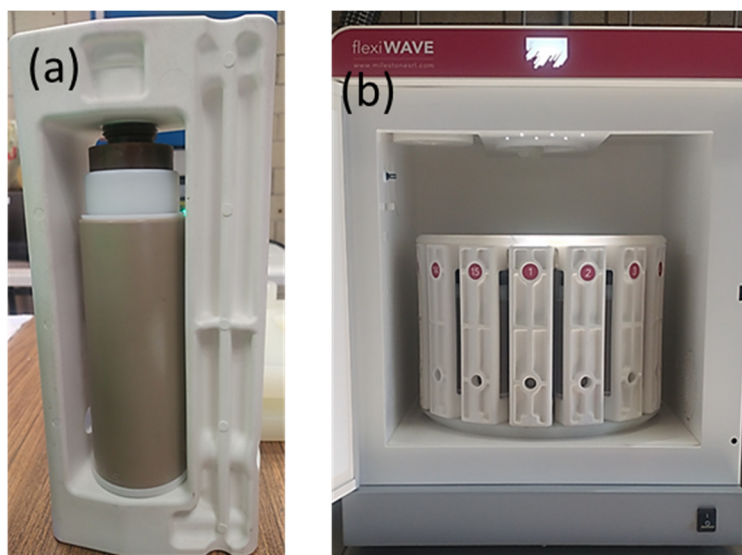
Fig 2.7: (a) The microwave sample holder, where zinc acetate, methanol, ethylene glycol, and sodium hydroxide mixture were added for the hydrothermal treatment (b) The microwave along with the holder used for the hydrothermal method

2.3.4 Synthesis of graphene oxide/zinc oxide composite

From the zinc oxide nanoparticles, graphene oxide/zinc oxide (GO/ZnO) composite was synthesized by the simple blending process. In 200 ml of deionized water definite amount of graphene oxide was dispersed, and in another 200 mL of deionized water, the synthesized ZnO nanoparticles were dispersed. The dispersion was ultrasonicated and mixed for the better dispersal of the nanoparticles. After 1.5 h of ultrasonication, the dispersion was kept for magnetic stirring overnight and filtered. The filtrate was dried to obtain the GO/ZnO composite for future applications.

2.3.5 Disk diffusion assay

One day prior to the test, isolated colonies of *E. coli K12* were chosen from the plates to obtain pure line colonies and grow them in 5 mL of Luria Bertani medium overnight to obtain a stationary phase. On the day of assay, the cultures were diluted to obtain a log phase of the bacteria after the standardization of the inoculum to 0.5 by observing the absorbance at 600 nm. At the same time, 100 mg/ml of the GO/ZnO composite dispersion was prepared using deionized water. By using Whatman filter paper, small circles of discs were made to be that can be placed in the agar plates. Carefully spread plating the nutrient agar plates with the optimized bacterial inoculum, load different dosages of the composite dispersion on the disc, and place them over the middle of

the nutrient agar plate. The plates were kept under irradiation for 2 h, followed by the overnight incubation at 37°C to observe the inhibition zone [8].

2.3.6 GO/TiO$_2$ nanocomposite synthesis

The synthesis of GO/TiO$_2$ nanocomposites at different loading ratio, i.e., 0.2/0.8, 0.3/0.7, 0.5/0.5, 0.7/0.3, and 0.8/0.2, was done through a one-step process mixing the TiO$_2$ nanoparticles, GO, and deionized water. In 200 ml of deionized water, the desired amount of GO was suspended to obtain an aqueous dispersion. In the same way, TiO$_2$ nanoparticles were also dispersed in deionized water and added to the GO dispersion. The whole mixture was sonicated for 1.5 h (Fig 2.8 (a)) and then magnetically stirred at room temperature for 12 h (Fig 2.8 (b)), so that a homogeneous suspension was obtained. The solid obtained after filtration (Fig 3.8 (c)) was further dried (Fig 2.8 (d)) in an oven at 50 °C for 4 h [9].
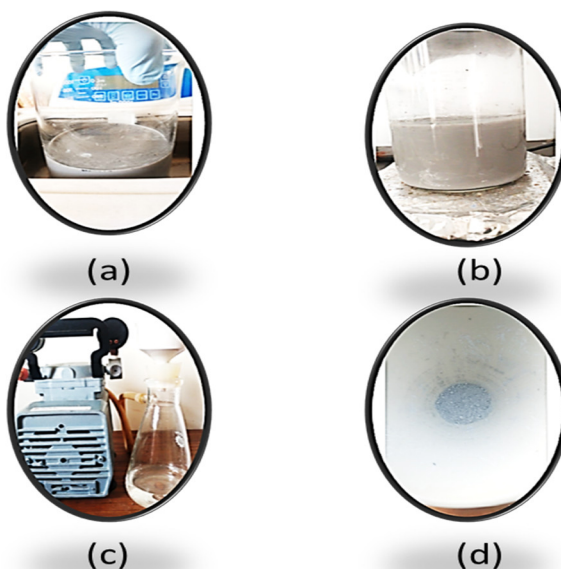
Fig 2.8: (a) The desired or weighed amount of GO and metal oxide was mixed in deionized water for ultrasonication (b) the ultrasonicated suspension was magnetically stirred for 12 h in room temperature (c) Overnight sample was filtered using a nylon membrane (d) the filtrate was dried to obtain the powder.

2.3.7 Synthesis of TiO$_2$ nanoparticles (optimizations)

Titanium dioxide (TiO$_2$) anatase nanoparticles were synthesized through the sol-gel process because it uses low-cost precursors, and the hydrolysis process can be easily controlled. To 15 ml of ethanol at 60°C, 1.5 ml of TiCl$_4$ were added dropwise with

continuous magnetic stirring. During the process, a large amount of HCl gas was liberated. A sol-gel with a light-yellow tint was formed after a period.

The parameters were fluctuated to reach the optimized conditions to obtain spherical TiO_2 anatase nanoparticles.

a. The reaction temperature was room temperature, and calcination temperature was 450°C.

b. The reaction temperature was room temperature, and the calcination temperature was 550°C.

c. The reaction temperature was 50°C, and calcined temperature was 450°C.

d. The reaction temperature was 60°C, and calcined temperature was 450°C.

2.4 Synthesis methods - Second stage

2.4.1 Synthesis of TiO_2 nanoparticles

Titanium dioxide (TiO_2) anatase nanoparticles were synthesized through $TiCl_4$ hydrolysis in ethanol because it uses low-cost precursors, and the hydrolysis process can be easily controlled. Briefly, to 15 mL of ethanol at 60˚C, 1.5 mL of $TiCl_4$ were added dropwise with continuous magnetic stirring. During the process, a large amount of HCl gas was released due to the hydrolysis of $TiCl_4$ with water (Fig 2.9 (a)). A gel with a light-yellow tint was formed after a period (Fig 2.9 (b)). The obtained gel was dried overnight at 100˚C and calcined at 450˚C [10].

2.4.2 Synthesis of $BiVO_4$ nanoparticles

Bismuth vanadate nanoparticles ($BiVO_4$ nps) synthesis through the sol-gel route involved two solutions prepared from the precursors as starters. Solution A was formed by dissolving $(BiNO_3)_3.H_2O$ in nitric acid, to which citric acid was added. NH_4VO_3 was dissolved at 80°C, and citric was added to have Solution B. Thereafter, Solution A was added dropwise to Solution B under continuous stirring (Fig 2.10). Meanwhile, pH was adjusted. The whole mixture was then heated at 80°C to form a gel. Once the gel was formed, it was dried at 100°C overnight. The dried sample was calcinated at 500°C for 2 h in an oven [11].
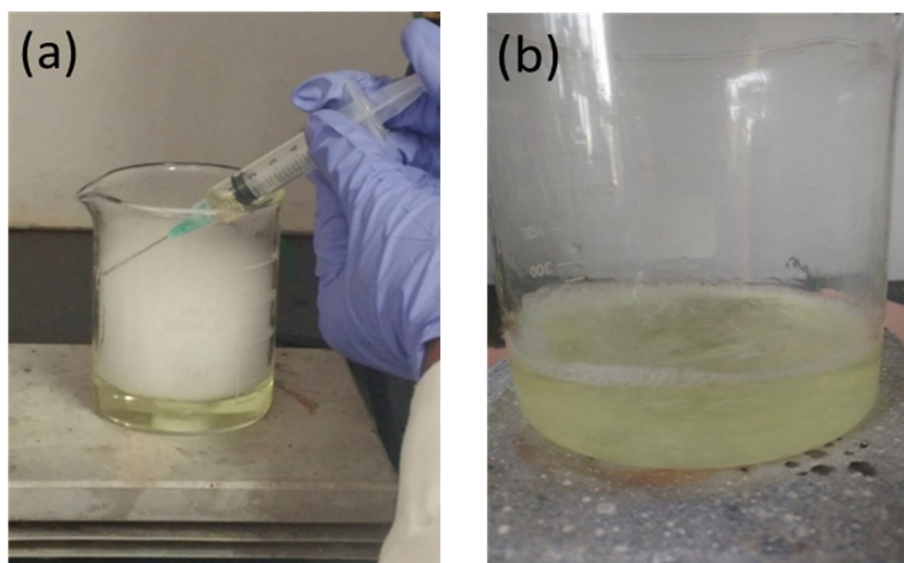
Fig 2.9: (a) During the addition of TiCl₄ to ethanol, a large amount of HCl gas was generated (b) a light-yellow tinted gel was formed through the sol-gel route
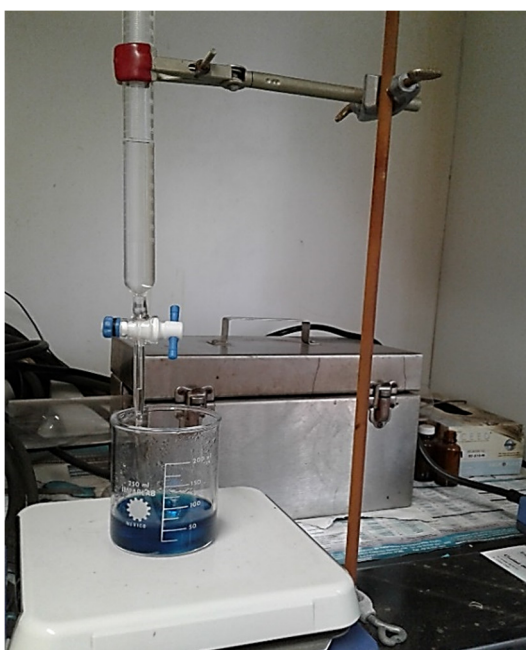
Fig 2.10: Dropwise addition of solution A ((BiNO₃)₃. H₂O in nitric acid to which citric acid was added) to solution B (ammonium vanadate and citric acid solution)

2.4.3 Synthesis of graphene oxide/MOx nanocomposites (xGOT and xGOB)

Five xGOT and xGOB nanocomposites were synthesized by one-step colloidal blending with synthesized TiO_2 or $BiVO_4$ nanoparticles. Either TiO_2 or $BiVO_4$ nanoparticles were dispersed in 200 mL deionized water (solution 1 at 8.4 mg/mL). At the same time, a definite amount of graphene oxide was dispersed in 200 mL

deionized water (solution 2). Solution 1 was added slowly to solution 2, sonicated, and stirred for 1.5 h, followed by mixing for 12 h on a magnetic stirrer to ensure the uniformity of dispersion of TiO_2 nanoparticles or $BiVO_4$ nanoparticles on GO.

The obtained powders were filtered and dried at 50°C for 4 h. The nanocomposites containing: 0.5, 1, 1.5, 2 and 2.5 wt.% of GO were shortly denoted as 0.5 GOT, 1.0 GOT, 1.5 GOT, 2.0 GOT, and 2.5 GOT, or 0.5 GOB, 1.0 GOB, 1.5 GOB, 2.0 GOB, and 2.5 GOB, respectively [9] (Fig 2.11)

Ultrasonication **Magnetic stirring**
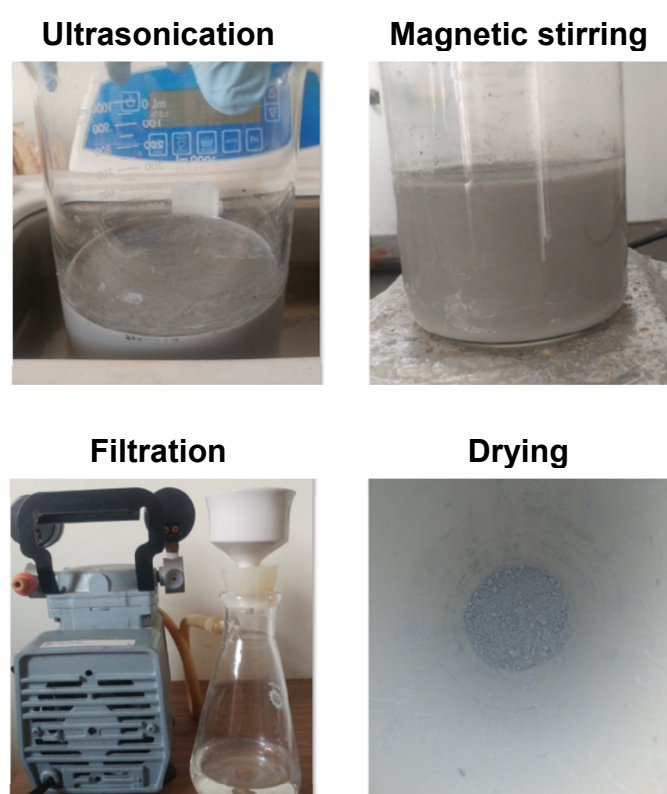
Filtration **Drying**

Fig 2.11: The four steps involved for nanocomposite synthesis, i.e., ultrasonication, magnetic stirring, filtration, and drying, are depicted for GO/TiO2 composite synthesis.

2.5 Nanocomposite pellets

For the formation of pellets, 0.975 g of the synthesized powder composite was transferred to a pellet mold of diameter 5 mm and thickness of 3 mm. The mold, along with the weighted composite, was given a uniaxial pressure of 2 Torr. Thus, formed pellets were covered completely with a stretch wrap, followed by the placement of a

balloon to cover the pellets to avoid moisture. The isostatic pressure was applied in a holder, where hydrostatic pressure and compressed gas function as a combined action. A pressure of approximately -4500 torr was provided. Once the process was finished, the wrapped pellet was taken out to dry for future applications (Fig 2.12).
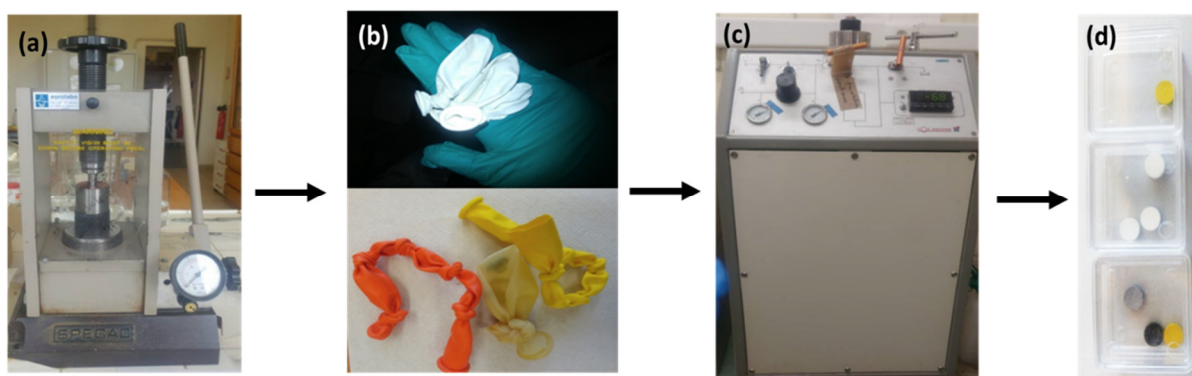
Fig 2.12: The step-by-step procedures that were carried out for the formation of pellets where successive techniques, i.e., uniaxial pressure and isostatic pressure was used.

The succession of two different processes were followed to prepare the pellet, i.e., uniaxial pressure and isostatic pressure, preventing the damage of the pellet during the photocatalytic study. At the same time, pellets safeguarded all the material properties and avoiding any disruption for the generation of ROS. The formed pellets did not use deionized water or any additives. To be noted, successful formation of pellets was attained by isostatic pressure, and pellets of thickness 2.89 mm and diameter 5 mm were obtained for the photocatalytic disinfection application of microalgae (Fig 2.13 (a)). The formed pellets by uniaxial pressure were not stable in deionized water or phosphate-buffered saline (PBS) as they got dissolved in 10 mins (Fig 2.13 (b)). But the pellets that followed isostatic pressure were stable for more than three days and were chosen for further studies (Fig 2.13 (c)).
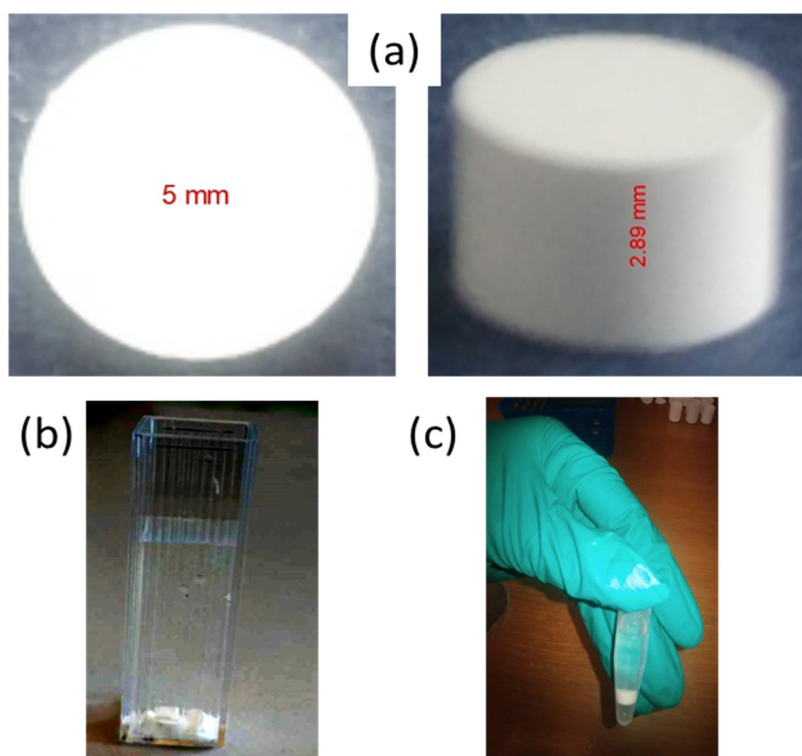
Fig 2.13: (a) Pellets of the thickness of ≈ 3mm and diameter of 5 mm (b) pellets dissolved in 15 min (formed by uniaxial pressure) (c) pellets are stable in PBS or deionized water for three days (formed by successive uniaxial and isostatic pressure)

2.6 Characterization techniques

2.6.1 Structural and elemental analysis

2.6.1(a) X-Ray diffraction

The study on the structural and elemental composition of composites was performed using the X-ray diffraction (XRD) technique. From the XRD measurements, the structure, oxidation state, and local symmetry were identified for the detailed study of crystalline structure, which is very important for a photocatalyst. This X-ray technique has an important role in the estimation of the size and distribution of the loading sites, which evaluate the catalytic site dispersion for the catalytic process [12–14]. This technique analyzes molecular and crystalline structures, quantitative resolution of chemical species, qualitative identification of various compounds, isomorphous substitutions, measuring the degree of crystallinity, polymorphisms, stacking faults, particle sizes, and phase transitions [15–18]. In XRD, X-ray light falls on the crystal leading to the formation of diffraction patterns. These patterns show the physicochemical features of the crystal (Fig 2.14).
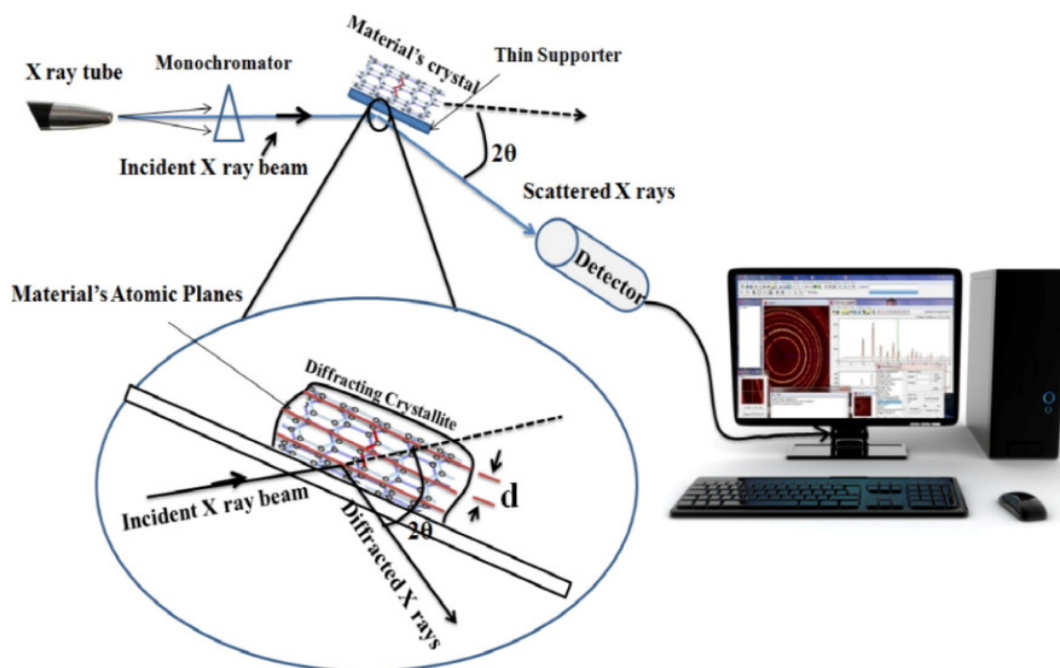
Fig 2.14: The XRD representation and the basic principle for the working during the analysis of samples [18]

By the Bragg's law, the incident light interact with the samples to give constructive interference and a diffracted ray, given by:

$$n\lambda = 2d\sin\theta \qquad Eq.\ 2.1$$

where n - an integer

    λ - wavelength of the X-rays

    d - interplanar spacing generating the diffraction

    θ - diffraction angle

In most cases, XRD patterns depict low intensity as well as broad diffraction peaks, which may be due to the small size and the amorphous nature of synthesized materials [19].

For the characterization of solid carbon matters, the XRD technique is very common now. The non-destructive XRD method, Debye functions, and pair distribution combine to give novel carbon particles with desired properties. XRD technique is considered as a "global eye" to perform characterization of carbon-related materials to the atomic level [20]. Through XRD, structural strains, detection of impurities, microscopic folding, defects, finding the number of atomic layers, thickness, calculating the interlayer distances, defining the functional groups of fabricated graphene sheets, determining

the lattice size and quality, and analyzing graphene-related composites [20–34]. For this study, Bruker D2 Phaser X-ray Diffractometer (XRD) with Cu K$_\alpha$ radiation (λ= 0.15406 Å) operating at 30 kV and 10 mA was used (Fig 2.15).

Fig 2.15: Bruker D2 phaser diffractogram (MREB, CINVESTAV)

2.6.1(b) Raman spectroscopy

Raman spectroscopy works on the principle of the Raman effect where, absorption *i.e.*, Stokes process, and emission, *i.e.*, anti-Stokes process, of phonons are involved [35]. This is a well-adapted technique for the structure determination and in-situ reaction monitoring. Raman spectroscopy is considered as the best tool for the investigation of structure and quality of carbon-based materials because of its strong, rapid, sensitive, and non-destructive analytical approach, thus giving qualitative and quantitative information of the materials [36–39].
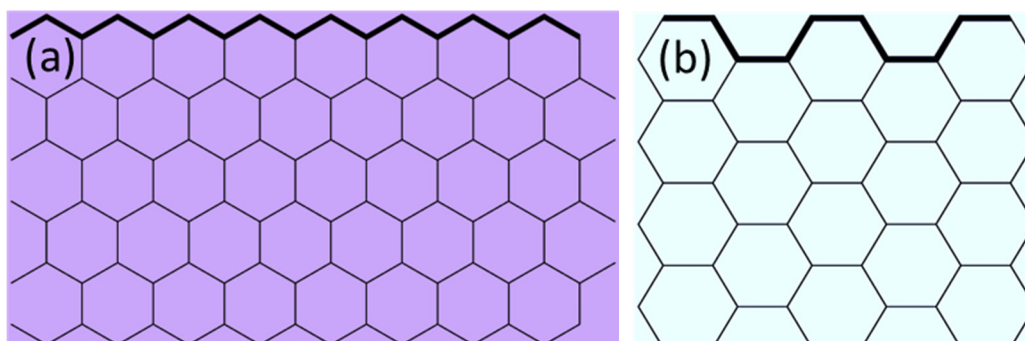
Fig 2.16: Graphene crystal structure (a) Zigzag, and (b) Armchair

Other than the detailed study of defects in graphene and its compound, Raman spectroscopy is also used for understanding the edges and grain boundaries of graphene crystals. Graphene crystal is made up of hexagonal structure and have ordered crystal edges with two main structures *i.e.*, zigzag, and armchair (Fig 2.16 (a) and (b)).

Fig 2.17: Raman spectroscopy analysis (SEES, CINVESTAV)

The D peak is the result of armchair edges, which could scatter charge carriers elastically. If the excitation laser is polarized in the direction that is parallel to the line of edge, a strong D peak will appear near the armchair edge and this effect is least observed for zigzag edges [40–44]. As per the literature, longitudinal optical phonon mode and transverse optical phonon mode are active near the armchair edge and zigzag edge, respectively. When graphene is doped, Fermi level is shifted away from the Dirac point, reducing the probability of the recombination of excited charge carriers. This results in non-adiabatic nature of photon disorders and thus abolishing the Kohn anomaly and increasing phonon energy and frequency of the G peak and decreasing the FWHM by narrowing G peak [45–47]. Raman analysis was recorded in the range between 0 and 2000 cm^{-1} at ambient temperature using a Horiba-Jobin-Yvon spectrometer (Lab RAM HR800) with a helium-neon laser of wavelength 632 nm as the excitation source (Fig 2.17).

2.6.2 Size and morphological analysis

2.6.2(a) Scanning electron microscope (SEM)

Fig 2.18: Scanning electron microscope (SEM) (MREB, CINVESTAV)

Scanning electron microscope or SEM works on high-energy electron beam that generate signals when it falls on the surface of specimens. These signals which are the outcome of electron-sample interactions, provide information on the external morphology, chemical composition, crystalline structure, and orientation of materials present in the sample. In this analysis, the data is collected over a selected area, thereby generating a two-dimensional image. Generally, areas ranging from 1 cm to 5 microns in width are imaged using a conventional SEM analysis where the magnification ranges from 20X to 30000X with a spatial resolution of 50 to 100 nm. SEM technique is a good tool to analyze the selected point locations on the sample to determine the chemical compositions *i.e.,* through EDS analysis (Fig 2.18) [48].

2.6.2(b) Transmission electron microscope (TEM)

Being one of the most powerful tools in the material science, high energy electron beams can fall through a very thin sample. The interaction between the electrons and atoms due to the electron beam can help in the observation of features like crystal structure, dislocations, and grain boundaries. Similar to SEM, chemical analysis can also be performed. To put into a nutshell, TEM analysis helps in the study of growth of layers, compositions, defects in semiconductors, quality, shape, size of nanoparticles (Fig 2.19) [49] .

Fig 2.19: Transmission electron microscope (TEM) (Physics department, CINVESTAV)

Electron-micrographs were taken with a Transmission Electron Microscope (TEM) JEOL, JEM 1010, with an operating voltage of 60 kV for nanomaterials and bacterial analysis. TEM JEM-2100 multipurpose microscope equipped with the Energy Dispersive X-ray Spectrometer (EDAX) was employed for sensitive analysis of the composite.

2.6.3 Band gap energy analysis

2.6.3(a) UV-visible spectroscopy

The diffuse reflectance data obtained from the UV-visible spectroscopy was used for the calculation or estimation of the band gap energy using the Kubelka -Munk (K-M) equation, where the outcome is F(R). This theory is based on the light absorption and partial scattering. The theory modelled that the resultant light is emerging from translucent and opaque media, assuming that, there are only two light channels traveling in opposite directions [50]. Considering the solid samples, UV-Vis diffuse reflectance spectroscopy uses the reflectance of the visible radiation spectrum because they cannot penetrate the sample [51]. The optical properties were evaluated using an Agilent-carry-5000 spectrophotometer. For the transmittance and absorbance studies of filters and microalgal concentration, respectively, double beam UV-visible spectrophotometer was used following the Beer-Lambert's law.

2.7 Model reaction study

The standard test for the photocatalytic activity of the synthesized TiO_2 and 1.5 GOT pellet was studied with the help of methylene blue dye degradation. The conditions, mainly photolysis with and without nitrogen influx, dark condition, photocatalysis with and without nitrogen influx was performed. The experiments were carried out in a 3 mL cuvette with an initial concentration of 20 mg/L along with a single pellet of TiO_2 or 1.5 GOT. Prior to the irradiation using an Oriel Xenon arc lamp source, the sample was kept in dark under stirring for 30 mins to obtain the adsorption-desorption equilibrium followed by 2 h of continuous light irradiation. About 100 µL aliquots were withdrawn at every 10 min, which was diluted with 2900 µL of deionized water. The absorbance measurements at regular intervals were performed at 664 nm absorbance using a double beam spectrophotometer (Perkin Elmer Lambda 75). The initial pH was maintained the same throughout the experiment [11,52].

2.8 Experimental set up

2.8.1 Experimental set-up for microbial disinfection

The bacterial concentration was determined after the bacterial growth curve study (Fig 2.20 (a) and (b)). All experiments were performed in 50 mL batch reactors in triplicates under simulated solar radiation. The suspension was magnetically stirred at 400 rpm and exposed to light for 2 h. The halogen lamp was focused at 15 cm above the reactor and used a solar simulator light source at a light intensity of 500 W/m^2. The xGO/MOx nanocomposites were sonicated in water for 30 min to ensure stable dispersion prior to each experiment. Subsequently, the bacterial stock solution was diluted in the reactor to the desired initial concentration (10^7 CFU/mL). Before irradiation, the mixture was kept in the dark, stirred for 30 min for reaching adsorption-desorption equilibrium. The bacterial viability was performed by the standard plate count method. Samples were drawn at different intervals during the experiment, after appropriate dilution, 100 µL of the sample were taken and put into Eosin-Methylene blue (EMB) agar plate and incubated overnight at 37°C (Fig 2.21). After optimizing the parameters, three control experiments were conducted under the same conditions. The control experiments were performed in the absence of photocatalyst. The disinfection percentage was determined using the equation (2.2) where, *N (control)* and *N (time)* was the number of viable cells counted from control and aliquots obtained at different time intervals, t, respectively.

$$Percentage\ of\ inactivation\ (\%) = \frac{N(control) - N(time)}{N(control)} \times 100\% \qquad Eq.\ 2.2$$
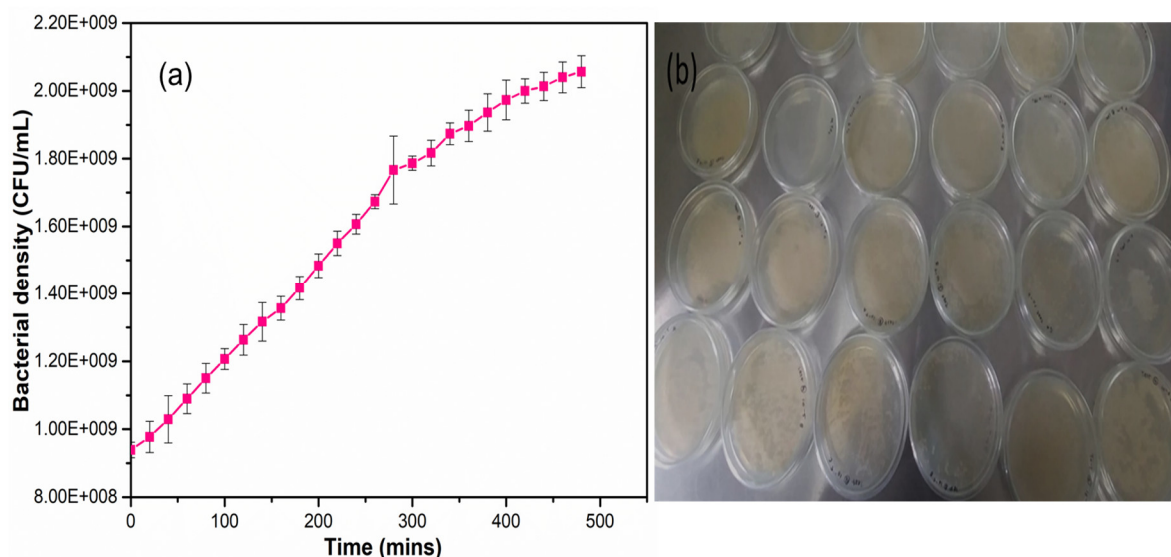
Fig 2.20: (a) Graph plotting the triplicate bacterial growth curve, (b) photographs after the nutrient agar plates was spread plated after the growth curve study.

2.8.2 Determination of ROS species

Scavenger study was performed to identify the ROS and to elucidate their role in the photocatalytic mechanism of GOT and GOB nanocomposites (Fig 2.21). A series of experiments were conducted using different scavengers to remove their corresponding active species and analyze their contribution in the bacterial inactivation. Isopropanol (0.5 mmol/L), benzoquinone (0.05 mmol/L), and chromium (VI) (0.05 mmol/L) were used for scavenging •OH, O_2^-, and e^-, respectively. The concentrations were adopted based on the preliminary reports, where the scavenging effect was maximized, thereby minimizing the bactericidal effect [53–55].
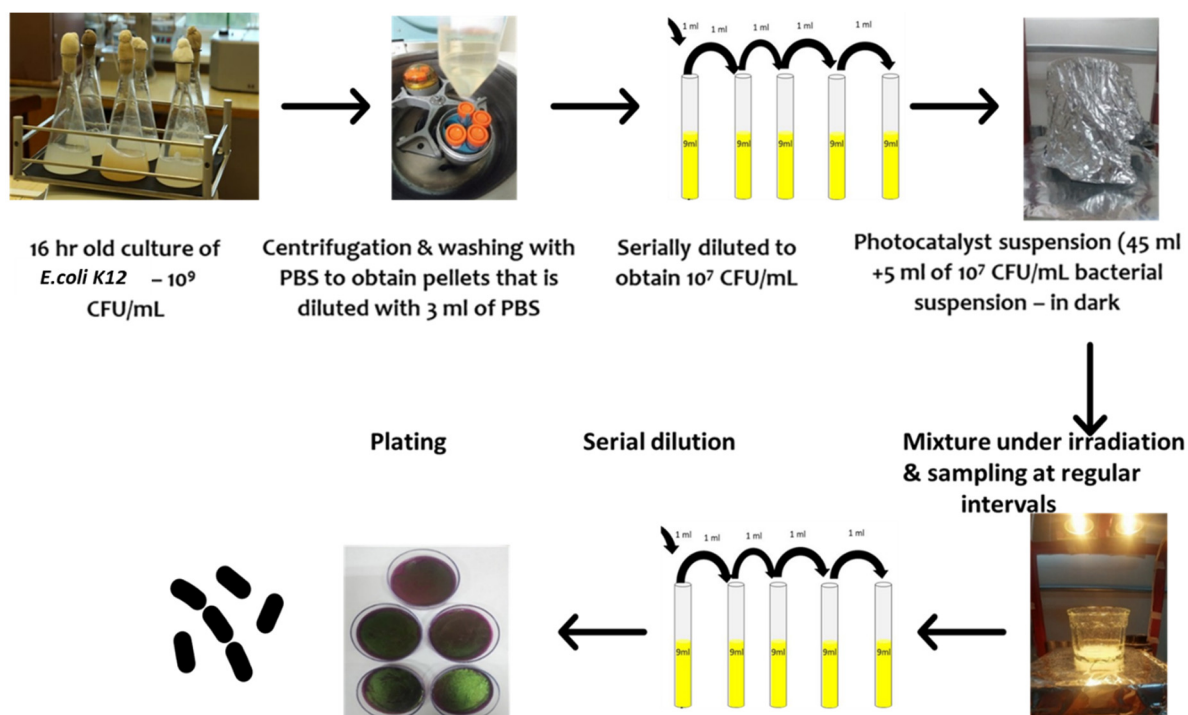
Fig 2.21: The sequential protocol followed for the microbial photocatalytic disinfection study using E. coli K12 as the model organism.

2.8.3 Experimental Set-up for Microalgal Disinfection

2.8.3 (a) Measurement and correction of the absorbance spectra recorded in situ

The room temperature in vivo absorbance spectra were measured using a double beam spectrophotometer (Perkin Elmer Lambda 750). The reference cuvette was filled with growth medium. The spectrophotometer was operated with the software from the spectrophotometer supplier. The spectra were only corrected for the baseline drift as follows. The features of each absorbance spectra were manually removed (dots in Fig 2.22 (a)). The remaining data were fitted mathematically using the software Curve Expert (version 2.0). Best fit was obtained using polynomial equation of degree 4 (dashed line in Fig 2.22 (a)) and was considered as the equation of the baseline (Fig 2.22 (b)). The absorbance corrected spectrum was obtained after subtraction of the baseline from the original spectrum (Fig 2.22 (b)).
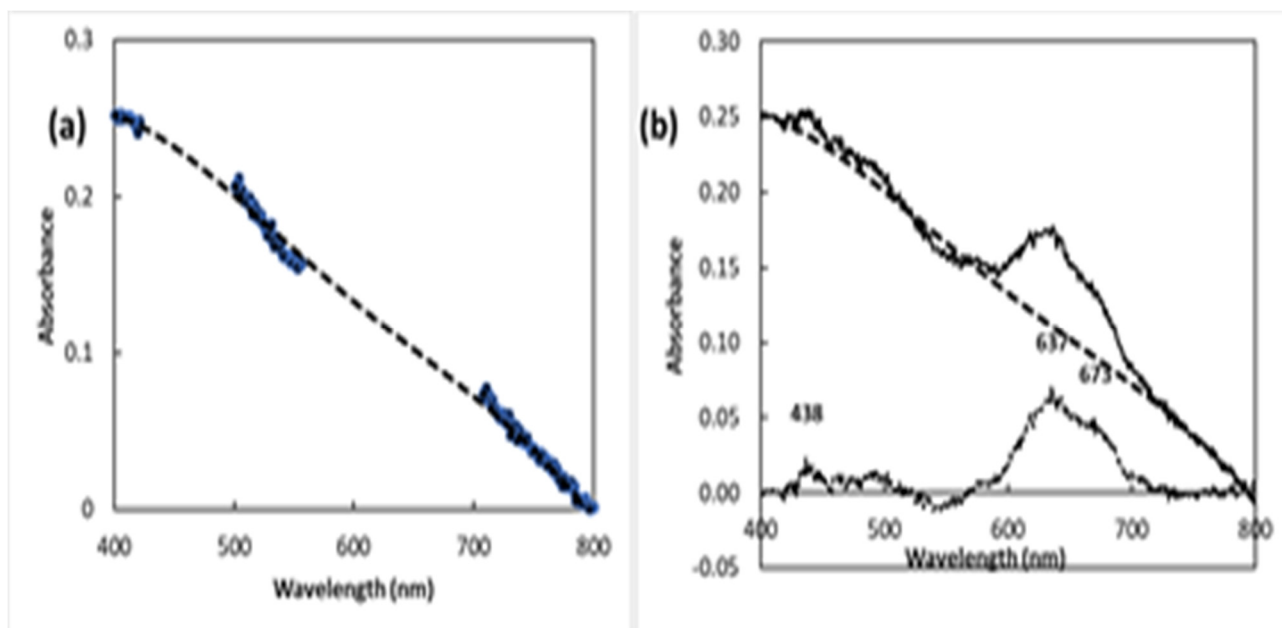
Fig 2.22. Procedure used for correcting the in vivo absorbance spectra.
(a) Mathematical fit (dashed curve) of the featureless absorbance spectrum recorded
in situ (full line)   (b) Corrected absorbance spectrum (dotted curve) as the result of
the operation 'original spectrum-minus-fitted baseline'

2.8.3 (b) Photolysis and photocatalytic study

The home-made setup was used for photolysis and photocatalysis experiments. The sample, in a cuvette (3 mL) with four transparent sides containing a magnetic stirrer, was irradiated by a collimated light beam (L-ACT) from an Oriel xenon arc lamp (model no. 6255), delivering a light having a spectral composition like the sunlight [56] (Fig. 2.23 (a)). The output light beam was filtered using a set of filters (Fig. 2.23 (a)) to (1) reduce sample heating, (2) allow absorbance by the nanomaterial used for ROS generation and (c) trigger photosynthesis. The transmission spectra of the filters are displayed in Fig 5.2, and the optical properties of the filters are summarized in Table 2.1. The actual photon flux density was 2500 µmol photons/m^{-2}s. It was reduced to 1700 µmol photons/m^{-2}s after the addition of an additional daylight blue filter (Fig.5.2). A fan (Fig. 2.23 (a)) was added behind the sample to speed up the residual heat removal and keep the temperature at 37 ± 2°C. For photocatalysis experiments, a pellet was placed over the stirrer (Fig. 2.23 (a)).

Table 2.1: Summary of the optical properties of the filters used for shaping the light beam.

	Type of filter	λ_{max} (nm)	Transmission at λ_{max} (%)	Supplier
Infra-red filter	High-pass filter	-	Circa 75%	Unknown
Visible filter	Long-pass filter	559, cut-off: 400	58, at 405 nm: 35%	Edmund Optics
Daylight blue filter	Band pass	425	68	Lee filters

The changes in the sample induced during photolysis or photocatalysis processes were either followed using a double beam spectrophotometer (Perkin Elmer) after sampling or online through the changes of the chlorophyll fluorescence yields using a Dual PAM-100 (Walz, German) piloted with the software provided by the supplier (https://www.walz.com/products/chl_p700/dual-pam-100/downloads.html). Prior to measurements, the sample, in plain on all four sides cuvette, was fed with sodium bicarbonate ($NaHCO_3$) to avoid the carbon starvation during the experiment [57].

2.8.3 (b1) Sampling for in situ absorbance measurements

The experiments were carried out in 3 mL cuvette with an initial concentration of 400 µL of Anabaena culture (OD750 = 6) and mixed with 2600 µL of BG11 media. The sample was kept in dark under stirring for 30 min to reach the adsorption-desorption equilibrium, followed by 2 h of continuous light irradiation. A 100 µL aliquot of the sample was taken every 10 min. The subsampling was diluted with 2900 µL of BG11 media before recording the in-situ absorbance spectra. To determine the changes in chlorophyll a at any time of the photocatalytic treatment, the difference between the absorbance spectra recorded after t min of illumination and the corresponding spectra recorded during photolysis treatment was calculated.

2.8.3 (b2) Online measurements of chlorophyll fluorescence

The device is equipped by two light emitter-detector heads [58]. Before measurement, the sample was placed in the darkness for 30 min in the presence of low intensity far-red light (FR-L, λ_{max}: 720 nm, intensity: 13 µmol photons/m^{-2} s) to empty the electron transport chain. After switching off FR-L, the sample was irradiated with a low intensity modulated light (FML, λ_{max}: 620 nm, frequency: 800 Hz, intensity: < 15 µmol photons/m^{-2} s) for 2 mins. The level of fluorescence recorded was denoted as F_0 (Fig. 2.23 (e)). FR-L was switched on again to favor the PSI activity. Then a saturating white light pulse (L-P, duration: 800 ms, intensity: > 1500 µmol photons/m^{-2}s) was delivered to the sample. The level of fluorescence recorded was denoted as F_M (Fig. 2.23 (e)). The sample was then illuminated by L-ACT for different times, ranging between 0.5 and 4h (Fig. 2.23 (e)).

During the illumination, the fluorescence reached a stationary level denoted as F_S (Fig. 2.23 (e)). During this period, the sample was regularly irradiated by saturating light pulses (L-P), eventually triggering a transient increase of the fluorescence level, denoted as F'_M (Fig. 2.23 (b)). At the end of the L-ACT period, L-ACT was switched off but FR, FML and L-P during 20 min. The latter illumination eventually triggered a transient increase of the fluorescence level, denoted as F''_M (Fig. 2.23 (e)). At the end of this 20 min period, the sample stayed on the bench overnight under the ambient light. The F_0, F_M and F''_M levels were then recorded (Fig. 2.23 (e)). From the measurements of the basic chlorophyll fluorescence yields, parameters allowing the characterization of the photosynthetic activity as well as the management of the absorbed light energy were calculated using the equation indicated in Table 2.2 [59].
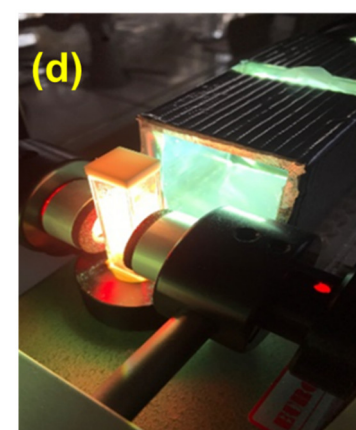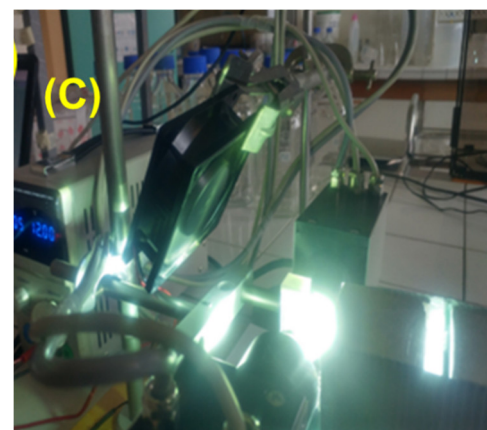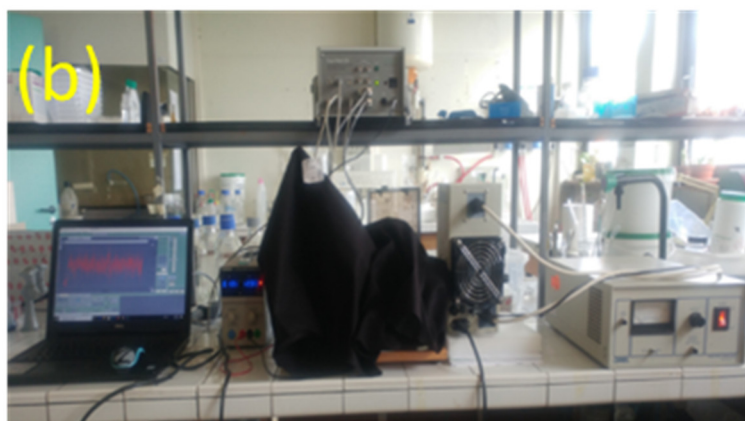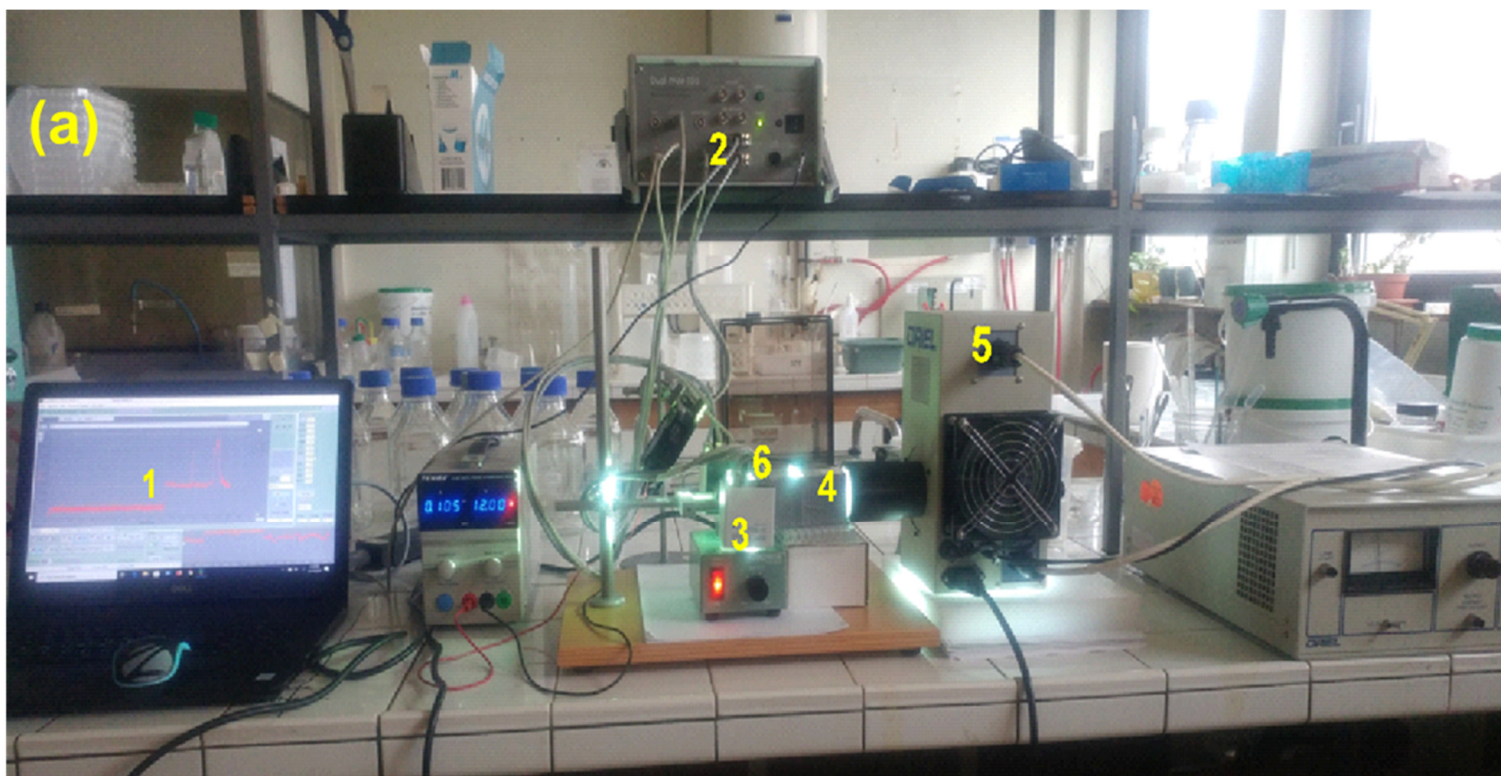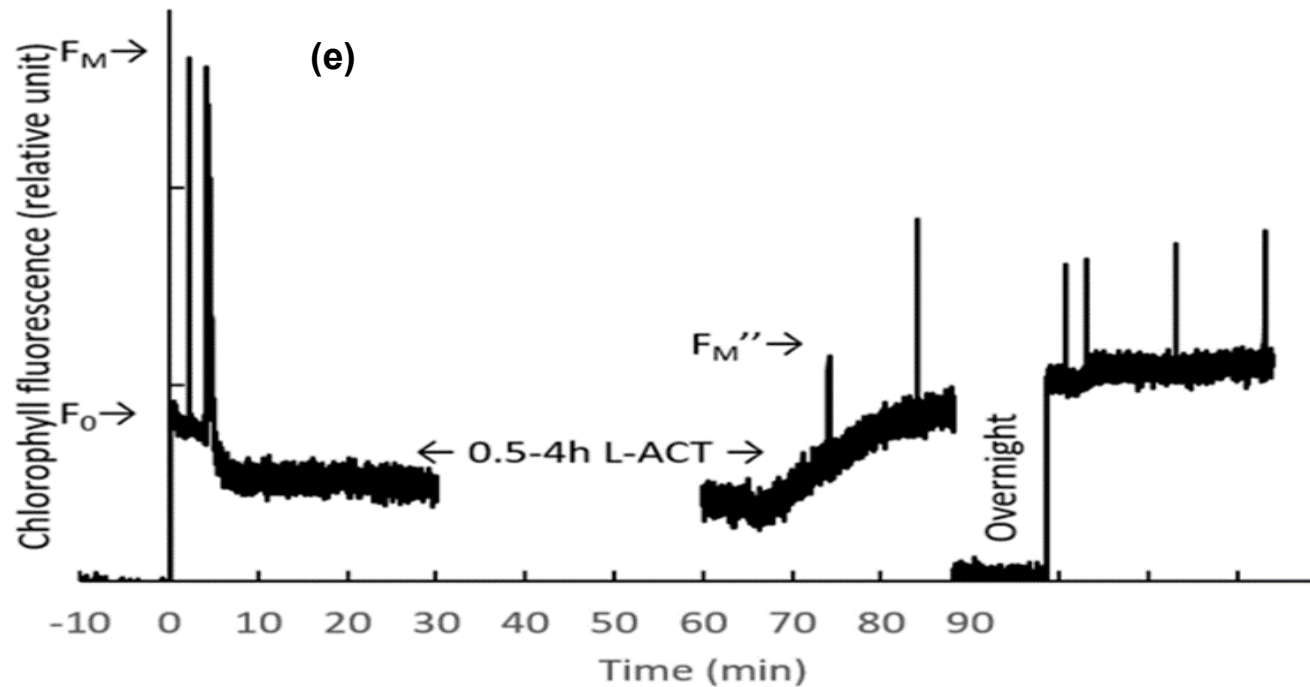
Fig 2.23: Experimental set up used for measuring the effect of photolysis and photocatalysis.

(a) the complete experimental setup: (1) computer piloting the PAM, (2) PAM control unit, (3) magnetic stirrer, (4) light filtering system, (5) UV lamp source and voltage control for the lamp source power supply for the exhaust fan, (6) cuvette holder masque by the PAM measuring head (b-d) Photographs of the measuring cells at different moments of the recording: (b) in darkness before the measurement, (c) under L-ACT, (d) under L-ACT and L-P. Please note in panel (c) the exhaust fan placed behind the sample to speed up the residual heat removal (e) Representative data of the variations of the chlorophyll fluorescence intensity

Table 2.2. *Description of the parameters used to characterized the photosynthetic activity and the equations used for calculation* [58,60]

No.	Model organization	Parameters	Description	Equation
1	-	F_V/F_M	Maximum quantum yield of photosystem II (PSII) photochemistry	$F_V/F_M = (F_M - F_0)/F_M$
2	Puddle, Lake	Y_{II}	Effective quantum yield of photochemical energy conversion in PSII	$Y_{II} = (F_M' - F_t)/F_M' = 1 - Y_{NPQ} - Y_{NO}$
3	-	NPQ	Nonphotochemical quenching	$NPQ = (FM - F_M')/F_M'$ ' = FM/FM
4	Lake	qL	Fraction of open PSII reaction centres in the lake model	$qL = \dfrac{(F_M' - F_t)\, F_0'}{(F_M' - F_0')\, F_t}$
5	Lake	Y_{NPQ}	Quantum yield of regulated energy dissipation	$Y_{NPQ} = 1 - Y(II) - 1/(NPQ+1+qL(F_M/F_t-1))$
6	Lake	Y_{NO}	Quantum yield of nonregulated energy dissipation	$Y_{NO} = 1/(NPQ+1+qL(F_M/F_0-1))$
7	Puddle	qN	Coefficient of nonphotochemical quenching	$qN = (F_M - F_M')/(F_M-F_0')$
8	Puddle	qP	Coefficient of photochemical quenching	$qP = (F_M -F)/(F_M '-F_0')$
9	Lake	qL	Coefficient of photochemical quenching	$qL = qP * F_0'/F_t$

After a period of darkness of 15 min in the presence of low-intensity FR-L, FR-L was switched off, and the sample was irradiated with FML for 2 min, allowing the measurement of the F0 level. The sample was irradiated with a single L-P, and the level FM is recorded. FR-L is switched on together with L-ACT for 0.5 to 4h. The chlorophyll fluorescence progressively decreased until reaching the FS level. During this period, the sample was regularly irradiated by L-P, allowing the measurement of level. At the end of the L-ACT period, all the light sources were switched off but FR, FML, and L-P, allowing the measurement of the levels and having the same meaning. The sample stayed on the bench overnight under the ambient light. The F0, FM, and levels were then recorded. The test using Evans blue (6,6'- [(3,3'-dimethyl[1,1'-biphenyl]-4,4'-diyl)bis(azo)]bis[4-amino-5-hydroxy-1,3-naphthalenedisulfonic acid] tetrasodium salt) dye was used to determine the viability of cells after the photocatalytic and photolytic studies [61]. When biotic or abiotic stress occurred, the response of the cells was presented as membrane damage. The health of a cell is lying on the cell membrane and can be used as a biomarker for the living or dead cells. Evans's blue is considered an azo dye that can penetrate through the ruptured or destructed cell membrane, and this dye is used as an assay for cell viability. This dye assay principle is that the stressed or destructed cells permeate the dye and, therefore, take up the dye coloration, *i.e.,* a blue protoplasmic stain. In contrast, healthy and live cells have better membrane integrity, blocking the entry of the dye [62]. The counting of algal cells was performed using a Neubauer hematocytometer.

References

[1]   A. De Martino, A. Meichenin, J. Shi, K. Pan, C. Bowler, Genetic and phenotypic characterization of Phaeodactylum tricornutum (Bacillariophyceae) accessions, J. Phycol. 43 (2007) 992–1009. https://doi.org/10.1111/j.1529-8817.2007.00384.x.

[2]   A. Pistone, A. Ferlazzo, M. Lanza, C. Milone, D. Iannazzo, A. Piperno, E. Piperopoulos, S. Galvagno, Morphological modification of MWCNT functionalized with HNO 3/H 2SO 4 mixtures, J. Nanosci. Nanotechnol. 12 (2012) 5054–5060. https://doi.org/10.1166/jnn.2012.4928.

[3]   A.M. Kamil, F.H. Hussein, A.F. Halbus, D.W. Bahnemann, Applications of MWCNTs / TiO 2 Composite, Int. J. Photoenergy. 2014 (2014) 1–8.

[4]   D. Beydoun, R. Amal, G.K.C. Low, S. McEvoy, Novel Photocatalyst: Titania-Coated Magnetite. Activity and Photodissolution, J. Phys. Chem. B. 104 (2000) 4387–4396. https://doi.org/10.1021/jp992088c.

[5]   J. Sigh, Uma, S. Banerjee, D. Gusain, Y.C. Sharma, Equilibrium modelling and thermodynamics of removal of orange g from its aqueous solutions, J. Appl. Sci. Environ. Sanit. 6 (2011) 317–326.

[6]   B. Divya, C. Karthikeyan, M. Rajasimman, Chemical synthesis of zinc oxide nanoparticles and its application of dye decolourization, Int. J. Nanosci. Nanotechnol. 14 (2018) 267–275.

[7]   G. S, A. Belay, C. Reddy AR, B. Z, Synthesis and Characterizations of Zinc Oxide Nanoparticles for Antibacterial Applications, J. Nanomed. Nanotechnol. s8 (2017) 1–8. https://doi.org/10.4172/2157-7439.s8-004.

[8]   GOLDBio, GoldBio Disk Diffusion Assay Protocol, GOLDBio Disk Diffus. Assay Protoc. (2018) 1–4.

[9]   T.D. Nguyen-Phan, V.H. Pham, E.W. Shin, H.D. Pham, S. Kim, J.S. Chung, E.J. Kim, S.H. Hur, The role of graphene oxide content on the adsorption-enhanced photocatalysis of titanium dioxide/graphene oxide composites, Chem. Eng. J. 170 (2011) 226–232. https://doi.org/10.1016/j.cej.2011.03.060.

[10]   L.S. Zaremba, W.H. Smoleński, Optimal portfolio choice under a liability constraint, Ann. Oper. Res. 97 (2000) 131–141. https://doi.org/10.1023/A.

[11]   K.T. Drisya, M. Solís-López, J.J. Ríos-Ramírez, J.C. Durán-Álvarez, A. Rousseau, S. Velumani, R. Asomoza, A. Kassiba, A. Jantrania, H. Castaneda, Electronic and optical competence of TiO2/BiVO4 nanocomposites in the photocatalytic processes, Sci. Rep. 10 (2020) 1–16. https://doi.org/10.1038/s41598-020-69032-9.

[12]   Z. He, M. Hu, X. Wang, Highly effective hydrodeoxygenation of guaiacol on Pt/TiO2: Promoter effects, Catal. Today. 302 (2018) 136–145. https://doi.org/10.1016/j.cattod.2017.02.034.

[13]   M. Hu, Z. Yao, X. Wang, Characterization techniques for graphene-based materials in catalysis, AIMS Mater. Sci. 4 (2017) 755–788. https://doi.org/10.3934/matersci.2017.3.755.

[14]   H. Zhang, W. Li, Y. Jin, W. Sheng, M. Hu, X. Wang, J. Zhang, Ru-Co(III)-Cu(II)/SAC catalyst for acetylene hydrochlorination, Appl. Catal. B Environ. 189 (2016) 56–64. https://doi.org/10.1016/j.apcatb.2016.02.030.

[15]   D.L. Dorset, X-ray Diffraction: A Practical Approach, 1998. https://doi.org/10.1017/S143192769800049X.

[16]   I. Ivanisevic, R.B. McClurg, P.J. Schields, Uses of X-Ray Powder Diffraction In the Pharmaceutical Industry, in: Pharm. Sci. Encycl., 2010. https://doi.org/10.1002/9780470571224.pse414.

[17]   A. Macchia, M. Laurenzi Tabasso, A.M. Salvi, M.P. Sammartino, S. Mangialardo, P. Dore, P. Postorino, Analytical characterization of corrosion products of copper and its alloys on stained stone surfaces, Surf. Interface Anal. 45 (2013) 1073–1080. https://doi.org/10.1002/sia.5220.

[18]   R. Das, M.E. Ali, S.B.A. Hamid, Current applications of x-ray powder diffraction - A review, Rev. Adv. Mater. Sci. 38 (2014) 95–109.

[19]   S. El-Sherbiny, F. Morsy, M. Samir, O.A. Fouad, Synthesis, characterization and application of TiO2 nanopowders as special paper coating pigment, Appl. Nanosci. 4 (2014) 305–313. https://doi.org/10.1007/s13204-013-0196-y.

[20]   T. Belin, F. Epron, Characterization methods of carbon nanotubes: A review, Mater. Sci. Eng. B Solid-State Mater. Adv. Technol. 119 (2005) 105–118. https://doi.org/10.1016/j.mseb.2005.02.046.

[21]   H.K. Chae, D.Y. Siberio-Pérez, J. Kim, Y.B. Go, M. Eddaoudi, A.J. Matzger, M. O'Keeffe, O.M. Yaghi, A route to high surface area, porosity and inclusion of large molecules in crystals, Nature. 427 (2004) 523–527. https://doi.org/10.1038/nature02311.

[22]   C.N.R. Rao, A.K. Sood, K.S. Subrahmanyam, A. Govindaraj, Graphene: The new two-dimensional nanomaterial, Angew. Chemie - Int. Ed. 48 (2009) 7752–7777. https://doi.org/10.1002/anie.200901678.

[23]   J.H. Chen, C. Jang, S. Xiao, M. Ishigami, M.S. Fuhrer, Intrinsic and extrinsic performance limits of graphene devices on SiO 2, Nat. Nanotechnol. 3 (2008) 206–209. https://doi.org/10.1038/nnano.2008.58.

[24]   C. Lee, X. Wei, J.W. Kysar, J. Hone, Measurement of the elastic properties and intrinsic strength of monolayer graphene, Science (80-.). 321 (2008) 385–388. https://doi.org/10.1126/science.1157996.

[25]   Y. Wang, Y. Hoang, Y. Song, X. Zhang, Y. Ma, J. Liang, Y. Chen, Room-temperature ferromagnetism of graphene, Nano Lett. 9 (2009) 220–224. https://doi.org/10.1021/nl802810g.

[26]   H.S.S. Ramakrishna Matte, K.S. Subrahmanyam, C.N.R. Rao, Novel magnetic properties of graphene: Presence of both ferromagnetic and antiferromagnetic features and other aspects, J. Phys. Chem. C. 113 (2009) 9982–9985. https://doi.org/10.1021/jp903397u.

[27]   A. Peigney, C. Laurent, E. Flahaut, R.R. Bacsa, A. Rousset, Specific surface area of carbon nanotubes and bundles of carbon nanotubes, Carbon N. Y. 39 (2001) 507–514. https://doi.org/10.1016/S0008-6223(00)00155-X.

[28]   C.N.R. Rao, A.K. Sood, R. Voggu, K.S. Subrahmanyam, Some novel attributes of graphene, J. Phys. Chem. Lett. 1 (2010) 572–580. https://doi.org/10.1021/jz9004174.

[29]   B. Das, R. Voggu, C.S. Rout, C.N.R. Rao, Changes in the electronic structure and properties of graphene induced by molecular charge-transfer, Chem. Commun. (2008) 5155–5157. https://doi.org/10.1039/b808955h.

[30]   A. Chakrabarti, J. Lu, J.C. Skrabutenas, T. Xu, Z. Xiao, J.A. Maguire, N.S. Hosmane, Conversion of carbon dioxide to few-layer graphene, J. Mater. Chem. 21 (2011) 9491–9493. https://doi.org/10.1039/c1jm11227a.

[31]   S. Hun, Thermal Reduction of Graphene Oxide, in: Phys. Appl. Graphene - Exp., 2011: p. 73. https://doi.org/10.5772/14156.

[32]   L.S. Schadler, S.C. Giannaris, P.M. Ajayan, Load transfer in carbon nanotube epoxy composites, Appl. Phys. Lett. 73 (1998) 3842–3844. https://doi.org/10.1063/1.122911.

[33]   K.S. Novoselov, A.K. Geim, S. V. Morozov, D. Jiang, Y. Zhang, S. V. Dubonos,

I. V. Grigorieva, A.A. Firsov, Electric field in atomically thin carbon films, Science (80-.). 306 (2004) 666–669. https://doi.org/10.1126/science.1102896.

[34] K.S. Novoselov, A.K. Geim, S. V. Morozov, D. Jiang, M.I. Katsnelson, I. V. Grigorieva, S. V. Dubonos, A.A. Firsov, Two-dimensional gas of massless Dirac fermions in graphene, Nature. 438 (2005) 197–200. https://doi.org/10.1038/nature04233.

[35] S.S. Nanda, M.J. Kim, K.S. Yeom, S.S.A. An, H. Ju, D.K. Yi, Raman spectrum of graphene with its versatile future perspectives, TrAC - Trends Anal. Chem. 80 (2016) 125–131. https://doi.org/10.1016/j.trac.2016.02.024.

[36] R. Beams, L. Gustavo Cançado, L. Novotny, Raman characterization of defects and dopants in graphene, J. Phys. Condens. Matter. 27 (2015) 1–26. https://doi.org/10.1088/0953-8984/27/8/083002.

[37] X. Cao, T. Hong, R. Yang, J.H. Tian, C. Xia, J.C. Dong, J.F. Li, Insights into the Catalytic Activity of Barium Carbonate for Oxygen Reduction Reaction, J. Phys. Chem. C. 120 (2016) 22895–22902. https://doi.org/10.1021/acs.jpcc.6b08267.

[38] P.R. Whelan, B.S. Jessen, R. Wang, B. Luo, A.C. Stoot, D.M.A. Mackenzie, P. Braeuninger-Weimer, A. Jouvray, L. Prager, L. Camilli, S. Hofmann, P. Bøggild, T.J. Booth, Raman spectral indicators of catalyst decoupling for transfer of CVD grown 2D materials, Carbon N. Y. 117 (2017) 75–81. https://doi.org/10.1016/j.carbon.2017.02.028.

[39] A. Barbon, F. Tampieri, Identification of slow relaxing spin components by pulse EPR techniques in graphene-related materials, AIMS Mater. Sci. 4 (2017) 147–157. https://doi.org/10.3934/matersci.2017.1.147.

[40] R. Saito, Raman spectroscopy of graphene edges, Graphene Its Fascin. Attrib. 9 (2011) 91–103. https://doi.org/10.1142/9789814329361_0006.

[41] D. Graf, F. Molitor, K. Ensslin, C. Stampfer, A. Jungen, C. Hierold, L. Wirtz, Spatially resolved raman spectroscopy of single- and few-layer graphene, Nano Lett. 7 (2007) 238–242. https://doi.org/10.1021/nl061702a.

[42] L.G. Cançado, M.A. Pimenta, B.R.A. Neves, M.S.S. Dantas, A. Jorio, Influence of the atomic structure on the Raman spectra of graphite edges, Phys. Rev. Lett. 93 (2004) 1–4. https://doi.org/10.1103/PhysRevLett.93.247401.

[43] L.G. Cançado, A. Jorio, M.A. Pimenta, Measuring the absolute Raman cross section of nanographites as a function of laser energy and crystallite size, Phys. Rev. B - Condens. Matter Mater. Phys. 76 (2007) 1–7. https://doi.org/10.1103/PhysRevB.76.064304.

[44] Y. You, Z. Ni, T. Yu, Z. Shen, Edge chirality determination of graphene by Raman spectroscopy, Appl. Phys. Lett. 93 (2008) 1–3. https://doi.org/10.1063/1.3005599.

[45] T. Enoki, S. Fujii, K. Takai, Zigzag and armchair edges in graphene, Carbon N. Y. 50 (2012) 3141–3145. https://doi.org/10.1016/j.carbon.2011.10.004.

[46] C. Cong, T. Yu, H. Wang, Raman study on the G mode of graphene for determination of edge orientation, ACS Nano. 4 (2010) 3175–3180. https://doi.org/10.1021/nn100705n.

[47] A. Das, S. Pisana, B. Chakraborty, S. Piscanec, S.K. Saha, U. V. Waghmare, K.S. Novoselov, H.R. Krishnamurthy, A.K. Geim, A.C. Ferrari, A.K. Sood, Monitoring dopants by Raman scattering in an electrochemically top-gated graphene transistor, Nat. Nanotechnol. 3 (2008) 210–215. https://doi.org/10.1038/nnano.2008.67.

[48] C. Ni, Scanning Electron Microscopy (SEM), Encycl. Tribol. (2013) 2977–2982. https://doi.org/10.1007/978-0-387-92897-5_1217.

[49]   C.Y. Tang, Z. Yang, Transmission Electron Microscopy (TEM), Membr. Charact. (2017) 145–159. https://doi.org/10.1016/B978-0-444-63776-5.00008-5.

[50]   H.R. Kang, Computational color technology, 2006. https://doi.org/10.1117/3.660835.

[51]   P. Tziourrou, J. Vakros, H.K. Karapanagioti, Using diffuse reflectance spectroscopy (DRS) technique for studying biofilm formation on LDPE and PET surfaces: laboratory and field experiments, Environ. Sci. Pollut. Res. 27 (2020) 12055–12064. https://doi.org/10.1007/s11356-020-07729-0.

[52]   A. Chithambararaj, N.S. Sanjini, S. Velmathi, A. Chandra Bose, Preparation of h-MoO3 and α-MoO3 nanocrystals: Comparative study on photocatalytic degradation of methylene blue under visible light irradiation, Phys. Chem. Chem. Phys. 15 (2013) 14761–14769. https://doi.org/10.1039/c3cp51796a.

[53]   Y. Shimizu, M. Ateia, M. Wang, D. Awfa, C. Yoshimura, Disinfection mechanism of E. coli by CNT-TiO2 composites: Photocatalytic inactivation vs. physical separation, Chemosphere. 235 (2019) 1041–1049. https://doi.org/10.1016/j.chemosphere.2019.07.006.

[54]   W. Wang, G. Huang, J.C. Yu, P.K. Wong, Advances in photocatalytic disinfection of bacteria: Development of photocatalysts and mechanisms, J. Environ. Sci. (China). 34 (2015) 232–247. https://doi.org/10.1016/j.jes.2015.05.003.

[55]   M. Pelaez, P. Falaras, V. Likodimos, K. O'Shea, A.A. de la Cruz, P.S.M. Dunlop, J.A. Byrne, D.D. Dionysiou, Use of selected scavengers for the determination of NF-TiO2 reactive oxygen species during the degradation of microcystin-LR under visible light irradiation, J. Mol. Catal. A Chem. 425 (2016) 183–189. https://doi.org/10.1016/j.molcata.2016.09.035.

[56]   S. Bell, G. Will, J. Bell, Light intensity effects on photocatalytic water splitting with a titania catalyst, Int. J. Hydrogen Energy. 38 (2013) 6938–6947. https://doi.org/10.1016/j.ijhydene.2013.02.147.

[57]   P. Heydarizadeh, W. Boureba, M. Zahedi, B. Huang, B. Moreau, E. Lukomska, A. Couzinet-Mossion, G. Wielgosz-Collin, V. Martin-Jézéquel, G. Bougaran, J. Marchand, B. Schoefs, Response of CO2-starved diatom phaeodactylum tricornutum to light intensity transition, Philos. Trans. R. Soc. B Biol. Sci. 372 (2017). https://doi.org/10.1098/rstb.2016.0396.

[58]   K. Roháček, J. Soukupová, M. Barták, Chlorophyll fluorescence: a wonderful tool to study plant physiology and plant stress, in: Plant Cell Compart. - Sel. Top., 2008: pp. 41–104. http://www.umbr.cas.cz/~rohacek/Publikace/RevChlFsemifin.pdf.

[59]   H. Walz, Dual-PAM-100 Measuring System for Simultaneous Assessment of P700 and Chlorophyll Fluorescence, System. (2006) 1–93.

[60]   C. Klughammer, U. Schreiber, Complementary PS II quantum yields calculated from simple fluorescence parameters measured by PAM fluorometry and the Saturation Pulse method, PAM Appl. Notes. 1 (2008) 27–35. http://www.walz.com/.

[61]   C.N. Huang, M.J. Cornejo, D.S. Bush, R.L. Jones, Estimating viability of plant protoplasts using double and single staining, Protoplasma. 135 (1986) 80–87. https://doi.org/10.1007/BF01277001.

[62]   P. NV, V. PA, R. Vemanna, S. MS, U. Makarla, Quantification of Membrane Damage/Cell Death Using Evan's Blue Staining Technique, Bio-Protocol. 7 (2017) e2519. https://doi.org/10.21769/bioprotoc.2519.

Chapter 3

Characterization of materials and optimization of nanocomposites

Chapter 3: Characterization of materials and optimization of nanocomposites

3.1 Introduction

Nanoparticles form the basis for the study and application in material science. These possess unique physical and chemical properties from the molecular levels associated to the standardized synthesis protocols or methodology for nanoparticle formation. These procedures have a direct compromise on the reproducibility of the results in the future. Therefore, a careful evaluation of different nanoparticles and various combinations researched as part of a preliminary step towards the application, *i.e.,* photocatalytic disinfection under visible light irradiation [1,2]. This chapter discusses the scientific background and justification for the challenges faced during the selection of the materials, the preliminary characterization results, and finalization of the dopant nanoparticles and nanocomposites for the photocatalytic antibacterial study. The flow chart shows the steps undertaken during the process of selection (Fig 3.1).
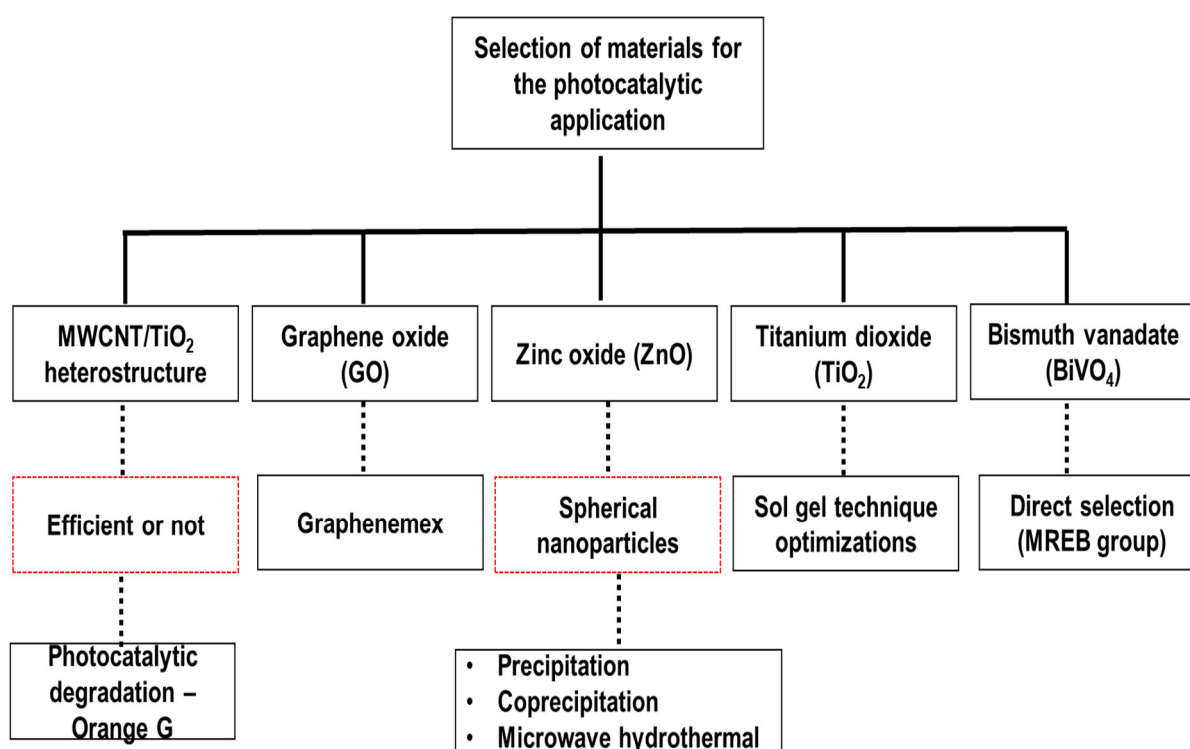
Fig 3.1: Flow chart represents the step-by-step accomplishment to confirm the nanoparticles and nanocomposites used for the photocatalytic disinfection study.

3.2 Results and Discussion

3.2.1 XRD analysis of MWCNT/TiO₂ composite

Following the acid treatment, the purchased MWCNTs were functionalized or oxidized as an initial step for incorporating TiO_2 anatase nanoparticles bought from Sigma Aldrich (Refer Chapter 2, section 2.3.1). The oxidized MWCNTs, TiO_2 anatase, and MWCNT/TiO₂ composite were characterized by XRD analysis to identify the crystalline quality and purity of the materials. XRD characterization is a better tool for measuring graphitization extent and the degree of the nanotube alignment in MWCNTs. Fig 3.2 shows the XRD spectra of the composite and the individual materials. The intense peak at $2\theta = 24°$ corresponds to the (002) reflection plane, whereas the lower intensity peak at $2\theta = 43.6°$ is typical to the (100) plane. These planes point out to the functionalized MWCNTs. From the literature, peaks at $2\theta = 25.2°$ and $2\theta = 44°$ corresponds to crude MWCNTs, and peaks show a downward shift due to an increase in the sp^2 C=C layer spacing. This literature provides evidence for keeping the crystallinity of MWCNTs after the oxidation or functionalization of MWCNTs by the acid treatment. The characteristic peaks of synthesized TiO_2 anatase defined in the XRD spectra, *i.e.*, diffraction peaks at $2\theta = 25.28°$, $37.8°$, $48.05°$, $53.89°$, and $55.06°$ corresponded to the (101), (004), (200), (105) and (211) crystallographic planes of TiO_2 anatase phase, respectively. However, with functionalized MWCNTs, the crystalline quality of TiO_2 anatase was seemingly decreased, observed from the XRD spectra. The same effect occurred with the TiO_2 anatase phase over MWCNTs that reduced the intensity of the characterization peak of MWCNTs, which was attributed to the intense peaks of TiO_2 anatase [3–5]. When the MWCNT/TiO₂ composite was analyzed, the reflection planes of (002) and (100), associated to the MWCNTs and (101) related to TiO_2 anatase were observed [5,6]. These observations gave a preliminary confirmation on the composite formation and suggested that the anatase phase was conserved during the chemical route of composite synthesis. The crystallite size of the MWCNTs and anatase nanoparticles was calculated using the Scherrer equation (Refer to Chapter 2, section 2.4.1) and was found to be 175.7 nm and 17.03 nm, respectively.
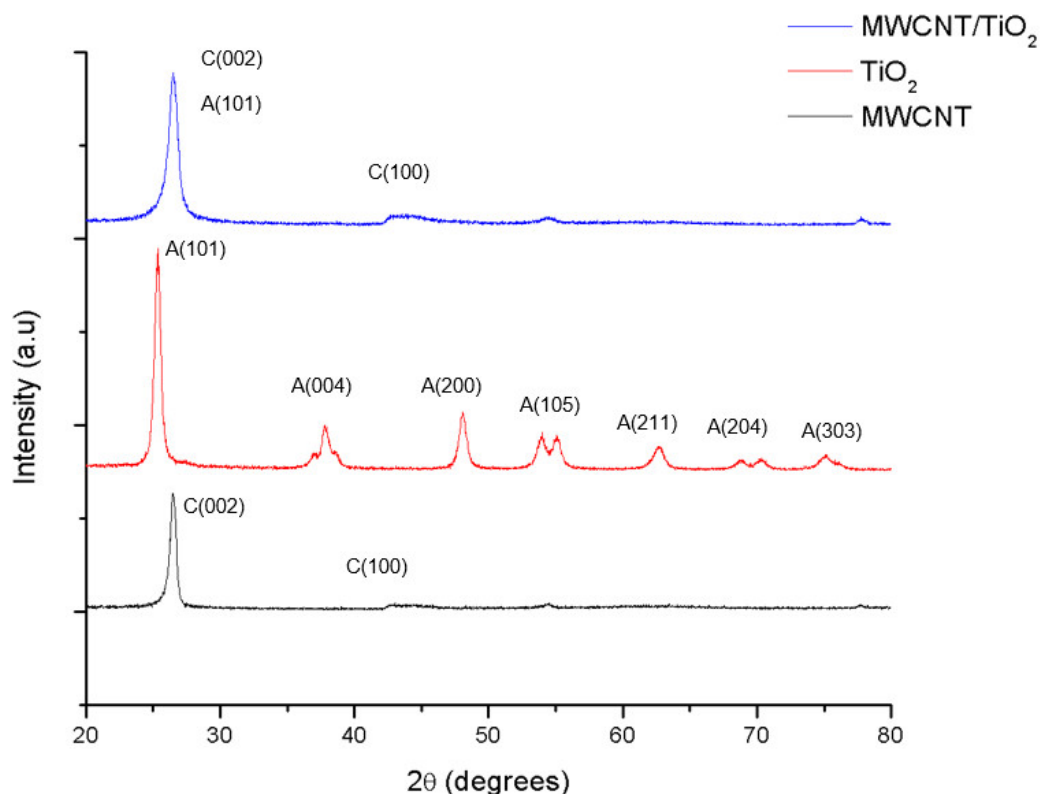
Fig 3.2: XRD analysis of MWCNTs, TiO$_2$ anatase, and MWCNT/TiO$_2$ heterostructure Graph represents the formation of MWCNT/TiO$_2$ composite through acid treatment.

3.2.2 Morphological confirmations

Morphological studies were carried out by SEM analysis to prove the incorporation of TiO$_2$ nanoparticles over the functionalized MWCNTs. Fig 3.3 shows the SEM images of the TiO$_2$ anatase nanoparticles (Fig 3.3 (a)) and the oxidized MWCNTs (Fig 3.3 (b)). From the SEM image of TiO$_2$ nanoparticles, large pieces or chunks of particles were observed with agglomeration. The SEM images indicated the distribution of TiO$_2$ nanoparticles on the nanotubes without any apparent agglomerations (Fig 3.3 (c)). TiO$_2$ nanoparticles were enclosed within the three-dimensional matrix by the presence of dispersed active sites of MWCNTs. Seen from the image, the accumulation or decoration of TiO$_2$ nanoparticles over the MWCNTs directs the supporting role played by MWCNTs acting as a core for the deposition and growth of TiO$_2$ nanoparticles throughout the nanotubes. This image also indicates the close contact that arises between MWCNTs and TiO$_2$ anatase nanoparticles [7–9]. This SEM image pointed to the confirmation for forming MWCNT/TiO$_2$ composite. The average crystallite size agreed with the XRD analysis [10–12].
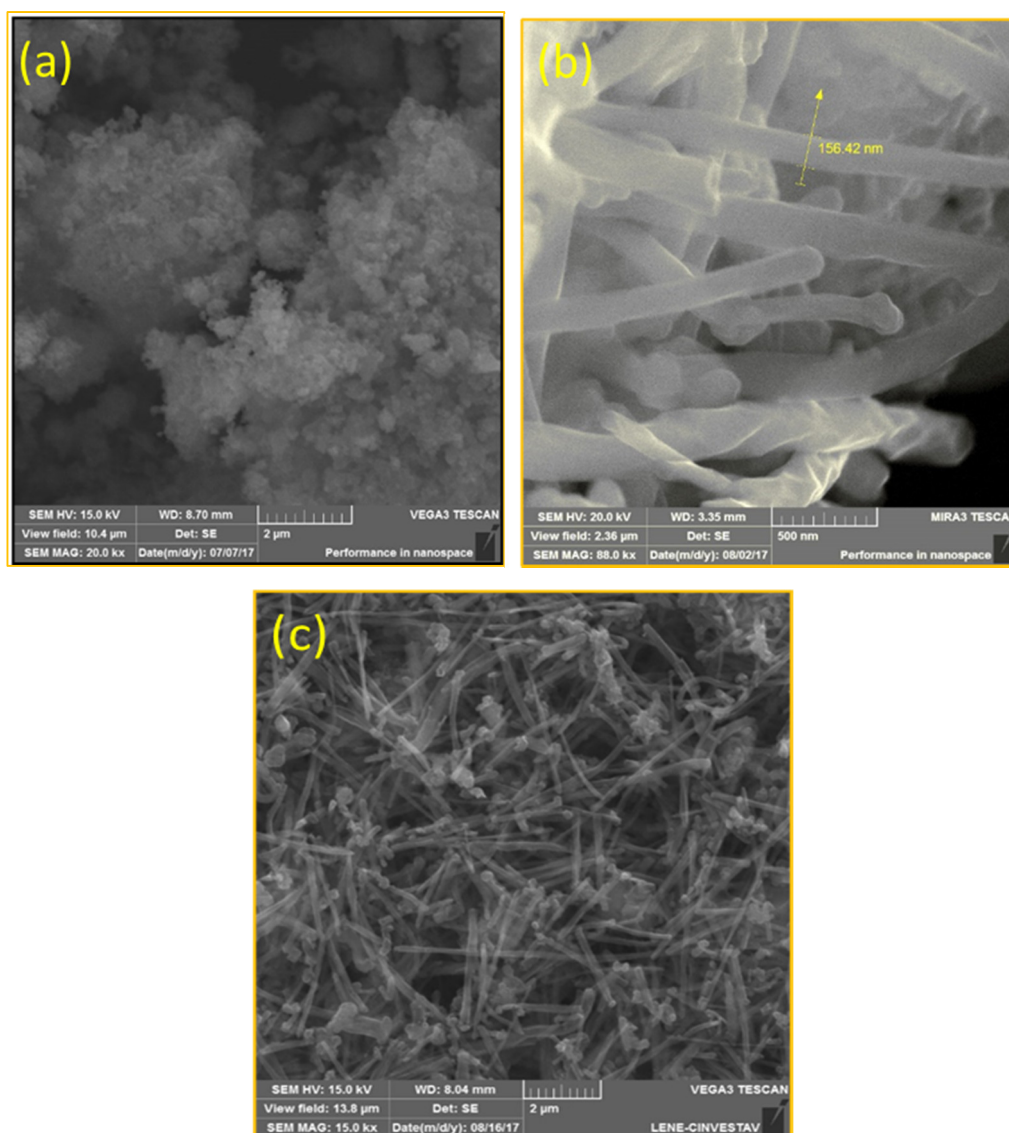
Fig 3.3: SEM images of the (a) agglomerated TiO$_2$ nanoparticles (b) oxidized or functionalized MWCNTs (c) TiO$_2$/MWCNTs composite confirming the incorporation of TiO$_2$ nanoparticles over the carbon nanotubes.

3.2.3 Dye degradation studies

The photocatalytic degradation study of Orange G by the synthesized MWCNT/TiO$_2$ composite was investigated using visible light irradiation (See Chapter 2, section 2.3.2). The degradation percentage was calculated by using the formula:

$$Degradation\ \% \ = \ \frac{C_0 - C}{C_0} * 1 \qquad\qquad Eq: 3.1$$

where C$_0$ = initial concentration of the Orange G dye

     C   = concentration of the Orange G dye at a different time interval, t

The proposed mechanism for the degradation of the dye using the MWCNTs/TiO$_2$ suspensions can be explained with three different hypotheses based on MWCNTs:

   i.   Act as a means of dispersion of TiO$_2$ nanoparticles

   ii. Act as a photosensitizer

   iii. Act as a co-adsorbent

When TiO$_2$ nanoparticles are grown along the nanotubes, the chemical groups of MWCNTs provide an anchor for the attachment of TiO$_2$ nanoparticles. The synergistic interaction that arises among MWCNTs and TiO$_2$ nanoparticles depend upon the size of TiO$_2$ nanoparticles, the crystalline phase composition of TiO$_2$ nanoparticles, and the surface chemistry of the MWCNTs/TiO$_2$ composite [3,13]. From Fig 3.4, changes in the relative concentration of Orange G were depicted for the composite. The enhanced photocatalytic activity was attributed to the adsorption properties of TiO$_2$ anatase nanoparticles decorated over the MWCNTs, thereby increasing the surface area. After 30 min of light irradiation, one-fourth of the dye was degraded (Fig 3.4) [14,15]. The low photocatalytic performance of the MWCNTs/TiO$_2$ composite can be due to large quantities of MWCNTs, scattering the incident light, and thus decreasing the photocatalytic process.

3.2.4 Justification for the selection of graphene oxide (GO)

An atom-thick sheet of carbon atoms, arranged in the form of a nanoscale chain-link fence, is graphene oxide (GO). GO is claimed to be a fundamental enabler for the development of new generation nanocomposites. When compared with chemical makeup and mechanical properties, GO, and MWCNTs are identical. But, for lending its properties to other materials when they are in a composite form, GO is a better candidate than MWCNTs even though both are strong. To be numbered for the advantages of GO over MWCNTs are [16–19]:

   i.   They are rough and possess a wrinkled surface texture due to high-density surface defects caused by thermal exfoliation.

   ii. As GO is a planar sheet with a large surface area, the contact area for the materials will be larger than the tube-shaped MWCNTs.

   iii. GO geometry is two-dimensional compared to the one-dimensional carbon nanotubes, which helps to maximize the energy that enhances its applications.

The results obtained for the degradation of Orange G dye, as part of a preliminary step for the photocatalytic disinfection study by MWCNT/TiO$_2$ composites, were not satisfied compared with the works of literature. Therefore, GO is considered for proceeding with the disinfection studies.
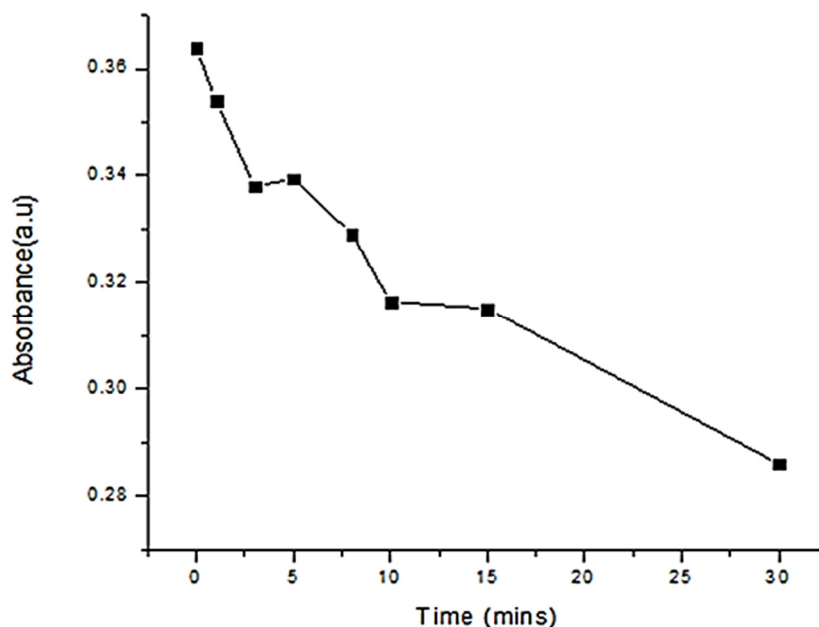
Fig 3.4: Photocatalytic degradation of orange G dye using MWCNTs/TiO$_2$ composite as a preliminary step for the selection of material for the photocatalytic disinfection study

3.2.5 Characterizations of synthesized ZnO nanoparticles

ZnO nanoparticles were synthesized through various methodologies, as mentioned in Chapter 2, section 2.3.3. From the XRD analysis (Fig 3.5), the different peaks of ZnO nanoparticles corresponded to the (100), (002), (101), (110), (103), (112), (201), and (202) reflection planes and were in good agreement with that previously reported in literature. All the ZnO nanoparticles formed by various methodologies possessed the wurtzite phase (cubic) [20]. Every sample had its strongest peak for (101), (002), and (101) planes, confirming the formation of ZnO nanoparticles, but not the expected hexagonal phase. Fig 3.6 shows the effect of various calcination temperatures after the coprecipitation method, and the XRD spectra revealing the narrowing of the peaks with increased intensity. The presence of additional peaks around 43° attributes towards the unreacted precursors during the synthesis process [21,22]. By the microwave-assisted hydrothermal method, the final amount obtained after every single synthesis was 0.8 g, which was a time-consuming process. The precipitation methods

followed for synthesis were of long duration, at the time of sedimentation or washing process. The formation of graphene oxide/zinc oxide (GO/ZnO) composite (Fig 3.8) is confirmed with the presence of peaks from ZnO, whereas there were no observable peaks of graphene oxide due to the dominant peaks of ZnO [23]. The XRD spectra of different ZnO nanoparticles during different synthesis routes are depicted in Fig 3.5.

To verify the formation of spherical ZnO nanoparticles, morphological analysis was performed through SEM. Unfortunately, all the formed nanoparticles were not in the expected shapes but obtained rod-shaped (Fig 3.7 (a)), cluster (Fig 3.7 (b)) and spindle-shaped (Fig 3.7 (c)). The nanoparticles showed a large size, which can significantly affect the efficiency of the photocatalytic disinfection process. All these variations in the size and shape of the synthesized ZnO nanoparticles were attributed to the precursors, and the synthesis steps [20,24].

The synthesized GO/ZnO composite was tested for preliminary identification of the efficiency in photocatalytic disinfection. For this, a disk diffusion assay was performed. After the overnight incubation, the inhibition zone was observed but in nominal diameter (Fig 3.9). The reduced inhibition zone shows that the ZnO nanoparticles could not perform the photocatalytic disinfection compared with the reported literature, which can be due to the phase formed, as well as to the large particle size blocking the active sites and low absorption of light irradiation.
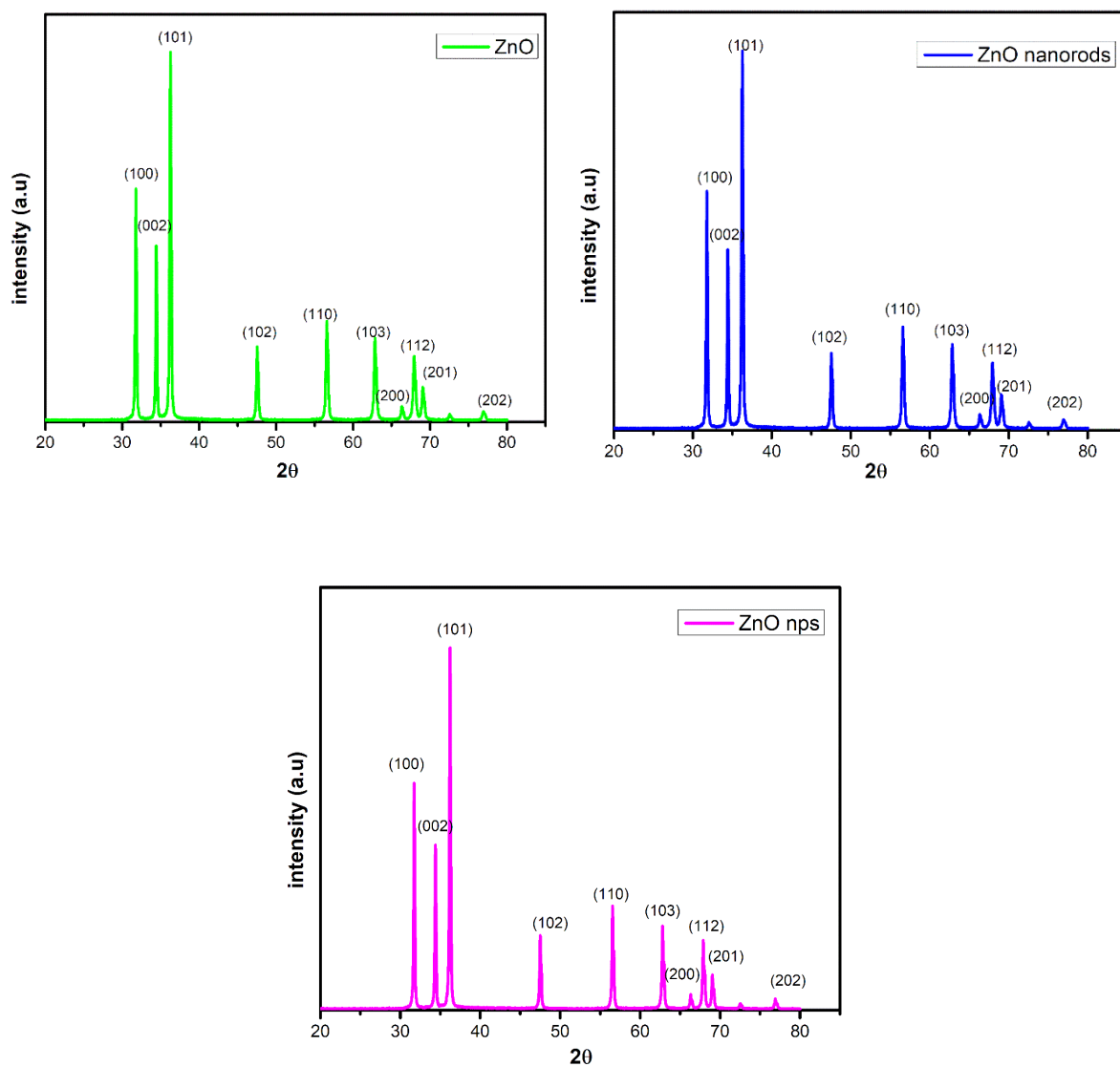
Fig 3.5: XRD spectra of ZnO nanoparticles obtained through different synthesis methods, i.e., precipitation method and coprecipitation method (with varying parameters)
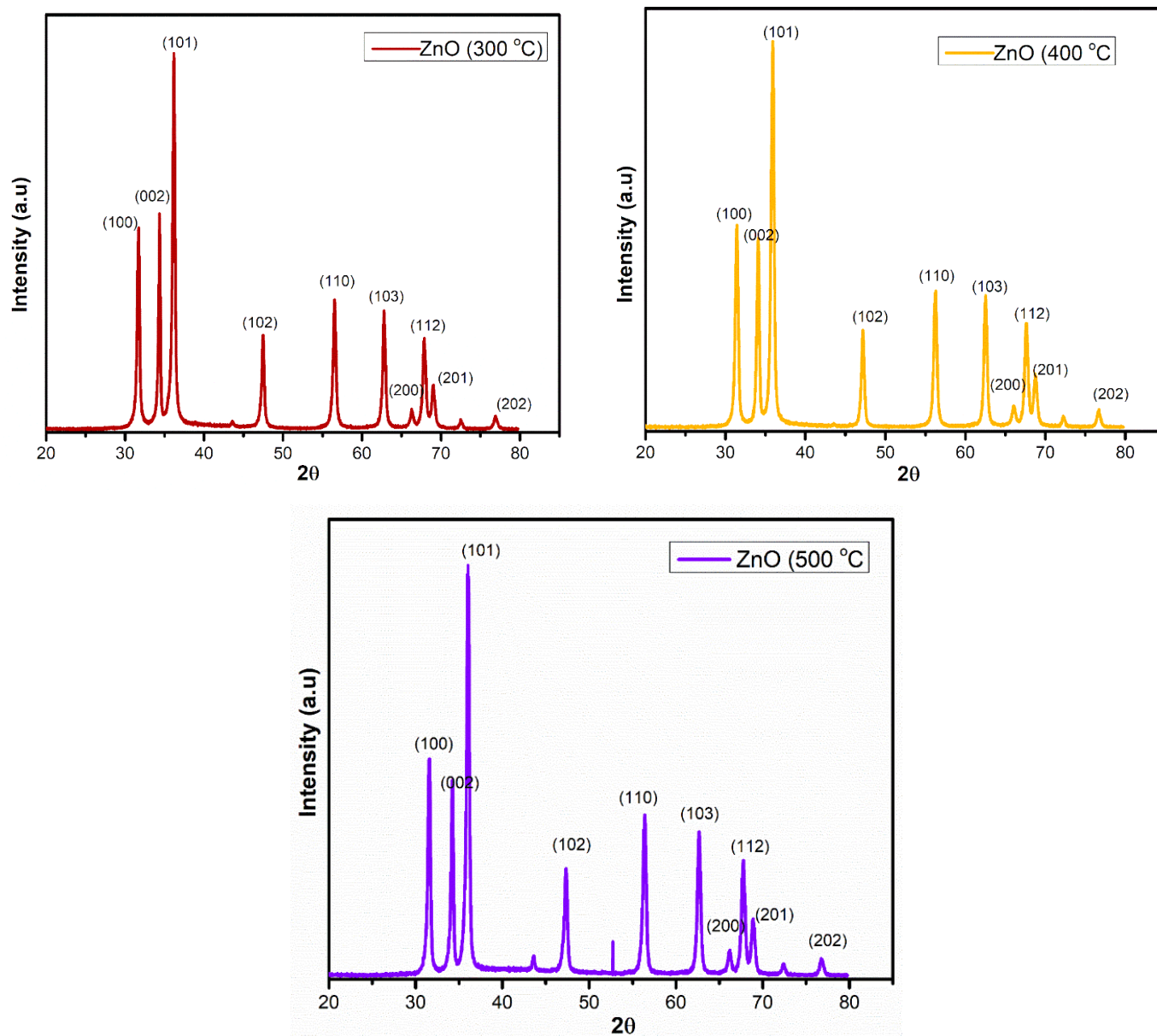
Fig 3.6: XRD spectra depicting the effect of annealing temperature. The XRD diffractogram of 300°C and 500°C showed an additional peak around 2θ = 43°, which was absent in the spectra of 400°C.
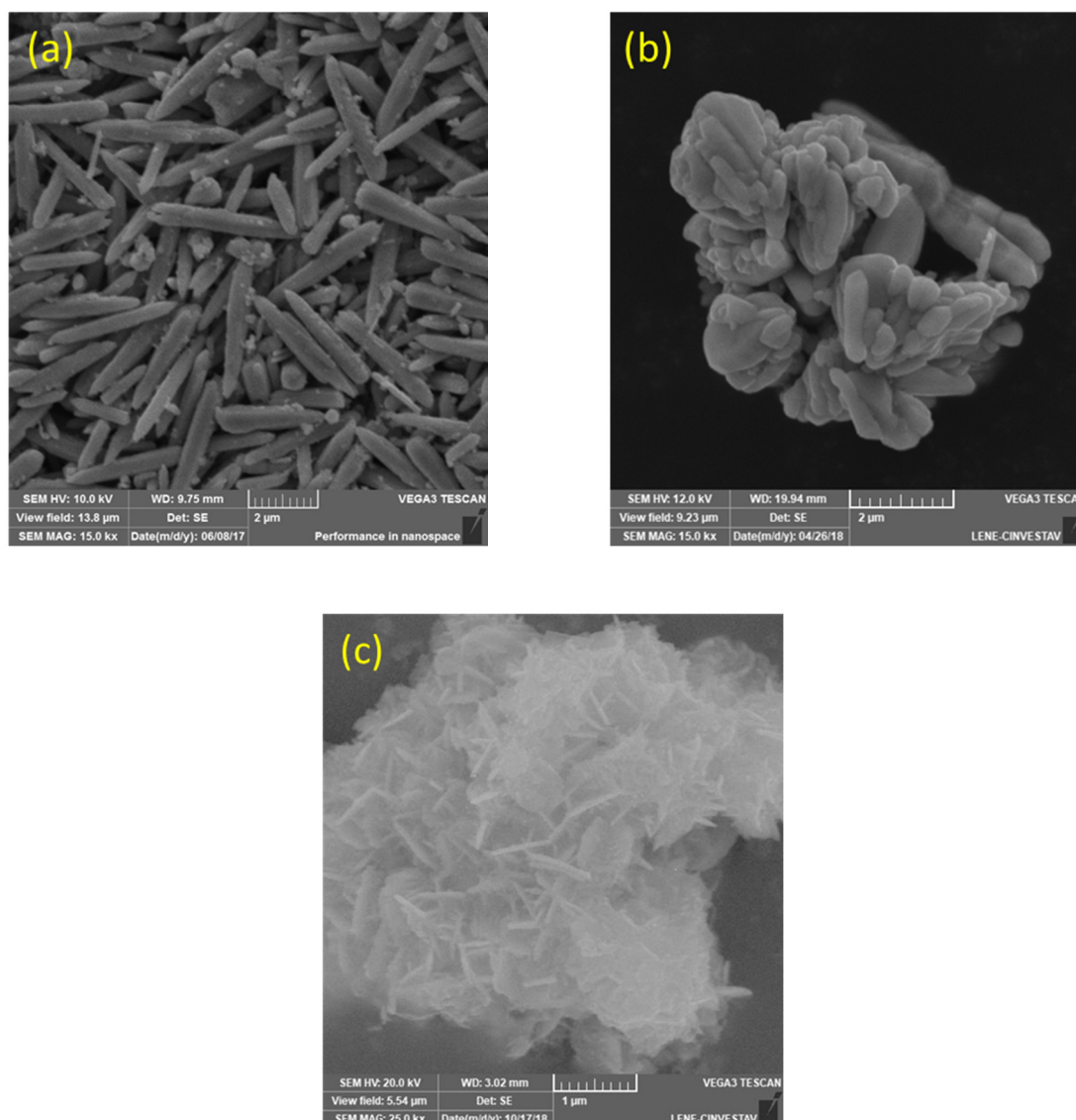
Fig 3.7: SEM morphologies (a) rod-shaped obtained by precipitation method (b) cluster of ZnO nanoparticles formed through the coprecipitation method using zinc acetate as the precursor (c) spindle shaped ZnO nanoparticles obtained when zinc acetate and sodium hydroxide used as precursors followed by seven times washing of the precipitate.
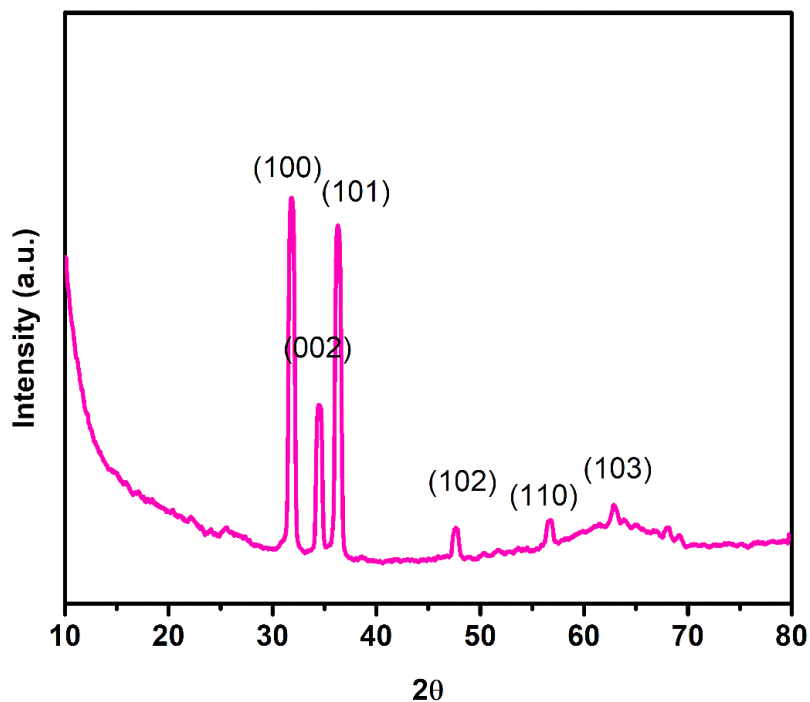
Fig 3.8: XRD spectra of GO/ZnO composite synthesized through the simple blending process, depicting defined peaks of ZnO nanoparticles.
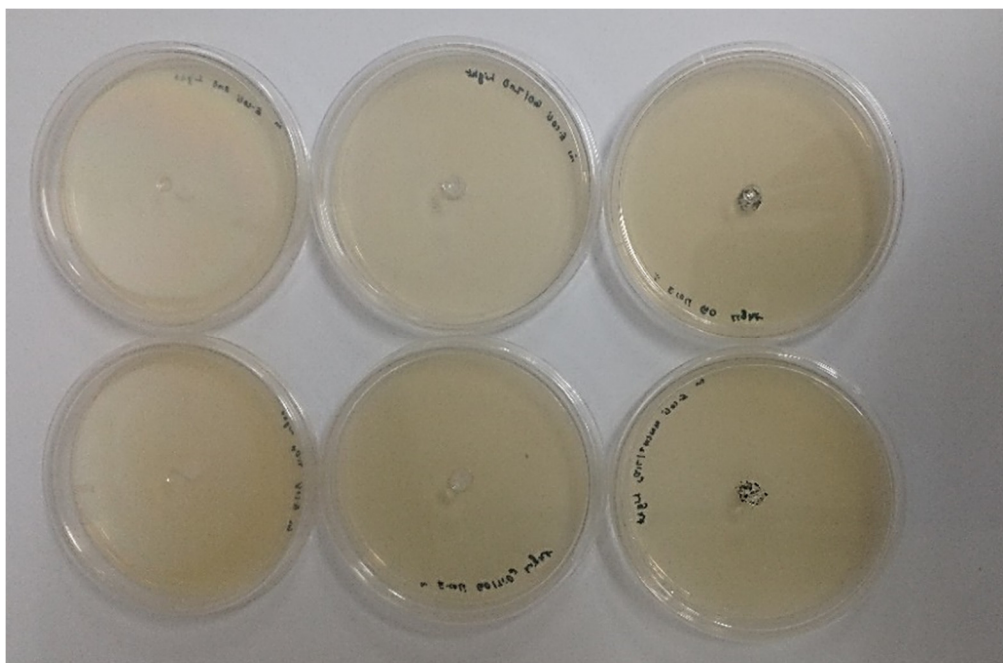
Fig 3.9: Photographs depicting the disk diffusion assay performed in nutrient agar plates spread with E. coli K12 suspension. It was identified that the zone of inhibition was formed by the effect of GO/ZnO composite after visible-light irradiation followed by overnight incubation.

3.2.6 GO/TiO$_2$ composite optimization

XRD pattern of the GO/TiO$_2$ composite is depicted in Fig 3.10. From the graphs, it was evident that the intensity of characteristic peak at the (101) reflection plane was diminishing as the concentration of GO content increased. This increase can be due to the sheet-like structure of GO covering the TiO$_2$ nanoparticles, thereby showing a low signal. But as per the literature, GO content must be restricted towards percentage amount to increase the efficiency of the composite and extract the versatile properties of GO. Therefore, these ratios were eliminated from the present study and were focusing on the low loadings of GO. The SEM analysis of the obtained composites is shown in Fig 3.11. It shows the decoration of TiO$_2$ nanoparticles over the GO sheets but has got large chunks or agglomerations.
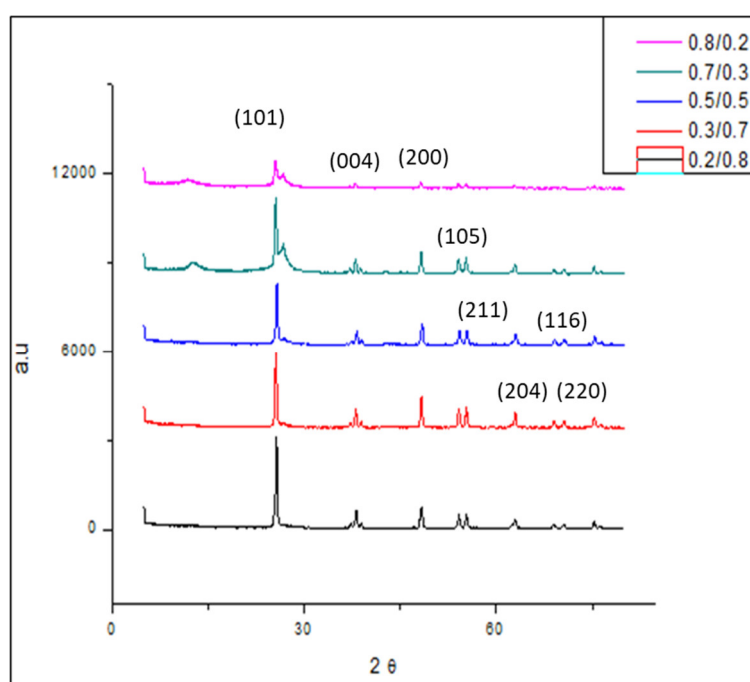
Fig 3.10: The XRD diffractometer of five different ratios, namely, 0.2/0.8, 0.3/0.7, 0.5/0.5, 0.7/0.3, and 0.8/0.2 GO/TiO$_2$ composite showing the intense peaks of the TiO$_2$ anatase phase.
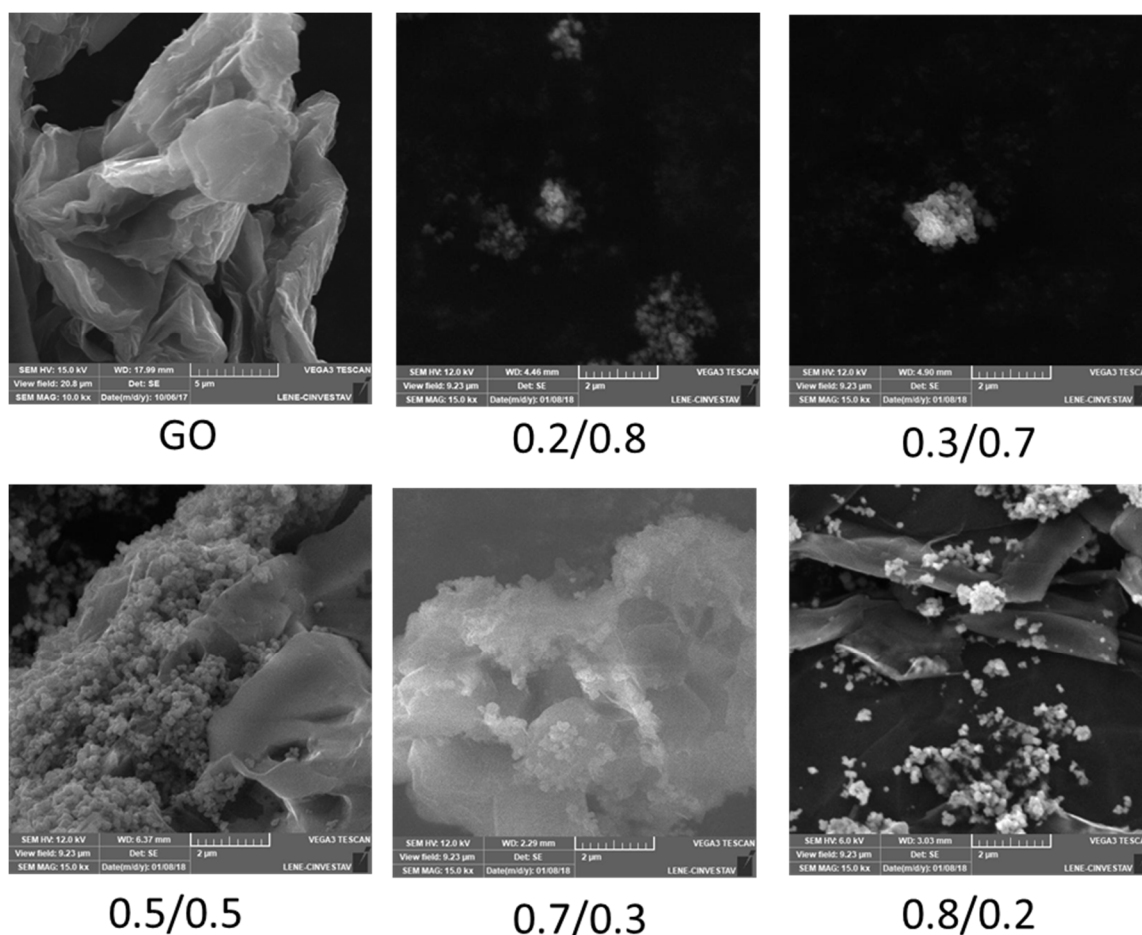
Fig 3.11: SEM analysis of GO with wrinkled structure and five different synthesized GO/TiO₂ composite (0.2/0.8, 0.3/0.7, 0.5/0.5, 0.7/0.3, and 0.8/0.2)

3.2.7 Optimization of TiO₂ nanoparticle synthesis

To obtain nanoparticles of better quality and foreseeing the efficiency in the application, *i.e.,* photocatalytic disinfection, TiO_2 nanoparticles were synthesized using titanium chloride as the precursor (see Chapter 2, section 2.6). The conditions were optimized by changing various parameters. The annealing temperature was fixed at 450°C, as the focus of the study is in the anatase phase, and the increase in the calcination temperature can cause the conversion of the anatase phase to the rutile phase. The synthesis temperature during the sol-gel route was varied as room temperature, 50°C, and 60°C, and the XRD spectra of the final powder obtained after these synthesis conditions are depicted in Fig 3.12. From the results, the spectra at room temperature and 60°C show promising crystalline quality nanoparticles. 60°C was chosen as the optimized parameter because the synthesis by room temperature was time-consuming. The morphology of the TiO_2 nanoparticles obtained after the sol-

gel route with synthesis temperature 60°C was found to be spherical, which was confirmed with SEM analysis (Fig 3.13)
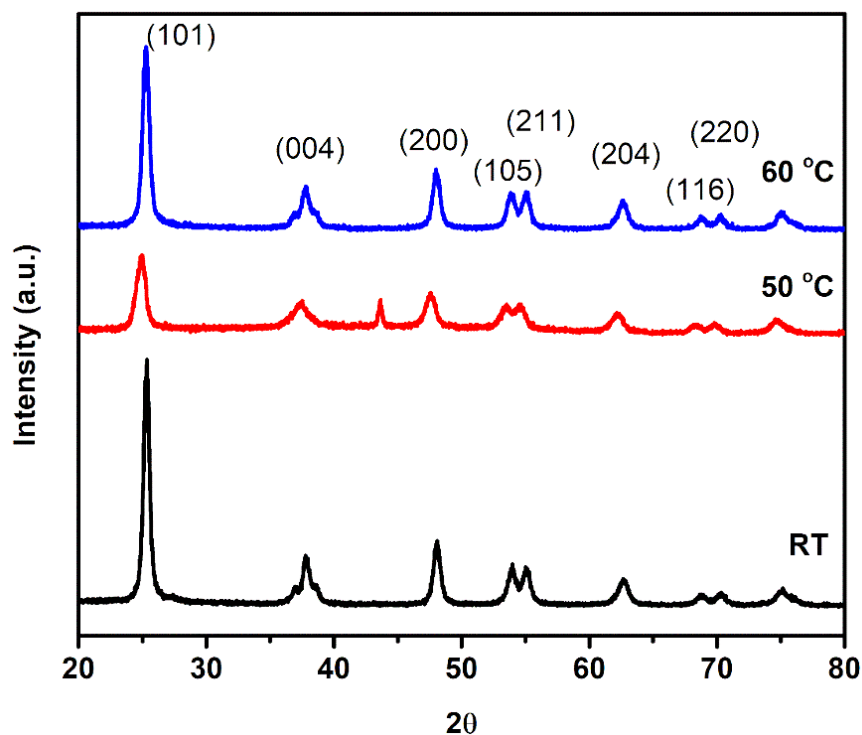
Fig 3.12: XRD spectra of TiO₂ nanoparticles synthesized through sol-gel method focused on the synthesis temperature, namely, room temperature, 50°C and 60°C
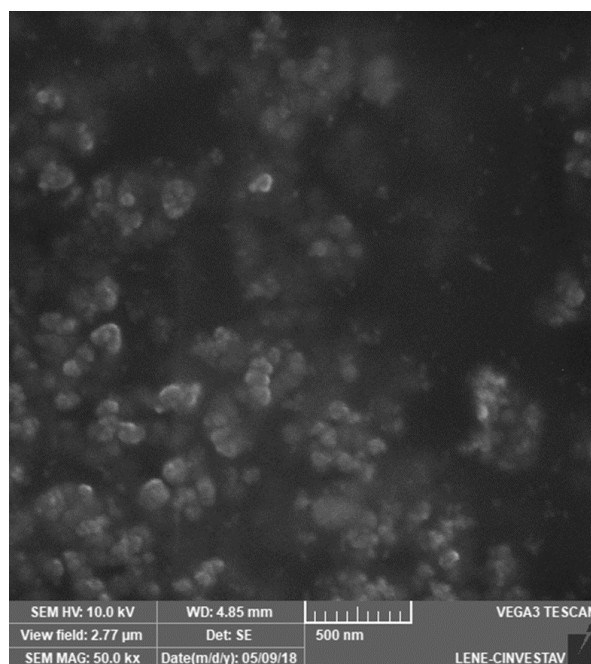
Fig 3.13: SEM images showed the spherical TiO₂ nanoparticles obtained through the sol-gel route with optimized parameters.

3.3 Conclusion

To be concluded from this chapter, various synthesis methodologies were adopted to develop highly efficient nanoparticles for photocatalytic disinfection studies. The main objective was to optimize the multiple conditions necessary to improve or enhance the photocatalytic activity. From the literature survey, GO was better in photocatalytic application compared to MWCNTs. With the well-established TiO_2 nanoparticles and the less researched $BiVO_4$ nanoparticles in the field of disinfection studies were chosen, and ZnO was eliminated from the study considering the low efficiency obtained. The optimized parameters performed from our group (MREB, CINVESTAV) were used to synthesize $BiVO_4$ nanoparticles through the sol-gel route (see Chapter 2, section 2.8) and were considered for the synthesis of GO/BiVO4 composite and their application in the photocatalytic disinfection studies.

References

[1]   A. Kumar, C.K. Dixit, Methods for characterization of nanoparticles, in: Adv. Nanomedicine Deliv. Ther. Nucleic Acids, 2017: pp. 44–58. https://doi.org/10.1016/B978-0-08-100557-6.00003-1.

[2]   S. Mourdikoudis, R.M. Pallares, N.T.K. Thanh, Characterization techniques for nanoparticles: Comparison and complementarity upon studying nanoparticle properties, Nanoscale. 10 (2018) 12871–12934. https://doi.org/10.1039/c8nr02278j.

[3]   S. Da Dalt, A.K. Alves, C.P. Bergmann, Photocatalytic degradation of methyl orange dye in water solutions in the presence of MWCNT/TiO2 composites, Mater. Res. Bull. 48 (2013) 1845–1850. https://doi.org/10.1016/j.materresbull.2013.01.022.

[4]   U. Caudillo-Flores, J. Lara-Romero, J. Zárate-Medina, M.J. Muñoz-Batista, R. Huirache-Acuña, E.M. Rivera-Muñoz, J.A. Cortés, Enhanced photocatalytic activity of MWCNT/TiO2 heterojunction photocatalysts obtained by microwave assisted synthesis, Catal. Today. 266 (2016) 102–109. https://doi.org/10.1016/j.cattod.2015.12.005.

[5]   A.M. Kamil, F.H. Hussein, A.F. Halbus, D.W. Bahnemann, Applications of MWCNTs / TiO 2 Composite, Int. J. Photoenergy. 2014 (2014) 1–8.

[6]   H. Bin Zhang, G.D. Lin, Z.H. Zhou, X. Dong, T. Chen, Raman spectra of MWCNTs and MWCNT-based H2-adsorbing system, Carbon N. Y. 40 (2002) 2429–2436. https://doi.org/10.1016/S0008-6223(02)00148-3.

[7]   W. Wang, P. Serp, P. Kalck, C.G. Silva, J.L. Faria, Preparation and characterization of nanostructured MWCNT-TiO2 composite materials for photocatalytic water treatment applications, Mater. Res. Bull. 43 (2008) 958–967. https://doi.org/10.1016/j.materresbull.2007.04.032.

[8]   K.D. Shitole, R.K. Nainani, P. Thakur, Preparation, characterisation and photocatalytic applications of TiO 2-MWCNTs composite, Def. Sci. J. 63 (2013) 435–441. https://doi.org/10.14429/dsj.63.4870.

[9]   B. Gao, G.Z. Chen, G. Li Puma, Carbon nanotubes/titanium dioxide (CNTs/TiO2) nanocomposites prepared by conventional and novel surfactant wrapping sol-gel methods exhibiting enhanced photocatalytic activity, Appl. Catal. B Environ. 89 (2009) 503–509. https://doi.org/10.1016/j.apcatb.2009.01.009.

[10]   S.-J. Kim, J.-S. Im, P.-H. Kang, T.-J. Kim, Y.-S. Lee, Photo Catalytic Activity of CNT-TiO 2 Nano Composite in Degrading Anionic and Cationic Dyes , Carbon Lett. 9 (2008) 294–297. https://doi.org/10.5714/cl.2008.9.4.294.

[11]   B.K. Vijayan, N.M. Dimitrijevic, D. Finkelstein-Shapiro, J. Wu, K.A. Gray, Coupling titania nanotubes and carbon nanotubes to create photocatalytic nanocomposites, ACS Catal. 2 (2012) 223–229. https://doi.org/10.1021/cs200541a.

[12]   X. Huang, M. Feng, X. Liu, Design of bristle-like TiO2-MWCNT nanotubes to improve the dielectric and interfacial properties of polymer-based composite films, RSC Adv. 4 (2014) 4985–4992. https://doi.org/10.1039/c3ra46306k.

[13]   R. Leary, A. Westwood, Carbonaceous nanomaterials for the enhancement of TiO2 photocatalysis, Carbon N. Y. 49 (2011) 741–772. https://doi.org/10.1016/j.carbon.2010.10.010.

[14]   F. Alosfur, M.H. Haji Jumali, S. Radiman, N.J. Ridha, M.A. Yarmo, A.A. Umar, Visible light-responsive TiO2 coated MWCNTs as a hybrid nanocatalysts, Int. J.

Electrochem. Sci. 8 (2013) 2977–2982.

[15]   W. Wang, P. Serp, P. Kalck, J.L. Faria, Visible light photodegradation of phenol on MWNT-TiO2 composite catalysts prepared by a modified sol-gel method, J. Mol. Catal. A Chem. 235 (2005) 194–199. https://doi.org/10.1016/j.molcata.2005.02.027.

[16]   M.A. Rafiee, J. Rafiee, I. Srivastava, Z. Wang, H. Song, Z.Z. Yu, N. Koratkar, Fracture and fatigue in graphene nanocomposites, Small. 6 (2010) 179–183. https://doi.org/10.1002/smll.200901480.

[17]   M.A. Rafiee, J. Rafiee, Z.Z. Yu, N. Koratkar, Buckling resistant graphene nanocomposites, Appl. Phys. Lett. 95 (2009) 1–4. https://doi.org/10.1063/1.3269637.

[18]   M.A. Rafiee, J. Rafiee, Z. Wang, H. Song, Z.Z. Yu, N. Koratkar, Enhanced mechanical properties of nanocomposites at low graphene content, ACS Nano. 3 (2009) 3884–3890. https://doi.org/10.1021/nn9010472.

[19]   S.K. and P.K.B. Boruah, Conversion of reduced graphene oxide into multi-walled conversion of reduced graphene oxide into multi-walled carbon nanotubes, J. Appl. Fundam. Sci. 4 (2018) 100–105.

[20]   S.P. Prakoso, R. Saleh, Synthesis and Spectroscopic Characterization of Undoped Nanocrytalline ZnO Particles Prepared by Co-Precipitation, Mater. Sci. Appl. 03 (2012) 530–537. https://doi.org/10.4236/msa.2012.38075.

[21]   M.A. Ismail, K.K. Taha, A. Modwi, L. Khezami, ZnO nanoparticles: Surface and X-ray profile analysis, J. Ovonic Res. 14 (2018) 381–393.

[22]   T.M. Al-saadi, T. Al-dhahir, E.E. Al-obodi, ZnO nanoparticles : synthesis and crystal structure study, Waist J. Sci. Med. 7 (2014) 87–95.

[23]   S.A. Hosseini, S. Babaei, Graphene oxide/zinc oxide (GO/ZnO) nanocomposite as a superior photocatalyst for degradation of methylene blue (MB)-process modeling by response surface methodology (RSM), J. Braz. Chem. Soc. 28 (2017) 299–307. https://doi.org/10.5935/0103-5053.20160176.

[24]   . J.M., Role of Salt Precursor in the Synthesis of Zinc Oxide Nanoparticles, Int. J. Res. Eng. Technol. 03 (2014) 43–45. https://doi.org/10.15623/ijret.2014.0303008.

Chapter 4

Characterization and microbial disinfection of GO/TiO$_2$ and GO/BiVO$_4$ composite
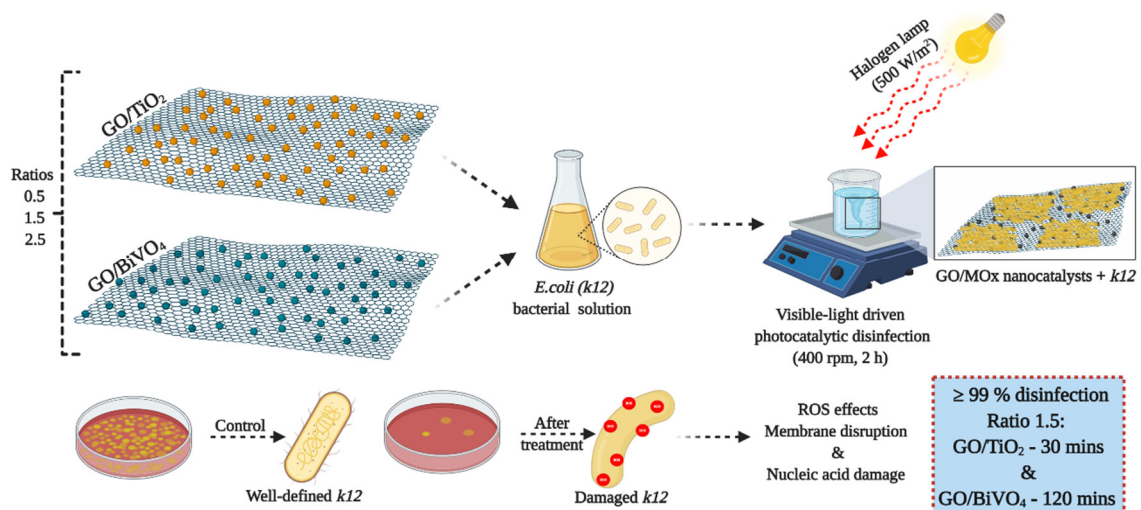
Chapter 4: Characterization and microbial disinfection of GO/TiO$_2$ and GO/BiVO$_4$ composite

4.1 Introduction

This chapter discussed the work aiming to develop a nanocomposite, eco-friendly and cost-effective and, importantly, to avoid the formation of DBPs. This study focuses on synthesizing various GO/MOx nanocomposites, *i.e.,* GO/TiO$_2$ (herein denoted as GOT) and GO/BiVO$_4$ (herein designated as GOB), using pristine nanoparticles by a simple blending method without the addition of any surfactants or protective agents. The synthesized nanocomposites were evaluated for photocatalytic antibacterial activity, ROS effect, and disinfection kinetics. *E. coli K12*, which is a model organism for the photocatalytic disinfection study, was used. The proposed research includes the facile synthesis method and efficient photocatalytic disinfection of bacteria *(E. coli K12)*. From the scavenger study, we also determined the mechanism which demonstrates the synergistic activity of GO and MOx nanoparticles on the photocatalytic disinfection process. The novelty of this work relies on a comparative assessment of the stable GO-based nanocomposites and their impact on visible light-mediated photocatalytic inactivation of *E.coli,* an indicator of drinking water quality [1–9]. The photocatalytic disinfection process involves a solid semiconductor photocatalyst that generates ROS during exposure to light. The most preferred photocatalyst is TiO$_2$ due to its low cost, non-toxicity, chemical stability, and activity near-ultraviolet region [10–12].   Microorganisms are composed of water (70 – 90 %) and cellular components like lipids, polysaccharides, lipids, proteins, and nucleic acids, prone to ROS attack, causing cell death. Therefore, photocatalysis has a significant efficiency in biocidal properties (Fig 4.1).
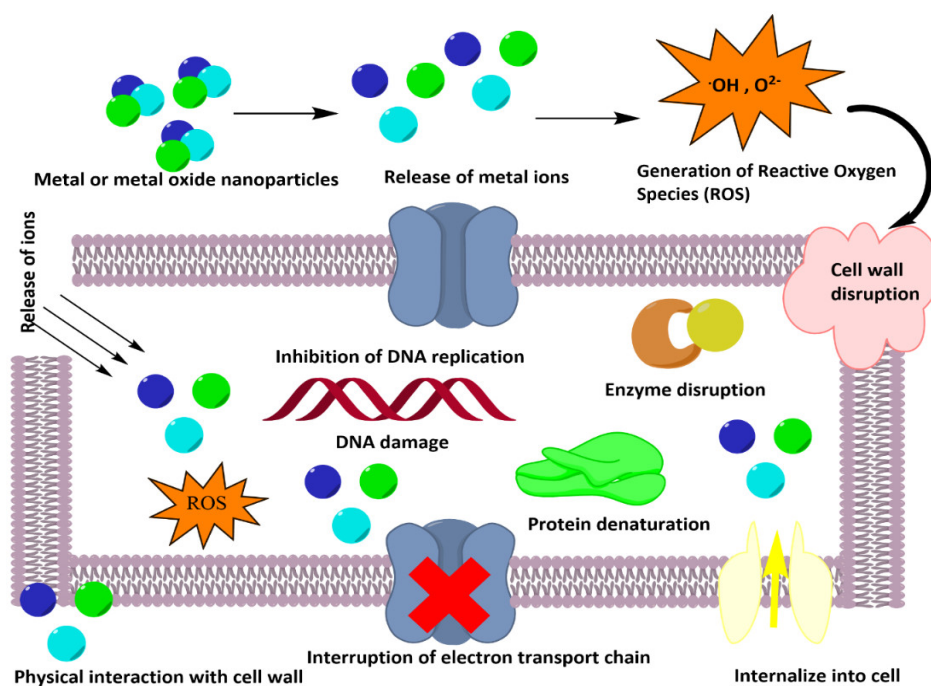
Fig 4.1: The illustration representing the typical microbial disinfection by a semiconductor photocatalyst (reproduced from [13])

4.2 Results and Discussions

4.2.1 XRD analysis

*x*GOT and *x*GOB nanocomposites (0.5, 1.5, and 2.5 wt.%) were synthesized (refer to Chapter 2, section 2.9) through a simple blending process previously reported with minor modifications [14]. From XRD analysis, crystalline properties of graphene oxide could be identified, with an intense peak at 2θ = 26.42°, corresponding to the (002) plane, it was related to the higher crystalline nature of pristine graphite having a d-spacing of 3.37 Å. At 2θ = 11.95°, a diffraction peak indicated GO with a d-spacing of 7.4 Å. The presence of oxygen functional groups is the reason behind larger d-spacing of GO [15,16]. TiO_2 anatase possesses a tetragonal structure, and the TiO_6 octahedron is distorted more. There are reports as the reactivity of anatase crystals is higher for (001) facets when compared to (101) facets [17]. $BiVO_4$ has three crystal structures, namely, tetragonal zircon phase, monoclinic scheelite phase, and tetragonal scheelite phase in which, monoclinic scheelite phase has got major applications [18]. In Fig 4.2 (a), the X-ray diffraction (XRD) patterns of GO, TiO_2, and *x*GOT nanocomposites are shown, while Fig 4.2 (b) shows the patterns corresponding to the GO, $BiVO_4$, and the *x*GOB nanocomposites. No impurity/secondary peaks and

phase transitions were observed, which confirms the purity of the as-synthesized products as well as crystalline phases. The characteristic peak of GO (International Centre for Diffraction Data-ICDD:00-065-1528) around a 2θ value of 10.8° was observed, which corresponds to the (001) plane. Besides, the sharp peak at 2θ = 26.14° that corresponds to interlayer distance (002) between sp2 carbon layers, linked to the crystallization peak of residual graphite oxide that was not oxidized during the process [19,20]. The interplanar or d-spacing of GO was found to be 0.656 Å for d_{001} [14].

Pure TiO_2 prepared through $TiCl_4$ hydrolysis showed an XRD diffraction pattern of anatase phase (ICDD:03-065-5714) with the tetragonal structure without other TiO_2 polymorphs [21–24]. Pure $BiVO_4$ (ICDD:01-075-1866) synthesized by sol-gel route displayed monoclinic scheelite phase [25,26] and the iconic twin peaks of $BiVO_4$ [27]. The GO peaks were not observed in the XRD pattern of nanocomposites (Fig 4.2 (a) and (b)) due to the overlapping intense peaks of anatase/monoclinic scheelite phase or the low detection limit of XRD technique or maybe by the reduction of GO to reduced GO [22,28]. Still, the formed MOx nanocomposites were highly crystalline with no phase transformation even after the physical synthesis route. In both nanocomposites, the intensity of the (101) plane of GOT and the (103) plane of GOB has significantly reduced with increasing GO content, resulting in the crystallinity enhancement as mentioned in Table 1. Conversely, for 2.5 GOT and GOB, the crystallinity has been increased, which can be assumed due to the increment in the GO content [29].

The crystallinity obtained for 1.5 GOT and GOB (Table 4.1) can result in boosted photocatalytic disinfection application. This is due to the increment of the surface area, light absorption, surface energy, and lattice distortion of the formed nanocomposites. Moreover, the energy of photo-generated radicals is increased with the decrement of the crystallite size, in association to the quantum confinement effect, thereby enhancing the photocatalytic disinfection process [30]. Fig 4.2 (a*) and Fig 4.2 (b*) show the enlarged view of the (101) anatase peak in GOT and (103) monoclinic phase of GOB nanocomposites. In GOT nanocomposite, there was a shift towards a higher 2θ angle, while a shift to lower 2θ angle in 0.5 GOB, and 1.5 GOB nanocomposites; for 2.5 GOB (the shift occurred toward higher angles). These results can be attributed

to the decrement of the lattice parameters by increasing the GO content. The crystallite size was obtained using the Scherrer equation [31].

$$D = \frac{k\lambda}{\beta cos\theta}$$
Eq: (4.1)

Where, K - Scherrer constant (0.94 for spherical particles),

λ - Wavelength of Cu – Kα_1 (approximately 1.5405 Å),

β - Full width at half maximum (FWHM) value,

θ - Bragg's angle (in radians).

Table 4.1. Structural and optical characterization of xGOT and xGOB nanocomposites and their components

Samples	Crystallite size (nm)	Band gap (eV)
GO	7.7	-
TiO_2	14.8	3.15
$BiVO_4$	11.0	2.43
GOT		
0.5	15.2	3.04
1.5	11.9	3.01
2.5	16.1	2.99
GOB		
0.5	10.4	2.41
1.5	9.0	2.39
2.5	12.3	2.38
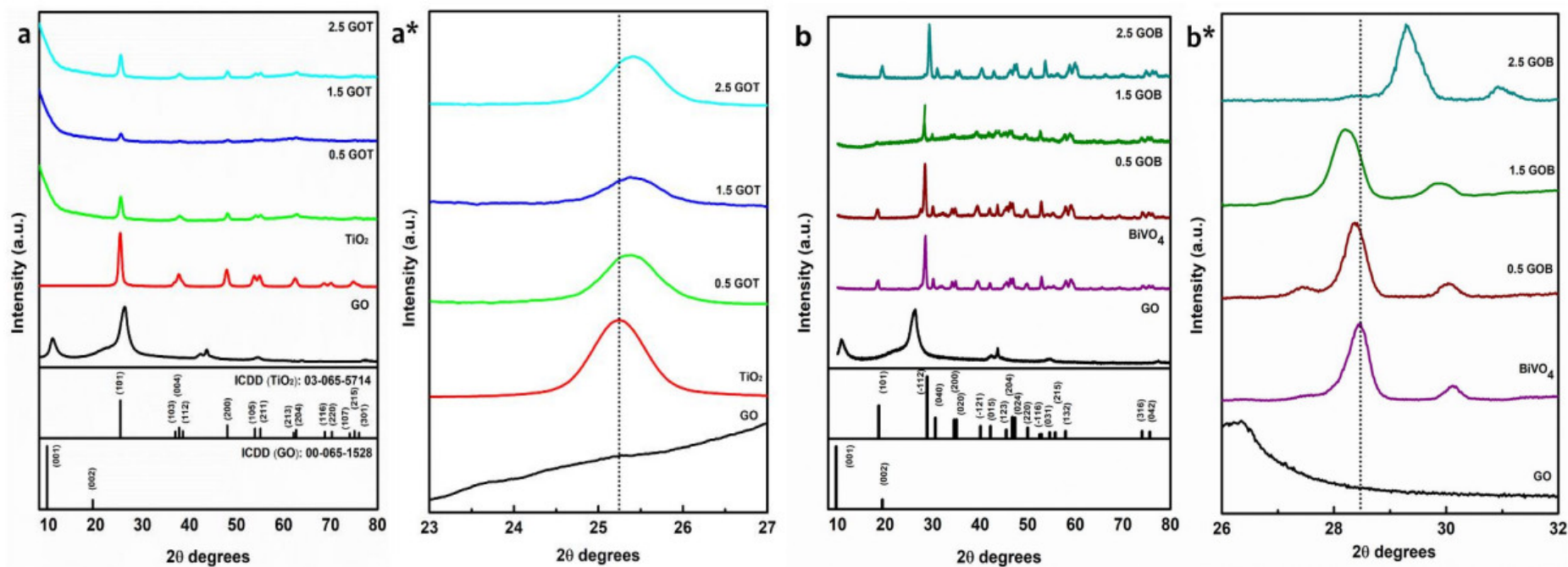
Fig 4.2: XRD patterns of (a) TiO₂ and its various nanocomposites, (a*) scanned (101) plane of GOT nanocomposites, (b) BiVO₄ and its different wt.% nanocomposites, (b*) scanned (103) plane of GOB nanocomposites.

4.2.2 Raman studies

Raman spectroscopy is one of the powerful techniques to analyze the crystal structure of carbon-based materials [32]. In oxide nanoparticles, several factors like lattice dynamics modifications are detailed by the transitional invariance, which is broken up due to the extension in the crystal structure (1-100 nm range), along with the explanation of atomic vibrations in a domain of that kind in terms of phonons is not possible with a well-defined wave vector and this forms the basis for the phonon confinement model (PCM). PCM was developed for the description of the intensity in first-order Raman scattering of semiconductor nanocrystals [33,34].

Raman spectra are based on vibrational modes, and therefore, graphene possesses six normal modes and two atoms per unit cell at Brillouin zone center (Γ), where (Γ) = $A_{2u} + B_{2g} + E_{1u} + E_{2g}$, in which E_{2g} phonons are more active. The three prominent peaks in the Raman spectra of graphene are D peak at 1320-1350 cm^{-1}, G peak at 1580-1605 cm^{-1}, and 2D or G' peak at 2640-2680 cm^{-1}, sometimes at 1602-1625 cm^{-1}. Defect and disorder level within the graphite layers is associated with the D mode, and the two-dimensional hexagonal lattice is related to G and 2D bands [35]. G band can be attributed to the first order scattering of the E_{2g} phonon of sp^2 carbon atoms. D band is the result of distension in the hexagonal symmetry of graphitic lattice due to the edge defects, internal structural defects, and dangling bonds, whereas the G band is attributed to the in-plane stretching motion of symmetric motion or the symmetric sp^2 C-C bonds. The narrowing of the G band is because there are fewer functional groups in the atomic lattice [36,37]. These peaks form the characteristic feature for the graphene-based materials, but slight variation can be observed for the parameters like linewidths, intensities, and peak position for the graphene-based material because of graphene (support) interaction, heteroatom doping, strain, number of graphene layers, etc.

During the oxidation of graphite to form graphite oxide, the G band may get broadened, and the D band is narrowed, or the intensity is increased, which are attributed to the considerable decrease in the size of in-plane sp^2 domains due to the introduction of oxygen-containing groups. Also, the shift in the G band is ascribed to the presence of isolated double bonds that prevails on the carbon network of graphite oxide [38]. The intensity ratio of D and G peaks, *i.e.*, I_D/I_G is calculated for the comparison of structural

defects. Raman spectroscopy is used for the study of the level of alteration on the GO surface. As per the group theory, TiO_2 anatase possesses six Raman active modes, namely, E_g (144 cm^{-1}), E_g (197 cm^{-1}), B_{1g} (399 cm^{-1}), B_{1g} (513 cm^{-1}), A_{1g} (519 cm^{-1}), and E_g (638.2 cm^{-1}) [39–41]. When there is a shift and broadening of the Raman peak (144 cm^{-1}), it can be due to the surface pressure or confinement effects. The high-intensity peak at 144 cm^{-1} can be the result of the long-range order of the anatase. Broadening of the peak indicates the contribution of phonons away from the Brillouin zone center [42].

TiO_2 anatase nanoparticles are well characterized and studied by Raman scattering spectroscopy. The size effects are interpreted by phonon confinement or non-stoichiometry [40,43–45]. $BiVO_4$ nanoparticles are excited by a red laser with a wavelength of 648 nm, and the typical Raman vibrational bands are 210 cm^{-1}, 324 cm^{-1}, 366 cm^{-1}, 640 cm^{-1}, 710 cm^{-1}, and 826 cm^{-1}. Raman band at 210 cm^{-1} can provide the structural information of $BiVO_4$, while bands centered at 324 cm^{-1} and 366 cm^{-1} are the asymmetric and symmetric VO_4 tetrahedron formations, respectively. The asymmetric stretching vibration of the shorter V-O bond is assigned at 640 cm^{-1}. Bands centered at 710 $cm^{-1,}$ and 826 cm^{-1} are the stretching modes of two vibrational modes of V-O bonds. The information regarding the variations in the structure is given by the two bands, 710 and 826 cm^{-1} [46–48].

The D (disordered or sp^3 defect) peak in the GO spectrum around $\sim$1350 cm^{-1} is due to the occurrence of –OH and epoxy groups, while G (graphitic or sp^2 defect) peak $\sim$of 1600 cm^{-1} is attributed to C-C and C≡C bonds. The intensity ratio of D (I_D) and G (I_G) peaks in carbon structures indicates the structure disorders (I_D/I_G>1, the structure is more disordered). The I_D/I_G ratio (around 1.01) proved that they had got a multilayer structure. The Raman spectra of xGOT nanocomposites are presented in Fig 4.3 (a) with the specific vibration modes located around 141 cm^{-1} (E_g), 389 cm^{-1} (B_{1g}), 512.38 cm^{-1} (A_{1g}+B_{1g}), and 636 cm^{-1} (E_g), indicating the presence of the anatase phase in all the composites [49]. Due to the minor redshift of TiO_2 anatase absorption band in the composites towards the visible region in the electromagnetic spectrum, a better resonance conditioning of Raman scattering was observed at the excitation at approximately 512 nm, providing an enhanced Raman signal. Maintaining similar vibrational mode positions for TiO_2 anatase and GOT composites showed that the

redshift of absorption edge was due to the bandgap narrowing compared to TiO_2 (see Fig 4.3 (a)) [50][51]. Moreover, all the spectra representing the D and G characteristic bands of GO, respectively, with negligible band shift were observed (Fig 4.3 (a*))[36]. Raman spectra modes (Fig 4.3 (b)) revealed the monoclinic phase of the $BiVO_4$ nanoparticles, where the stretching and bending vibrations, modes result from the VO_4^{3-} tetrahedron. In the spectra, the intense peak at 780.7 cm^{-1} was dominated by the symmetric V-O stretching mode (v_s), and a weak shoulder at 661.1 cm^{-1} was associated to the antisymmetric V-O stretching mode (v_{as}). 314.99 cm^{-1} was associated to the symmetric bending mode (δ_s $(VO_4)^{3-}$), and the peak at 280.11 cm^{-1}, was related to the antisymmetric bending mode (δ_{as} $(VO_4)^{3-}$). The external rotational mode was observed at 235 cm^{-1}, which belongs to the vanadate ion. The twin band, δ_s $(VO_4)^{3-}$ and δ_{as} $(VO_4)^{3-}$ was merged, showing a single peak as the GO content is increased due to the phase transition from monoclinic to tetragonal. The decrease in the intense peak v_s. was attributed to the increase in the loading of GO [52].

All these modes were typical for pure monoclinic scheelite phase of $BiVO_4$ nanoparticles [53]. The presence of the D and G band of GO in the Raman spectra of nanocomposites confirmed the presence of GO which was not observed in the XRD pattern proving the sensitive analysis by Raman spectroscopy. A shift is kept at the positions of D and G bands in the GOB composites (Fig 4.3 (b*)) when GO content was increased [54–56]. This was clear evidence on the nanocomposite formation in both cases without any crystalline phase changes.

4.2.3 UV-Vis DRS analysis

Due to the presence of π-π* sp^2 clustered C=C chromophore units, a predominant absorption maximum was observed at approximately 230 nm. At about 300 nm, the presence of a shoulder was shown due to its n-π* plasmon peak of autochrome, which has got carboxyl, carbonyl, and hydroxyl functional groups. Absorption at approximately 212 nm is caused by the π-π* aromatic transition of the C-C bond, and this defines the sp^3 feature of GO. There can be a change in this behavior if there is a reduction in the oxygen groups of graphene oxide [57,58]. TiO_2 was found to be a large bandgap semiconductor, with a bandgap value of 3.2 eV. The valence band of TiO_2 consists of 2p orbitals where oxygen is hybridized with 3d orbitals of titanium, and the conduction band is composed of 3d orbitals of titanium
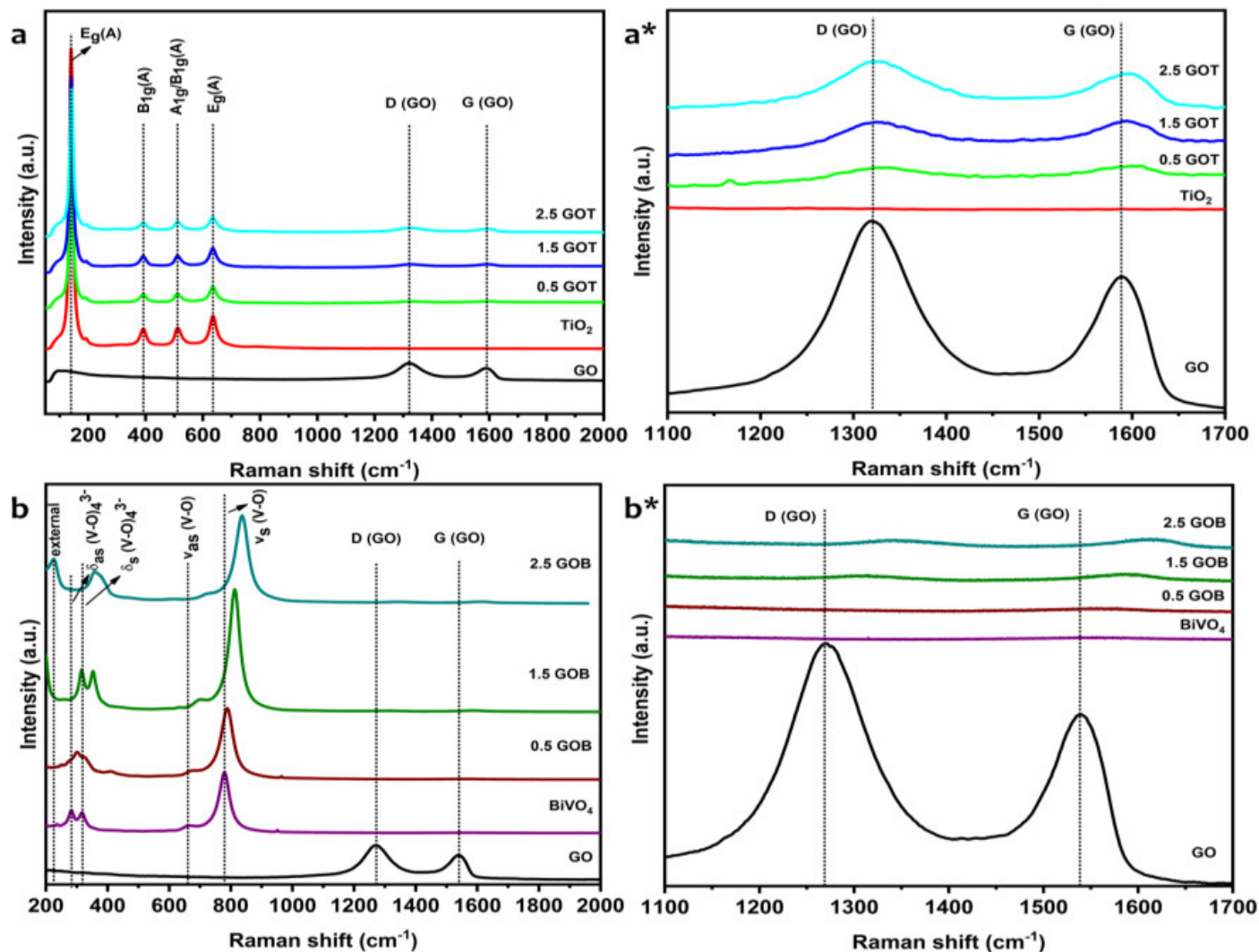
Fig 4.3: Raman spectra of pristine GO, TiO₂ and BiVO₄ nanostructures and (a) 0.5, 1.5, 2.5 GOT nanocomposites, (b) 0.5, 1.5, 2.5 GOB nanocomposites, D and G band of GO region-of-interest from 1100–1700 cm⁻¹ (a*) GOT and (b*) GOB nanocomposites.

When TiO$_2$ is irradiated with UV light, the valence band electrons get excited towards the conduction band, thereby leaving behind the photo-holes. Due to the difference in their pairing, the transition probability of these electrons decreases to the valence band, thus reducing the probability of electron-hole pair recombination [59–62].

BiVO$_4$ has better visible light absorbance due to the low bandgap caused by the lone pair distribution among the Bi 6s orbital. Given the overlap of O 2p and Bi 6s valence band orbitals, BiVO$_4$ possesses improved mobility of photo-generated charge carriers [63,64].

The UV-Visible DRS spectra of as-synthesized TiO$_2$ and BiVO$_4$ nanoparticles, and the GOT and GOB ratios nanocomposites represented in Fig 4.4 (a) and (b). The plot denotes the relationship between $(\alpha h\nu)^{1/2}$ versus photon energy (eV), and the bandgap is sketched according to the equation (3) [65,66]

$$\alpha h\nu = B(h\nu - Ebg)^2 \qquad (5.2)$$

Where, $\alpha = (1-R)^2/2R$

$\qquad$ R - Reflectance of a solid layer

$\qquad$ B - Absorption coefficient

$\qquad$ hν - Photon energy in eV (1239/λ)
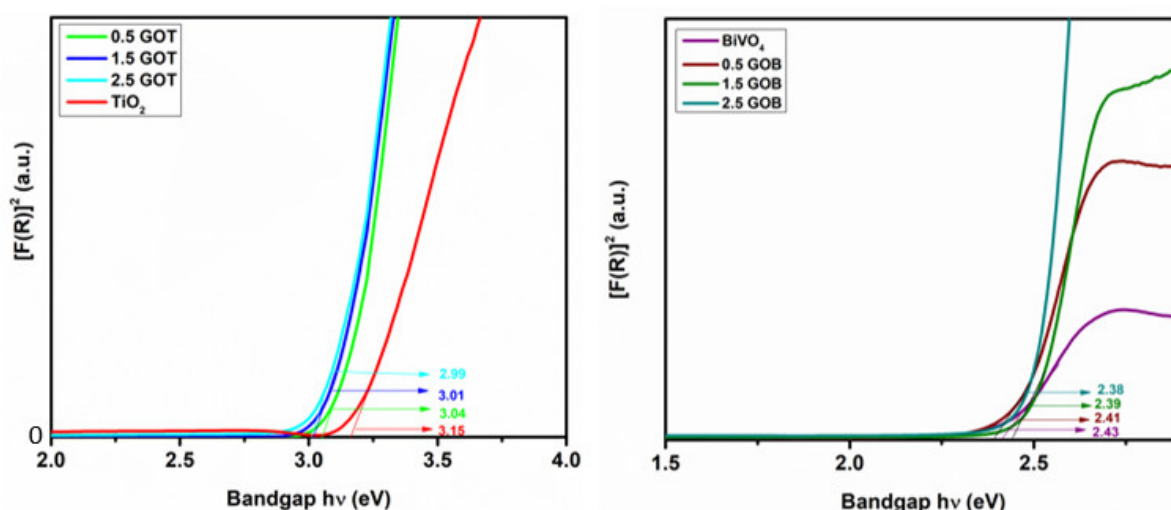
Fig 4.4: UV-Vis-DRS spectra of pristine and nanocomposites
(a) TiO$_2$, 0.5, 1.5, 2.5 GOT, (b) BiVO$_4$, 0.5, 1.5, 2.5 GOB .

It is observed that the typical absorption edges of GOT were shifted toward the visible region, giving rise to a bathochromic phenomenon. The visible-light absorption of composites increased compared to pristine TiO_2 nanoparticles, due to the interaction of Ti ions with oxygen groups (Table 4.1). The bandgap of GOT nanocomposites leads to the broad coverage of UV-Visible light and suppresses the recombination rate of electron-hole pairs. The bandgap was estimated by extrapolating the linear portion of the plot to the photon energy axis. The optical bandgap values of GOT were decreased from 3.09 to 2.98 eV as the content of GO increased in the composite. The reduction of bandgap in the composite is due to the mutual interaction between unpaired electrons of GO and photo-electron present on the surface of TiO_2, which is favorable for the enhanced photocatalytic activity (Fig 4.4 (a)) [51]. The bandgap value of $BiVO_4$ was 2.49 eV, estimated using the Kubelka-Munk function. It was observed that the bandgap values of GOB nanocomposites shifted a little lower (bathochromic shift or redshift) when compared with pure $BiVO_4$ (Table 1). The bandgap values were decreased with the increment of the GO content in the composites.(Fig 4.4 (b)) [53].

4.2.4 Morphological analysis
4.2.4 (a) SEM and elemental mapping

The GO showed the wrinkle-curtain-like structure, where the folding can be due to the stacking (Fig 4.5). In MOx nanoparticles, the particle aggregation and bulkiness of the material were seen but with the uniform distribution of the corresponding elements (carbon-C, oxygen-O, titanium-Ti, bismuth-Bi, vanadium-V).

Figs 4.6 and 4.7 represent the GOT and GOB nanocomposites with different loading ratios, showing the decoration of MOx nanoparticles onto the GO sheets evenly distributed. When the MOx loading were increased from 0.5 to 2.5, the detection or exposure of C element signal of the GO decreases, proving the MOx nanoparticles homogeneous interaction. In both the composites, particularly 2.5 GOT/B, the distribution of nanoparticles almost covered the GO sheets, thereby giving enhanced signals for the nanoparticles [67–70].
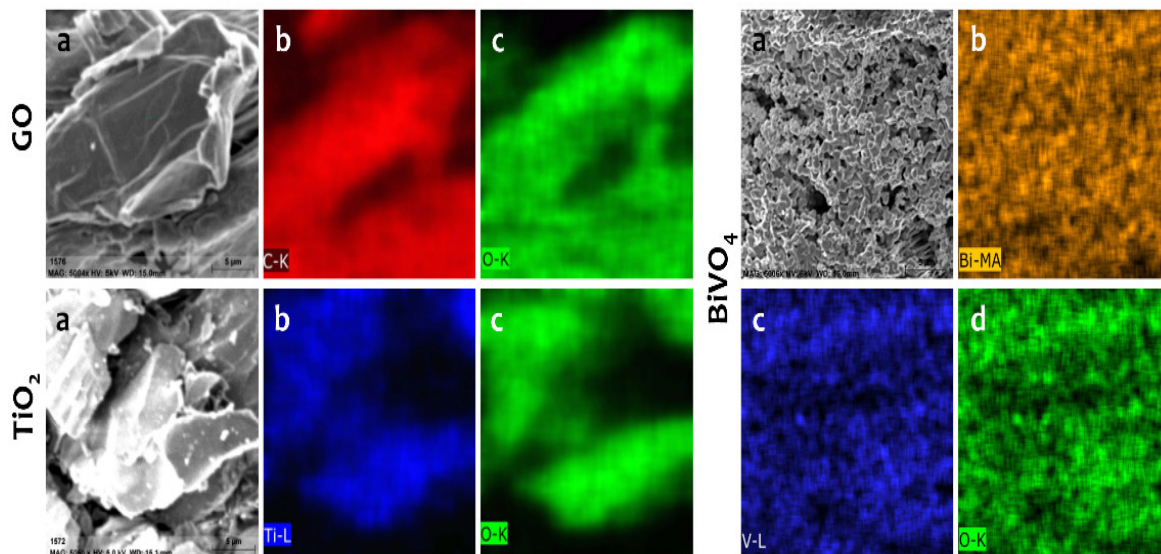
Fig 4.5: SEM images and the corresponding elemental mapping of pristine nanostructures, such as GO, TiO₂, BiVO₄
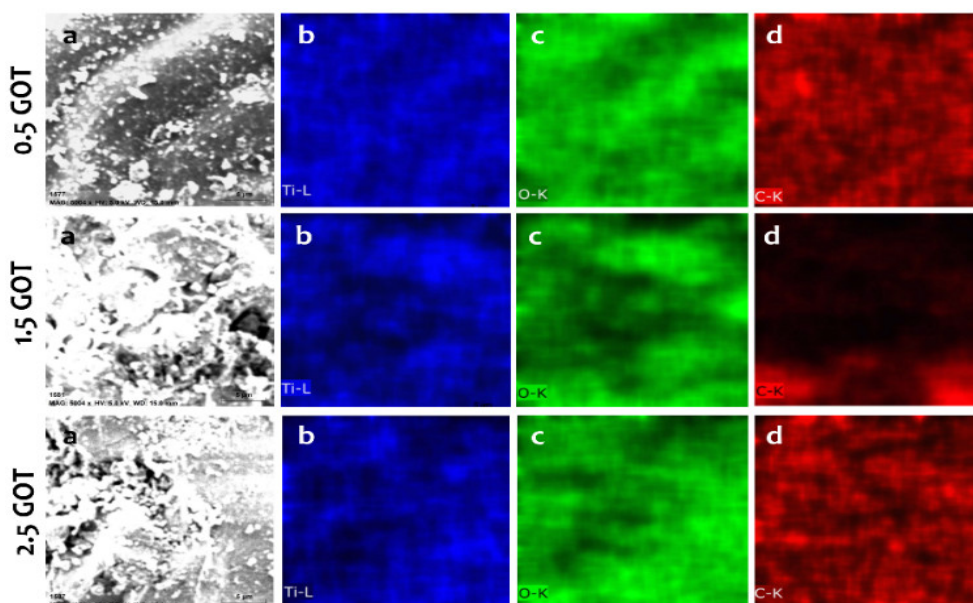
Fig 4.6: SEM images and the corresponding elemental mapping of 0.5, 1.5, and 2.5 wt.% of GOT nanocomposites.
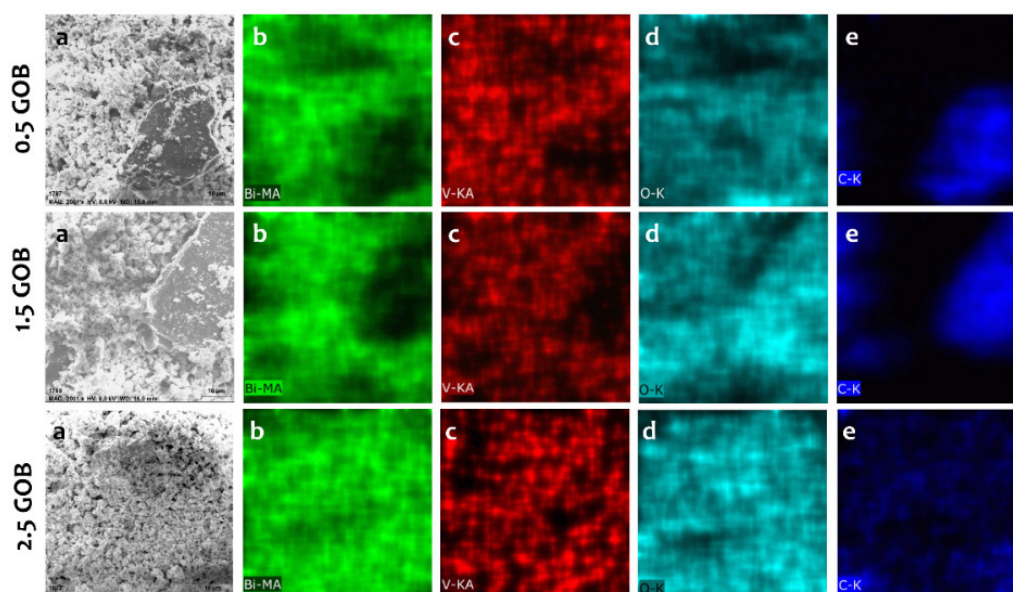
Fig 4.7: SEM images and the corresponding elemental mapping of 0.5, 1.5, and 2.5 wt.% of GOB nanocomposites.

The elemental analysis confirmed the GO/MOx nanocomposite formation, depending on the wt.% ratios with no other impurities. These results were consistent with the optical and structural characterizations discussed in the above sections.

4.2.4 (b) TEM micrographs
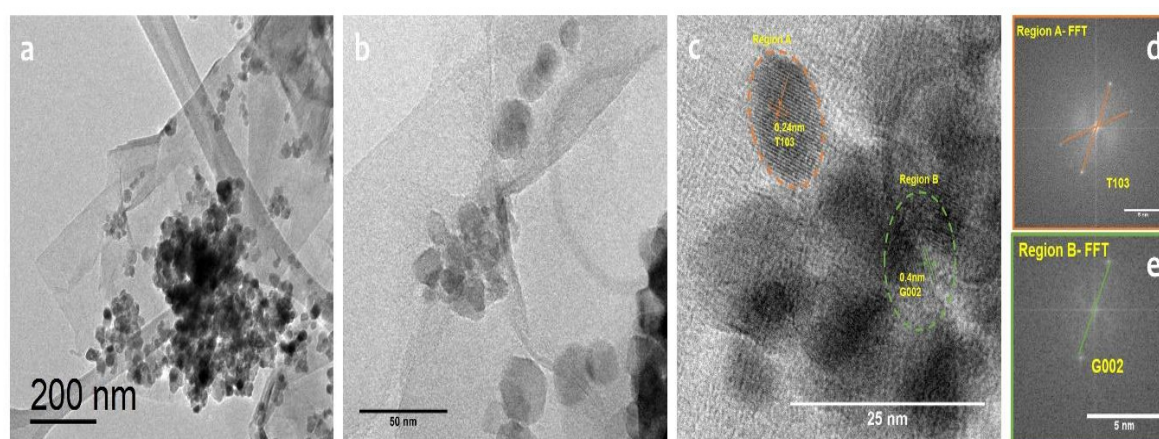
Fig 4.8: (a), (b) Low-resolution, (c) high-resolution TEM image, (d) and (e) corresponding FFT pattern of 1.5 GOT, respectively.

The morphological features of both 1.5 GOT and GOB were explored by TEM, and the obtained micrographs are shown in Fig 4.8 and 4.9 (a)-(e). It was confirmed that the GO has got a layered lamellar structure with a flat and smooth surface, signifying its perfect exfoliation [71]. Both micrographs revealed the uniform decoration of highly dense MO_x nanoparticles (Fig 4.8 (a) and 4.9 (a)) over the GO sheets. The dark contrast attributes to MO_x nanoparticles, while the lighter region was responsible for the GO sheets [72]. The nanoparticles had a spherical appearance, as seen in Fig 4.8 (a) and (b) for TiO_2 nanoparticles and in Fig 4.9 (a) and (b) for $BiVO_4$ nanoparticles. Based on the calculated lattice fringes, the planes of the composites were confirmed. The fast-Fourier-transform (FFT) from the marked oval area exhibited the reflections typical to the respective 1.5 GOT (Fig 4.8 (c)-(e)) and 1.5 GOB (Fig 4.9 (c)-(e)). From the high-resolution TEM analysis, the size of TiO_2 nanoparticles was found to be 13-17 nm, while for $BiVO_4$ nanoparticles, it was around 6-8 nm (Fig 4.8 (c) and 4.9 (c)). The d-spacing of the adjacent fringes in 1.5 GOT was 0.24 nm, which was associated with (103) *hkl* plane of anatase and the (002) plane of GO (Fig 4.8 (d) and (e)). In the case of 1.5 GOB, d-spacing of 0.3 nm indexed for the (013) plane of the monoclinic scheelite phase (Fig 4.9 (d) and (e)), while 0.39 nm was consistent with the (002) plane of GO. All the planes from both 1.5 GOT and 1.5 GOB were identified by the standard ICDD files that were referred from XRD analysis, *i.e.*, ICDD:00-065-1528 (GO), ICDD:03-065-5714 (TiO_2), and ICDD:01-075-1866 ($BiVO_4$). The obtained results were in good understanding with XRD diffractogram, which proposes the crystallite phases and the intercalation of MO_x nanoparticles on the GO sheet surface [73–76].
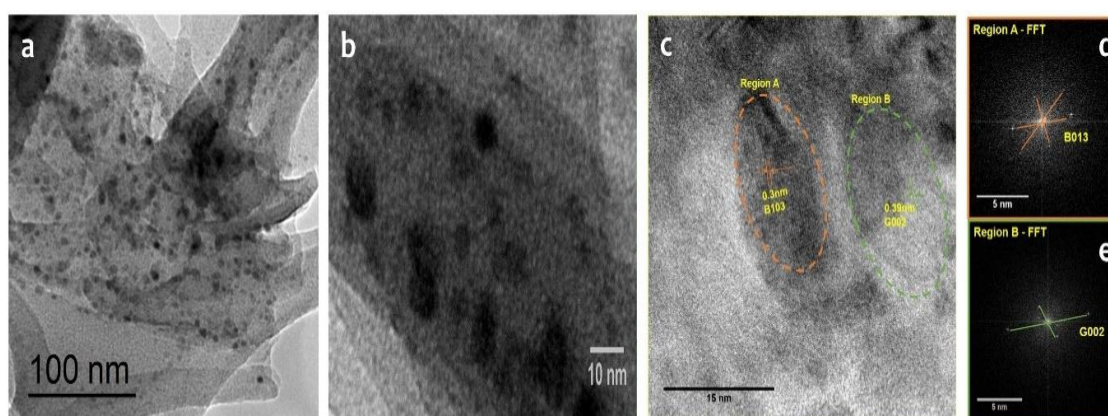
Fig 4.9: (a), (b) Low-resolution, (c) high-resolution TEM image, (d) and (e) corresponding FFT pattern of 1.5 GOB, respectively

4.2.4 (c) EDAX analysis
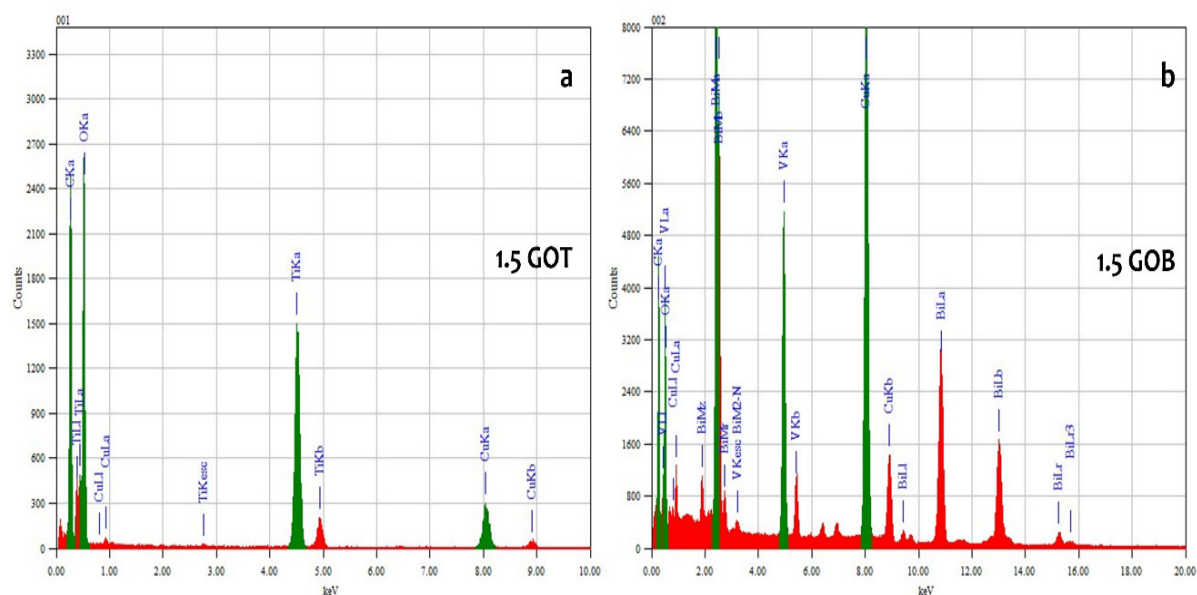
Fig 4.10: Energy dispersive analysis of (a) 1.5 GOT (b) 1.5 GOB.

From Fig 4.10, EDAX spectra of 1.5 GOT (a) and 1.5 GOB (b) are depicted. The purity and elemental composition of the 1.5 GOT, and 1.5 GOB nanocomposites was confirmed [77]. The results showed the elements Ti, C, and O, from 1.5 GOT and Bi, V, C, and O elements in the 1.5 GOB nanocomposite [72]. The signal corresponding to C is from GO, and signals of Ti and O are originated from TiO_2, assuring the formation of GOT nanocomposite. In contrast, signals attributed to Bi, V, and O of $BiVO_4$ and C of GO contribute to the construction of GOB nanocomposite [78]. This confirmed the successful formation of nanocomposites and their stability. The copper-Cu was also detected in both the spectra, due to the Cu grid used for the sample analysis.

4.2.5 Applications of nanocomposites

4.2.5 (a) Photocatalytic disinfection experiments

Fig 4.11 (a) and (b) depict the visible-light-induced photocatalytic disinfection of water using the nanocomposites after 120 min (see Chapter 2, section 2.5.1). During photolysis, nearly 15% of inactivation was observed in 60 min, whereas with TiO_2 nanoparticles, around 20% disinfection was seen in 30 min. Interestingly, in the presence of nanocomposites, disinfection activity was enhanced by more than 60%, which was influenced by the loading of GO and TiO_2. Among the three GOT

nanocomposite ratios, 1.5 GOT showed better bactericidal activity towards *E. coli K12,* resulting in more than 99% disinfection in 30 min, which was decreased when GO content was increased in the nanocomposite (Fig 4.11 (a)). In logarithmic terms, 3-log reduction of *E. coli K12* was observed using 1.5 GOT.
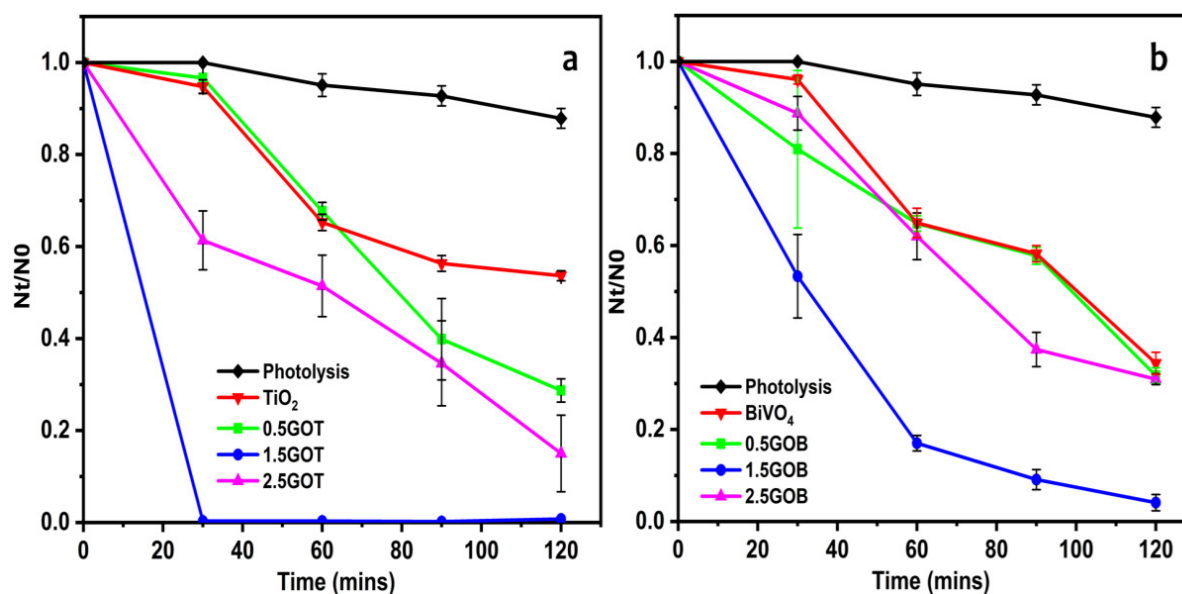
Fig 4.11: E. coli K12 survival after photocatalytic disinfection is depicted as the ratio of viable to total cells (N_t/N_0). (a) GOT nanocomposites (b) GOB nanocomposites.

The antibacterial ability of $BiVO_4$ and the three different GOB nanocomposites was also evaluated, and the data is represented in Fig 4.11 (b). It was observed that *E. coli K12* was not killed in the absence of photocatalyst, while the addition of $BiVO_4$ resulted in the inactivation of bacterial cells. However, by incorporating GO into $BiVO_4$ to form GOB nanocomposites, there was a significant decrease in the bacterial concentration, giving rise to 89% of disinfection by 1.5 GOB in 60 min. This means, 1-log reduction of *E. coli K12* was observed for 1.5 GOB. The low activity of $BiVO_4$, compared to that observed with nanocomposites, can be due to the fast recombination of photo-generated electron-hole pairs in the semiconductor [79]. The EMB agar plate images (aliquots taken after 60 min) provide the visual confirmation of the disinfection effect of the nanoparticles (Fig 4.12 (a)-(d)) and the nanocomposites (Fig 4.13 (a)-(f)).
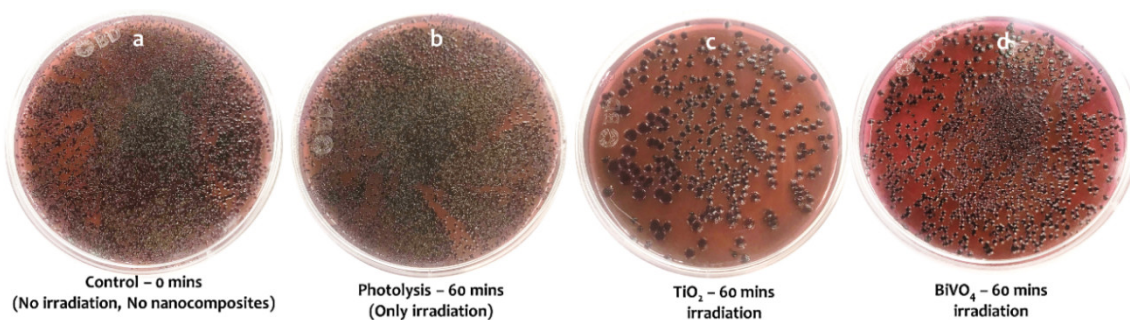
Fig 4.12: Photographs of photocatalytic disinfectant activity of pristine nanoparticle and the corresponding E. coli K12 colonies on EMB agar plate
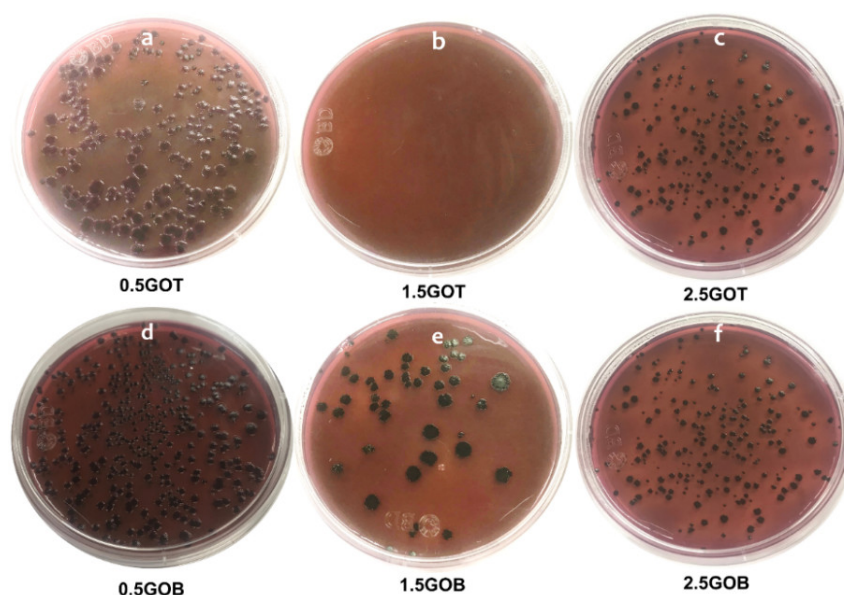
Fig 4.13: Images of E. coli K12 colonies on EMB agar medium after irradiation with GO/MOx nanocomposites, respectively.

After 120 min of light exposure, no significant disinfection activity was found for any of the composites. It is possible that, the availability of active sites might have reduced after a certain period. The decrement in the photocatalytic activity can be ascribed to excess GO, which can increase the opacity and light scattering of the nanocomposites, impeding the MOx nanoparticles from light absorption. A decrease in the activity can also be because of the short half-life period of radicals generated, usually in the order of microseconds or ROS formed in a low concentration. As a result, bacteria can have a defense mechanism to protect themselves, thereby causing bacterial recovery and re-growth [80–83].
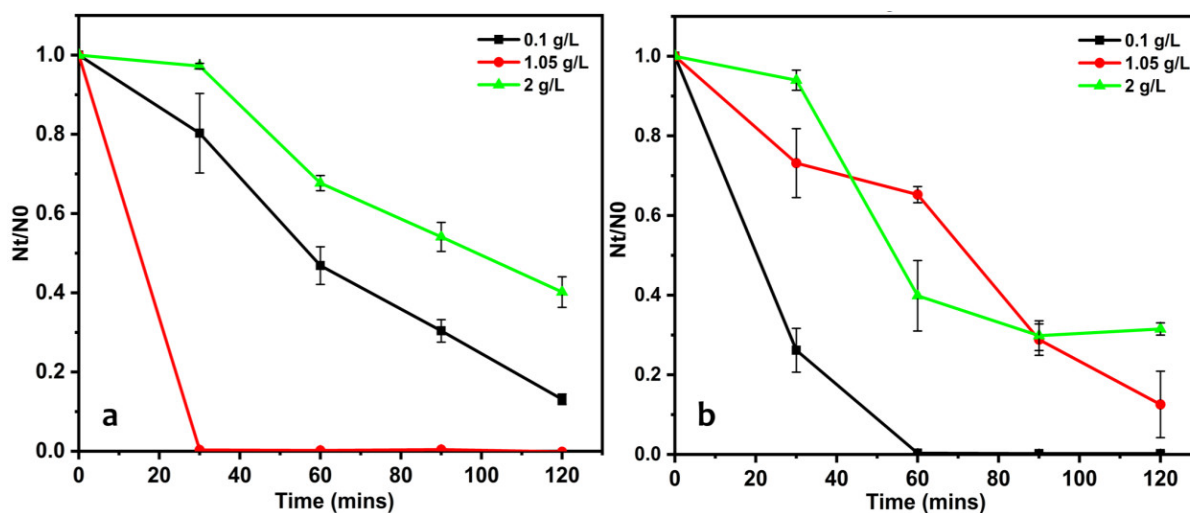
Fig 4.14: Effect of dosage on photocatalytic inactivation of E.coli K12 by
(a) 1.5 GOT (b) 1.5 GOB

Among the three different GOT composites, 99.9% in 30 min was spotted for 1.5 GOT nanocomposite with a dosage of 1.05 g/L (Fig 4.14 (a)), and amongst GOB composites, 80% of disinfection activity in 30 min was proved for 1.5 GOB nanocomposite for a dosage of 0.1 g/L (Fig 4.14 (b)) for a bacterial concentration of 10^7 CFU/mL. An excellent and enhanced disinfection activity of 1.5 GOT and GOB nanocomposites under visible-light irradiation might be associated with a broad absorption range of light and effective separation of photo-generated electron-hole pairs, which is contributed by GO as it is both an electron acceptor and transporter [76]. Apart from the other facts, high crystallinity enhances photocatalytic efficiency, confirmed by the XRD (Fig 4.2). Therefore, in conclusion, 1.5 GOT with a dosage of 1.05 g/L, and 1.5 GOB with a dosage of 0.1 g/L were chosen for further studies.

4.2.5 (b) Bacterial morphology studies

The damage of bacterial cells concerning the various ROS species upon contact with 1.5 GOT and GOB was investigated by TEM. Electron micrographs show a dramatic change between control bacteria and nano catalyst-treated ones. Fig 4.15 (a) displays an intact and well-defined morphology with a characteristic bacterial shape. The electron-dense region corresponds to the cellular components, including nucleic acids and proteins, whereas the electron-lucent refers to the cell wall or lipopolysaccharide outer membrane.
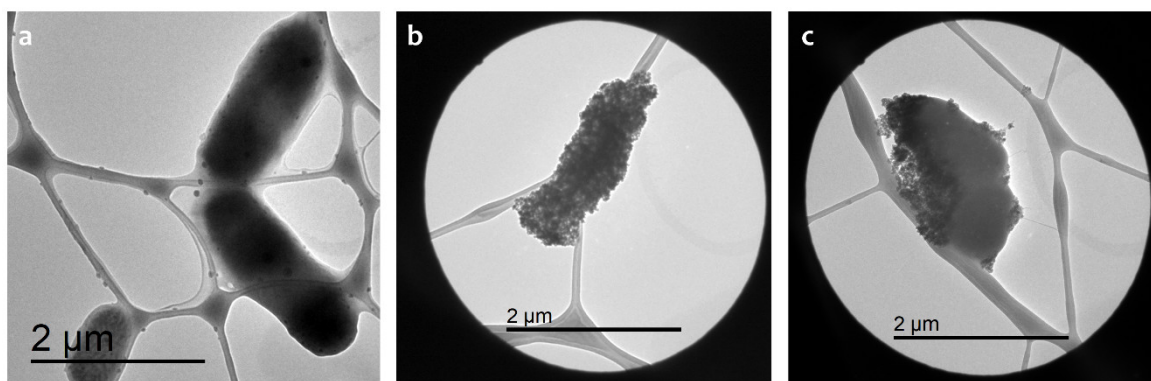
Fig 4.15: TEM micrographs of (a) E. coli K12 control, bacteria treated with (b) 1.5 GOT (c) 1.5 GOB nanocomposite after 60 min

As presented in Fig 4.15 (b) and (c), nano catalyst treated *E. coli K12* by 1.5 GOT, and GOB resulted in an irregular shape after 60 min of light irradiation with significant structural changes clear interaction of composites. TEM studies depicted severe bacterial and cell wall damage suggesting the inactivation by photocatalytic activity. For instance, the decomposition of the cell membrane leads to the leakage of internal cell components resulting in the cell becoming white or translucent. The two-way synergistic mechanism of nanocomposites causes this. The MOx nanoparticles produce ROS, while GO can act as nano-knives that penetrate into the bacterial cells, resulting in the membrane disruption [84,85]. Thus, the TEM investigation proved the impact of GO/MOx composite altering cell membrane permeability and intracellular leakage of components, killing bacteria cells.

4.2.5 (c) Scavenger studies

From the ROS scavenger study (see Chapter 2, section 2.5.2) of 1.5 GOT nanocomposite with the addition of chromium (VI), the photocatalytic disinfection was not affected. This proves that the role of e$^-$ for disinfection is low. Due to the addition of $C_6H_4O_2$ for the removal of $O_2\bullet^-$ radicals, the disinfection was inhibited more when compared to chromium (VI) scavenger, which shows that $O_2\bullet^-$ radicals have a crucial role in antibacterial activity. By adding isopropanol as $\bullet$OH radical scavenger, photocatalytic disinfection was inhibited completely, showing the importance of $\bullet$OH radical for the disinfection (Fig 4.16 (a)) [86]. Considering the 1.5 GOB nanocomposite, the photocatalytic inactivation was repressed by the addition of $C_6H_4O_2$ and CH_3CH_2OH, proving that the $O_2\bullet^-$ and $\bullet$OH radicals have a major role in the disinfection

process, where $O_2\bullet^-$ radical has more involvement than $\bullet OH$ radical while, no characteristic effect was shown after the addition of chromium (VI) indicating that the electrons did not have much role in the photocatalytic activity (Fig 4.16 (b)). The added scavengers can rapidly react with the ROS generated during the photocatalytic reaction, thereby reducing the disinfection rate of the targeted bacteria [87].
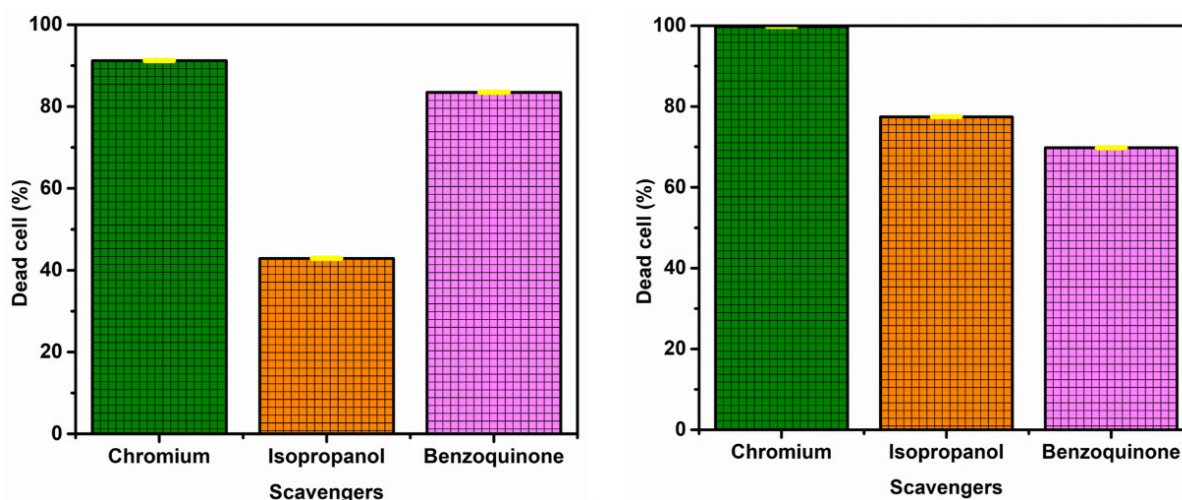
Fig 4.16: Effect of scavenger study on photocatalytic inactivation of E. coli K12 by (a) 1.5 GOT, (b) 1.5 GOB nanocomposites

4.2.5 (d) Mechanism of bacterial inactivation

Antibacterial performance of the composites through the photocatalytic process was confirmed through a disinfection kinetic study. Taking into consideration of various dosages of 1.5 GOT and 1.5 GOB nanocomposite, pseudo-first-order kinetics were observed, and they fitted very well into the Weibull deactivation function, which is given by the equation:

$$N_t / N_0 = e^{-kt} \qquad \textit{Eq: (4.3)}$$

where, N_t = Number of viable cells at time t (mins)

N_0 = Number of viable cells at time 0 (mins)

k = disinfection rate constant

The results also pointed out the importance of low dosage as there was a decrease in the reaction rate constant when the dosage was increased. This is due to two main reasons:

1) either the light that falls on the composite is not used, ultimately resulting in less ROS production, or

2) when the concentration of the nanocomposite is in excess, the light absorption increased resulting in the maximum generation of ROS that causes the suspension to be turbid. This turbidity blocks the utilization of photons, and therefore, a decline in photocatalytic efficiency is seen [86,88].

With the incident light absorption of a specific wavelength by the photocatalyst, a photoreduction phase occurred. Here, the electrons from the valence band (VB) excite towards the conduction band (CB), leaving behind the positive photo-holes (h^+). These electrons can convert the adsorbed oxygen to hydroxyl ($\bullet$OH) radicals and superoxide radicals ($O_2\bullet^-$). These generate highly reactive radicals and intermediates for the inactivation of the bacteria. A proposed mechanism of disinfection is depicted in Fig 4.17. The steps involved in the disinfection mechanism of GOT composite is as follows [89,90]:

$$TiO_2 \;+\; hv \;\rightarrow TiO_2\;(e^- \;+ h^+)$$
$$GO + e^- \;\rightarrow GO\;(e^{\cdot -})$$
$$H_2O + h^+ \;\rightarrow HO^\cdot + H^+$$
$$O_2 + TiO_2\;(e^-) \rightarrow O_2{}^{\cdot -}$$
$$O_2 + GO\;(e)^- \rightarrow O_2{}^{\cdot -}$$

$$O_2{}^{\cdot -} \;+\; H^+ \;\rightarrow HO_2{}^\cdot$$
$$H^+ \;+ O_2{}^{\cdot -} \;+\; HO_2{}^\cdot \rightarrow H_2O_2 + O_2$$
$$H_2O_2 + hv \;\rightarrow 2HO^\cdot$$
$$O_2{}^{\cdot -} \;+ HO^\cdot \;+ bacteria \;\rightarrow disinfection$$
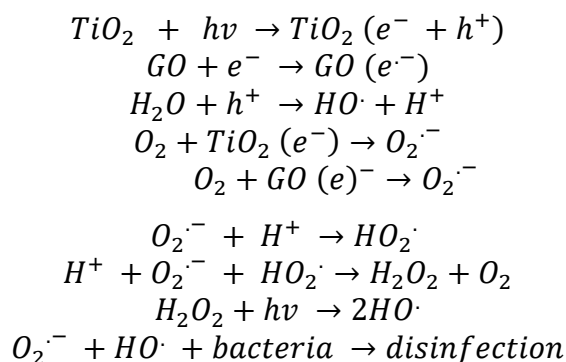
The mechanism followed for the GOB nanocomposites is below [91]:

$$BiVO_4 \;+\; hv \;\rightarrow BiVO_4\;(e^- \;+ h^+)$$
$$GO + e^- \;\rightarrow GO\;(e^{\cdot -})$$
$$H_2O + h^+ \;\rightarrow HO^\cdot + H^+$$
$$O_2 + BiVO_4\;(e^-) \rightarrow O_2{}^{\cdot -}$$
$$O_2 + GO\;(e)^- \rightarrow O_2{}^{\cdot -}$$

$$O_2{}^{\cdot -} \;+\; H^+ \;\rightarrow HO_2{}^\cdot$$
$$H^+ \;+ O_2{}^{\cdot -} \;+\; HO_2{}^\cdot \rightarrow H_2O_2 + O_2$$
$$H_2O_2 + hv \;\rightarrow 2HO^\cdot$$
$$O_2{}^{\cdot -} \;+ HO^\cdot \;+ bacteria \;\rightarrow disinfection$$
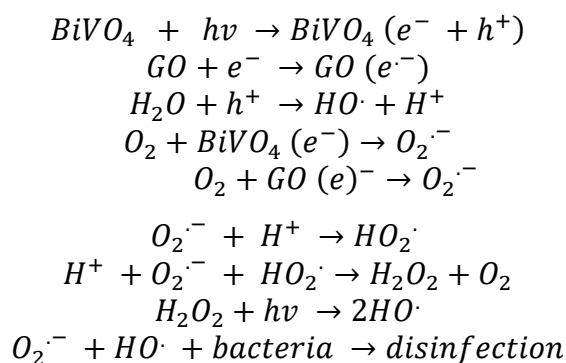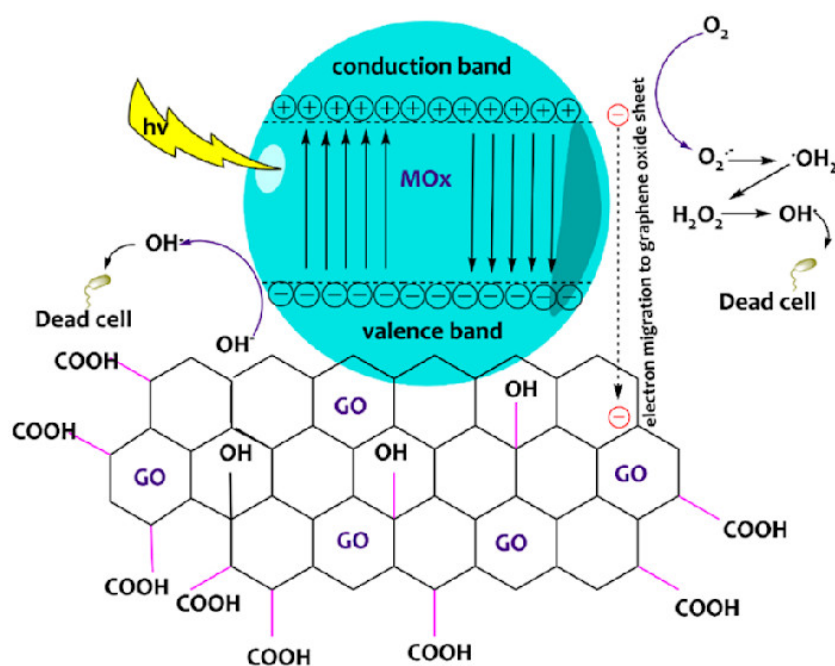
Fig 4.17: Mechanism of photocatalytic inactivation of E. coli K12 by 1.5 GO/MOx nanocomposites

The mechanism of photocatalytic disinfection of a GO/MO*x* nano catalyst can be explained in brief as follows. When 1.5 GOT/GOB and *E. coli K12* are in contact, the catalysts got adhered over the bacterial cells. Then, the catalyst gains energy greater than its bandgap to generate ROS, which causes seizures on the microbial cell membrane and thereby allows the entry of particles that possibly reacts with the major cellular components. Once the cellular integrity and the nucleic acid or protein synthesis system are damaged, the cells are lysed, leaving behind the cellular debris [92,93].

4.3 Conclusions

GO/MO*x* nano catalysts were synthesized by adopting a green, facile, eco-friendly, and cost-effective method (one-step blending). Several characterization techniques were performed to demonstrate the formation of the nanocomposites. The morphological analysis (TEM and EDAX) revealed the homogeneous distribution of TiO_2 and $BiVO_4$ nanoparticles decorated over the GO sheets, having a curtain-like structure with wrinkles. According to Raman results, the corresponding D and G bands were identified at around 1323 and 1600 cm^{-1}, respectively, indicating the crystalline

quality of the synthesized nanocomposites and strong evidence of composite formation. The band gap values were decreased with increasing the GO content as verified from the DRS analysis, suitable for the visible-light-driven photocatalysts, which is one of the foremost objectives of the incorporation of GO with TiO_2 or $BiVO_4$ nanoparticles. In addition to the formation of GOT and GOB nanocomposites, the enhancement in catalytic efficiency under illumination was reflected by the photocatalytic inactivation test. The disinfection was achieved to its maximum by 1.5 GOT at an optimum dosage of 1.05 g/L, providing 99.9% inactivation of *E. coli K12* (10^7 CFU/mL) in 30 min under visible-light irradiation, while for 1.5 GOB 89% of disinfection with a very low dosage of 0.1 g/L, for a bacterial concentration of 10^7 CFU/mL, in 60 min. The kinetics of photocatalytic inactivation fitted well with the Weibull deactivation function and followed pseudo-first-order kinetics. The antibacterial reaction using photocatalysts is confirmed with the interaction of ROS by scavenger study.

Moreover, it was found that •OH radicals are responsible for the disinfection, which is followed by O_2•$^-$ and e$^-$, while for GOB nanocomposites, it was found to be driven majorly by superoxide (O_2•$^-$) radicals. TEM image revealed the bacterial inactivation validation caused by 1.5 GOT and 1.5 GOB. There was a 3-log reduction and 1-log reduction of *E. coli K12* for 1.5 GOT and 1.5 GOB nanocomposites, respectively. This result demonstrates the synergistic behavior of GO and nanoparticles that could enhance the adherence towards the bacteria for boosted disinfection. The in-depth study delivered a new insight and provided great potentiality in various biomedical applications.

References

[1] P.C. Maness, S. Smolinski, D.M. Blake, Z. Huang, E.J. Wolfrum, W.A. Jacoby, Bactericidal activity of photocatalytic TiO2 reaction: Toward an understanding of its killing mechanism, Appl. Environ. Microbiol. 65 (1999) 4094–4098. https://doi.org/10.1128/aem.65.9.4094-4098.1999.

[2] J. Marugán, R. van Grieken, C. Sordo, C. Cruz, Kinetics of the photocatalytic disinfection of Escherichia coli suspensions, Appl. Catal. B Environ. 82 (2008) 27–36. https://doi.org/10.1016/j.apcatb.2008.01.002.

[3] A.G. Rincón, C. Pulgarin, Photocatalytical inactivation of E. coli: Effect of (continuous-intermittent) light intensity and of (suspended-fixed) TiO 2 concentration, Appl. Catal. B Environ. 44 (2003) 263–284. https://doi.org/10.1016/S0926-3373(03)00076-6.

[4] A.G. Rincón, C. Pulgarin, Bactericidal action of illuminated TiO2 on pure Escherichia coli and natural bacterial consortia: Post-irradiation events in the dark and assessment of the effective disinfection time, Appl. Catal. B Environ. 49 (2004) 99–112. https://doi.org/10.1016/j.apcatb.2003.11.013.

[5] D.M.A. Alrousan, P.S.M. Dunlop, T.A. McMurray, J.A. Byrne, Photocatalytic inactivation of E. coli in surface water using immobilised nanoparticle TiO2 films, Water Res. 43 (2009) 47–54. https://doi.org/10.1016/j.watres.2008.10.015.

[6] C. Srinivasan, N. Somasundaram, Bactericidal and detoxification effects of irradiated semiconductor catalyst, TiO2, Curr. Sci. 85 (2003) 1431–1438.

[7] K. Sunada, Y. Kikuchi, K. Hashimoto, A. Fujishima, Bactericidal and detoxification effects of TiO2 thin film photocatalysts, Environ. Sci. Technol. 32 (1998) 726–728. https://doi.org/10.1021/es970860o.

[8] R.J. Watts, S. Kong, M.P. Orr, G.C. Miller, B.E. Henry, Photocatalytic inactivation of coliform bacteria and viruses in secondary wastewater effluent, Water Res. 29 (1995) 95–100. https://doi.org/10.1016/0043-1354(94)E0122-M.

[9] C. Wei, W.Y. Lin, Z. Zainal, N.E. Williams, K. Zhu, A.P. Kruzlc, R.L. Smith, K. Rajeshwar, Bactericidal Activity of TiO2 Photocatalyst in Aqueous Media: Toward a Solar-Assisted Water Disinfection System, Environ. Sci. Technol. 28 (1994) 934–938. https://doi.org/10.1021/es00054a027.

[10] D.S. Bhatkhande, V.G. Pangarkar, A.A.C.M. Beenackers, Photocatalytic degradation for environmental applications - A review, J. Chem. Technol. Biotechnol. 77 (2002) 102–116. https://doi.org/10.1002/jctb.532.

[11] K. Rajeshwar, C.R. Chenthamarakshan, S. Goeringer, M. Djukic, Titania-based heterogeneous photocatalysis. Materials, mechanistic issues, and implications for environmental remediation, Pure Appl. Chem. 73 (2001) 1849–1860. https://doi.org/10.1351/pac200173121849.

[12] K. Kabra, R. Chaudhary, R.L. Sawhney, Treatment of hazardous organic and inorganic compounds through aqueous-phase photocatalysis: A review, Ind. Eng. Chem. Res. 43 (2004) 7683–7696. https://doi.org/10.1021/ie0498551.

[13] P.V. Laxma Reddy, B. Kavitha, P.A. Kumar Reddy, K.H. Kim, TiO2-based photocatalytic disinfection of microbes in aqueous media: A review, Environ. Res. 154 (2017) 296–303. https://doi.org/10.1016/j.envres.2017.01.018.

[14] V. Sivasankar, E. Senthil Kumar, R. Suresh Babu, S. Raghu, R.A. Kalaivani, Facile synthesis of graphene via sulfur intercalation and thermal exfoliation and its application in electrochemical sensing of L-Tryptophan, Rasayan J. Chem. 10 (2017) 1232–1241. https://doi.org/10.7324/RJC.2017.1041749.

[15] H.M. Ju, S.H. Choi, S.H. Huh, X-ray diffraction patterns of thermally-reduced graphenes, J. Korean Phys. Soc. 57 (2010) 1649–1652.

https://doi.org/10.3938/jkps.57.1649.

[16] J. Chen, B. Yao, C. Li, G. Shi, An improved Hummers method for eco-friendly synthesis of graphene oxide, Carbon N. Y. 64 (2013) 225–229. https://doi.org/10.1016/j.carbon.2013.07.055.

[17] S.M. Gupta, M. Tripathi, A review of TiO2 nanoparticles, Chinese Sci. Bull. 56 (2011) 1639–1657. https://doi.org/10.1007/s11434-011-4476-1.

[18] A. Malathi, J. Madhavan, M. Ashokkumar, P. Arunachalam, A review on BiVO4 photocatalyst: Activity enhancement methods for solar photocatalytic applications, Appl. Catal. A Gen. 555 (2018) 47–74. https://doi.org/10.1016/j.apcata.2018.02.010.

[19] S. Wang, J. Zhu, Y. Rao, B. Li, S. Zhao, H. Bai, J. Cui, Polydopamine modified graphene oxide-TiO2 nanofiller for reinforcing physical properties and anticorrosion performance ofwaterborne epoxy coatings, Appl. Sci. 9 (2019) 1–18. https://doi.org/10.3390/app9183760.

[20] K.A. Wanderley, A.M. Leite, G. Cardoso, A.M. Medeiros, C.L. Matos, R.C. Dutra, P.A.Z. Suarez, Graphene oxide and a GO/ZnO nanocomposite as catalysts for epoxy ring-opening of epoxidized soybean fatty acids methyl esters, Brazilian J. Chem. Eng. 36 (2019) 1165–1173. https://doi.org/10.1590/0104-6632.20190363s20180540.

[21] M. Stefan, O. Pana, C. Leostean, C. Bele, D. Silipas, M. Senila, E. Gautron, Synthesis and characterization of Fe3O4-TiO2core-shell nanoparticles, J. Appl. Phys. 116 (2014) 1902. https://doi.org/10.1063/1.4896070.

[22] K. Alamelu, V. Raja, L. Shiamala, B.M. Jaffar Ali, Biphasic TiO 2 nanoparticles decorated graphene nanosheets for visible light driven photocatalytic degradation of organic dyes, Appl. Surf. Sci. 430 (2018) 145–154. https://doi.org/10.1016/j.apsusc.2017.05.054.

[23] C. Chen, W. Cai, M. Long, B. Zhou, Y. Wu, D. Wu, Y. Feng, Synthesis of visible-light responsive graphene oxide/TiO2 composites with p/n heterojunction, ACS Nano. 4 (2010) 6425–6432. https://doi.org/10.1021/nn102130m.

[24] R.C. Pawar, C.S. Lee, Single-step sensitization of reduced graphene oxide sheets and CdS nanoparticles on ZnO nanorods as visible-light photocatalysts, Appl. Catal. B Environ. 144 (2014) 57–65. https://doi.org/10.1016/j.apcatb.2013.06.022.

[25] K. Pingmuang, N. Wetchakun, W. Kangwansupamonkon, K. Ounnunkad, B. Inceesungvorn, S. Phanichphant, Photocatalytic mineralization of organic acids over visible-light-driven Au/BiVO4 photocatalyst, Int. J. Photoenergy. 2013 (2013) 1–7. https://doi.org/10.1155/2013/943256.

[26] K.T. Drisya, M. Solís-López, J.J. Ríos-Ramírez, J.C. Durán-Álvarez, A. Rousseau, S. Velumani, R. Asomoza, A. Kassiba, A. Jantrania, H. Castaneda, Electronic and optical competence of TiO2/BiVO4 nanocomposites in the photocatalytic processes, Sci. Rep. 10 (2020) 1–16. https://doi.org/10.1038/s41598-020-69032-9.

[27] A. Wang, S. Shen, Y. Zhao, W. Wu, Preparation and characterizations of BiVO4/reduced graphene oxide nanocomposites with higher visible light reduction activities, J. Colloid Interface Sci. 445 (2015) 330–336. https://doi.org/10.1016/j.jcis.2015.01.017.

[28] S. Phanichphant, A. Nakaruk, K. Chansaenpak, D. Channei, Evaluating the photocatalytic efficiency of the BiVO4/rGO photocatalyst, Sci. Rep. 9 (2019) 1–9. https://doi.org/10.1038/s41598-019-52589-5.

[29] N. Lv, Y. Li, Z. Huang, T. Li, S. Ye, D.D. Dionysiou, X. Song, Synthesis of

GO/TiO2/Bi2WO6 nanocomposites with enhanced visible light photocatalytic degradation of ethylene, Appl. Catal. B Environ. 246 (2019) 303–311. https://doi.org/10.1016/j.apcatb.2019.01.068.

[30] X. Wang, L. Sø, R. Su, S. Wendt, P. Hald, A. Mamakhel, C. Yang, Y. Huang, B.B. Iversen, F. Besenbacher, The influence of crystallite size and crystallinity of anatase nanoparticles on the photo-degradation of phenol, J. Catal. 310 (2014) 100–108. https://doi.org/10.1016/j.jcat.2013.04.022.

[31] A. Tayel, A.R. Ramadan, O.A. El Seoud, Titanium dioxide/graphene and titanium dioxide/graphene oxide nanocomposites: Synthesis, characterization and photocatalytic applications for water decontamination, Catalysts. 8 (2018). https://doi.org/10.3390/catal8110491.

[32] P. Rai, S.K. Dubey, Raman spectroscopy: A potential characterization tool for carbon materials, in: Handb. Mater. Charact., 2018: pp. 405–434. https://doi.org/10.1007/978-3-319-92955-2_11.

[33] I.H. Campbell, P.M. Fauchet, The effects of microcrystal size and shape on the one phonon Raman spectra of crystalline semiconductors, Solid State Commun. 58 (1986) 739–741. https://doi.org/10.1016/0038-1098(86)90513-2.

[34] C.E. Bottani, C. Mantini, P. Milani, M. Manfredini, A. Stella, P. Tognini, P. Cheyssac, R. Kofman, Raman, optical-absorption, and transmission electron microscopy study of size effects in germanium quantum dots, Appl. Phys. Lett. 69 (1996) 2409–2411. https://doi.org/10.1063/1.117653.

[35] D. Deng, X. Pan, L. Yu, Y. Cui, Y. Jiang, J. Qi, W.X. Li, Q. Fu, X. Ma, Q. Xue, G. Sun, X. Bao, Toward N-doped graphene via solvothermal synthesis, Chem. Mater. 23 (2011) 1188–1193. https://doi.org/10.1021/cm102666r.

[36] L.L. Tan, W.J. Ong, S.P. Chai, A.R. Mohamed, Reduced graphene oxide-TiO2 nanocomposite as a promising visible-light-active photocatalyst for the conversion of carbon dioxide, Nanoscale Res. Lett. 8 (2013) 1. https://doi.org/10.1186/1556-276X-8-465.

[37] Y.B. Tang, C.S. Lee, J. Xu, Z.T. Liu, Z.H. Chen, Z. He, Y.L. Cao, G. Yuan, H. Song, L. Chen, L. Luo, H.M. Cheng, W.J. Zhang, I. Bello, S.T. Lee, Incorporation of graphenes in nanostructured TiO2 films via molecular grafting for dye-sensitized solar cell application, ACS Nano. 4 (2010) 3482–3488. https://doi.org/10.1021/nn100449w.

[38] E.J. Yoo, T. Okata, T. Akita, M. Kohyama, J. Nakamura, I. Honma, Enhanced electrocatalytic activity of Pt subnanoclusters on graphene nanosheet surface, Nano Lett. 9 (2009) 2255–2259. https://doi.org/10.1021/nl900397t.

[39] T. Ohsaka, F. Izumi, Y. Fujiki, Raman spectrum of anatase, TiO2, J. Raman Spectrosc. 7 (1978) 321–324. https://doi.org/10.1002/jrs.1250070606.

[40] W.F. Zhang, Y.L. He, M.S. Zhang, Z. Yin, Q. Chen, Raman scattering study on anatase TiO2 nanocrystals, J. Phys. D. Appl. Phys. 33 (2000) 912–916. https://doi.org/10.1088/0022-3727/33/8/305.

[41] O. Frank, M. Zukalova, B. Laskova, J. Kürti, J. Koltai, L. Kavan, Raman spectra of titanium dioxide (anatase, rutile) with identified oxygen isotopes (16, 17, 18), Phys. Chem. Chem. Phys. 14 (2012) 14567–14572. https://doi.org/10.1039/c2cp42763j.

[42] M. Šćepanović, S. Aškrabić, V. Berec, A. Golubović, Z. Dohčević-Mitrović, A. Kremenović, Z. V. Popović, Characterization of La-Doped TiO2 nanopowders by Raman spectroscopy, Acta Phys. Pol. A. 115 (2009) 771–774. https://doi.org/10.12693/APhysPolA.115.771.

[43] G. Li, J. Boerio-Goates, B.F. Woodfield, L. Li, Evidence of linear lattice

expansion and covalency enhancement in rutile TiO 2 nanocrystals, Appl. Phys. Lett. 85 (2004) 2059–2061. https://doi.org/10.1063/1.1790596.

[44] A. Fujishima, T.N. Rao, D.A. Tryk, Titanium dioxide photocatalysis, J. Photochem. Photobiol. C Photochem. Rev. 1 (2000) 1–21. https://doi.org/10.1016/S1389-5567(00)00002-2.

[45] J.C. Parker, R.W. Siegel, Calibration of the Raman spectrum to the oxygen stoichiometry of nanophase TiO2, Appl. Phys. Lett. 57 (1990) 943–945. https://doi.org/10.1063/1.104274.

[46] J. Yu, A. Kudo, Effects of structural variation on the photocatalytic performance of hydrothermally synthesized BiVO4, Adv. Funct. Mater. 16 (2006) 2163–2169. https://doi.org/10.1002/adfm.200500799.

[47] Y.K. Kho, W.Y. Teoh, A. Iwase, L. Mädler, A. Kudo, R. Amal, Flame preparation of visible-light-responsive BiVO 4 oxygen evolution photocatalysts with subsequent activation via aqueous route, ACS Appl. Mater. Interfaces. 3 (2011) 1997–2004. https://doi.org/10.1021/am200247y.

[48] A. Galembeck, O.L. Alves, BiVO4 thin film preparation by metalorganic decomposition, Thin Solid Films. 365 (2000) 90–93. https://doi.org/10.1016/S0040-6090(99)01079-2.

[49] Y. Liu, X. Zhu, D. Yuan, W. Wang, L. Gao, Preparation and characterization of TiO2 based on wood templates, Sci. Rep. 10 (2020). https://doi.org/10.1038/s41598-020-69440-x.

[50] J. Surmacki, P. Wroński, M. Szadkowska-Nicze, H. Abramczyk, Raman spectroscopy of visible-light photocatalyst - Nitrogen-doped titanium dioxide generated by irradiation with electron beam, Chem. Phys. Lett. 566 (2013) 54–59. https://doi.org/10.1016/j.cplett.2013.02.066.

[51] A.S. Ahmed, T. Ahamad, N. Ahmad, M.Z. Khan, Removal enhancement of acid navy blue dye by GO - TiO2 nanocomposites synthesized using sonication method, Mater. Chem. Phys. 238 (2019). https://doi.org/10.1016/j.matchemphys.2019.121906.

[52] C. Regmi, Y.K. Kshetri, T.H. Kim, R.P. Pandey, S.W. Lee, Visible-light-induced Fe-doped BiVO4 photocatalyst for contaminated water treatment, Mol. Catal. 432 (2017) 220–231. https://doi.org/10.1016/j.mcat.2017.02.004.

[53] D. Fang, X. Li, H. Liu, W. Xu, M. Jiang, W. Li, X. Fan, BiVO4-rGO with a novel structure on steel fabric used as high-performance photocatalysts, Sci. Rep. 7 (2017) 1–9. https://doi.org/10.1038/s41598-017-07342-1.

[54] C. Li, P. Zhang, R. Lv, J. Lu, T. Wang, S. Wang, H. Wang, J. Gong, Selective deposition of Ag3PO4 on monoclinic BiVO4(040) for highly efficient photocatalysis, Small. 9 (2013) 3951–3956. https://doi.org/10.1002/smll.201301276.

[55] C. Li, P. Zhang, R. Lv, J. Lu, T. Wang, S. Wang, H. Wang, J. Gong, Photocatalysis: Selective Deposition of Ag 3 PO 4 on Monoclinic BiVO 4 (040) for Highly Efficient Photocatalysis (Small 23/2013) , Small. 9 (2013) 3950–3950. https://doi.org/10.1002/smll.201370147.

[56] J. Sun, C. Wang, T. Shen, H. Song, D. Li, R. Zhao, X. Wang, Engineering the dimensional interface of BiVO4-2D reduced graphene oxide (RGO) nanocomposite for enhanced visible light photocatalytic performance, Nanomaterials. 9 (2019). https://doi.org/10.3390/nano9060907.

[57] M. Shafiul Islam, A Review on Common Methods for Characterizing Graphene Oxide (GO), Asian J. Appl. Chem. Res. (2019) 1–8. https://doi.org/10.9734/ajacr/2019/v4i230109.

[58] E. Aliyev, V. Filiz, M.M. Khan, Y.J. Lee, C. Abetz, V. Abetz, Structural characterization of graphene oxide: Surface functional groups and fractionated oxidative debris, Nanomaterials. 9 (2019) 1–15. https://doi.org/10.3390/nano9081180.

[59] G. Li, L. Chen, M.E. Graham, K.A. Gray, A comparison of mixed phase titania photocatalysts prepared by physical and chemical methods: The importance of the solid-solid interface, J. Mol. Catal. A Chem. 275 (2007) 30–35. https://doi.org/10.1016/j.molcata.2007.05.017.

[60] W. Wunderlich, T. Oekermann, L. Miao, N.T. Hue, S. Tanemura, M. Tanemura, Electronic properties of Nano-porous TiO2- and ZnO-Thin Films-comparison of simulations and experiments, J. Ceram. Process. Res. 5 (2004) 343–354.

[61] A. Paxton, L. Thiên-Nga, Electronic structure of reduced titanium dioxide, Phys. Rev. B - Condens. Matter Mater. Phys. 57 (1998) 1579–1584. https://doi.org/10.1103/PhysRevB.57.1579.

[62] S. Banerjee, J. Gopal, P. Muraleedharan, A.K. Tyagi, B. Raj, Physics and chemistry of photocatalytic titanium dioxide: Visualization of bactericidal activity using atomic force microscopy, Curr. Sci. 90 (2006) 1378–1383.

[63] Y. Hu, J. Fan, C. Pu, H. Li, E. Liu, X. Hu, Facile synthesis of double cone-shaped Ag4V2O7/BiVO4 nanocomposites with enhanced visible light photocatalytic activity for environmental purification, J. Photochem. Photobiol. A Chem. 337 (2017) 172–183. https://doi.org/10.1016/j.jphotochem.2016.12.035.

[64] S. Sun, W. Wang, Advanced chemical compositions and nanoarchitectures of bismuth based complex oxides for solar photocatalytic application, RSC Adv. 4 (2014) 47136–47152. https://doi.org/10.1039/c4ra06419d.

[65] G. Regmi, M. Rohini, P. Reyes-Figueroa, A. Maldonado, M. de la Luz Olvera, S. Velumani, Deposition and characterization of ultrathin intrinsic zinc oxide (i-ZnO) films by radio frequency (RF) sputtering for propane gas sensing application, J. Mater. Sci. Mater. Electron. 29 (2018) 15682–15692. https://doi.org/10.1007/s10854-018-9166-1.

[66] P. Makuła, M. Pacia, W. Macyk, How To Correctly Determine the Band Gap Energy of Modified Semiconductor Photocatalysts Based on UV-Vis Spectra, J. Phys. Chem. Lett. 9 (2018) 6814–6817. https://doi.org/10.1021/acs.jpclett.8b02892.

[67] H. Zhang, X. Wang, N. Li, J. Xia, Q. Meng, J. Ding, J. Lu, Synthesis and characterization of TiO2/graphene oxide nanocomposites for photoreduction of heavy metal ions in reverse osmosis concentrate, RSC Adv. 8 (2018) 34241–34251. https://doi.org/10.1039/c8ra06681g.

[68] R. Wang, K. Shi, D. Huang, J. Zhang, S. An, Synthesis and degradation kinetics of TiO2/GO composites with highly efficient activity for adsorption and photocatalytic degradation of MB, Sci. Rep. 9 (2019) 1–9. https://doi.org/10.1038/s41598-019-54320-w.

[69] D.K.C. Ramos, M.V. González, R.A.E. Muñóz, J.S. Cruz, F.J. De Moure-Flores, S.A. Mayén-Hernández, Obtaining and Characterization of TiO2-GO Composites for Photocatalytic Applications, Int. J. Photoenergy. 2020 (2020) 1–9. https://doi.org/10.1155/2020/3489218.

[70] L.Y. Ozer, Y. Shin, A. Felten, H. Oladipo, O. Pikuda, C. Muryn, C. Casiraghi, G. Palmisano, Growing N-doped multiphase TiO2 nanocomposites on reduced graphene oxide: Characterization and activity under low energy visible radiation, J. Environ. Chem. Eng. 5 (2017) 5091–5098. https://doi.org/10.1016/j.jece.2017.09.042.

[71] S. Kumari, P. Sharma, S. Yadav, J. Kumar, A. Vij, P. Rawat, S. Kumar, C. Sinha, J. Bhattacharya, C.M. Srivastava, S. Majumder, A Novel Synthesis of the Graphene Oxide-Silver (GO-Ag) Nanocomposite for Unique Physiochemical Applications, ACS Omega. 5 (2020) 5041–5047. https://doi.org/10.1021/acsomega.9b03976.

[72] B. Jaleh, E. Zare, S. Azizian, O. Qanati, M. Nasrollahzadeh, R.S. Varma, Preparation and Characterization of Polyvinylpyrrolidone/Polysulfone Ultrafiltration Membrane Modified by Graphene Oxide and Titanium Dioxide for Enhancing Hydrophilicity and Antifouling Properties, J. Inorg. Organomet. Polym. Mater. 30 (2020) 2213–2223. https://doi.org/10.1007/s10904-019-01367-x.

[73] H.P. Qi, H.L. Wang, D.Y. Zhao, W.F. Jiang, Preparation and photocatalytic activity of Ag-modified GO-TiO 2 mesocrystals under visible light irradiation, Appl. Surf. Sci. 480 (2019) 105–114. https://doi.org/10.1016/j.apsusc.2019.02.194.

[74] G. Wang, W. Guo, D. Xu, D. Liu, M. Qin, Graphene oxide hybridised TiO2 for visible light photocatalytic degradation of phenol, Symmetry (Basel). 12 (2020) 1–16. https://doi.org/10.3390/SYM12091420.

[75] A. Kumar, A. Bansal, B. Behera, S.L. Jain, S.S. Ray, Ternary hybrid polymeric nanocomposites through grafting of polystyrene on graphene oxide-TiO2 by surface initiated atom transfer radical polymerization (SI-ATRP), Mater. Chem. Phys. 172 (2016) 189–196. https://doi.org/10.1016/j.matchemphys.2016.01.064.

[76] A.R. Nanakkal, L.K. Alexander, Graphene/BiVO4/TiO2 nanocomposite: tuning band gap energies for superior photocatalytic activity under visible light, J. Mater. Sci. 52 (2017) 7997–8006. https://doi.org/10.1007/s10853-017-1002-0.

[77] V. Vinesh, A.R.M. Shaheer, B. Neppolian, Reduced graphene oxide (rGO) supported electron deficient B-doped TiO2 (Au/B-TiO2/rGO) nanocomposite: An efficient visible light sonophotocatalyst for the degradation of Tetracycline (TC), Ultrason. Sonochem. 50 (2019) 302–310. https://doi.org/10.1016/j.ultsonch.2018.09.030.

[78] S.P. Sundaran, C.R. Reshmi, P. Sagitha, A. Sujith, Polyurethane nanofibrous membranes decorated with reduced graphene oxide–TiO2 for photocatalytic templates in water purification, J. Mater. Sci. 55 (2020) 5892–5907. https://doi.org/10.1007/s10853-020-04414-y.

[79] M. Li, G. Xu, Z. Guan, Y. Wang, H. Yu, Y. Yu, Synthesis of Ag/BiVO 4 /rGO composite with enhanced photocatalytic degradation of triclosan, Sci. Total Environ. 664 (2019) 230–239. https://doi.org/10.1016/j.scitotenv.2019.02.027.

[80] Metcalf, Eddy, Metcalf & Eddy, Inc. Wastewater Engineering Teatment and Reuse, 2003.

[81] M. Cho, H. Chung, W. Choi, J. Yoon, Different inactivation behaviors of MS-2 phage and Escherichia coli in TiO2 photocatalytic disinfection, Appl. Environ. Microbiol. 71 (2005) 270–275. https://doi.org/10.1128/AEM.71.1.270-275.2005.

[82] H. Ikai, K. Nakamura, M. Shirato, T. Kanno, A. Iwasawa, K. Sasaki, Y. Niwano, M. Kohno, Photolysis of hydrogen peroxide, an effective disinfection system via hydroxyl radical formation, Antimicrob. Agents Chemother. 54 (2010) 5086–5091. https://doi.org/10.1128/AAC.00751-10.

[83] J.A. Byrne, P.S.M. Dunlop, J.W.J. Hamilton, P. Fernández-Ibáñez, I. Polo-López, P.K. Sharma, A.S.M. Vennard, A review of heterogeneous photocatalysis for water and surface disinfection, Molecules. 20 (2015) 5574–

5615. https://doi.org/10.3390/molecules20045574.

[84] S. Joshi, R. Siddiqui, P. Sharma, R. Kumar, G. Verma, A. Saini, Green synthesis of peptide functionalized reduced graphene oxide (rGO) nano bioconjugate with enhanced antibacterial activity, Sci. Rep. 10 (2020). https://doi.org/10.1038/s41598-020-66230-3.

[85] K.H. Tan, S. Sattari, I.S. Donskyi, J.L. Cuellar-Camacho, C. Cheng, K. Schwibbert, A. Lippitz, W.E.S. Unger, A. Gorbushina, M. Adeli, R. Haag, Functionalized 2D nanomaterials with switchable binding to investigate graphene-bacteria interactions, Nanoscale. 10 (2018) 9525–9537. https://doi.org/10.1039/c8nr01347k.

[86] K. Ouyang, K. Dai, S.L. Walker, Q. Huang, X. Yin, P. Cai, Efficient photocatalytic disinfection of Escherichia coli O157:H7 using C70-TiO2 hybrid under visible light irradiation, Sci. Rep. 6 (2016) 1–8. https://doi.org/10.1038/srep25702.

[87] X. Zhang, J. Zhang, J. Yu, Y. Zhang, F. Yu, L. Jia, Y. Tan, Y. Zhu, B. Hou, Enhancement in the photocatalytic antifouling efficiency over cherimoya-like InVO4/BiVO4 with a new vanadium source, J. Colloid Interface Sci. 533 (2019) 358–368. https://doi.org/10.1016/j.jcis.2018.06.090.

[88] A. Pal, X. Mint, L.E. Yu, S.O. Pehkonen, M.B. Ray, Photocatalytic inactivation of bioaerosols by TiO 2 coated membrane, Int. J. Chem. React. Eng. 3 (2005) A45. https://doi.org/10.2202/1542-6580.1236.

[89] A. Kubacka, M.S. Diez, D. Rojo, R. Bargiela, S. Ciordia, I. Zapico, J.P. Albar, C. Barbas, V.A.P. Martins Dos Santos, M. Fernández-García, M. Ferrer, Understanding the antimicrobial mechanism of TiO 2 -based nanocomposite films in a pathogenic bacterium, Sci. Rep. 4 (2014). https://doi.org/10.1038/srep04134.

[90] J. Luo, Z. Yan, R. Liu, J. Xu, X. Wang, Synthesis and excellent visible light photocatalysis performance of magnetic reduced graphene oxide/ZnO/ZnFe2O4 composites, RSC Adv. 7 (2017) 23246–23254. https://doi.org/10.1039/c7ra02083j.

[91] R. Sharma, Uma, S. Singh, A. Verma, M. Khanuja, Visible light induced bactericidal and photocatalytic activity of hydrothermally synthesized BiVO4 nano-octahedrals, J. Photochem. Photobiol. B Biol. 162 (2016) 266–272. https://doi.org/10.1016/j.jphotobiol.2016.06.035.

[92] N.M. El-Shafai, M.E. El-Khouly, M. El-Kemary, M.S. Ramadan, M.S. Masoud, Graphene oxide-metal oxide nanocomposites: Fabrication, characterization and removal of cationic rhodamine B dye, RSC Adv. 8 (2018) 13323–13332. https://doi.org/10.1039/c8ra00977e.

[93] V. Dutta, P. Singh, P. Shandilya, S. Sharma, P. Raizada, A.K. Saini, V.K. Gupta, A. Hosseini-Bandegharaei, S. Agarwal, A. Rahmani-Sani, Review on advances in photocatalytic water disinfection utilizing graphene and graphene derivatives-based nanocomposites, J. Environ. Chem. Eng. 7 (2019) 103132. https://doi.org/10.1016/j.jece.2019.103132.

Chapter 5

Study on micro algal photocatalytic destruction

Chapter 5 : Study on micro algal photocatalytic destruction

5.1 Introduction

Strictly, aquatic oxygenic photosynthetic microorganisms divide in two groups, denoted as cyanobacteria and microalgae. The former groups prokaryotic organisms whereas the latter groups eukaryotic organisms. Both groups have colonized every type of ecological niches [1], including water reservoirs [2]. Both groups use nitrogen, phosphorus, sunlight, carbon dioxide, and water to generate biomass according to abiotic constraints. Under certain circumstances, cyanobacteria and microalgae can divide out of control, forming blooms [3–5]. Despite recent attempts to valorize the biomass produced during the blooms [6], cyanobacteria and microalgal blooms have generally a negative impact on economic activities, directly, for example by killing fishes [7] or indirectly, by rendering the water unfit for consumption. The increase in bloom frequency and the change in their geographic distribution makes bloom a very worrying events [8], especially regarding the phenomenon occurring in potable water reservoirs because water constitutes an increasing crucial resource [9]. In this frame, it is crucial to find adequate ways to efficiently treat the water contaminated by cyanobacteria and/or microalgae. To reach this goal, several possibilities of physical treatments such as plasma treatments have been tested. Recently, the availability of nanomaterials opened new avenues for water decontamination as illustrated in chapter 4.

However, the use of nanomaterials should be taken with caution because when dispersed in water, they can enter any type of organisms, and possibly be toxic to non-target organisms. In all cases, internalized nanomaterials risk being returned to the environment upon the death of the organisms that absorbed them, which could constitute a source of pollution [10,11]. To avoid these possibilities, compressed nanomaterials, *i.e.,* pellets (see chapter 2 for preparation) have been used in this chapter because pellets can resemble the films in terms of activity, films being the most common application for nanoparticles generating ROS. In addition, the use of dispersed nanoparticles, may result in ROS generation both internally and externally because nanomaterials have been internalized. The latter possibility vanishes using pellets, offering the possibility to study the effects of externally generated ROS alone

on microalgae and determined the potential of externally generated ROS for water decontamination.

The photosynthetic process can be seen as the combination of reactions relying on different principles. In the biochemical phase responsible for carbon fixation, relies on biochemistry and is characterized by slow constant rates (in the range of s to min). In contrast, photo biochemical phase responsible for light absorption and, electron generation and transport, relies on physics and chemistry with fast constant rates (slowest in the ms range). From these statements arises the view that both types of reactions will be saturated very differently. According to the chemistry and physics rules, the oxidative risk, *i.e.*, the generation of ROS in a photosynthetic cell, is significantly elevated because this process manipulates light energy, electrons, and oxygen, the latter being produced through the photooxidation of water. Living for several billion years in a cellular environment with a high oxidative risk, photosynthetic organisms have developed inducible mechanisms aiming at limiting the extent of the risk. Those mechanisms are powerful. Besides the classical enzymatic tools such as superoxide dismutase, catalases, and peroxidases, the photosynthetic cells can eliminate the excess of light energy absorbed as heat using several nonphotochemical quenching mechanisms. They play crucial roles in decreasing the internal ROS generation [12,13].

The photosynthetic apparatus contained two different types of pigment-protein complexes, namely photosystem I and photosystem II. Each photosystem is composed of a light-harvesting complex, meant to harvesting photons and transferring the associated energy to a reaction centre. The light-harvesting complex contains several pigments, including chlorophylls and carotenoids. For this work, only PSII is considered, because the chlorophyll fluorescence is mostly arising from this complex (see however [14]). Two extreme models have been created to explain how the photosystems are cooperating in the thylakoid membrane. At one extreme, the puddle model proposes that each photosynthetic unit is independent from the neighbouring photosynthetic units. At the other extreme, one finds the lake model according to which the photosynthetic units are cooperating to generate oxygen. Actually, many intermediate models have been proposed (reviewed in [15]). The degree of connexion between the photosynthetic units is given by the connectivity factor [16].

The performance of the photosynthetic apparatus has been studied by different means, including the variations of the chlorophyll fluorescence yield. Since the pioneering publication of Kautsky *et al*,1960 [17], the analysis of the modifications of the chlorophyll fluorescence yield has been developed until it becomes a major and popular method of the study of the photosynthetic activity [18]. Several protocols are available, including the saturation pulse method (for reviews, see [18–20]). The saturation pulse method can provide information during steady-state illumination, *e.g.*, under field conditions and applied to every type of photosynthetic organisms, including lichen and phytoplankton. The method presents several other advantages, such as its sensitivity, easiness to manage, great flexibility and a rather simple mathematical formalism. It is based on the recording of the variation of two chlorophyll fluorescence yields of dark-adapted samples and in the light. It is out of the scope of this contribution to review the experimental procedures leading to the measurement of the different chlorophyll fluorescence yields. The interested readers are referred to excellent recent reviews on the topic [17–20]. Briefly, the time course of chlorophyll fluorescence yields is recorded in dark-adapted samples and in the light. These chlorophyll fluorescence yields are F_0 and F_M and, F_t and F_M', respectively (for nomenclature see [13]). Based on these basic yields, a myriad of fluorescence parameters has been defined (see Chapter 2, Table 2.2). They are used to characterize the photochemical and non-photochemical mechanisms occurring in the photosynthetic apparatus during an illumination. They are only described shortly here – for a review see [18,19,21].

- *Maximum quantum yield of PS II* photochemistry: it is usually called the FV/FM ratio) and quantifies the maximum photochemical efficiency (capacity) of open RCs II. In this work, ΦPo is equivalent to Y_{II} in the dark.

- *Photochemical quenching of variable Chl fluorescence*: These parameters qP and qL indicate the actual photochemical capacity of PSII during a continuous illumination. It is related to the photochemical energy conversion by charge separation in the reaction center of photosystem II. It quantifies the actual fraction of RCs II being open, *i.e.,* with oxidised QA.

- *Nonphotochemical quenching of variable Chl fluorescence*: The coefficients qN, BPQ, Y_{NO} and Y_{NPQ} reflect the activation of several processes of nonphotochemical nature during the light period and mostly leading to nonradiative deactivation of the excitation energy as heat (thermal dissipation).

They include the pH-gradient build up, state-transitions, ATP-synthesis regulation, inactivation of photosystem II, conformational changes within thylakoid membranes, activation of the xanthophyll cycle, *etc*. The lake model differentiates the regulated mechanisms (Y_{NPQ}) from the nonregulated ones (Y_{NO}).

The definitions of the parameters presented in Table 2.2 does not need to know the level of connectivity between photosynthetic units [21]. Most of the studies on this topic have been dedicated to the photosynthetic apparatus of land plants and it has been concluded that the lake model generally prevails [21], even though sometimes the connectivity was not observed during the first hours of bean leaf greening [22]. Even though several studies claimed that the model is also valid in algae, the type of organization of the photosynthetic apparatus in phytoplankton, including diatoms, is far to be investigated thoroughly. Nevertheless, a formal puddle model seems unrealistic because it is established that PSII reaction centres form functional dimers in the diatom thylakoids [23]. Several elegant measurements have shown that the photosynthetic units are well approximated by the lake model, but are most accurately described by intermediate models [15]. However, studying the marine diatom *Thalassiosira pseudonana* [24], Xu *et al* found rather low value for the PSII connectivity [25]. Interestingly, the values were increasing with the light intensity (30 *versus* 350 µmol/m^{-2} s), suggesting that an increase of proportion of the photosynthetic units in the configuration of the lake model would occur at high light intensities. Unfortunately, very high light intensities such as those used in this study were not tested and therefore the limit of this increase cannot be evaluated. Wu *et al* also working with *T. pseudonana* reported an opposite variation *i.e.* a decrease of the connectivity under an increase of blue light irradiation (30 *versus* 450 µmol/m^{-2}s) [26]. Lavaud *et al* reported that the connectivity might greatly differ between diatoms [27]. They reported that the connectivity was almost zero in *Phaeodactylum tricornutum* (0.02) and much higher (0.16) in *Skeletonema costatum.* Being unable to conclude about the type of model prevailing in *P. tricornutum,* both puddle and lake models were considered. It is important to note that the mathematical derivation have demonstrated that the parameter Y_{II} has the same equations in both models [28].

In aquatic environments, nanoparticles can aggregate, dissolve or precipitate depending on their properties and their liquid medium, like size, coating material, shape, pH, ionic strength, and dissolved organic matter. Nanoparticles can interact with the algae surrounding them, similar to that occurring in bacteria [29–36]. The toxicity of nanoparticles or algal killing by the photocatalytic activity is by the physical restraints and oxidative stress [37] (Fig 2.2). When there is a large aggregation of nanoparticles over and around the microalgae, the availability of light for photosynthesis is reduced and blocks the nutrient uptake [38,39]. By the exposure of algae with the nanoparticles, oxidative stress occurs due to the over-accumulation of the ROS generated [40–44]. The exposure to nanoparticles results in ROS production, thus causing lipid peroxidation of the membrane and activating antioxidative enzymes, *i.e.,* SOD and POD. The ROS can cause the impairment of photosynthetic activity and deterioration of mitochondrial membrane and DNA. At a certain point, the ROS generation can cause suppression of genes encoding for the reaction center protein of PSII, light-harvesting proteins of photosystem, electron transport chain, and RuBisCO associated with carbon fixation. NADPH synthesis is lowered, inhibiting the CO_2 assimilation, and decreasing the production of sugars in the Calvin cycle [37].
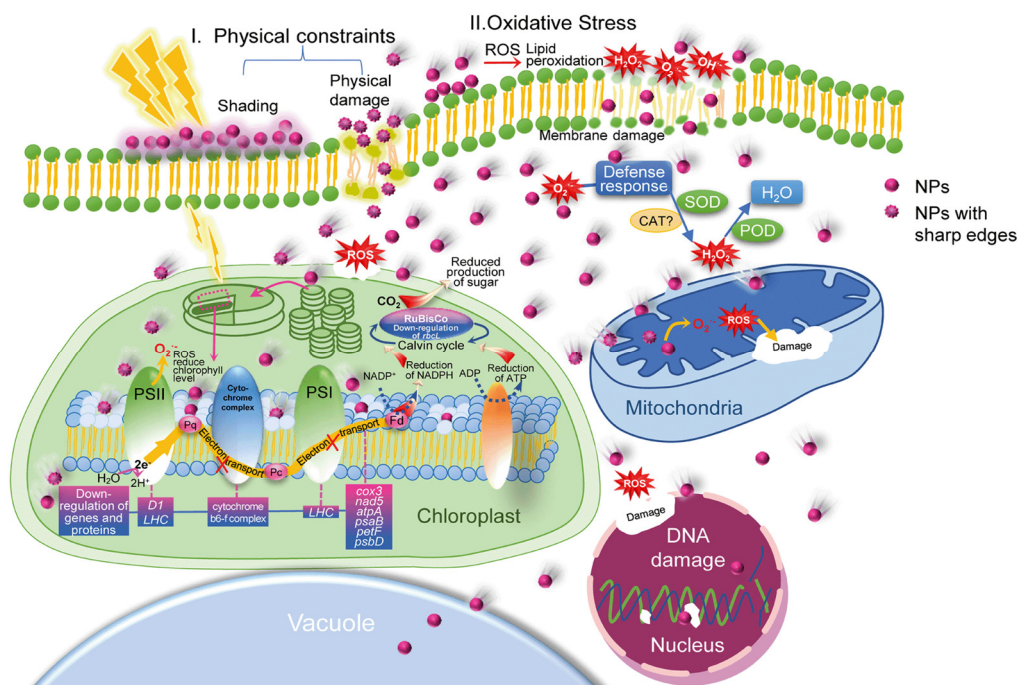

Fig 5.1: The image shows the mechanism in which the nanoparticles cause the detrimental effect for the microalgae [37]

This chapter discusses the effect of nanoparticles on cyanobacteria and microalgae in various conditions as a preliminary step towards microalgal disinfection.

5.2 Results and Discussion

### 5.2.1 Shaping the light beam to allow photosynthesis and photocatalytic ROS generation

The two objectives of this work were to synthesize innovative photocatalyst generating ROS under visible light irradiation (see Chapter 2) and using the generated ROS for decontaminating water from bacteria, cyanobacteria, and microalgae. From the above sections, a description of the characteristics of the innovative photocatalysts in terms of bandgap, corresponding at an absorbance at 405 nm, was reported (refer to Chapter 4, section 4.2.3). On the other hand, cyanobacteria and microalgae are photosynthetic organisms, *i.e.*, they convert the energy associated with photons into biochemical energy [45,46] using a range of pigments, *i.e.*, molecules able to absorb light [47]. For instance, the pigment set of the diatom *P. tricornutum* absorbs light in the visible range of electromagnetic spectrum, including the blue region. Therefore, the light beam used for ROS generation can also be used for photosynthesis. The chapter 2, section 2.8.3 indicated that the light source used in photocatalytic assays provided a light spectrum close to one sun. Therefore, it needed to be filtered to select a beam with a maximum of 405 nm, thus avoiding ROS formation by UV light while allowing photosynthesis. The ideal filter should fulfil the following conditions:

- no transmission in the UV region,
- large transmission in the visible region
- no or weak transmission in the IR region to avoid sample heating

The broad band-pass filters available in the laboratory failed to meet this goal because they did not absorb light below 405 nm and IR radiation (Fig 5.2 (a)). Consequently, several filters had to be combined to meet the requirements:

- The filtering of the wavelengths below 400 nm was performed using a long-pass filter, with a cut off at 400 nm and a transmission value at 405 nm equal to 35% (Fig 5.2 (b)).
- The IR filter was a faintly blue-green tinted glass that can absorb 40% of infrared radiations while absorbing only 25% of the incident visible light (Fig 5.2 (c)). The absorbance spectrum of the combined filters is presented in Fig 5.2 (e).

The resulting light intensity was high enough to saturate the photosynthetic machinery, a situation that may result in ROS formation within the cells. Photosynthetic cells have evolved several mechanisms allowing to reduce cell ROS formation. These includes enzymatic machineries as well as nonphotochemical nonradiative energy dissipation (see below). Therefore, the study of the effects of externally generated ROS by the photocatalytic materials requires the comparison of experiments performed in the absence (photolysis) and in the presence (photocatalysis) of the photocatalytic material
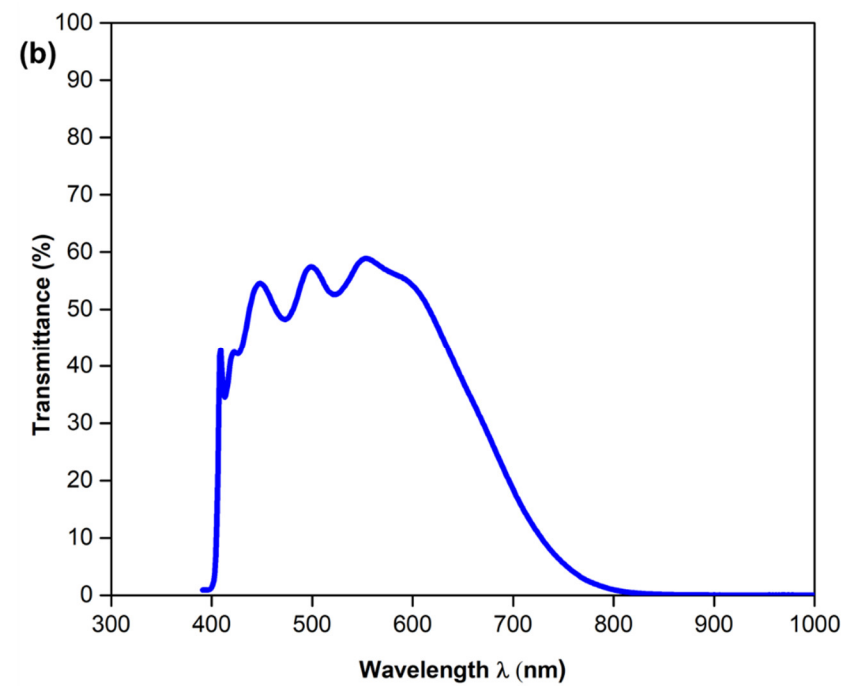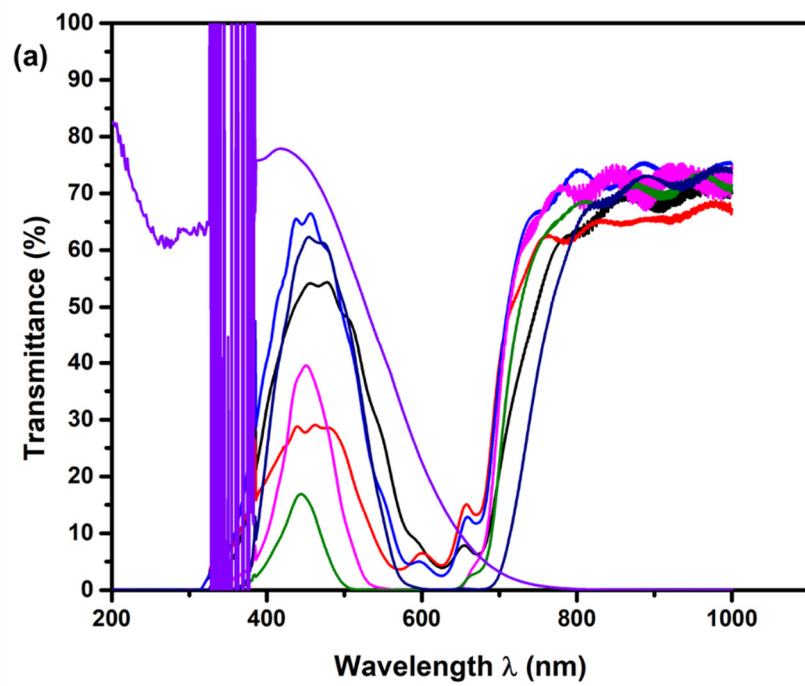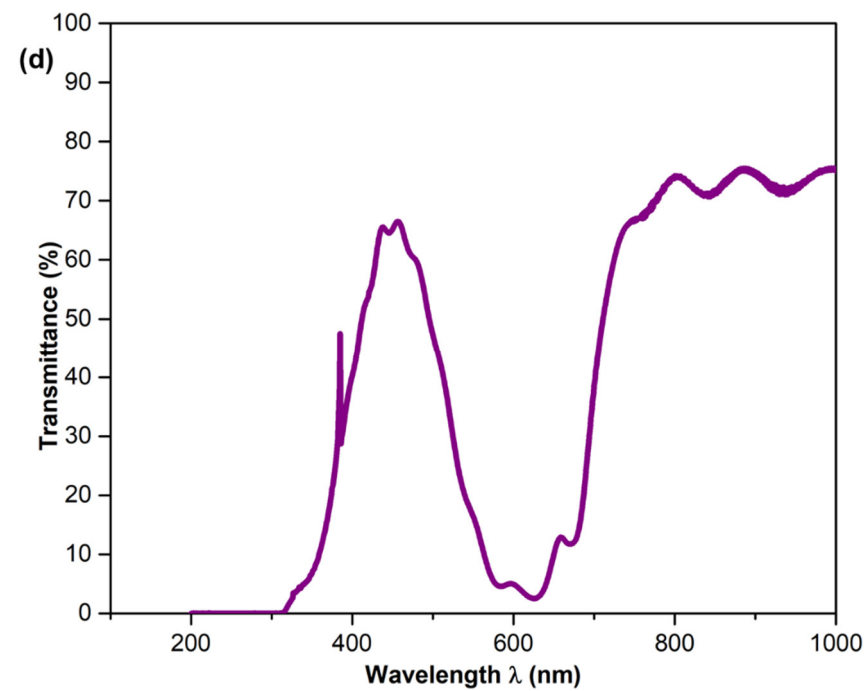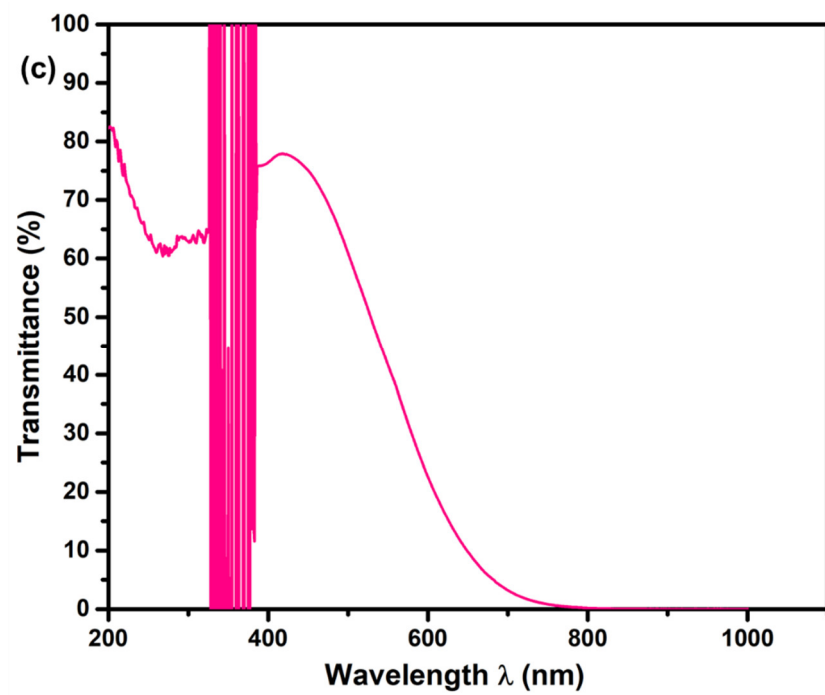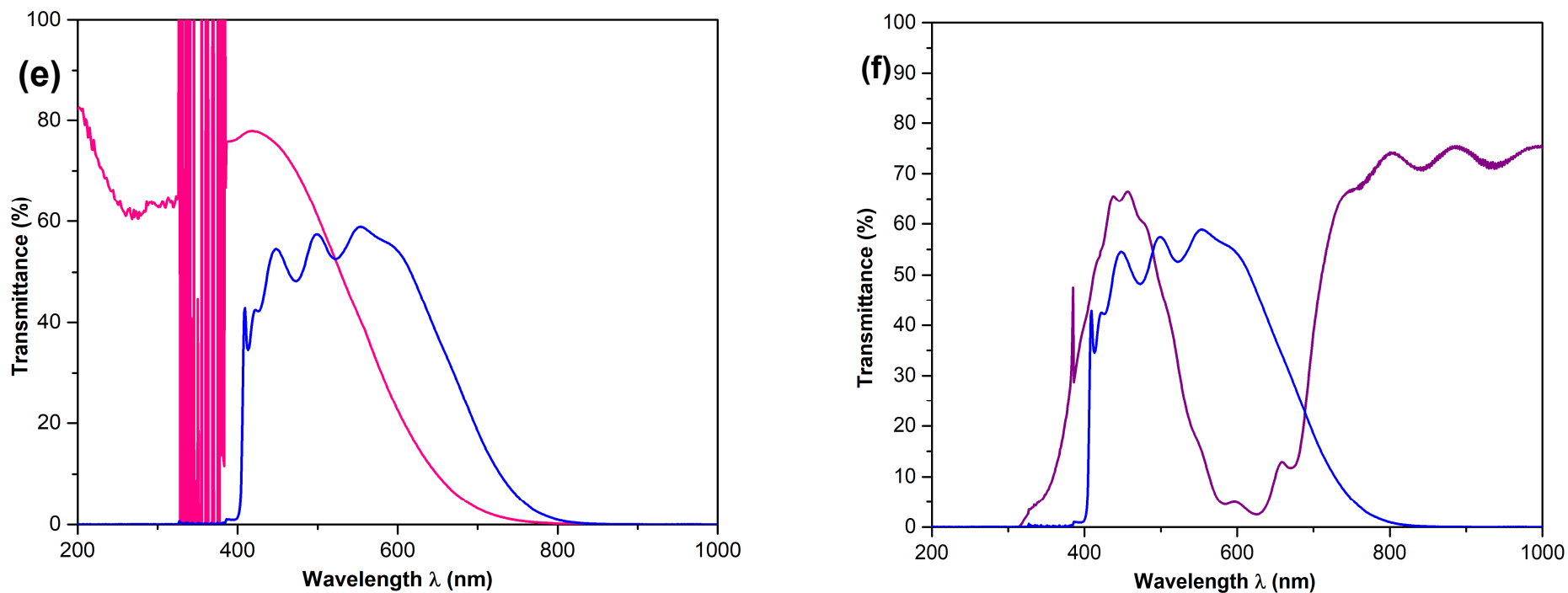
Fig 5.2. Absorbance spectrum of the filter set used for experiments

(a) Absorbance spectra of the band-pass filters (b) Absorbance spectrum of the long-pass filter used to block the wavelength below 400 nm (c) Absorbance spectrum of the IR filter (d) Absorbance spectra of the daylight blue filter (e) Absorbance spectrum of the combined filters (blue - green tinted glass filter and IR filter) (f) Absorbance spectrum of the combined filters (daylight blue filter and IR filter)
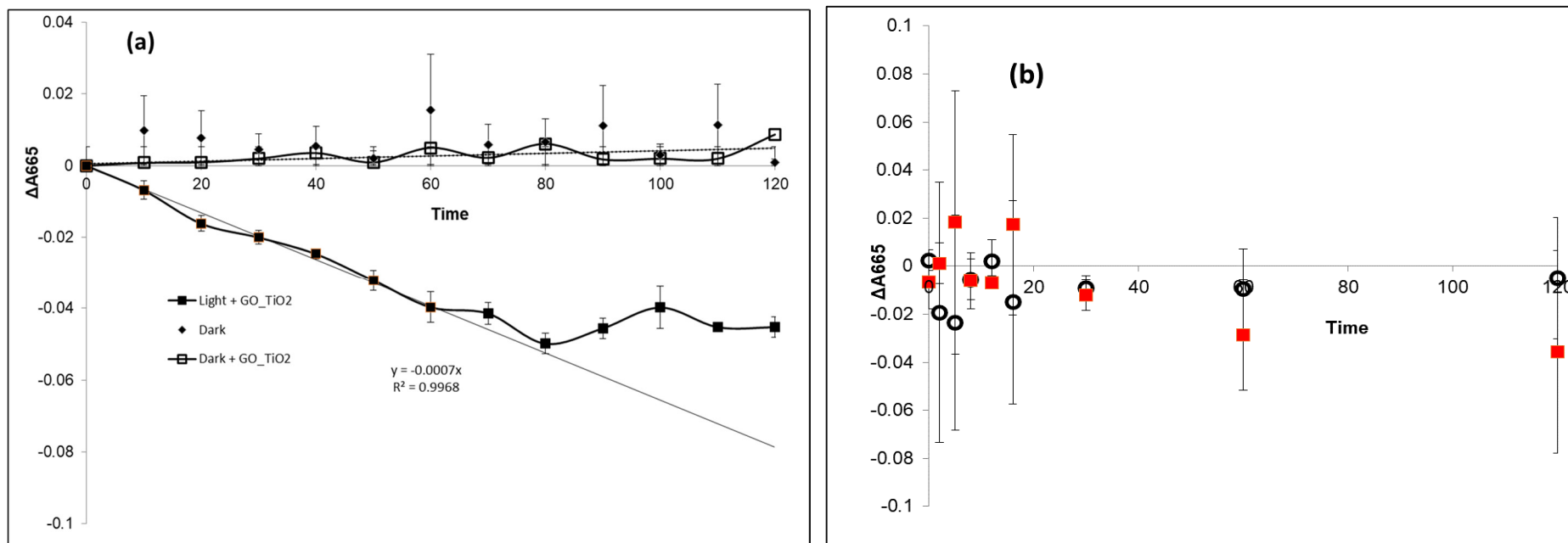
Fig 5.3 (a) Degradation kinetics of MB dye in the dark (losange), in the dark and in the presence of 1.5 GOT pellet (open squares), in the dark and in the presence of 1.5 GOT pellet (close squares)

(b) Degradation kinetics of MB dye in the dark, in the presence of 1.5 GOT pellet (dark squares) and in the presence of nitrogen bubbling (close circle). The data represented the mean of three assays

5.2.2 Photocatalytic ROS generation of pellets

To demonstrate the capacity of pellets to generate ROS, methyl blue degradation was followed by recording the variation of the absorbance at 665 nm ($\Delta A665 = A665_{t=0}$ - $A665_{t=t}$) in different conditions (Fig. 5.3 (a)). Methylene blue is considered as a standard dye for the photocatalytic experiments. The absorbance spectra were corrected as explained in chapter 2, section 2.8.3 (a). Regardless the presence of nanomaterials, no significant variation of the absorbance was observed in the absence of light (yellow squares and black diamond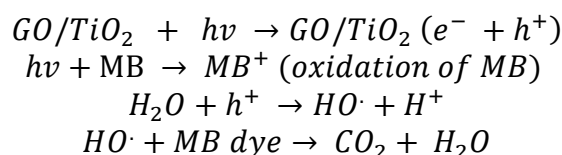s in Fig. 5.3 (a). In the presence of light and nanomaterials (1.5 GOT), the absorbance at 665 nm decreased linearly before to saturate after 80 min of illumination (black squares in Fig. 5.3 (a)). To demonstrate that the decrease in the absorbance at 665 nm is due to photocatalysis, the experiment was repeated with nitrogen bubbling inside the cuvette, limiting ROS formation. In this condition no significant variation of $\Delta A665$ was recorded (Fig 5.3 (b)). The mechanism involved is as follows [48]:

$$GO/TiO_2 \ + \ hv \ \rightarrow GO/TiO_2 \, (e^- \ + h^+)$$
$$hv + \text{MB} \ \rightarrow \ MB^+ \, (oxidation \ of \ MB)$$
$$H_2O + h^+ \ \rightarrow HO^{\cdot} + H^+$$
$$HO^{\cdot} + MB \ dye \rightarrow \ CO_2 \ + \ H_2O$$

5.2.3 Photocatalytic disinfection of *Anabaena*

Anabaena is a filamentous cyanobacteria (Fig 5.4). Some taxa are famous for forming blooms and toxins [49].

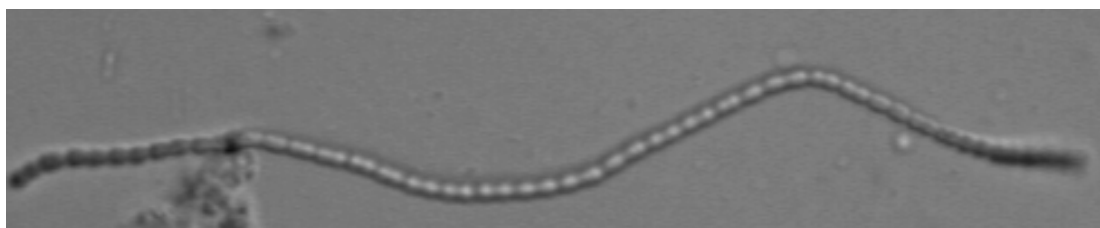*Fig 5.4. Filamentous Anabaena sp. observed in phase contrast light microscope ©Prof. B. Schoefs (Le Mans University, France)*

Traditionally, the evaluation of disinfection requires enumeration of the living organisms as explained in the previous chapter. Unfortunately, even if they are bacteria, cyanobacteria, especially filamentous cyanobacteria, grow much slower than

non-photosynthetic bacteria. In addition, the enumeration of filamentous cyanobacteria_requires a specific chamber allowing the sample to settle. Once sedimented, the individuals are counted by direct counts under the microscope. This method is called the Utermöhl method [50]. Because this method is very time-consuming, it was decided to follow the variations of an internal marker of the cyanobacteria, such as phycocyanin or chlorophyll *a*. To reach this goal, *in situ* absorbance spectroscopy was chosen because it is fast and relatively sensitive. Measuring absorbance spectra *in situ* is always tricky because of the featureless nonselective light scattering of the sample [51] This scattering depends on cell size and shape and results from changes in the refractive index at the interphase boundaries *e.g.*, between medium, cell, cytosol, and intracellular structures [52]. In addition, a selective scattering with prominent spectral features related to sharp changes in the refractive index in the region of light absorption by aggregated pigments embedded in thylakoid membranes is observed [53–56]. Scattering is also wavelength dependent, and proportional to the inverse of the fourth power of the wavelength. To summarize, the absorbance spectrum of a scattering sample presents two typical characteristics:

- a baseline with a strong drift
- shrunken absorbance peaks, especially in the blue region.

These characteristics were observed in the recorded absorbance spectra of the cyanobacteria *Anabaena flos-aquae* PCC 7120 (Fig. 2.22). The original and corrected spectra are again presented in Fig 5.5. The baseline-corrected absorbance spectrum presents maxima at 438, 637, and 673 nm, typical of chlorophyll *a* (673 and 438 nm) and phycobilisomes (637 nm) (Fig. 5.5). Similar spectra were obtained by Mezlyak *et al* [51]. The correction was not perfect because the corrected spectrum presented a weak distortion zone around 550 nm and was not valid for the blue region (Fig. 5.5 (b)). Because the blue region was not used in this work, the small distortion around 550 nm was considered as negligible. The absorbance was measured far from this distortion zone, *i.e.,* between 600 and 700 nm.

From the above discussion on the damping effect of scattering on the amplitude of the absorbance bands, it was first determined how many algae are needed to record a signal in the range of 600 to 700 nm. For such a purpose, absorbance spectra of

increasing amount of cyanobacteria were recorded by diluting increasing volume of a mother culture (OD_{750} = 6) in the recording cuvette (3 mL) (Fig 5.5 (c)) and corrected according to the procedure explained above. The absorbance at 750 nm in noncorrected absorbance spectra (A750) and the absorbance at 637 nm in corrected absorbance spectra (ΔA637) were taken as proxies for the number of cyanobacteria and the phycocyanin amount, respectively.

Fig 5.5(d) displays the calibration curves obtained with both wavelengths. The fitting with linear regression was good in both cases (R^2_{A750} = 0.99 and $R^2_{\Delta637}$ = 0.96). When normalized, both curves superimposed almost perfectly (inset Fig 5.5 (d)), demonstrating that the correct procedure provided coherent results indicating that (1) the correction procedure was adequate and (2) the ratio between the proxies reflected the cellular quota in phycocyanin. Among the tested dilutions, the highest absorbance variations were obtained with 400 µL of mother culture, this volume was used for further investigations. Higher volumes were not tested because the values of ΔA637 started to saturate (data not shown).
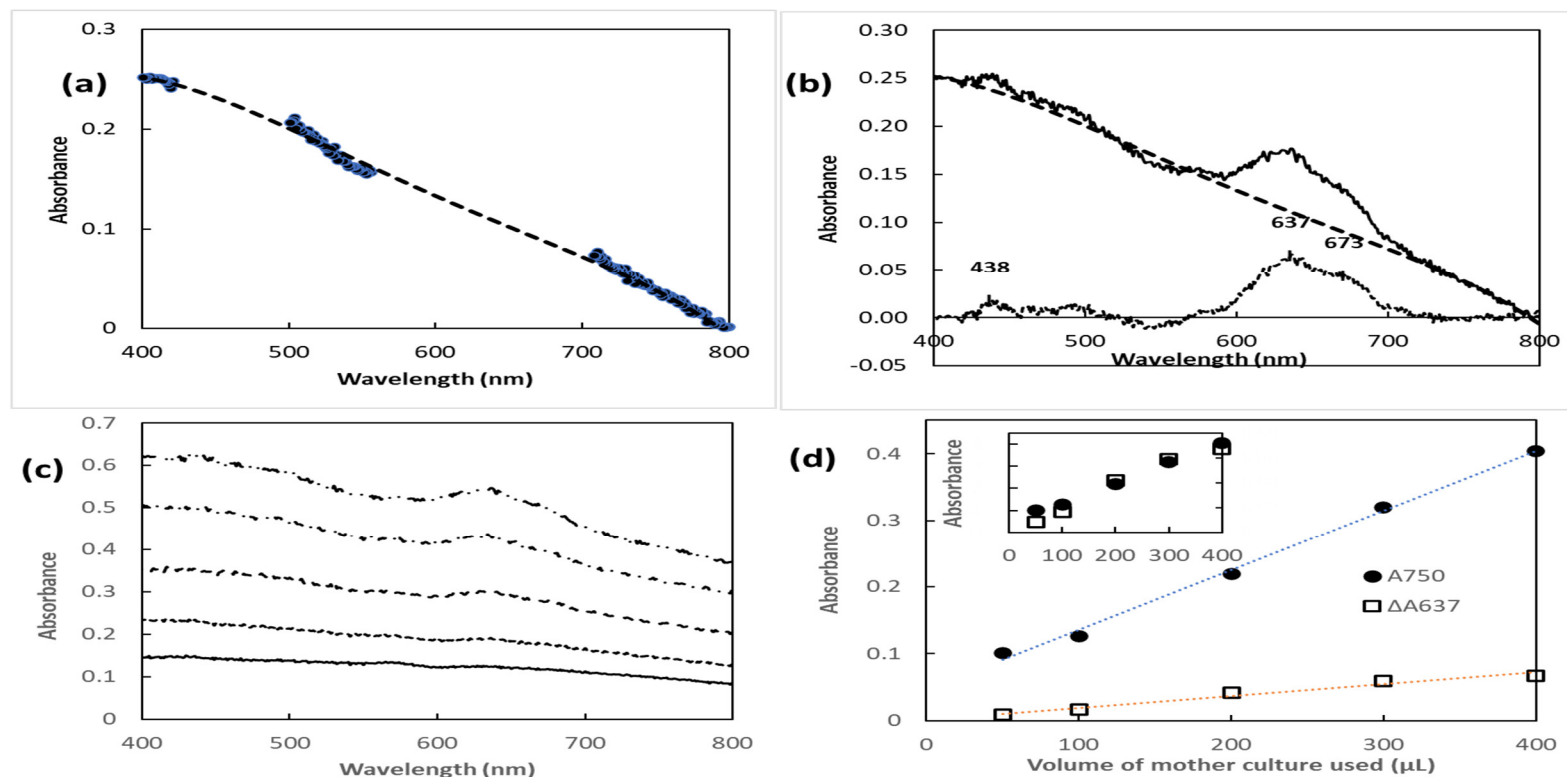
Fig 5.5: Calibration curve of Anabaena concentration (a) Mathematical fit (dashed curve) of the featureless absorbance spectrum recorded in situ (full line)   (b) Corrected absorbance spectrum (dotted curve) as the result of the operation 'original spectrum-minus-fitted baseline'   (c) In situ absorbance spectra recorded with 50 (full curve), 100 (dotted curve), 200 (dashed curve), 300 (dot-dash curve) and 400 μL (double dots-dash curve) of a mother cyanobacterial culture   (d) Calibration curves for A750 and ΔA637 measured in the absorbance spectra and the corrected absorbance spectra, respectively. In both cases, the absorbance varies linearly with the culture volume. The insert presents the normalized data showing that the amount of pigment per cell is constant in the range of tested volume (50-400 μL).

The procedure explained above was applied to the quantification of the chlorophyll *a* (665 nm) during the photocatalytic treatment of *Anabaena*. Fig 5.6 displays the kinetics of the changes in chlorophyll *a* that are specific of the photocatalytic treatment. Surprisingly, the kinetic presented a positive trend suggesting that during the treatment chlorophyll *a* was produced.
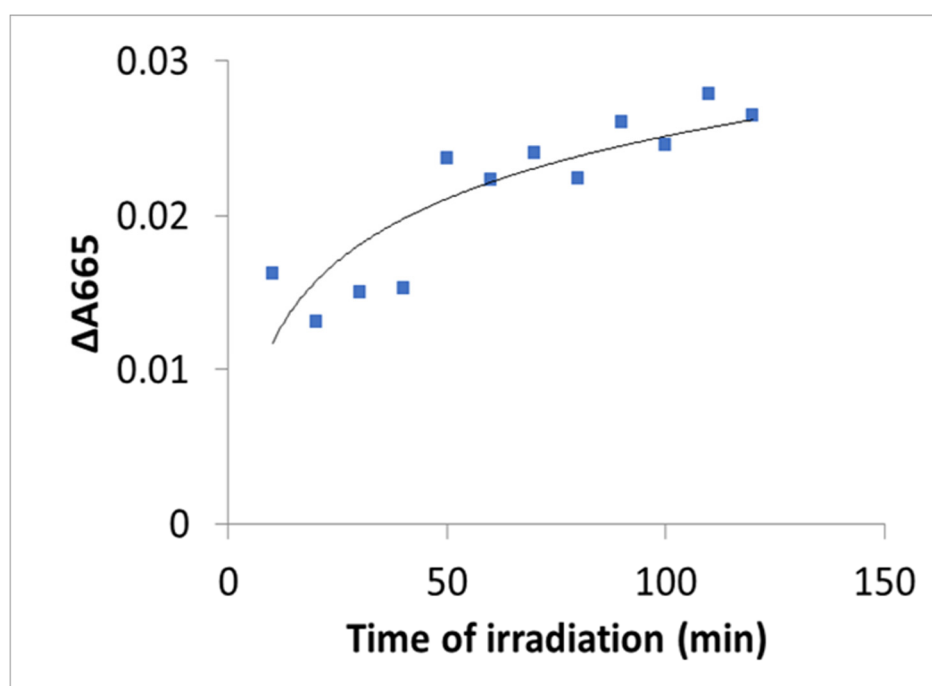
Fig 5.6: Kinetic of the absorbance at 665 nm changes specific to the photocatalytic treatment

Further studies are required to fully understand this result. The absence of effect can be due to the low disinfection activity for the *Anabaena sp.,* where a disinfection efficiency of more than 90 % was attained in bacterial disinfection with the same 1.5 GOT composites. This can be assumed due to the following reasons [57,58]. This alga possesses a one-dimensional multicellular chain structure, as shown in Fig 5.4, with a diameter between 3 and 5 µm. Therefore,

i. *Anabaena* cells are much larger when compared to *Escherichia coli*.

ii. The quanta of generated reactive oxygen species (ROS) by the interaction of 1.5 GOT pellet photocatalyst, and the light irradiation was not enough for the disinfection process.

iii. The age of the culture is an important parameter as the resistivity of the cells increases with time due to the protective coating which is formed outside the cell.

iv. The method used to follow the disinfection may be not adequate. Actually, irradiation using UVA, UVB or a combination of both during 24 h only slightly decreased the cellular quota in chlorophyll *a* [59]. For this reason, another method was used to follow the disinfection of media containing diatoms.

5.2.4 Photocatalytic disinfection of *Phaeodactylum tricornutum*

Phaeodactylum tricornutum is a marine unicellular diatom famous for its morphological modifications depending on the culture conditions [60,61]. In most conditions, it occurs under pennate morphotype as displayed in Fig 5.7. *P. tricornutum* was chosen for this work because under axenic conditions in artificial seawater *e.g.,* f2 medium, cells divide approximately once a day. In addition, its genome has been sequenced [61] and the literature about its physiology, biochemistry, stress response and biotechnological applications is abundant [62–64].
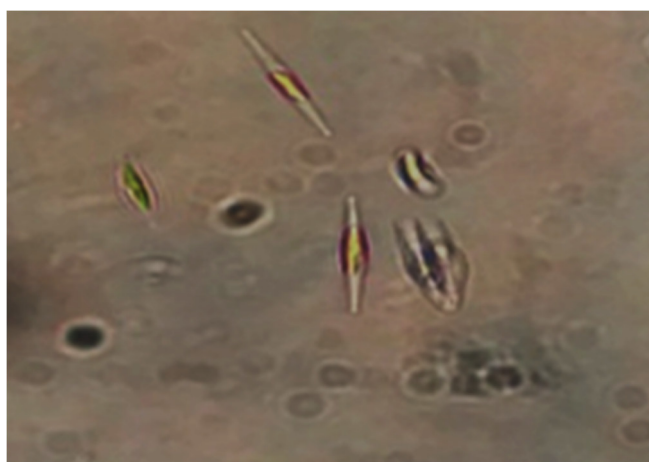

Fig 5.7. Microscopic pictures of the marine diatom Phaeodactylum tricornutum.

Using this diatom will extend the data about the potential of using the nanoparticles prepared in this study for decontamination of marine organisms, that also form blooms [3].

5.2.4 (a) Effect of light intensity on the diatom inactivation by photocatalysis

When working with microalgae and a photocatalytic material excited in the blue region, light play a dual role: it is used for generating ROS and to drive photosynthesis. If the former activity is positively impacted by light, the second one is not always because excess of photons and may increase the internal oxidative risk. To find a compromise between these two opposite actions of light, the effect of two light intensities on the efficiency of photocatalytic algal removal in freshwater media at 22 °C was studied in the absence (photolysis) and in the presence of the photocatalytic material. To modulate the intensity of the continuous light, an additional band pass filters, was added to the filter set defined above (see chapter 2, section 2.8.3 (b)). Both filters are characterized by a similar maximum transmission (Table 2.1) and differed by their respective transmission capacity: 68% for the daylight blue and 75% for the glass filter (see table 2.1 and Fig 5.2). Consequently, the addition of either filter to the experimental setup modified the light intensity but not the emission spectrum: it was around 1700 µmol photons/m^{-2}s with the former and around 2500 µmol photons/m^{-2} s with the latter.

Qualitatively, the kinetics of fluorescence are very similar. In each condition, a large chlorophyll fluorescence quenching developed rapidly after the onset of the continuous illumination. Interestingly, a transient variation was observed after the onset of the continuous illumination (open arrow in Fig 5.8). It is generally admitted that this slow and transient change reflects adjustments between the increasing capacity of the Calvin cycle to use the products of the light phase (ATP and NADPH). However, the interpretation might be more complex as shown with the green microalga *Haematococcus pluvialis* [65]. Despite its interest, this aspect will not be discussed here. During the period of darkness, the quenching mechanisms relaxed [66], as demonstrated by the decrease of the qN and Y_{NPQ} and the increase of qP (Fig 5.8 (c)-(d)). Interestingly, the cells recovered faster after the photocatalytic treatment than after the photolysis one.
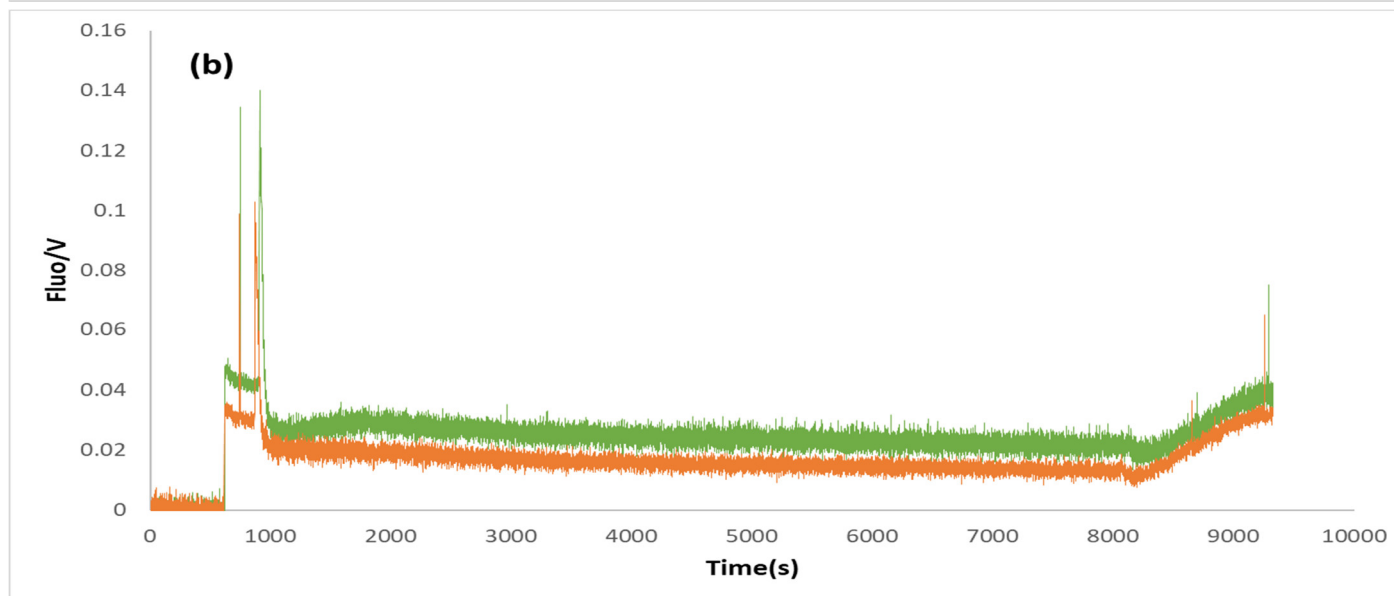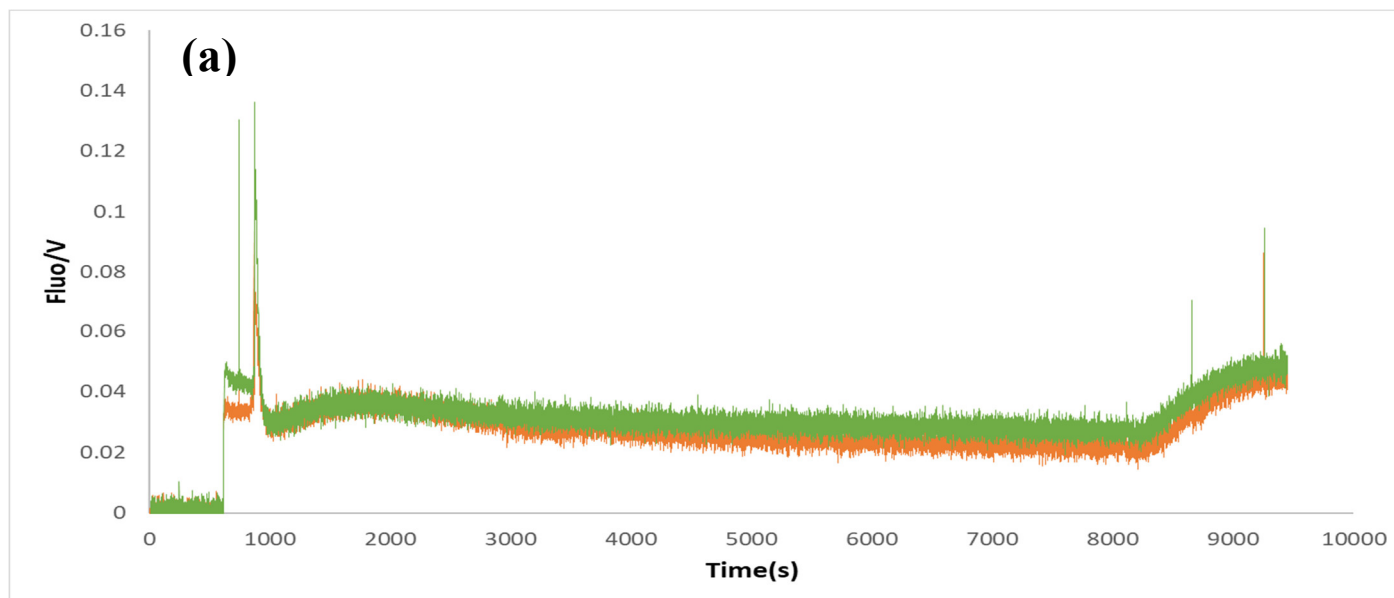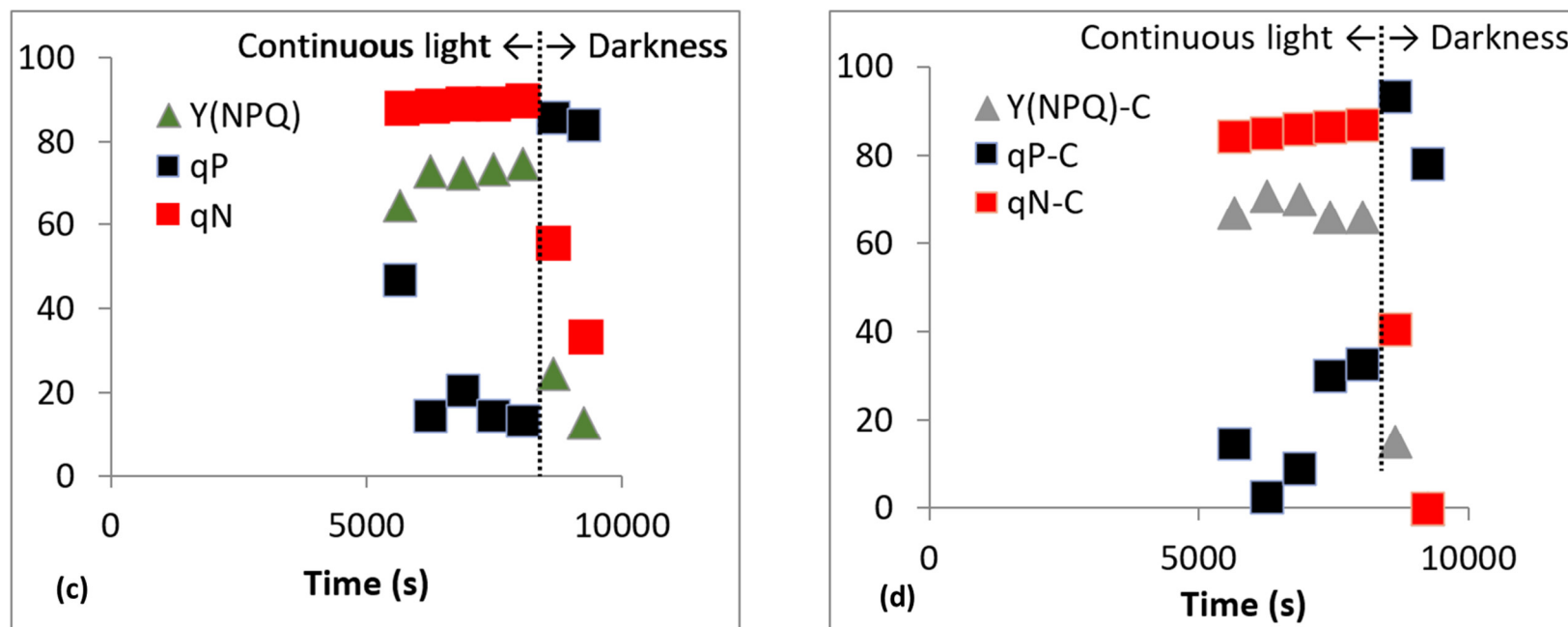
Fig 5.8. Effects of light intensity of the continuous illumination on the chlorophyll fluorescence recorded in the absence (green) or in the presence (orange) of photocatalytic material.

(a) light intensity of 1700 µmol photons/m^{-2}s (b) light intensity of 2500 µmol photons/m^{-2}s

(c-d) variations of quenching parameters during a period of darkness (20 min) following a continuous illumination of 1h 40 min in 1700 µmol photons/m^{-2}s (c) in the absence or (d) the presence of photocatalytic material

The open arrow points on the transient change in the chlorophyll fluorescence yield.

The effect of light intensity is also counter-intuitive because the recovery was faster under the highest light intensity. These apparently striking results may mean that the externally generated ROS, eventually combined with high light intensity have enhanced the defence mechanisms of the algae against the oxidative risk more efficiently than in the absence of externally generated ROS. These mechanisms would include the activation of the enzymatic arsenal (peroxidases, superoxide dismutase, catalases) inside the cells but also outside, with the externalization of superoxide dismutase in the extracellular medium [67] (for a review, see [68]). This last possibility may be efficient enough to decrease the externally generated ROS under a level lower than under the one generated during lysis conditions. Altogether, these reasonings allow me to propose that diatoms might also be able to sense the externally generated ROS. To this end, it is worth to mention that ROS sensors located in plasma membranes for ROS detection in plant cell apoplast have been reported (for a review, see [66]).

5.2.4 (b) Effects of diatom density on diatom inactivation by photocatalysis

Two different concentrations of diatoms were tested in f2 media to study the effects of algal density on the photocatalytic disinfection of *P. tricornutum*. Fig 5.9 compares the chlorophyll fluorescence kinetics recorded in the absence (photolysis) and the presence of a pellet containing nanoparticles (later denoted as the photocatalytic material). The kinetics are normalized on the F_M level. Clearly, the signal-to-noise ratio is much lower using a dense culture. As explained on the materials and methods section (chapter 2), the chlorophyll fluorescence yield decreased during the actinic illumination until a minimum level is reached. However, the decrease in photolysis and photocatalysis differed qualitatively, *i.e.,* a stationary level, F_S, is not really reached under photocatalysis conditions, and quantitatively, *i.e.,* the quenching of the chlorophyll fluorescence is more intense under photocatalysis conditions (Fig 5.9). Quenching analysis according to the puddle and lake models are presented in Fig 5.9 (c) and Fig 5.9 (d).

Regardless the presence of the photocatalytic materials, the values of Y_{II} decreased very rapidly after the onset of the continuous light showing the rapid saturation of PSII in these conditions (close diamonds: Y_{II-L} and open diamonds: Y_{II-C}). This was expected because photosynthesis in *P. tricornutum* starts to be saturated around 300

µmol/m^{-2}s [69], a light intensity over 1000 µmol/m^{-2}s constitute a strong stress [63]. This stress activates defence mechanisms, including the nonphotochemical quenching. Whereas in the puddle model, only the parameter qN is used to describe the energy lost non photochemically. In the lake model, the two parameters are used, the first one (Y_{NPQ}), reflects the energy lost by the regulated pathways, whereas the second one (Y_{NO}), reflects the other energy loses *i.e.* the nonregulated pathways [28]. During the continuous illumination, the parameter Y_{NO} remained low and constant, suggesting that the main pathways for deexcitation are the regulated ones, reflected by the changes of Y_{NPQ} (Fig 5.9). The values of Y_{NPQ} recorded in the absence of the photocatalytic material were weaker than in its presence suggesting that the photocatalyst is responsible for an additional stress to the algae (Fig 5.9). A similar trend was also observed for qN parameter, but the difference was weaker (Fig 5.9).
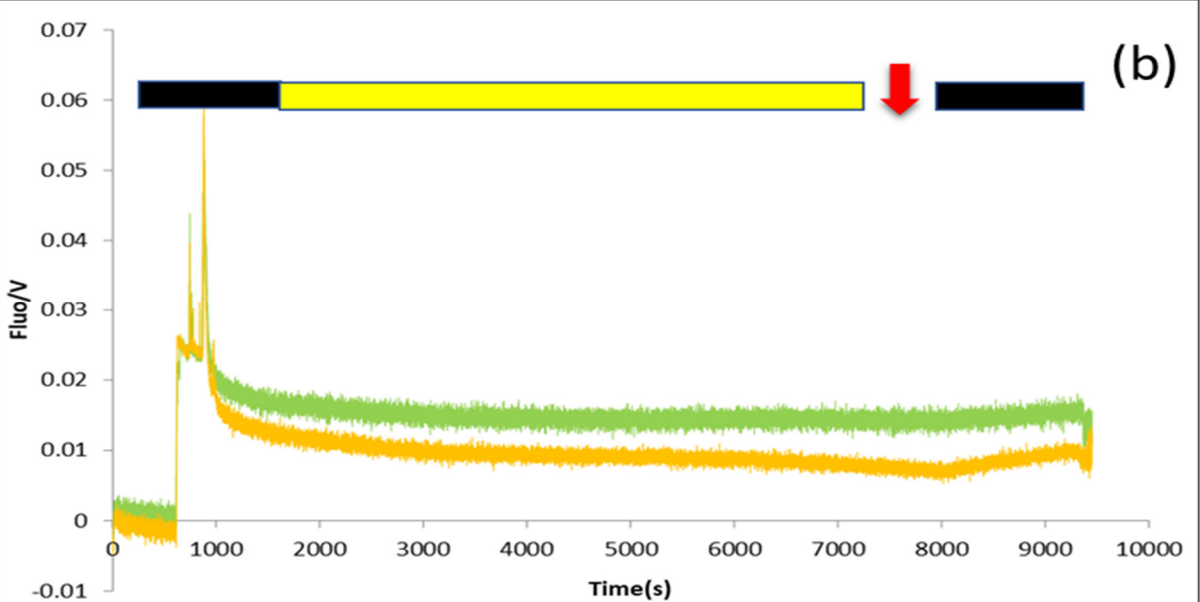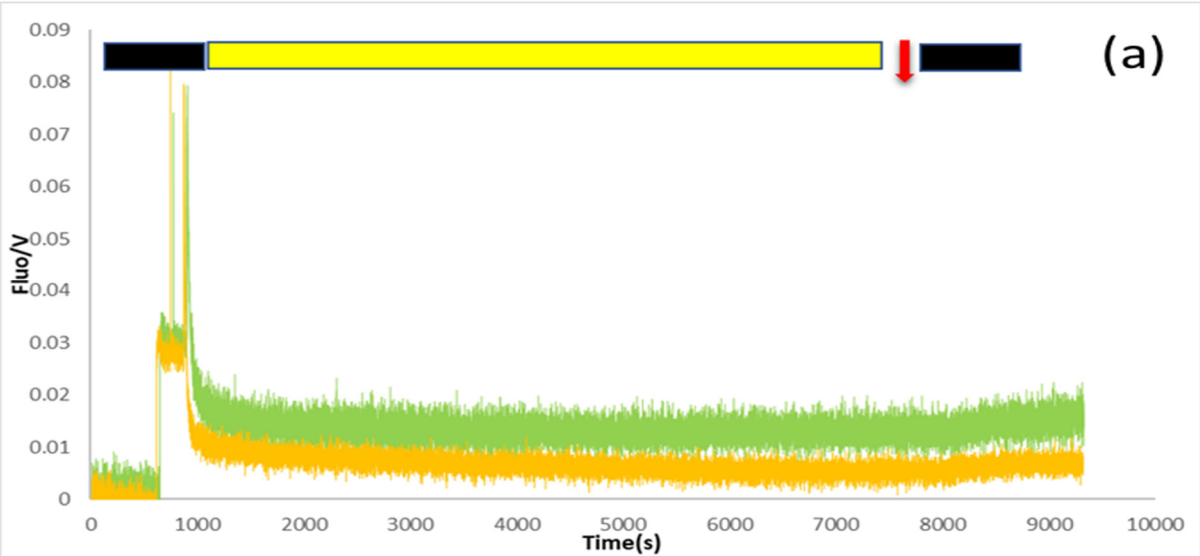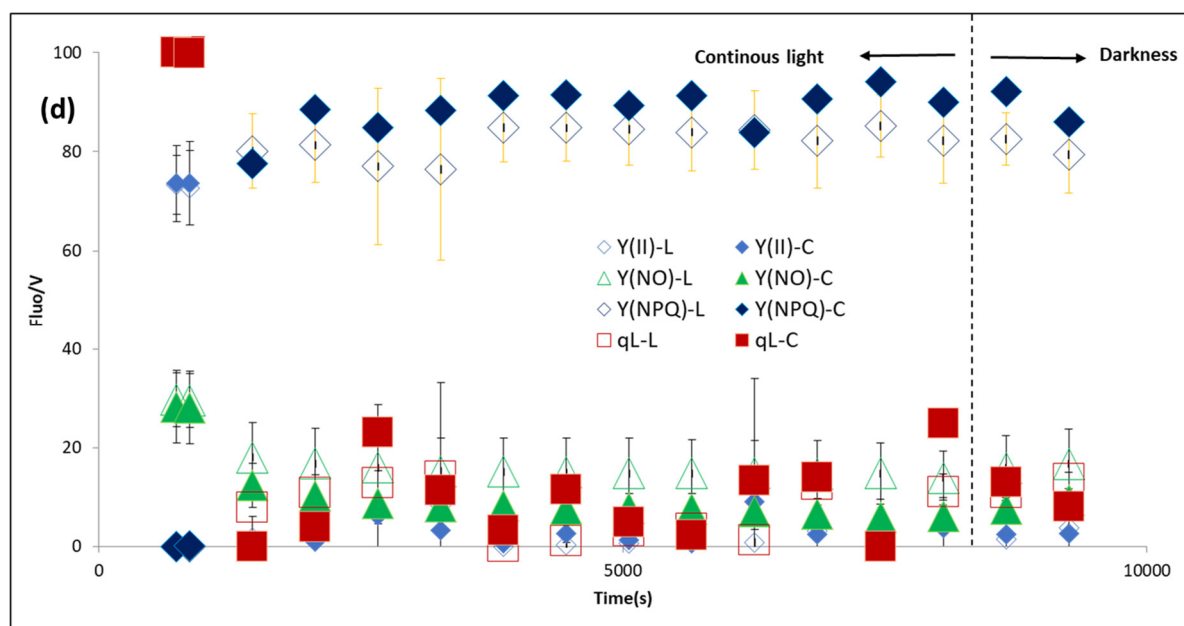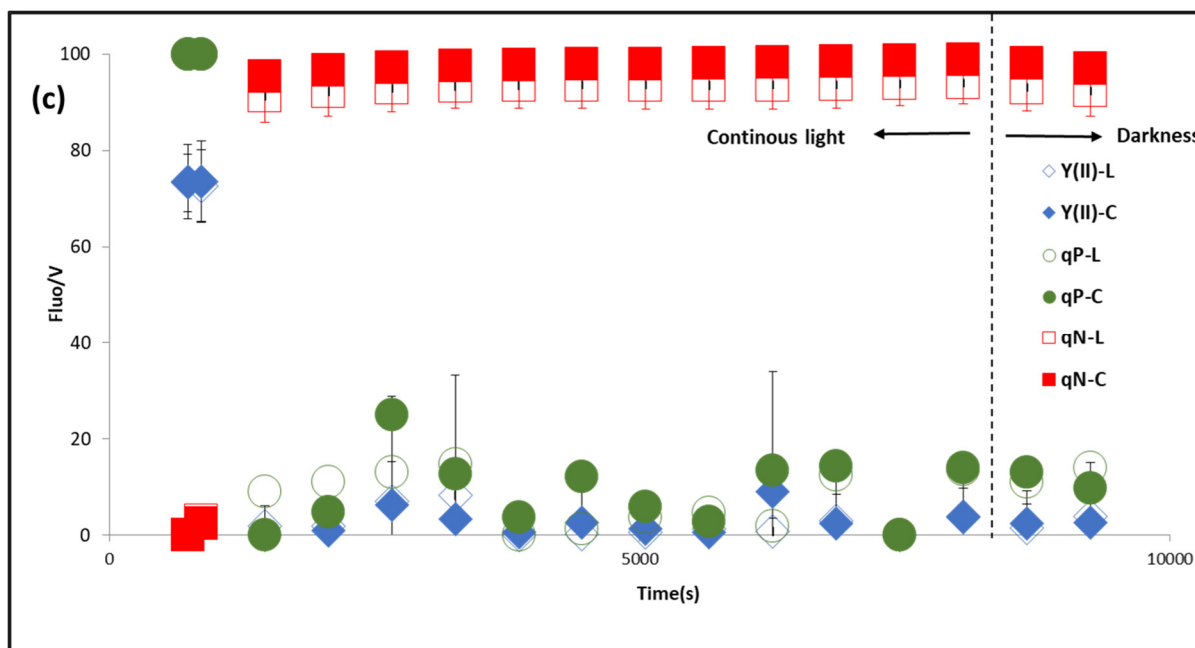
Fig 5.9. Impact of the cell density on the variations of the chlorophyll fluorescence levels in the absence and in the presence of the photocatalytic material. (a-b) Typical chlorophyll fluorescence curves recorded with (a) a low and (b) a high cell density in the absence (green) or in the presence (orange) of the photocatalytic material. (c-d) Variations of the chlorophyll fluorescence yield and parameters of (c) the puddle and (d) lake models describing the response of the microalgae to the environmental conditions.

5.2.4 (c) Effect of time on the destruction of algal cells

The data described in the previous sections indicated that increasing the light intensity to boost externally ROS production might have a counter-productive effect on microalgal cell destruction because it would enhance the intensity of the defence mechanisms. If we take into account that (1) these defence mechanisms are costly from the cell energy and $NAD(P)H/NAD(P)^+$ consumption point of views [67], (2) under prolonged light irradiation, photosynthetic activity is saturated and even reduced, and (3) externally produced antioxidative enzymes have a short half-life time (human-SOD: 7-20 h [70]) and therefore have to be regularly renewed. The following hypothesis was formulated according to which increasing the duration of the continuous light treatment over 1.5 h may have a positive effect on the disinfection process. Consequently, the effects of the duration of the continuous illumination on the destruction of *P. tricornutum* was studied. Four different timings were selected: 0.5, 1, 2, and 4 h. Slow kinetics of chlorophyll fluorescence were recorded (Fig. 5.10) and analysed (Fig 5.11) as explained earlier (see chapter 2, section 2.8.3 (b2)).
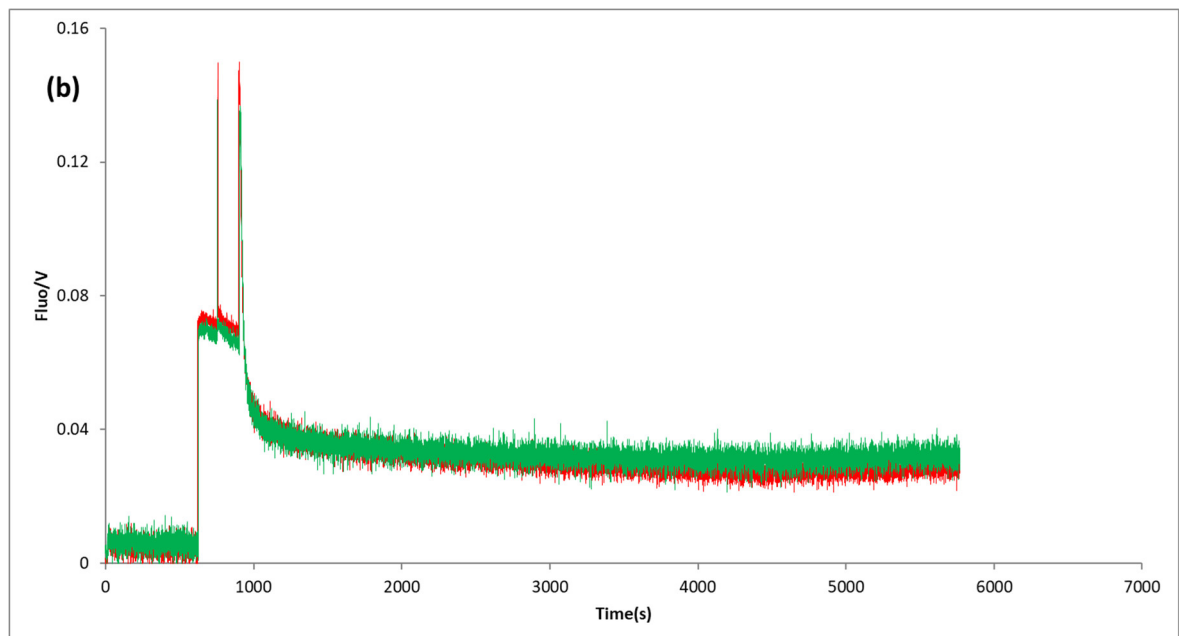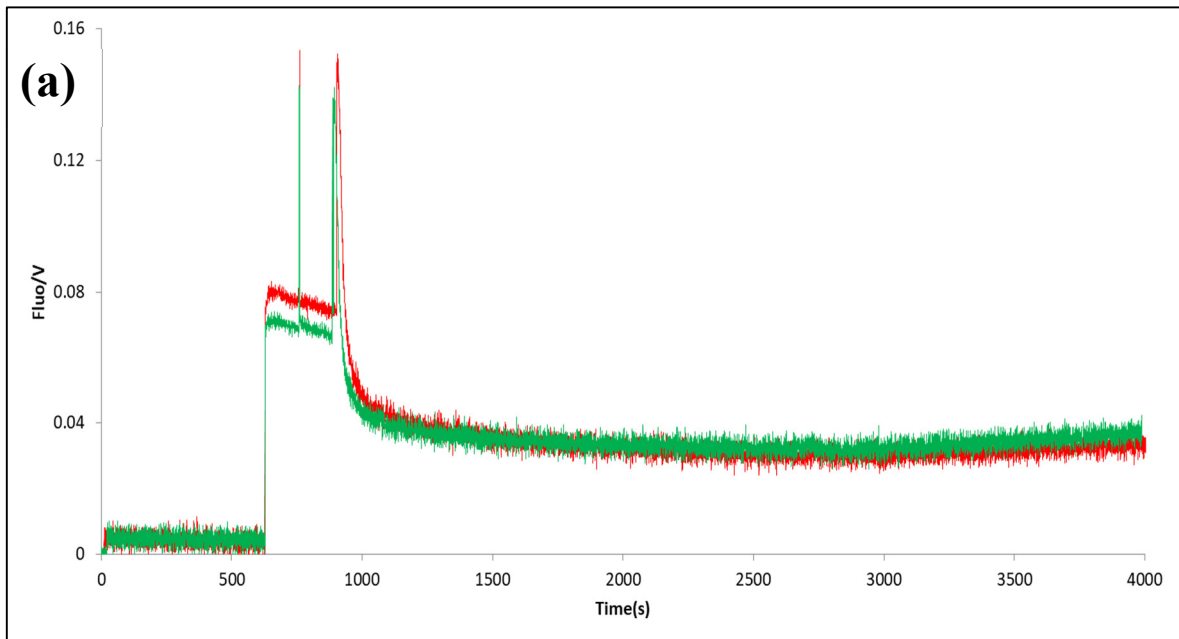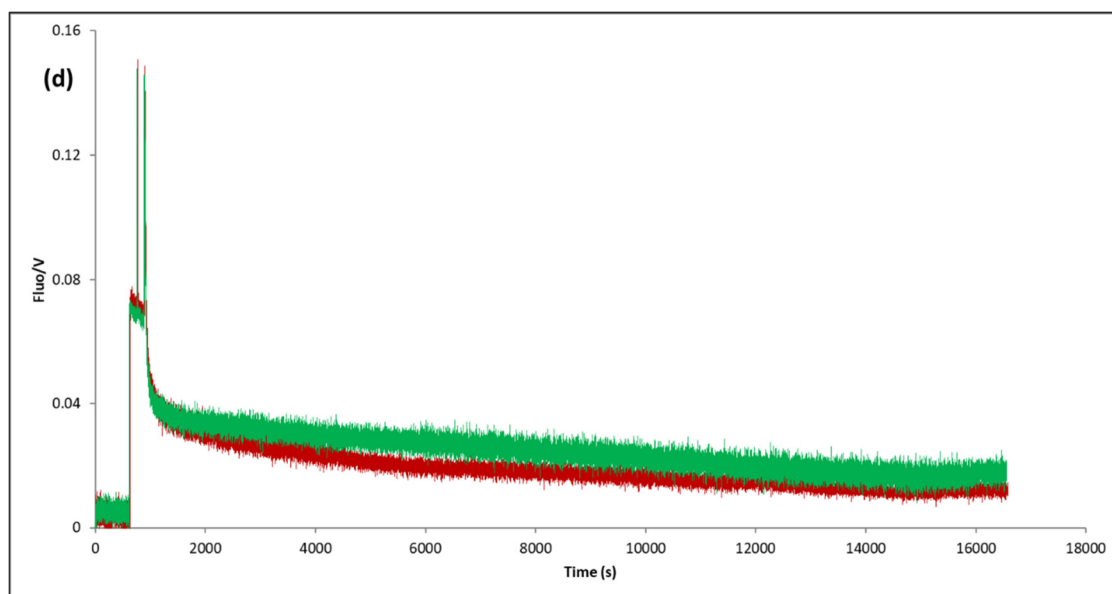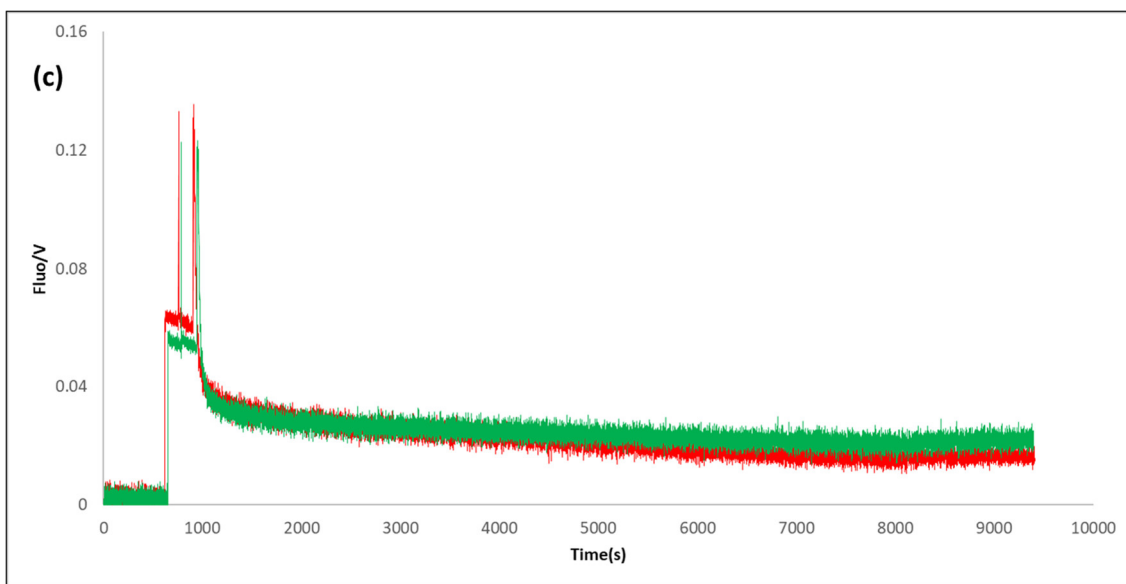
Fig 5.10. Effects of the duration of the continuous illumination on the chlorophyll fluorescence induction curves recorded in the absence (green) or on the presence (yellow) of photocatalytic material.

(a) 30 min of illumination (b) 1h of illumination

(c) 2h of illumination (d) 4h of illumination

As already mentioned, the curves recorded in the absence or in the presence of the photocatalytic material appeared similar. With the increase of the duration of the continuous illumination, differences appeared more clearly: (1) after two hours of continuous illumination, the F_S level was no longer stationary in the presence of photocatalytic material and (2) after 4 h of continuous illumination either treatment resulted in a nonstationary F_S level.
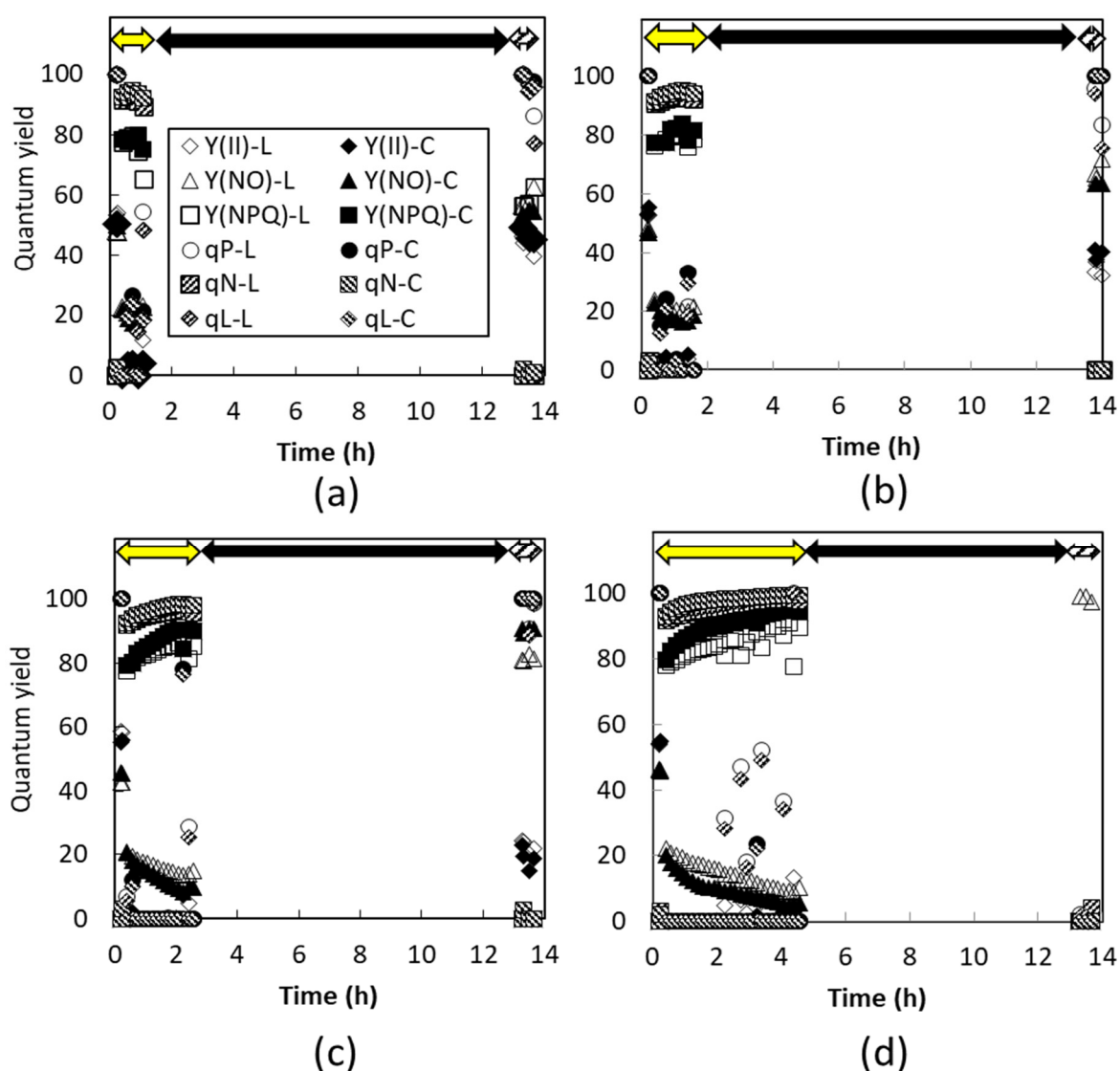
Fig 5.11. Variations of the chlorophyll fluorescence during the increasing continuous illumination and after one night of recovery (a): 0.5 h of continuous illumination (b) 1h of continuous illumination (c) 2 h of continuous illumination (d) 4 h of continuous illumination The period of illumination and of recovery are indicated by yellow and black arrows, respectively. The dashed arrows indicate the period of test of the quality of recovery.

From the qualitative point of view, when the continuous illumination time was under 1 h, the kinetics of the different parameters followed the same trends regardless the presence or the absence of the photocatalytic material. For instance qP, which reflects the actual fraction of PSII being in the open state [18], decreased during the continuous illumination and reached the initial values during the recovery period of darkness (Fig 5.11 (a),(b)). This suggests that after 1h of continuous illumination, either treatment was not efficient in killing diatoms. This agrees with the results presented above (Fig. 5.11). For longer continuous illuminations, clear differences appeared in the responses of the microalgae to the photocatalytic treatment. The differences were more intense when the parameters describing the lake model are used. When the continuous illumination exceeded 1 h, the intensity of Y_{NPQ} became more intense in the presence of the photocatalytic material than in its absence (squares in Fig 5.11(a), (b)), suggesting that the need to dissipate the excess of absorbed energy as heat through regulated mechanisms (*e.g.,* the xanthophyll cycle) is higher during the photocatalytic treatment. Mathematically (see equation 6 in table 2.2), Y_{NO}, which reflects the excess of energy dissipated through the nonregulated mechanisms, became much less intense in the presence of the photocatalytic material. Interestingly, after 4 h of continuous illumination, any of the energy dissipation mechanism, but Y_{NO-L}, relaxed (Fig 5.11 (d)) after one night of darkness, suggesting that the presence of the photocatalytic material might have an additional effect on the photosynthetic activity of diatoms.

To provide a better view of the phenomenon, the variations of Y_{NO} in the absence (Y_{NO-L}) against those observed in the presence (Y_{NO-C}) of the photocatalytic material have been plotted (Fig 5.12). When the levels of Y_{NO} before the illumination (red symbols) are compared to those reached after one night of relaxation (black symbols), a progressive lack of proportionality in the development of Y_{NO} was observed, demonstrating the inability of the microalgae irradiated in the presence of the photocatalytic material to recover during the night. After 2 h of continuous illumination, the recovery was around 50%, whereas it was around 80% in the absence of the photocatalytic treatment. After 5 h of continuous illumination, the diatoms did not recover at all (Fig 5.12 (a)).
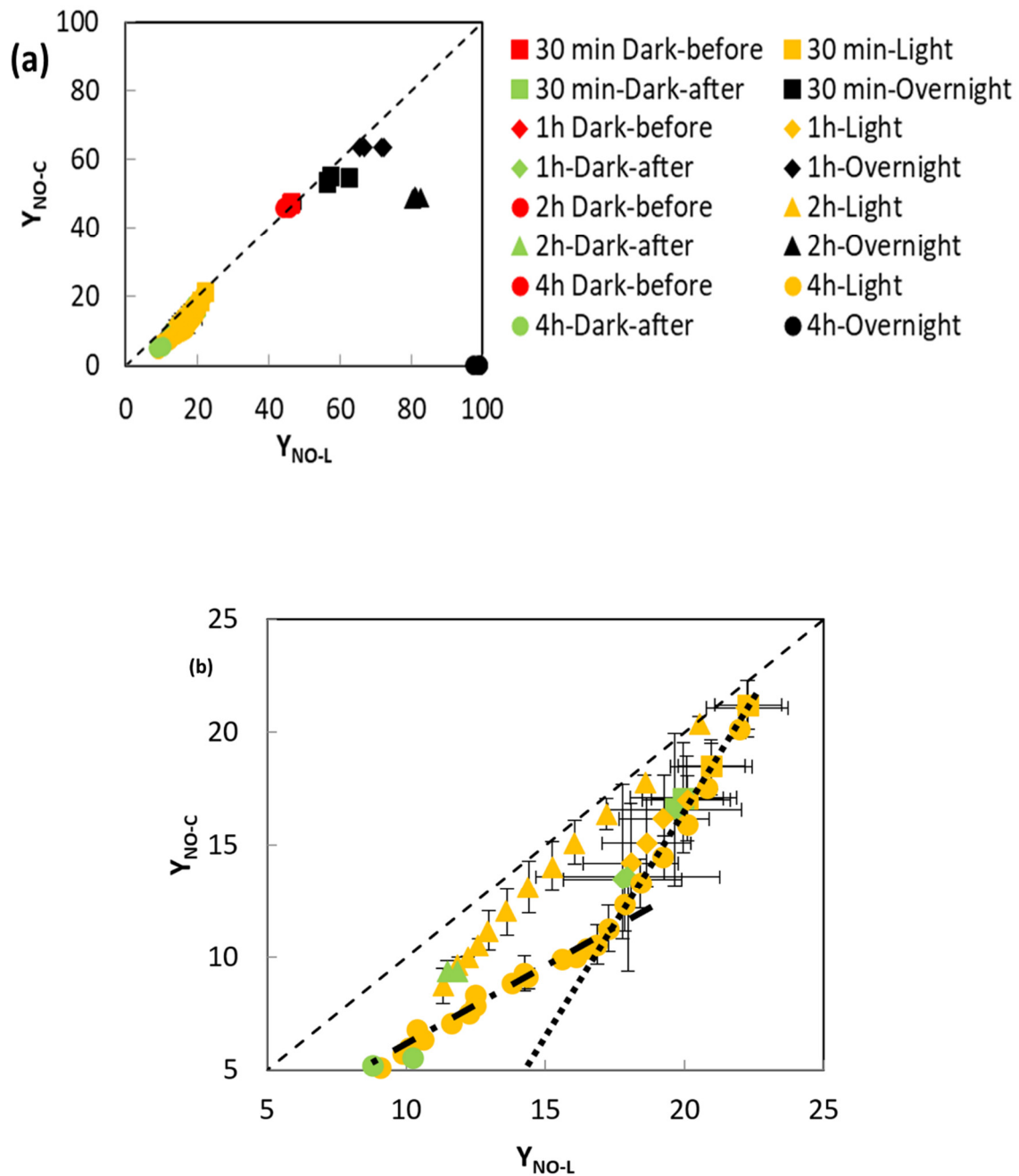
Fig 5.12. Variations of the parameters Y_{NO} during continuous illumination of diatoms in the absence (Y_{NO-L}) or in the presence (Y_{NO-C}) of photocatalytic material (a) Variations before (red symbols), during illumination (yellow), after a dark period of 20 min following the illumination (green) and after one night of darkness (black) (b) Variations during illumination (yellow) and after a dark period of 20 min following the illumination (green). The dashed line figures out proportional variations of Y_{NO-L} and Y_{NO-C}. The dotted and dot dashed lines represent the slopes of the two phases of the variations of Y_{NO-C} versus Y_{NO-C}.

The progressive lack of recovery is likely linked to the progressive oversaturation of the mechanisms that dissipate the excess of absorbed energy as demonstrated in Fig 5.12 (b). In this panel are compared the values of Y_{NO-L} as a function of Y_{NO-C} during continuous illuminations at different durations. It clearly appeared that the values of Y_{NO-C} are affected more quickly in the presence of the photocatalytic material. The kinetic presents two phases. The first one (dotted line) suggests that at the start of continuous illumination (up to 2 h), the diatoms in the presence of the photocatalytic material are essentially affected. This can be due to the rapid adsorption of microalgae onto the surface of pellet of the nanocomposite, thereby causing the immediate destruction of cells through ROS in the vicinity of the photocatalyst pellet. It can also be assumed that during this phase, the microalgal cells could be trapped over the surface of the pellet because of porosity.

Beyond 2 h of illumination (dot dashed line), the diatoms treated in the absence of the photocatalytic material were also affected. This condition is however completely reversed during the dark period, which was not the case for illuminated diatoms in the presence of the photocatalytic material (Fig 5.12 (a)). No recovery could take place because the diatoms illuminated in the presence of the photocatalytic material are:

- **Bleached**: The absorbance peaks reflecting the presence of chlorophyll *a* (675 nm) and chlorophyll c (645 nm) and carotenoids (400-500 nm) have disappeared (compare Fig 5.13 (b) with Fig 5.13 (a)). The pigment disappearance results in a visual impression of a clear solution (Fig 5.13 (c)).
- **Disintegrated**: Microscopic observations revealed the low presence of alive diatoms in the photocatalytic sample when compared to the dead diatoms (Fig 5.13 (d) *versus* Fig 5.13 (c)).
- **Dead**: In addition to scarcity, those diatoms that were observed no longer viable (Fig 5.13 (d)). This conclusion is because cell viability is lying on plasmalemma integrity. Therefore, cell staining with a dye that is not penetrating naturally in cell unless plasmalemma has been disrupted can be used as a proxy of cell viability. Evans's blue, an azo dye exhibits this property [66], was used for such a purpose. The samples were observed after photocatalysis for maximum uptake of blue coloration, pointing out to the lost membrane integrity of the algal cells.

These results heavily contrast with those obtained without the photocatalytic treatment, with diatoms viable from the physiological point of view (Fig 5.13 (a), (c), (e)). The photographs gave visual confirmation of the disinfection activity and clear evidence for removing algal cells from the samples during photocatalysis. No change in the colour of the photolytic sample was seen Fig 5.13 (e). In panel (d), black material corresponding to detached nanomaterial was observed in the solution. It is likely due to the erosion of the pellet during the experiment. This observation raises the question about the reusability of the pellets. The reusability test was performed for the pellets used for the studies. The above-mentioned experimental details are the mean average of eight trials using the same 1.5 GOT pellet.

And therefore, to have more evidence in ROS generation by the same pellet, the methylene blue dye degradation test was performed. The results were quite convincing as there was a substantial decline in the dye concentration after 2 h of visible light irradiation. The graph (Fig 5.15) depicts the reusability efficiency of the pellet, and this pellet has not stopped generating the reactive oxygen species responsible for the photocatalytic activity. Overnight incubation of the samples after photocatalysis and photolysis was carried out to have a strong confirmation of the destruction of the algal cells. The dark incubation was performed by continuous stirring and with the addition of sodium bicarbonate as the carbon source to avoid the starving of the cells during incubation. After the overnight incubation, the chlorophyll fluorescence measurement was performed to observe absorption peaks representing the presence of chlorophyll pigment. Surprisingly, the dark incubation test shown the destruction or removal of chlorophyll pigment. In contrast, the photolytic samples showed strong peaks of chlorophyll content, indicating the liveness of the *diatom* cells (Fig 5.14). This also proves that there was no chance of recovery in the photocatalytic sample.
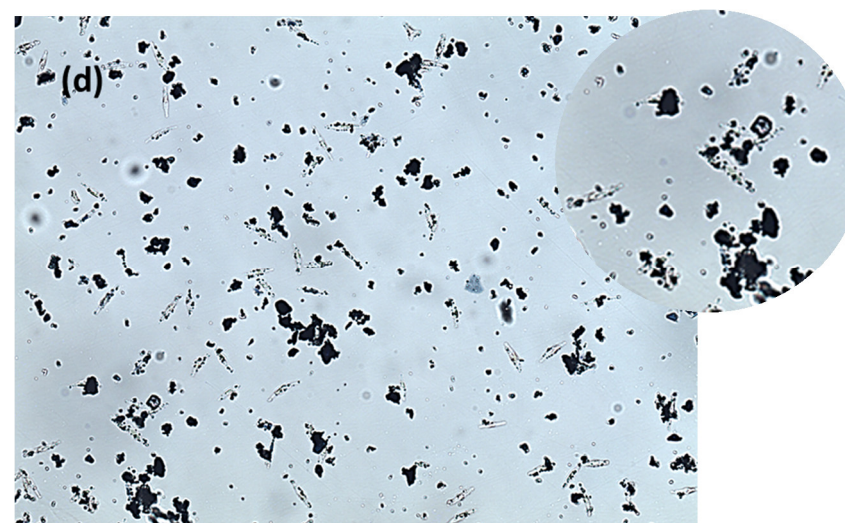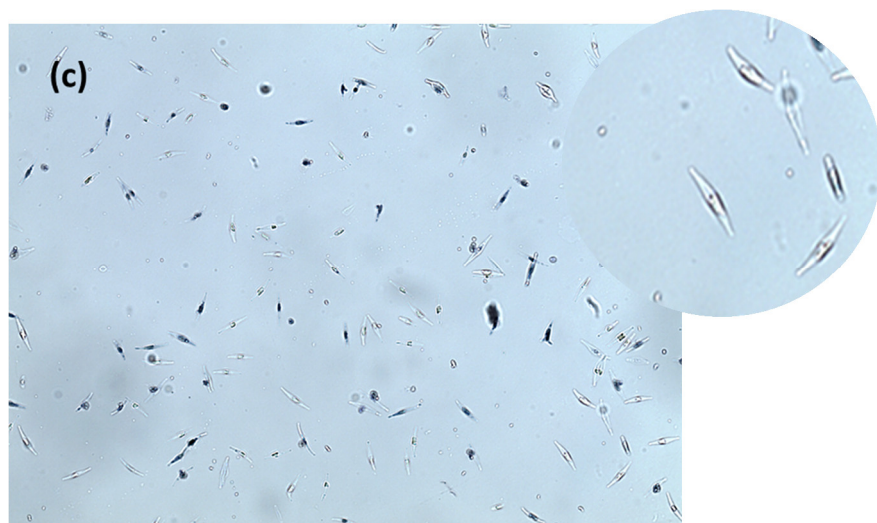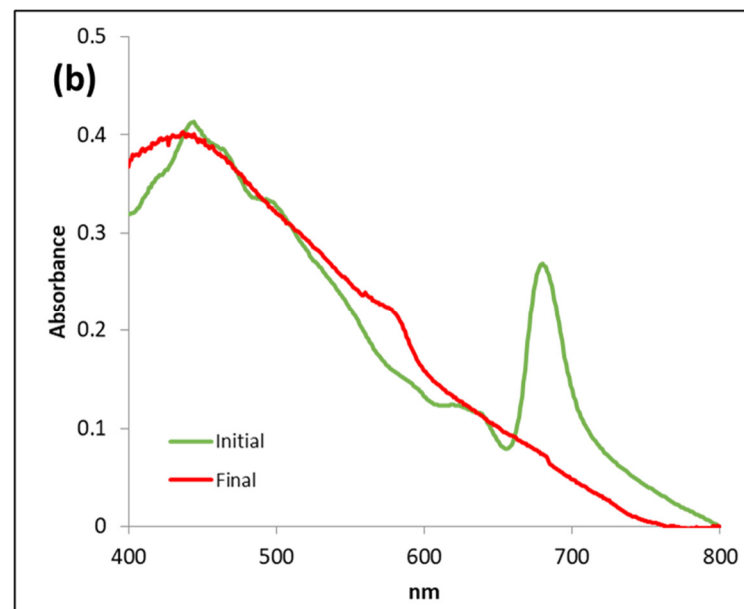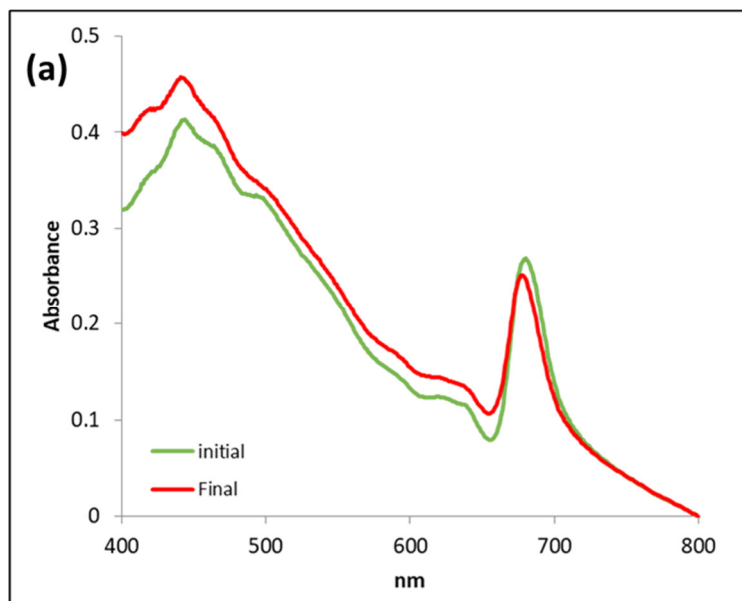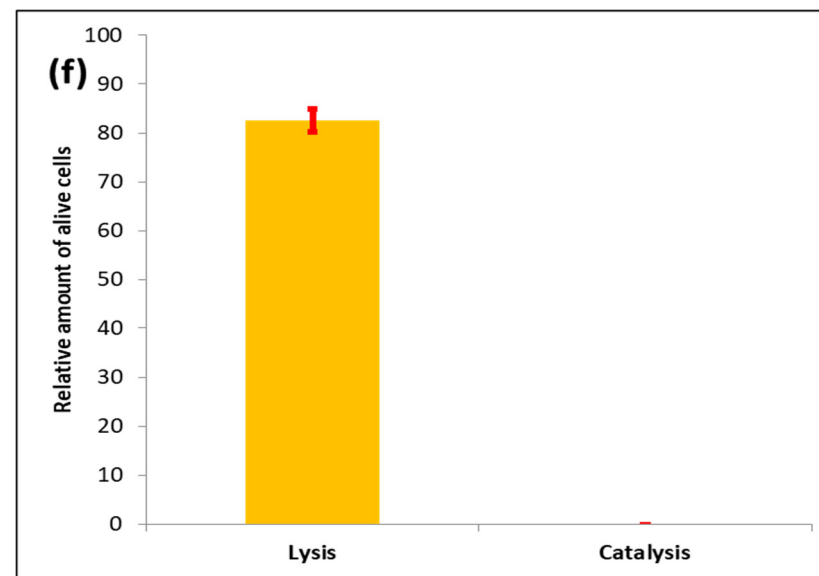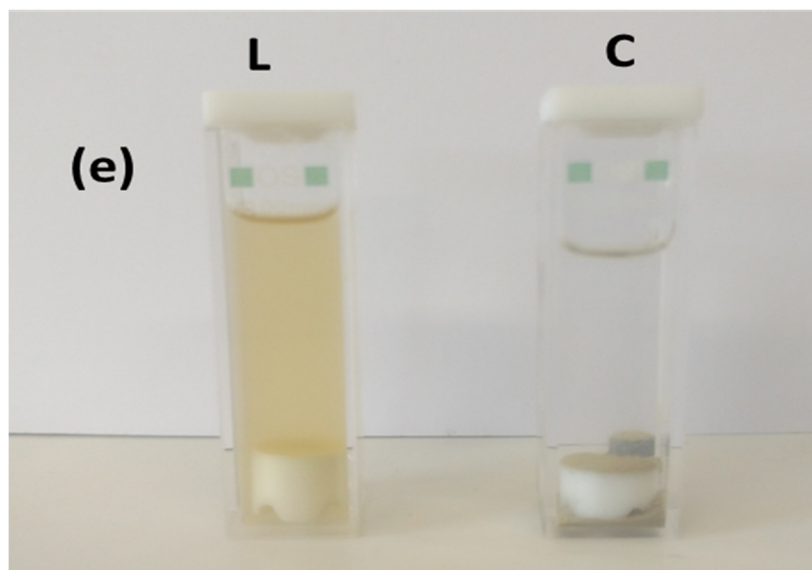
Fig 5.13 Characterization of the cells illuminated during 4 h in the absence or the presence of photocatalytic materials

(a,b) room temperature absorbance spectra in the absence (a) or (b) the presence of photocatalytic material.

(c,d) bright field observations of the diatoms stained with Evans blue, a marker of cell viability

(e) displays a visual view of the culture after the treatments.

Pigment discoloration after photocatalysis (marked C) while no change in the sample after photolysis (marked L)

(f) Graph depicting the relative number of alive cells after photolysis and photocatalysis where 376×10^4 cells/mL (triplicates) of alive cells was observed after counting photolysis sample which was nill in photocatalytic sample
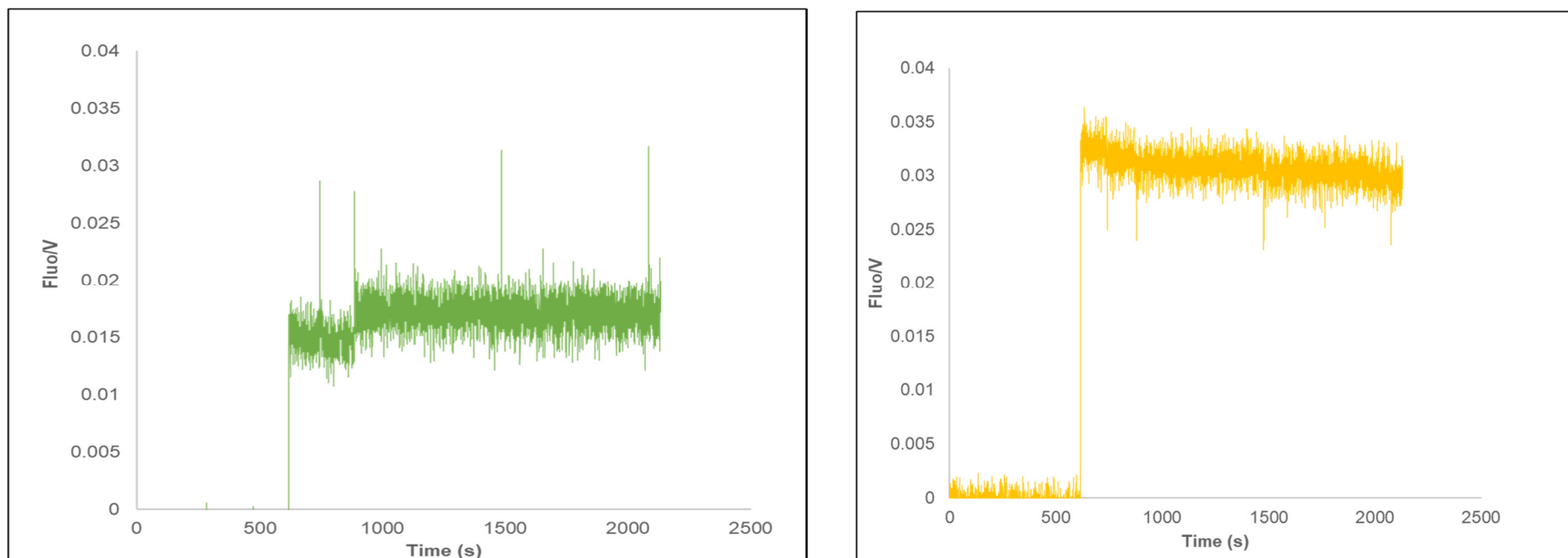
Fig 5.14: Overnight dark incubation test with graph representing peaks associated with chlorophyll a (green color) and inverted peaks with no chlorophyll a presence (orange color)
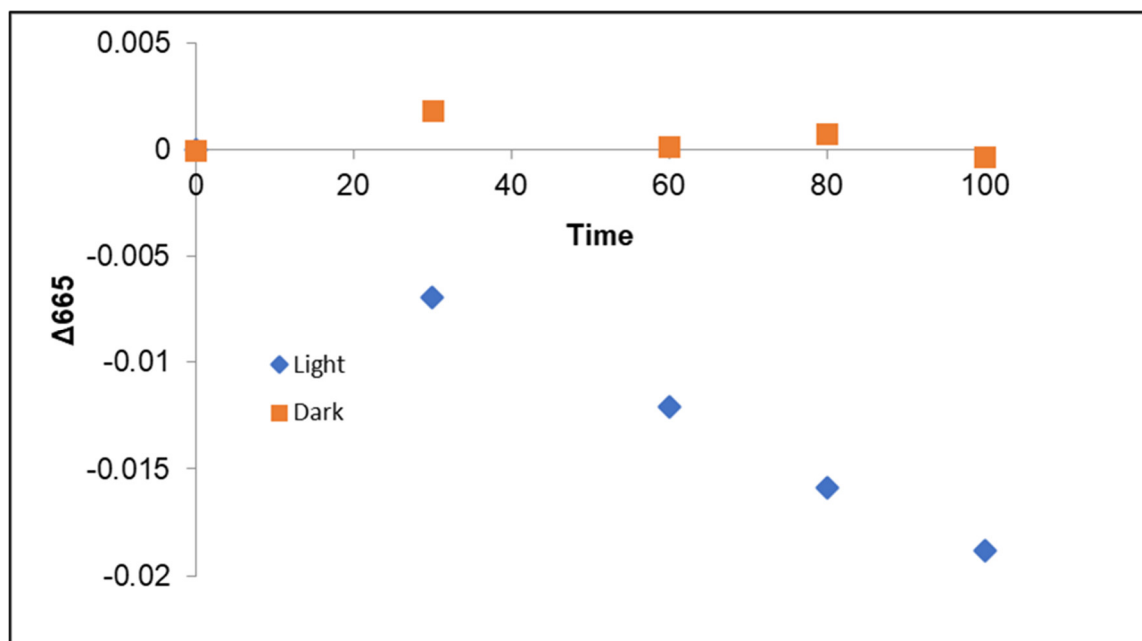
Fig 5.15: Reusability test by methylene blue dye degradation

5.3 Conclusion

Through various trial and error method, several experiments were carried out to bring an experimental set up for the microalgal disinfection study. In this research, live cyanobacterial and microalgal cells were used throughout the experiments without interrupting their normal photosynthetic activity instead of using cyanotoxins or algal toxins that cause harmful agal blooms in drinking water. Therefore, various possible mechanisms for the microalgal disinfection can be assumed and has been discussed in this chapter. The results obtained after the preliminary studies on the photocatalytic destruction of the microalgae were quite promising for future application. One of the innovative ideas formulated in this work was the development of pellets made up of the synthesized, optimized, and characterized nanocomposites, which can diminish the recalling disadvantage of nanoparticle release in the water treatment. These results are the very first to be reported based on the composite used and the type of algae studied. Further studies are necessary to have a solid basis for the reasons behind the mechanism of microalgal photocatalytic disinfection.

References

[1]   B. Schoefs, B. Van de Vijver, C.E. Wetzel, L. Ector, Introduction : From diatom species identification to ecological and biotechnological applications, Bot. Lett. 167 (2020) 2–6. https://doi.org/10.1080/23818107.2020.1719883.

[2]   H. Horn, Growth of Blue-Green Algae in the Saidenbach Reservoir and its Relationship to the Silicon Budget, Int. Rev. Der Gesamten Hydrobiol. Und Hydrogr. 75 (1990) 461–474. https://doi.org/10.1002/iroh.19900750404.

[3]   G. Schleyer, A. Vardi, Algal blooms, Curr. Biol. 30 (2020) R1116–R1118. https://doi.org/10.1016/j.cub.2020.07.011.

[4]   D. Sanchis, D. Carrasco, C. Padilla, F. Leganés, E. Fernández-Valiente, F.F. Del Campo, A. Quesada, Spatial and temporal heterogeneity in succession of cyanobacterial blooms in a Spanish reservoir, Ann. Limnol. 38 (2002) 173–183. https://doi.org/10.1051/limn/2002015.

[5]   R.S. Sathishkumar, A. Sundaramanickam, G. Sahu, A.K. Mohanty, T. Ramesh, S.A. Khan, Intense bloom of the diatom Hemidiscus hardmanianus (Greville) in relation to water quality and plankton communities in Tuticorin coast, Gulf of Mannar, India, Mar. Pollut. Bull. 163 (2021). https://doi.org/10.1016/j.marpolbul.2020.111757.

[6]   S. Plude, G.N. Demirer, Valorization of harmful algal blooms and food waste as bio-methane, Environ. Prog. Sustain. Energy. 40 (2021). https://doi.org/10.1002/ep.13561.

[7]   S. Sakamoto, W.A. Lim, D. Lu, X. Dai, T. Orlova, M. Iwataki, Harmful algal blooms and associated fisheries damage in East Asia: Current status and trends in China, Japan, Korea and Russia, Harmful Algae. 102 (2021). https://doi.org/10.1016/j.hal.2020.101787.

[8]   O.G. Oyeku, S.K. Mandal, Historical occurrences of marine microalgal blooms in Indian peninsula: Probable causes and implications, Oceanologia. 63 (2021) 51–70. https://doi.org/10.1016/j.oceano.2020.08.008.

[9]   Z.W. Kundzewicz, Some for all, forever — sustainable development and management of water resources, Int. J. Sustain. Dev. World Ecol. 8 (2001) 290–298. https://doi.org/10.1080/13504500109470087.

[10]   J. Jeevanandam, A. Barhoum, Y.S. Chan, A. Dufresne, M.K. Danquah, Review on nanoparticles and nanostructured materials: History, sources, toxicity and regulations, Beilstein J. Nanotechnol. 9 (2018) 1050–1074. https://doi.org/10.3762/bjnano.9.98.

[11]   R. Gupta, H. Xie, Nanoparticles in daily life: Applications, toxicity and regulations, J. Environ. Pathol. Toxicol. Oncol. 37 (2018) 209–230. https://doi.org/10.1615/JEnvironPatholToxicolOncol.2018026009.

[12]   A. Smerilli, S. Balzano, M. Maselli, M. Blasio, I. Orefice, C. Galasso, C. Sansone, C. Brunet, Antioxidant and photoprotection networking in the coastal diatom skeletonema marinoi, Antioxidants. 8 (2019). https://doi.org/10.3390/antiox8060154.

[13]   K. Roháček, M. Bertrand, B. Moreau, B. Jacquette, C. Caplat, A. Morant-Manceau, B. Schoefs, Relaxation of the non-photochemical chlorophyll fluorescence quenching in diatoms: Kinetics, components and mechanisms, Philos. Trans. R. Soc. B Biol. Sci. 369 (2014). https://doi.org/10.1098/rstb.2013.0241.

[14]   U. Schreiber, C. Klughammer, Evidence for variable chlorophyll fluorescence of photosystem I in vivo, Photosynth. Res. 149 (2021) 213–231. https://doi.org/10.1007/s11120-020-00814-y.

[15] J. Lavergne, H.W. Trissl, Theory of fluorescence induction in photosystem II: derivation of analytical expressions in a model including exciton-radical-pair equilibrium and restricted energy transfer between photosynthetic units, Biophys. J. 68 (1995) 2474–2492. https://doi.org/10.1016/S0006-3495(95)80429-7.

[16] A. Joliot, P. Joliot, Etude cinétique de la réaction photochimique libérant l'oxygène au cours de la photosynthèse, C.R. Acad. Sc. Paris. 53 (1964).

[17] H. KAUTSKY, W. APPEL, H. AMANN, Chlorophyll fluorescence and carbon assimilation. Part XIII. The fluorescence and the photochemistry of plants., Biochem. Z. 332 (1960) 277–292.

[18] K. Roháček, J. Soukupová, M. Barták, Chlorophyll fluorescence: a wonderful tool to study plant physiology and plant stress, in: Plant Cell Compart. - Sel. Top., 2008: pp. 41–104. http://www.umbr.cas.cz/~rohacek/Publikace/RevChlFsemifin.pdf.

[19] U. Schreiber, Pulse-Amplitude-Modulation (PAM) Fluorometry and Saturation Pulse Method: An Overview, Chlorophyll a Fluoresc. 1367 (2007) 279–319. https://doi.org/10.1007/978-1-4020-3218-9_11.

[20] N.R. Baker, Chlorophyll fluorescence: A probe of photosynthesis in vivo, Annu. Rev. Plant Biol. 59 (2008) 89–113. https://doi.org/10.1146/annurev.arplant.59.032607.092759.

[21] J.A. Winkelstein, J.A. Bocchini, G. Schiffman, The role of the capsular polysaccharide in the activation of the alternative pathway by the pneumococcus., J. Immunol. 116 (1976) 367–70. http://www.ncbi.nlm.nih.gov/pubmed/2634.

[22] B. Schoefs, F. Franck, Photosystem II assembly in 2-day-old bean leaves during the first 16 hrs. of greening, Comptes Rendus l'Academie Des Sci. - Ser. III. 313 (1991) 441–445.

[23] O. Levitan, M. Chen, X. Kuang, K.Y. Cheong, J. Jiang, M. Banal, N. Nambiar, M.Y. Gorbunov, S.J. Ludtke, P.G. Falkowski, W. Dai, Structural and functional analyses of photosystem II in the marine diatom Phaeodactylum tricornutum, Proc. Natl. Acad. Sci. U. S. A. 116 (2019) 17316–17322. https://doi.org/10.1073/pnas.1906726116.

[24] K. Xu, J.L. Grant-Burt, N. Donaher, D.A. Campbell, Connectivity among Photosystem II centers in phytoplankters: Patterns and responses, Biochim. Biophys. Acta - Bioenerg. 1858 (2017) 459–474. https://doi.org/10.1016/j.bbabio.2017.03.003.

[25] K. Xu, J. Lavaud, R. Perkins, E. Austen, M. Bonnanfant, D.A. Campbell, Phytoplankton σPSII and excitation dissipation; Implications for estimates of primary productivity, Front. Mar. Sci. 5 (2018). https://doi.org/10.3389/fmars.2018.00281.

[26] H. Wu, S. Roy, M. Alami, B.R. Green, D.A. Campbell, Photosystem II photoinactivation, repair, and protection in marine centric diatoms, Plant Physiol. 160 (2012) 464–476. https://doi.org/10.1104/pp.112.203067.

[27] J. Lavaud, C. Six, D.A. Campbell, Photosystem II repair in marine diatoms with contrasting photophysiologies, Photosynth. Res. 127 (2016) 189–199. https://doi.org/10.1007/s11120-015-0172-3.

[28] D.M. Kramer, G. Johnson, O. Kiirats, G.E. Edwards, New fluorescence parameters for the determination of QA redox state and excitation energy fluxes, Photosynth. Res. 79 (2004) 209–218. https://doi.org/10.1023/B:PRES.0000015391.99477.0d.

[29] A. Quigg, W.C. Chin, C.S. Chen, S. Zhang, Y. Jiang, A.J. Miao, K.A. Schwehr, C. Xu, P.H. Santschi, Direct and indirect toxic effects of engineered nanoparticles on algae: Role of natural organic matter, ACS Sustain. Chem. Eng. 1 (2013) 686–702. https://doi.org/10.1021/sc400103x.

[30] K. Zhou, Y. Hu, L. Zhang, K. Yang, D. Lin, The role of exopolymeric substances in the bioaccumulation and toxicity of Ag nanoparticles to algae, Sci. Rep. 6 (2016). https://doi.org/10.1038/srep32998.

[31] E. Navarro, A. Baun, R. Behra, N.B. Hartmann, J. Filser, A.J. Miao, A. Quigg, P.H. Santschi, L. Sigg, Environmental behavior and ecotoxicity of engineered nanoparticles to algae, plants, and fungi, Ecotoxicology. 17 (2008) 372–386. https://doi.org/10.1007/s10646-008-0214-0.

[32] Z. Wang, J. Li, J. Zhao, B. Xing, Toxicity and internalization of CuO nanoparticles to prokaryotic alga microcystis aeruginosa as affected by dissolved organic matter, Environ. Sci. Technol. 45 (2011) 6032–6040. https://doi.org/10.1021/es2010573.

[33] S. Ma, K. Zhou, K. Yang, D. Lin, Heteroagglomeration of oxide nanoparticles with algal cells: Effects of particle type, ionic strength and pH, Environ. Sci. Technol. 49 (2015) 932–939. https://doi.org/10.1021/es504730k.

[34] M. Zhu, H. Wang, A.A. Keller, T. Wang, F. Li, The effect of humic acid on the aggregation of titanium dioxide nanoparticles under different pH and ionic strengths, Sci. Total Environ. 487 (2014) 375–380. https://doi.org/10.1016/j.scitotenv.2014.04.036.

[35] C. Zhang, J. Wang, L. Tan, X. Chen, Toxic effects of nano-ZnO on marine microalgae Skeletonema costatum: Attention to the accumulation of intracellular Zn, Aquat. Toxicol. 178 (2016) 158–164. https://doi.org/10.1016/j.aquatox.2016.07.020.

[36] N. Von Moos, P. Bowen, V.I. Slaveykova, Bioavailability of inorganic nanoparticles to planktonic bacteria and aquatic microalgae in freshwater, Environ. Sci. Nano. 1 (2014) 214–232. https://doi.org/10.1039/c3en00054k.

[37] F. Chen, Z. Xiao, L. Yue, J. Wang, Y. Feng, X. Zhu, Z. Wang, B. Xing, Algae response to engineered nanoparticles: Current understanding, mechanisms and implications, Environ. Sci. Nano. 6 (2019) 1026–1042. https://doi.org/10.1039/c8en01368c.

[38] F. Li, Z. Liang, X. Zheng, W. Zhao, M. Wu, Z. Wang, Toxicity of nano-TiO2 on algae and the site of reactive oxygen species production, Aquat. Toxicol. 158 (2015) 1–13. https://doi.org/10.1016/j.aquatox.2014.10.014.

[39] M. Li, D. Chen, Y. Liu, C.Y. Chuang, F. Kong, P.J. Harrison, X. Zhu, Y. Jiang, Exposure of engineered nanoparticles to Alexandrium tamarense (Dinophyceae): Healthy impacts of nanoparticles via toxin-producing dinoflagellate, Sci. Total Environ. 610–611 (2018) 356–366. https://doi.org/10.1016/j.scitotenv.2017.05.170.

[40] L. Barhoumi, D. Dewez, Toxicity of superparamagnetic iron oxide nanoparticles on green alga Chlorella vulgaris, Biomed Res. Int. 2013 (2013) 1–11. https://doi.org/10.1155/2013/647974.

[41] L.J. Hazeem, F.A. Waheed, S. Rashdan, M. Bououdina, L. Brunet, C. Slomianny, R. Boukherroub, W.A. Elmeselmani, Effect of magnetic iron oxide (Fe3O4) nanoparticles on the growth and photosynthetic pigment content of Picochlorum sp., Environ. Sci. Pollut. Res. 22 (2015) 11728–11739. https://doi.org/10.1007/s11356-015-4370-5.

[42] L.J. Hazeem, M. Bououdina, S. Rashdan, L. Brunet, C. Slomianny, R.

Boukherroub, Cumulative effect of zinc oxide and titanium oxide nanoparticles on growth and chlorophyll a content of Picochlorum sp., Environ. Sci. Pollut. Res. 23 (2016) 2821–2830. https://doi.org/10.1007/s11356-015-5493-4.

[43] C.H. da Costa, F. Perreault, A. Oukarroum, S.P. Melegari, R. Popovic, W.G. Matias, Effect of chromium oxide (III) nanoparticles on the production of reactive oxygen species and photosystem II activity in the green alga Chlamydomonas reinhardtii, Sci. Total Environ. 565 (2015) 951–960. https://doi.org/10.1016/j.scitotenv.2016.01.028.

[44] R. Mittler, ROS Are Good, Trends Plant Sci. 22 (2017) 11–19. https://doi.org/10.1016/j.tplants.2016.08.002.

[45] R.G. Joseph Seckbach, Diatoms: Fundamentals and Applications, 2019. https://doi.org/10.1002/9781119370741.

[46] A. Sánchez-Bayo, V. Morales, R. Rodríguez, G. Vicente, L.F. Bautista, Cultivation of Microalgae and Cyanobacteria: Effect of Operating Conditions on Growth and Biomass Composition, Molecules. 25 (2020) 1–17. https://doi.org/10.3390/molecules25122834.

[47] P. Heydarizadeh, I. Poirier, D. Loizeau, L. Ulmann, V. Mimouni, B. Schoefs, M. Bertrand, Plastids of marine phytoplankton produce bioactive pigments and lipids, Mar. Drugs. 11 (2013) 3425–3471. https://doi.org/10.3390/md11093425.

[48] Z.Z. Vasiljevic, M.P. Dojcinovic, J.D. Vujancevic, I. Jankovic-Castvan, M. Ognjanovic, N.B. Tadic, S. Stojadinovic, G.O. Brankovic, M. V. Nikolic, Photocatalytic degradation of methylene blue under natural sunlight using iron titanate nanoparticles prepared by a modified sol–gel method, R. Soc. Open Sci. 7 (2020). https://doi.org/10.1098/rsos.200708.

[49] L. Krienitz, A. Ballot, C. Wiegand, K. Kotut, G.A. Codd, S. Pflugmacher, Cyanotoxin-producing bloom of Anabaena flos-aquae, Anabaena discoidea and Microcystis aeruginosa (Cyanobacteria) in Nyanza Gulf of Lake Victoria, Kenya, J. Appl. Bot. 76 (2002) 179–183.

[50] M. Czaplik, R. Rossaint, E. Koch, A. Fahlenkamp, W. Schröder, P. Pelosi, W.M. Kübler, J. Bickenbach, Methods for quantitative evaluation of alveolar structure during in vivo microscopy, Respir. Physiol. Neurobiol. 176 (2011) 123–129. https://doi.org/10.1016/j.resp.2011.02.009.

[51] M.N. Merzlyak, O.B. Chivkunova, I.P. Maslova, K.R. Naqvi, A.E. Solovchenko, G.L. Klyachko-Gurvich, Light absorption and scattering by cell suspensions of some cyanobacteria and microalgae, Russ. J. Plant Physiol. 55 (2008) 420–425. https://doi.org/10.1134/S1021443708030199.

[52] B.A. OSBORNE, J.A. RAVEN, Light Absorption By Plants and Its Implications for Photosynthesis, Biol. Rev. 61 (1986) 1–60. https://doi.org/10.1111/j.1469-185x.1986.tb00425.x.

[53] K.R. Naqvi, M.N. Merzlyak, T.B. Melø, Absorption and scattering of light by suspensions of cells and subcellular particles: An analysis in terms of Kramers–Kronig relations, Photochem. Photobiol. Sci. 3 (2004) 132–137. https://doi.org/10.1039/b304781d.

[54] P. Latimer, E. Rabinowitch, Selective scattering of light by pigments in vivo, Arch. Biochem. Biophys. 84 (1959) 428–441. https://doi.org/10.1016/0003-9861(59)90605-8.

[55] K.R. Naqvi, T.B. Melø, B.B. Raju, T. Jávorfi, G. Garab, Comparison of the absorption spectra of trimers and aggregates of chlorophyll a/b light-harvesting complex LHC II, Spectrochim. Acta - Part A Mol. Biomol. Spectrosc. 53 (1997) 1925–1936. https://doi.org/10.1016/S1386-1425(97)00110-8.

[56] R.F. Pasternack, P.J. Collings, Resonance light scattering: A new technique for studying chromophore aggregation, Science (80-.). 269 (1995) 935–939. https://doi.org/10.1126/science.7638615.

[57] P. Wu, J.A. Imlay, J.K. Shang, Mechanism of Escherichia coli inactivation on palladium-modified nitrogen-doped titanium dioxide, Biomaterials. 31 (2010) 7526–7533. https://doi.org/10.1016/j.biomaterials.2010.06.032.

[58] L. Wilk, M. Strauss, M. Rudolf, K. Nicolaisen, E. Flores, W. Kühlbrandt, E. Schleiff, Outer membrane continuity and septosome formation between vegetative cells in the filaments of Anabaena sp. PCC 7120, Cell. Microbiol. 13 (2011) 1744–1754. https://doi.org/10.1111/j.1462-5822.2011.01655.x.

[59] Y.Y. He, D.P. Häder, UV-B-induced formation of reactive oxygen species and oxidative damage of the cyanobacterium Anabaena sp.: Protective effects of ascorbic acid and N-acetyl-L-cysteine, J. Photochem. Photobiol. B Biol. 66 (2002) 115–124. https://doi.org/10.1016/S1011-1344(02)00231-2.

[60] A. De Martino, A. Meichenin, J. Shi, K. Pan, C. Bowler, Genetic and phenotypic characterization of Phaeodactylum tricornutum (Bacillariophyceae) accessions, J. Phycol. 43 (2007) 992–1009. https://doi.org/10.1111/j.1529-8817.2007.00384.x.

[61] C. Bowler, A.E. Allen, J.H. Badger, J. Grimwood, K. Jabbari, A. Kuo, U. Maheswari, C. Martens, F. Maumus, R.P. Otillar, E. Rayko, A. Salamov, K. Vandepoele, B. Beszteri, A. Gruber, M. Heijde, M. Katinka, T. Mock, K. Valentin, F. Verret, J.A. Berges, C. Brownlee, J.P. Cadoret, A. Chiovitti, C.J. Choi, S. Coesel, A. De Martino, J.C. Detter, C. Durkin, A. Falciatore, J. Fournet, M. Haruta, M.J.J. Huysman, B.D. Jenkins, K. Jiroutova, R.E. Jorgensen, Y. Joubert, A. Kaplan, N. Kröger, P.G. Kroth, J. La Roche, E. Lindquist, M. Lommer, V. Martin-Jézéquel, P.J. Lopez, S. Lucas, M. Mangogna, K. McGinnis, L.K. Medlin, A. Montsant, M.P.O. Le Secq, C. Napoli, M. Obornik, M.S. Parker, J.L. Petit, B.M. Porcel, N. Poulsen, M. Robison, L. Rychlewski, T.A. Rynearson, J. Schmutz, H. Shapiro, M. Siaut, M. Stanley, M.R. Sussman, A.R. Taylor, A. Vardi, P. Von Dassow, W. Vyverman, A. Willis, L.S. Wyrwicz, D.S. Rokhsar, J. Weissenbach, E.V. Armbrust, B.R. Green, Y. Van De Peer, I. V. Grigoriev, The Phaeodactylum genome reveals the evolutionary history of diatom genomes, Nature. 456 (2008) 239–244. https://doi.org/10.1038/nature07410.

[62] M.J. Khan, Harish, A. Ahirwar, B. Schoefs, A. Pugazhendhi, S. Varjani, K. Rajendran, S.K. Bhatia, G.D. Saratale, R.G. Saratale, V. Vinayak, Insights into diatom microalgal farming for treatment of wastewater and pretreatment of algal cells by ultrasonication for value creation, Environ. Res. 201 (2021). https://doi.org/10.1016/j.envres.2021.111550.

[63] P. Heydarizadeh, B. Veidl, B. Huang, E. Lukomska, G. Wielgosz-Collin, A. Couzinet-Mossion, G. Bougaran, J. Marchand, B. Schoefs, Carbon orientation in the diatom Phaeodactylum tricornutum: The effects of carbon limitation and photon flux density, Front. Plant Sci. 10 (2019). https://doi.org/10.3389/fpls.2019.00471.

[64] R. Gordon, R. Gordon, C.R. Merz, S. Gurke, B. Schoefs, Bubble Farming: Scalable Microcosms for Diatom Biofuel and the Next Green Revolution, in: Diatoms Fundam. Appl., 2019: pp. 583–654. https://doi.org/10.1002/9781119370741.ch22.

[65] A. Fratamico, P. Tocquin, F. Franck, The chlorophyll a fluorescence induction curve in the green microalga Haematococcus pluvialis: further insight into the nature of the P–S–M fluctuation and its relationship with the "low-wave"

phenomenon at steady-state, Photosynth. Res. 128 (2016) 271–285. https://doi.org/10.1007/s11120-016-0241-2.

[66] P. NV, V. PA, R. Vemanna, S. MS, U. Makarla, Quantification of Membrane Damage/Cell Death Using Evan's Blue Staining Technique, Bio-Protocol. 7 (2017) e2519. https://doi.org/10.21769/bioprotoc.2519.

[67] J.M. Diaz, S. Plummer, C.M. Hansel, P.F. Andeer, M.A. Saito, M.R. McIlvin, NADPH-dependent extracellular superoxide production is vital to photophysiology in the marine diatom Thalassiosira oceanica, Proc. Natl. Acad. Sci. U. S. A. 116 (2019) 16448–16453. https://doi.org/10.1073/pnas.1821233116.

[68] M. Rezayian, V. Niknam, H. Ebrahimzadeh, Oxidative damage and antioxidative system in algae, Toxicol. Reports. 6 (2019) 1309–1313. https://doi.org/10.1016/j.toxrep.2019.10.001.

[69] P. Heydarizadeh, W. Boureba, M. Zahedi, B. Huang, B. Moreau, E. Lukomska, A. Couzinet-Mossion, G. Wielgosz-Collin, V. Martin-Jézéquel, G. Bougaran, J. Marchand, B. Schoefs, Response of CO2-starved diatom phaeodactylum tricornutum to light intensity transition, Philos. Trans. R. Soc. B Biol. Sci. 372 (2017). https://doi.org/10.1098/rstb.2016.0396.

[70] K. Karlsson, J. Sandstrom, A. Edlund, S.L. Marklund, Turnover of extracellular-superoxide dismutase in tissues, Lab. Investig. 70 (1994) 705–710.

General conclusions

The research work presented and discussed in this thesis aims to portray the significant water quality issues around the globe. The work details the drawbacks of currently available disinfection techniques, claiming the importance and versatility of nanoparticles and their application in heterogeneous photocatalytic disinfection. In this work specifically, we have designed a nanocomposite by embedding metal oxides, *i.e.*, titanium dioxide (TiO_2) and bismuth vanadate ($BiVO_4$) over graphene oxide (GO) sheets by an environmental-friendly and green methodology, one-step simple blending process, and used for the photocatalytic disinfection of microorganisms as well as microalga.

First, we have explored various nanoparticles and their synthesis methodologies to conclude the selection of materials for an efficient photocatalytic antibacterial property. This study consisted of synthesis of TiO_2 anatase nanoparticles through sol-gel method using titanium chloride and ethanol as the precursors and formation of five different graphene oxide/titanium dioxide (GO/TiO_2) composites (0.5 %, 1 %, 1.5 %, 2 %, 2.5 %) using a simple method without the addition of any surfactants or protective agents. All the characterizations were conducted to confirm the formation of the GO/TiO_2 (GOT) nanocomposite. The synthesized composites were checked for photocatalytic antibacterial activity, ROS effect, and disinfection kinetics. *Escherichia coli K12*, which is a model organism for the photocatalytic disinfection study, was used. From the results, the best efficiency was found for the 1.5% GO/TiO_2 composite with 99.9 % disinfection in 30 min for a bacterial concentration of 10^7 CFU/mL, by a dosage of 1.05 g/L. All these provide a novelty to this work to the best of our knowledge.

We have also explored water disinfection using graphene oxide/bismuth vanadate ($GO/BiVO_4$) or GOB nanocomposite against *Escherichia coli K12 (E. coli K12)*. The composite was developed through a facile and simple blending method at room temperature. Bismuth vanadate ($BiVO_4$) nanoparticles synthesized through the sol-gel method with a particle size of 21.3 nm were used to decorate graphene oxide (GO) sheets. The composites where of five different combinations, namely, 0.5 %, 1 %, 1.5 %, 2 % and 2.5% of $GO/BiVO_4$ (wt.% of GO). The characterization confirmed the

formation of the nanocomposite. The antibacterial ability of all the synthesized five different composites was tested using a visible-light-driven homemade photoreactor. The results revealed the efficiency of the 1.5 GOB nanocomposite at 0.1 g/L, giving 89% disinfection in 60 mins under visible light irradiation for an initial bacterial loading of 10^7 CFU/mL.

Finally, the optimized nanocomposite used for the bacterial disinfection was extended to apply the microalgal destruction by the photocatalysis process. The preliminary studies on photocatalytic disinfection using microalgae were performed against *Anabaena sp.* and *Phaeodactylum tricornutum*. For this study, we have used the nanocomposite in pellet form when compared to the bacterial disinfection. A brief description of the parameters responsible for the photocatalytic disinfection mechanism was also discussed.

Future prospects

With the promising outcomes obtained from the above investigations, future work is aimed to assess these nanoparticle systems in actual samples, and to scrutinize the effects and applications in the field would be interesting. To achieve this, it would be ideal using the synthesized nanocomposites to produce a film or pellet to gain a better microbial disinfection activity considering future applications. By keeping in mind, the application on a large-scale wastewater treatment process and avoiding the further contamination of drinking water by the powdered nanocomposite or avoiding the negative interaction with the waste elements in polluted water, better understanding of the waste nanocomposite is essential. So, prospects of microbial disinfection activity aim to reach an efficient model for the application in the sewage water treatment process and largescale drinking water treatment systems.

The preliminary results obtained from the investigation of microalgal disinfection activity are optimistic for the fight against harmful algal blooms and their toxins. As mentioned before in the microbial disinfection, more optimizations in dosage and a detailed study in the mechanism and the interaction of these nanocomposites with the salinity are essential for the active exploration of the material activity, paving the way in the destruction of microalgal cells. The effect of the ROS activity due to the nanoparticles has to be discovered for various types of microalgae, as it has got complex structure compared to the bacteria.

Contributions

- **National and International Conferences**

❏ XXVI International Materials Research Congress (IMRC 2017), August 20-25, 2017, Cancun, Mexico.

❏ XXVII International Materials Research Congress (IMRC 2018), August 19-24, 2018, Cancun, Mexico

❏ XXIX International Materials Research Congress (IMRC 2021), August 15-20, 2021, Cancun, Mexico

❏ Second Edition of the International Multidisciplinary Conference (OCEANEXT 2019), July 3, 4 and 5, 2019, Nantes, France

❏ Taller de Tratamiento de Agua con Tecnologías Sustentables (Taller 2020), February 25 and 25, 2020

❏ International E-symposium on Advanced Techniques for Energy Harvesting and storage applications (E- Sensol), July 8 – July 10, 2020

❏ XXVII Congress Iberoamericano de catalysis 2020 (CICAT 2020, October 26 – October 28, 2020

❏ 17th International Conference on Electrical Engineering, Computing Science and Automatic Control (CCE 2020), November 11 – November 13, 2020

- **Presentations**

❏ **Poster** presentation entitled "Synthesis and characterization of TiO_2/multi-walled carbon nanotubes heterostructure. Study of the photocatalytic properties on the pollutants degradation in aqueous phase", *Thomas Ch-Th,* R. Hernandez-Maya *M. Solís-López, Mercyrani B, S. Velumani,* XXVI International Materials Research Congress (IMRC 2017), August 20-25, 2017, Cancun, Mexico

❏ **Oral** presentation entitled "Graphene oxide/TiO_2 nanocomposites for *Escherichia coli* photocatalytic inactivation: the role of reactive oxygen species" *Thomas Ch-Th, M. Solís-López, S. Velumani,* XXVII International Materials Research Congress (IMRC 2018), August 19-24, 2018, Cancun, Mexico

- ❏ **Oral** presentation entitled "Photocatalytic wastewater disinfection by nanocomposite (GO/TiO₂) ROS generation: application to cyanobacteria", ***Thomas Ch-Th,*** *Brigitte Veidl, Justine Marchand, Abdelhadi Kassiba, Velumani Subramaniam, Benoît Schoefs,* Second Edition of the International Multidisciplinary Conference (OCEANEXT 2019), July 3, 4 and 5, 2019, Nantes, France

- ❏ **Poster** presentation entitled "Synthesis and characterization of GO/TiO₂ composites for photocatalytic disinfection", ***Thomas Ch-Th,*** *M. Solís-López, S. Velumani,* Taller de Tratamiento de Agua con Tecnologías Sustentables (Taller 2020), February 25 and 25, 2020

- ❏ **Poster** presentation entitled on "Photocatalityc inactivation of *Escherichia coli K12* by GO/BiVO₄ nanocomposites", ***Thomas Ch-Th****, M.Solis-Lopez, K.T.Drisya , B. Schoefs, S. Velumani ,* XXVII Congress Iberoamericano de catalysis 2020 (CICAT 2020, October 26 – October 28, 2020.

- ❏ **Poster** presentation entitled on "Photooxidation of Arsenic (III) by BiVO₄-TiO₂ nanocomposites: optimization using central composite design", *K.T. Drisya, M. Solís-López,* ***Thomas Ch-Th****, A. Kassiba and S. Velumani,* XXVII Congress Iberoamericano de catalysis 2020 (CICAT 2020, October 26 – October 28, 2020.

- ❏ **Oral** presentation entitled on "GO/BiVO₄ nanocomposites for *Escherichia coli K12* photocatalytic inactivation", ***Thomas Ch-Th****, K. T. Drisya, M. Solis -Lopez, A. Romero Nuñez, S.Velumani,* 17th International Conference on Electrical Engineering, Computing Science and Automatic Control (CCE 2020), November 11 – November 13, 2020.

- ❏ **Poster** presentation entitled on **"**Intrinsic and Al-doped ZnO thin films using radio frequency magnetron sputtering as window layer in CISe solar cell", *G. Regmi, A. Adhikari,* ***Thomas Ch-Th****, K. T. Drisya, S, Velumani,* XXIX International Materials Research Congress (IMRC 2021), August 15-20, 2021, Cancun, Mexico

- ❏ **Oral** presentation entitled on "Photocatalytic disinfection of microalgae using GO/TiO₂ nanocomposite", ***Thomas Ch-Th****, Ravichandran Manisekaran, K. T. Drisya, G. Regmi, Brigitte Veidl, Justine Marchand, A. Kassiba, Benoit Schoefs,*

S. Velumani, XXIX International Materials Research Congress (IMRC 2021), August 15-20, 2021, Cancun, Mexico.

❑ **Oral** presentation entitled on "Application of central composite design/response surface methodology for the optimization of parameters for the visible-lightinduced photocatalytic oxidation of arsenite using $TiO_2/BiVO_4$ nanocomposites", K.T. *Drisya, M. Solís-López,* **Thomas Ch-Th**, *G. Regmi, S. Velumani,* XXIX International Materials Research Congress (IMRC 2021), August 15-20, 2021, Cancun, Mexico.

● **Peer-reviewed publications**

❑ ***Thomas Ch-Th**, Ravichandran Manisekaran, Jaime Santoyo Salazar, B. Schoefs, S. Velumani, H. Castaneda, A. Jantrania*, "Graphene oxide decorated TiO_2 and $BiVO_4$ nanocatalysts for enhanced visible-light-driven photocatalytic bacterial inactivation", ***Journal of Photochemistry and Photobiology A : Chemistry***, https://doi.org/10.1016/j.jphotochem.2021.113374

❑ *Mercyrani B., R. Hernandez-Maya, M. Solís-López,* **Thomas Ch-Th**, *Velumani S,* "Photocatalytic degradation of Orange G using TiO_2/Fe_3O_4 nanocomposites", ***Journal of Materials Science Materials in Electronics*** https://doi.org/10.1007/s10854-018-9069-1

● **Conference proceedings**

❑ ***Thomas Ch-Th**, K. T. Drisya, M. Solis -Lopez, A. Romero Nuñez, S.Velumani,* "GO/$BiVO_4$ Nanocomposites for *Escherichia coli K12* Photocatalytic Inactivation", ***IEEE***, https://doi.org/10.1109/CCE50788.2020.9299170

❑ *K. T. Drisya,* **Thomas Ch-Th**, *M. Solis -Lopez, A. Romero Nuñez, S.Velumani* "Characterization of $BiVO_4$ Modified TiO_2 and its Application in the Water Treatment", ***IEEE***, https://doi.org/ 10.1109/CCE50788.2020.9299197

● **Review paper**

❑ Water treatment using Nanozymes as a photocatalytic disinfectant – under preparation.